Doctoral theses at NTNU, 2014:66

Øyvind Ygre Rogne

Numerical and Experimental Investigation of a Hinged 5-Body Wave Energy Converter

ISBN 978-82-326-0056-4 (printed version)
ISBN 978-82-326-0057-1 (electronic version)
ISSN 1503-8181

NTNU
Norwegian University of Science and Technology
Thesis for the degree of Philosophiae Doctor
Faculty of Engineering Science and Technology
Department of Marine Technology

NTNU – Trondheim
Norwegian University of
Science and Technology

Doctoral Thesis

Øyvind Ygre Rogne

Doctoral theses at NTNU, 2014:66

NTNU

NTNU – Trondheim
Norwegian University of
Science and Technology

Øyvind Ygre Rogne

Numerical and Experimental Investigation of a Hinged 5-Body Wave Energy Converter

Thesis for the degree of philosophiae doctor

Trondheim, February 2014

Norwegian University of Science and Technology
Faculty of Engineering Science and Technology
Department of Marine Technology

NTNU – Trondheim
Norwegian University of
Science and Technology

NTNU
Norwegian University of Science and Technology

Thesis for the degree of philosophiae doctor

Faculty of Engineering Science and Technology
Department of Marine Technology

ISBN 978-82-326-0056-4 (printed version)
ISBN 978-82-326-0057-1 (electronic version)
ISSN 1503-8181

Doctoral Theses at NTNU, 2014:66

Printed by Skipnes Kommunikasjon as

Abstract

This thesis deals with modeling and simulation of a hinged 5 body wave energy converter (WEC), including verification by comparison with experimental results. The WEC consists of a shallow draft cylindrical center floater hinged to 4 semisubmerged spherical buoys. One important design feature is that the hinges are submerged such that the buoys will move in a diagonal-like mode of motion.

In the first part of the thesis, the linear theory of power absorption by oscillating bodies is reviewed, having particular emphasis on multi-degree-of-freedom systems and optimization of power take-off parameters bounded by motion amplitude constraints (and a few other constraints).

The major part of the thesis deals with time domain analysis and address some modeling challenges associated with the hinged 5-body WEC and similar WECs. These modeling challenges are associated with:

- Strongly frequency dependent added mass and damping and a long hydrodynamic "memory", representing a challenge when a time domain representation of the radiation forces are sought in the form of a state space model.
- Complex equations of motion accounting for rigid hinge constraints.
- Large angular motion, particularly in the hinges, giving rise to inertia force nonlinearities.
- Large amplitude motion giving rise to greatly varying wetted body surface, making the validity of linear hydrodynamic theory questionable.

The first challenge is addressed by introducing a new frequency domain identification technique, originally developed for complex electrical networks, which (to the author's knowledge) have not been used on hydrodynamic radiation forces before. Assessment and enforcement of the physical property of *passivity* of the obtained state space models (related to the stability of the equations of motion) will also be addressed. We show that the method is capable of obtaining passive and accurate state space radiation models for the hinged 5-body WEC and an even more challenging system consisting of 17 equidistant circular cylinders.

Equations of motion (EOM) for the hinged 5-body WEC are developed assuming rigid hinge constraints and by using a minimal number of generalized coordinates. Large angular motions are accounted for. We show that by describing the velocities of all bodies in the body fixed frame of the center floater, the EOM simplify significantly. The large angular motion yields inertia force nonlinearities manifested as a hinge angle dependent mass matrix and a Coriolis-Centrifugal force term. However, a numerical study of the hinged 5-body WEC in a typical operating condition shows that a linearized EOM, assuming small angles, will suffice when the aim is to predict the mean power absorption. Still, the inertia force nonlinearities yields nonlinear behavior and affects the largest maxima and minima significantly, especially in the pitch mode of the center floater.

The most important type of nonlinearity is associated with the greatly varying submergence of the bodies, especially for the buoys. In the numerical model, this nonlinearity is accounted for in a simplified manner by including nonlinear Froude-Krylov and restoring forces, while still relying on linear radiation and diffraction forces.

The aim of the experiments conducted as part of the thesis work was to verify the numerical model. In addition, different numerical models based on different physical assumptions have been compared. The experiments included five sea states corresponding to typical operating conditions. The overprediction of mean absorbed power by the simulation model in these sea states is between -15% (underprediction) and 18%. When the Froude-Krylov and restoring forces are linearized in the traditional manner, the overprediction range from 60%, in a sea state producing large amplitude motion, down to 15%, occurring for a milder sea state. The experiments revealed that mean and low frequency motions of the same order of magnitude as the wave frequency motions are present in all modes of motion except for the collective heave mode. The nonlinear simulation model captures this effect with reasonable accuracy. One interesting finding is that the mean and low frequency surge motion is well captured *without* inclusion of the explicit second order wave forces traditionally used to analyze slow drift motions.

Acknowledgments

This project emerged from a screening study of ocean renewable energy technologies conducted by my employer Aker Solutions. I'm grateful for the financial support from Aker Solutions and the Research Council of Norway through the Industrial PhD program.

I want to thank Professor Torgeir Moan, who has been my main supervisor. Thank you for your valuable comments and for encouraging me to be an independent researcher. Also thanks to my colleague and co-supervisor Dr. Svein Ersdal. Thanks for the many discussions about novel concepts and for convincing me to include experiments as part of my research.

I would also like to thank my fellow PhD students at CeSOS and IMT in Trondheim for making my two years stay in Trondheim memorable. In particular, I would like to thank Erin Bachynski, Jacobus de Vaal and Eirik Bøckmann for rewarding collaboration with the courses and exercises during the first year. I would also like to thank Dr. Adi Kurniawan, Dr. Limin Yang and Made Muliawan for discussions regarding wave energy conversion.

Moreover, I would like to thank Torgeir Wahl and Valentin Chabaud from NTNU and Knut Arne Heggstad and his colleagues at MARINTEK for help with the scale model and the planning of the experiments.

Thanks also goes to my colleagues in Aker Solutions; Henrik Hannus and Per-Kristian Bruun for ensuring progress in the Wave Energy project, Anne Kathrine Bratland and Ragnvald Børresen for always being up for a discussion about hydrodynamics. My former colleague Thomas B. Johannessen (now in DNV) should be thanked for convincing me to pursue a PhD in the first place, a decision I do not regret.

Most of all I would like to thank Reidun and my little daughter Emmy, who makes me want to leave the office in time every day, although I have such an interesting job. The readers can thank them for preventing this thesis from being too lengthy.

Contents

Nomenclature

The nomenclature is not complete and not all symbols are uniquely defined. The reader should therefore consult the proximate text for the meaning of a symbol. Note in particular that the meaning of uppercase and lowercase letters will be different in different sections of the thesis. In sections where forces (as an example) are expressed in both the time and frequency domains, $\mathbf{F}(\omega)$ (a vector) is taken to mean the Fourier transform of $\mathbf{f}(t)$. In sections where we solely consider time domain quantities, we let $\mathbf{F}(t)$ denote a vector of generalized forces, whereas $\mathbf{f}(t)$ is reserved for Cartesian force vectors. The same goes for velocities, where $\mathbf{V}$ means either independent velocities or its Fourier transforms, whereas $\mathbf{v}$ (always in the time domain) means either independent velocities or a Cartesian velocity vector.

Abbreviations

BEM	Boundary element method
DOF	Degrees of freedom
EOM	Equations of motion
FK	Froude-Krylov
MDOF	Multiple degrees of freedom
MIMO	Multiple input multiple output
ODE	Ordinary differential equation
PTO	Power take-off
QCQP	Quadratically constrained quadratic programming
QP	Quadratic programming
SDOF	Singe degree of freedom
SISO	Single input single output
SP	Strictly proper

WEC	Wave energy converter

Operators and general notation

$\Re[.]$	Real part
$\Im[.]$	Imaginary part
$\|.\|$	Absolute value
arg(.)	Polar angle of complex number (phase of complex amplitude)
x^*	Complex conjugate of x
$\tilde{v}$	Complex amplitude of harmonic function v(t)
$\dot{v}$	Time derivative of v
$\ddot{v}$	Double time derivative of v
$\mathcal{F}(.)$	Fourier transform
$\mathcal{F}^{-1}(.)$	Inverse Fourier transform
$\mathbf{X}, \mathbf{x}$	Matrix (bold upright font)
$\mathbf{X}^T$	Transpose
$\mathbf{X}^\dagger$	Complex conjugate transpose

Symbols

γ	JONSWAP spectrum peakedness factor
λ	Wave length
$\boldsymbol{\omega}_{j/i}^{(k)}$	Angular velocity vector of frame j relative to frame i decomposed in frame k
$\boldsymbol{\omega}_{j}^{(k)}$	Angular velocity vector of frame j decomposed in frame k
ω	Angular frequency
ω_p	Spectrum peak (angular) frequency
ϕ_0	Velocity potential of undisturbed waves
ρ	Density of sea water

ρ_p	Coefficient of variation of power
σ	Standard deviation
σ_ξ	Standard deviation of wave elevation
$\sigma_{Vi,Vj}$	Covariance of velocities in mode i and mode j
ξ	Wave elevation
ξ_A	Wave amplitude
ξ_q,Ω_q	Denominator coefficients in rational transfer matrix (term number q)
$\mathbf{a}_q$,$\mathbf{b}_q$	Nominator coefficient matrices in rational transfer matrix (term number q)
$\bar{\mathbf{A}}$	6n-by-6n added mass matrix of n-body system without hinge constraints
$\hat{\mathbf{A}}$	Approximation of added mass matrix from rational transfer matrix
$\mathbf{A}$	Added mass matrix
$\mathbf{A}_\infty$	Added mass matrix for infinite frequency
$\boldsymbol{\mathcal{A}}$	System matrix of the wave radiation state space model
$\boldsymbol{\mathcal{A}}_{FM}$	System matrix of the force-to-motion system
A	Added mass
b_u	Power take-off (useful) damping. $b_u = \Re[Z_u]$.
$\bar{\mathbf{B}}$	6n-by-6n damping matrix of n-body system without hinge constraints
$\hat{\mathbf{B}}$	Approximation of damping matrix from rational transfer matrix
$\mathbf{B}$	Wave radiation damping matrix
$\mathbf{B}_u$	Power take-off (useful) damping matrix
$\boldsymbol{\mathcal{B}}$	Input matrix of the wave radiation state space model
B	Wave radiation damping
c_g	Wave group velocity

c_p	Wave phase velocity
$\bar{\mathbf{C}}$	6n-by-6n Coriolis-centrifugal matrix of n-body system (hinge constraints removed)
$\mathbf{C}$	(Generalized) Coriolis-centrifugal matrix
$\boldsymbol{\mathcal{C}}$	Output matrix of the wave radiation state space model
C_D	Drag coefficient
D	Diameter
$\mathbf{f}$	Generalized forces in the time domain. In some sections reserved for Cartesian force vectors.
$\mathbf{f}_R$	Time domain radiation forces
$\mathbf{f}_{SPR}$	Strictly proper part of time domain radiation forces
f	Force. Sometimes moment.
$f_i(\mathbf{x})$	Objective function (i=0) or constraint function (i>0) of general optimization problem
f_u	Power take-off (useful) force or moment
f_{exc}	Wave excitation force
$\bar{\mathbf{F}}$	6n-by-1 external force vector of n-body system
$\bar{\mathbf{F}}_c$	6n-by-1 constraint force vector of n-body system
$\mathbf{F}$	Vector of generalized forces (in time or frequency domain)
$\mathbf{F}_u$	Power take-off (useful) forces or moments
$\mathbf{F}_D$	Diffraction forces
$\mathbf{F}_{exc}$	Wave excitation forces
$\mathbf{F}_{FK}$	Froude-Krylov forces
$\mathbf{F}_{HSFK}$	Nonlinear Froude-Krylov and hydrostatic forces
$\mathbf{F}_{HS}$	Hydrostatic forces (from hydrostatic pressure and body weight)
$\mathbf{F}_R$	Wave radiation forces

F	Cummulative probability distribution
$F_{visc,i}$	Viscous force in mode i
g	Acceleration of gravity
$\mathbf{G}$	Restoring matrix
G	Restoring coefficient
h	Water depth
$\mathbf{H}$	General transfer function matrix
$\mathbf{H}_{F_D}$	Wave elevation to diffraction forces transfer functions (vector)
H	Wave height
H_s	Significant wave height
$\mathbf{i}_j$	X direction unit vector of frame j
$\mathbf{I}_{n\times n}$	n-by-n identity matrix
$\mathbf{j}_j$	Y direction unit vector of frame j
j	Imaginary unit
$\mathbf{J}$	Non-square transformation matrix between independent and dependent velocities
$\mathbf{J}_0$	0'th order approximation of transformation matrix, $\mathbf{J}_0 = \mathbf{J}\left(\mathbf{q} = \mathbf{0}\right)$
$\hat{\mathbf{k}}(t)$	Retardation function matrix from rational approximation
$\mathbf{k}$	Retardation function matrix
$\mathbf{k}_j$	Z direction unit vector of frame j
k	Wave number
$\hat{\mathbf{K}}$	Rational approximation of $\mathbf{K}$
$\mathbf{K}$	Retardation function matrix in the frequency domain
K_R	Beach reflection coefficient
m	Mass

$\bar{\mathbf{M}}$	6n-by-6n mass matrix of n-body system (hinge constraints removed)
$\mathbf{M}$	Mass matrix (generalized)
p	Power
p_k	Pole number k
p_m	Mean absorbed power (SI unit W)
p_u	Undisturbed pressure (static + dynamic)
p_w	Wave energy transport (SI unit W/m)
T_p	Spectrum peak period
$\mathbf{q}$	Generalized (displacement) coordinates
q	Displacement. Sometimes generalized coordinate.
$\mathbf{r}$	Position vector
$\mathbf{r}_j$	Position of body number j (origin of its frame)
$\mathbf{r}_j^{(k)}$	Position of body number j, decomposed in frame k
$\mathbf{r}_{j/i}$	$\equiv \mathbf{r}_j - \mathbf{r}_i$
$\mathbf{R}^{(i)}$	The rotation matrix that takes a vector from the the inertial frame to frame i
$\mathbf{R}_j$	The rotation matrix that takes a vector from frame j to the inertial frame
$\mathbf{R}_j^{(i)}$	The rotation matrix that takes a vector from frame j to frame i
$\mathbf{R}_k$	Residue matrix k (corresponding to pole number k)
$\mathbf{R}_x$,$\mathbf{R}_y$,$\mathbf{R}_z$	Elementary rotation matrices
s	Complex argument in the Laplace transform
$S(\omega)$	Wave (power) spectrum
$\mathbf{S}(.)$	Cross product matrix operator
τ	Moment about hinge

τ_m	Meassured moment about hinge
$L_\perp$	Lever arm
t	Time
$\mathbf{T}$	Square transformation matrix betweeen rate of change of generalized coordinates and independent velocities
$\mathbf{T}_r$	Transformation matrix between rate of change of Euler angles and angular velocities
T	Wave period
T_z	Zero-upcrossing period of wave elevation
$\mathbf{v}_j^{(i)}$	Velocity vector of origin of frame j decomposed in frame i
v	Velocity
$\bar{\mathbf{V}}$	Vector of dependent velocities
$\mathbf{V}$	Vector of independent velocities (in time or frequency domain)
$\boldsymbol{\mathcal{X}}$	State vector of the wave radiation state space model
$\mathbf{Z}$	Impedance matrix
$\mathbf{Z}_i$	Intrinsic impedance matrix
$\mathbf{Z}_u$	Power take-off (useful) impedance matrix
Z	Impedance. The real part is the damping. The imaginary part is the reactance.
Z_i	Intrinsic impedance
Z_u	Power take-off (useful) impedance

1 Introduction

1.1 Background and motivation

Ocean wave energy converters (WECs) of the oscillating body type extract power by the product of their velocity and the force opposing this velocity. The opposing force can be provided by the seabed or by other moving bodies. WECs that use the seabed to provide the opposing force can be called *bottom-referenced* whereas WECs that use the relative velocity and forces acting between multiple bodies can be called *self-referenced.* The bottom-referenced WECs are suited for near-shore, shallow water areas and may use the seabed connection as a combined power take-off (PTO) and taut mooring system. The self-referenced WECs are suitable for offshore deep water locations and typically employ a slack mooring system, preferably not affecting the relative motion used by the PTO system. Notable examples of the bottom-referenced WECs are the Oyster (www.aquamarinepower.com), which is a rotating flap mounted on the seabed, and the Seabased WEC (www.seabased.com), which is a small heaving buoy acting against the seabed. Notable examples of self-referenced WECs are the Wavebob (www.wavebob.com), which is a heaving two-body system, and the Pelamis (www.pelamiswave.com), which is a snake-like WEC utilizing the relative rotation between rigid, tubular segments.

The two types of WECs have different challenges, in terms of mathematical modeling, but more importantly in terms of performance, survivability and cost. The bottom referenced systems perhaps have an advantage in that they combine the PTO and mooring systems. This may however also be a challenge. Systems with taut mooring/PTO would have to adapt to changing tides and wave heights. If this is not handled, large tension and zero tension, with subsequent snap loads, may be experienced. The PTO must then be designed either to allow for large excursions or to withstand the forces needed to limit these excursions.

When the mooring and PTO system are separated, the mooring can be designed to be soft enough not to attract large, wave frequency forces, and only need to withstand the smaller mean and slowly varying forces associated with wind, wave drift and current. In this case, energy is extracted by the relative motion between bodies. Since the high, potentially harmful waves also have a longer period, the system of bodies can be designed to have large

relative motion in the shorter useful waves, and smaller relative motions in the longer and higher waves. A disadvantage of using slack mooring is the larger footprint of the spread mooring lines comprising the total system. This may pose a challenge when WECs are to be combined in large parks.

There are types of WECs that do not belong to any of the two categories mentioned above. Notable examples are Oscillating Water Columns (OWCs), overtopping devices and WECs that use flexible material to absorb the energy. These can be either free-floating or fixed to the sea-bottom or to the shore.

The main focus in this thesis is on self-referenced WECs. It is not an aim to discuss advantages and disadvantages of this working principle over other principles, but rather to address some modeling challenges associated with this type of WECs. Some of these challenges are related to the hydrodynamic interaction between the bodies, and is as such relevant also for farms of bottom referenced WECs that do not have mechanical interaction. Another challenge lies in the modeling of interconnected bodies that have this type of mechanical interaction.

A particular WEC will be used as a case study throughout the thesis. This WEC is referred to as the hinged 5-body WEC and consists of a circular center floater hinged to 4 smaller spherical buoys (see Figure 2.8 on page 52). The energy is absorbed through the relative rotation in the hinges. These hinges are submerged such that the buoys will oscillate in a sloped mode of motion, which has been shown to be beneficial for the power absorbing capabilities. A particular modeling challenge for this and similar WECs is the non-linearity associated with large angle excursions in the hinges.

The hinged 5-body WEC emerged from an internal screening of ocean renewable energy technologies conducted by my employer Aker Solutions, which is also funding the thesis work together with the Research Council of Norway through the Industrial PhD program.

Initially, the thesis work was intended to further develop the concept and optimize the design. However, it was early realized that such design optimization would rely heavily on the underlying physical models, and that the development of such models was itself enough of a challenge. It was also decided to include experiments as part of the early thesis work. Then, it became more sensible to "freeze" the design employed in the model tests and to use it for benchmarking of the numerical models.

1.2 Previous work

There is a large amount of literature dealing with the hydrodynamic interaction between multiple bodies. Newman (2001) treats wave effects on multiple bodies and provides numerical examples as well as a literature survey on the topic.

The paper discuss hydrodynamic phenomena such as near-trapping occurring for periodic arrays of bodies, and includes first and second order frequency domain results. These effects are captured by state of the art boundary element codes such as (for instance) WAMIT, which is a commercially available software used in the numerical examples presented by Newman as well as in the numerical examples presented in this thesis.

Hydrodynamic interaction between floating bodies is particularly relevant for WECs, since they are most often envisaged as being part of an array (or park) of WECs in order to be economically viable. Important early work on the topic of WEC arrays were conducted by Budal (1977), Evans (1979) and Falnes (1980). A very recent paper by Babarit (2013) provides guidelines for designing the layout of arrays of oscillating WECs, as well as for when their interaction needs to be included in the mathematical model. It is stated that: "for small arrays (fewer than 10 devices of 10-20 m typical dimension) with standard layouts (regular or shifted grids with separating distance of 100-200 m), the park effect can be neglected: studies show that it usually accounts for less than a few percent of the mean annual power." For larger arrays (more than 10 devices of 10-20 m typical dimension with 100-200 m spacing), the layout of the array will matter, and it is stated that when the array consists of many rows (lines of WECs perpendicular to the incoming waves), interaction can have a significant destructive effect on the array performance. It does however not seem to be a limit to the number of WECs in each row, provided that their distance is sufficiently large. The studies that support these guidelines consider WECs that oscillate in different modes of motions, and it should be noted that the mode of motion is important for the interaction between the WECs in an array.

With regard to the hinged 5-body WEC studied in this thesis, the spacing between the bodies as compared to their size is so small that interactions needs to be accounted for. We will also refer to it as a multibody WEC rather than as an array of 5 WECs. Since there is only 5 bodies, the computational burden associated with solving for the full, linear velocity potential without any approximation can be overcome. Thus, wide-spacing approximations (see e.g. Falnes, 2002) and similar approximations will not be treated in this thesis. When the full linear solution is sought, there is little principle difference in the theory between a single body with several degrees of freedom as compared to a multibody system. The main difference lies in the obtained solution. In a multibody system, the added mass and damping is often strongly frequency dependent, especially if resonant fluid motion occur between the bodies. The associated impulse response function will also have a long memory and oscillatory behavior, especially for the cross-coupling terms. This fact represents a challenge when a state space representation of the radiation forces is sought,

and this will be a major topic that will be covered in Chapter 3.

The task of finding a state space representation of a linear system based on another type of system description can be seen as a system identification problem. Identification of hydrodynamic state space models in the time domain, in which the impulse response function (retardation function) is approximated, is considered by e.g. Yu and Falnes (1995), Yu and Falnes (1998) and Babarit et al. (2005), where the latter reference used a time domain potential flow solver to obtain the impulse response functions of the radiation problem directly. Identification in the frequency domain, in which the frequency response function (comprising the added mass and damping in the case of the radiation problem), are considered by e.g. Damaren (2000), Perez and Fossen (2009) and Perez and Fossen (2011). Taghipour et al. (2008) considered both frequency and time domain identification as well as identification by using realization theory. They concluded that both frequency domain identification and realization theory work well for the container ship studied. Time domain identification was only considered for a generic rational transfer function. Unneland (2007) also compared time and frequency domain identification of wave radiation state space models, and concluded that both work well for the two single body systems under study. She noted that the frequency domain methods are more direct, since the hydrodynamic coefficients are most often obtained in the frequency domain. She also compared different methods for model order reduction (which is out of scope of this thesis). It should be mentioned that earlier works than those mentioned above exist on the topic of state space representation of hydrodynamic force models.

In this thesis, a frequency domain identification method originally developed for use with electrical power systems will be employed. The method was developed by Gustavsen and Semlyen (1999) and later improved by Gustavsen (2006) and Deschrijver et al. (2008). Methods for assessing and enforcing passivity of the obtained state space models are treated by Gustavsen (2008) and Semlyen and Gustavsen (2009). The identification method is particularly suited for strongly frequency dependent problems, and is thus suited for multibody floating systems.

WECs consisting of closely spaced bodies has previously been studied by e.g. Rogne (2007) and Taghipour and Moan (2008) which both analyze the FO3 WEC, a floating semisubmersible platform with 21 buoys translating vertically along rods fixed to the platform. Both references use frequency domain methods to analyze the performance and dynamic behavior of the WEC and both obtained the hydrodynamic coefficients (including coupling terms) using WAMIT. Whereas the first reference used WAMITs multibody approach with subsequent post-processing to reduce the number of degrees of freedom, the latter used WAMITs generalized modes approach, which enabled utilization of

FO3s two vertical planes of symmetry. Taghipour and Moan showed that the two approaches gave the same results, although the utilization of geometrical symmetry resulted in a speed-up factor of 10-15 in solving the hydrodynamic problem. In order to utilize the symmetry, it is necessary to redefine the modes of motion in such a manner that the velocity potentials of the different radiation problems are either symmetrical or anti-symmetrical about the geometrical planes of symmetry. In this thesis, WAMITs multibody approach is used to model the hinged 5-body WEC because of its ease of use, although it is acknowledged that a large speed-up can be gained by utilizing the two vertical planes of symmetry.

Hals et al. (2007) considered a heaving 2-body WEC consisting of a semisubmersible platform and a single buoy, both restricted to heave motion only (2 DOFs). The platform was similar to the platform of the FO3, consisting of four slender columns with increased diameter in the bottom such as to benefit from force compensation (or force cancellation). A realistic hydraulic PTO system subject to phase control was included in the mathematical model, which was simulated in the time domain. The mathematical model included a state-space representation of the radiation forces and accounted for the coupling of the 2 DOFs.

De Backer et al. (2010) carried out frequency domain studies of an array of closely spaced heaving buoys with emphasis on optimization of the PTO parameters. Arrays consisting of 12 and 21 buoys were considered, the latter with the same layout as the FO3 WEC.

Weller et al. (2010) carried out experimental studies of an array of 12 heaving buoys in regular and irregular waves. The array had a regular grid layout consisting of 4 rows perpendicular to the incoming waves, each comprising 3 buoys. The center-center spacing in both directions was 2 diameters. Their investigations showed that interactions between the buoys significantly affected the performance of the array both in regular and irregular waves.

Whereas arrays of bottom referenced WECs only have hydrodynamic interaction, self-referenced WECs consisting of multiple bodies have both hydrodynamic and mechanical interaction. The calculation of hydrodynamic forces and interaction within the framework of linear potential flow theory rests on a number of assumptions such as for instance low wave steepness, small amplitude motion and irrotational, inviscid flow. Some of these assumptions are clearly questionable in many practical situations. In that context, the assumptions that forms the basis for modeling of mechanical interactions, such as e.g. that the rigid bodies are in fact rigid, and that rotation about hinges are free of friction, are most often less worrying, especially if the small angle approximation is removed. Still, the inertia forces in multibody systems with mechanical constraints (such as e.g. hinges) are often linearized by assuming small angles,

which will simplify the equations of motion significantly. One can argue that this linearization is consistent with the linear hydrodynamic forces. However, a consistent mathematical model is not necessarily the most accurate model, and it is worth investigating if the removal of the small angle approximation (as well as other approximations) in the calculation of some of the force terms in the equations of motion can give increased accuracy.

Ó'Catháin et al. (2008) presents a general modeling methodology for multi-body systems with application to WECs. They focus on the formulation of equations of motion in terms of a minimal number of modes of motion, including inertia force nonlinearities due to large angular motion. In this thesis, we will apply this methodology to the hinged 5-body WEC, and compare it to a different approach based on Lagrange's equation (the approach of Ó'Catháin et al. was based on the Newton-Euler equations). We will show that the two approaches are equivalent. Because the numerical implementation of the equations of motion are rather complex, comparing these two implementations are useful as a debugging aid. The numerical example given by Ó'Catháin et al. had two DOFs, both of which were rotations. In this case, the selection of generalized coordinates and independent velocities is rather obvious. The hinged 5-body WEC includes a center floater which is free to move in 6 degrees of freedom. The selection of generalized coordinates and independent velocities (the latter of which is not necessarily the time derivative of the former) is less obvious in this case, and the choice made will have an impact on the complexity of the resulting equations of motion.

One example of a linearized modeling approach for a vertical pendulum contained within a floating body (the SEAREV WEC) using a minimal number of DOFs is given by Babarit et al. (2005). A nonlinear (large angle) modeling approach of a similar device consisting of a planar pendulum contained within a floating body is described by Bretl (2009).

Several authors have attempted to extend the applicability of linear hydrodynamic theory to problems with large amplitude motions without resolving to more time-consuming alternatives such as fully non-linear BEM or CFD. Notable contributions from the wave energy community are the work by Babarit et al. (2009), Gilloteaux et al. (2008) and Merigaud et al. (2012). These articles were motivated by the fact that, under certain circumstances, the Froude-Krylov and hydrostatic forces will dominate over the radiation and diffraction forces. The numerical model developed as part of this thesis will include non-linear Froude-Krylov and hydrostatic forces, while relying on linear diffraction and radiation forces. This modeling approach will be presented in Chapter 5.

A different approach, including nonlinear radiation and diffraction forces based on the so-called weak scatterer free surface conditions, is reported by Bretl (2009). His work was aimed at describing the dynamic behavior of a

small data collecting buoy whose characteristic length is an order of magnitude smaller than the amplitude of the incoming waves. As described above, the buoy contained an internal planar pendulum for power absorption. A nonlinear desingularized BEM method was developed that required absorbing beaches in the boundary of the computational domain and discretisation of the free surface as well as the body surface. His studies were restricted to regular waves.

1.3 Objectives

The main objectives of the thesis work are to:

1. Review the well established linear theory of power absorption by oscillating bodies with emphasis on multi-degree-of-freedom (MDOF) systems.

2. Suggest numerical schemes for optimization of the power take-off (PTO) system parameters of a MDOF WEC in regular and irregular waves. The optimization should account for constraints on the amplitudes of individual motion components (as well as other constraints), meaning that closed form solutions are unavailable.

3. Employ the aforementioned frequency domain techniques and optimization schemes to the hinged 5-body WEC in order to determine its theoretical power absorption limit under various constraints.

4. Develop a nonlinear numerical model of the hinged 5-body WEC. The model is intended to be used for future design optimization, requiring parameter variation and a large number of simulations. For this reason, the model is based on computationally efficient hydrodynamic force models based on linear diffraction and radiation and the commercial BEM code WAMIT. Key features of the numerical model are:

    a) A formulation that treats the hinge constraints as completely rigid, meaning that the 5-body system will have 6 collective DOFs and 4 hinge DOFs (10 DOFs in total). Based on a suitable definition of independent parameters describing the displacements and velocities in the system, exact (large angle) kinematic relationships will be developed.

    b) Inclusion of inertia force nonlinearities, manifested as a Coriolis-centrifugal force term and a hinge angle dependent mass matrix.

    c) Inclusion of the fluid memory effect by using an efficient state space representation of the radiation forces including coupling between the

bodies. As part of this, it is necessary to find a robust identification technique suitable for multibody systems, which is typically characterized by strongly frequency dependent added mass and damping.

d) Inclusion of non-linear Froude-Krylov and hydrostatic forces. This force model accounts for the effect of time varying wetted body surface under the undisturbed waves.

5. Compare the numerical model with model test results in sea states that represent typical operating conditions.

6. Assess the importance of the nonlinearities included in the numerical model.

1.4 Scope

An important topic in the analysis of WECs is the modeling of realistic PTO systems, which may comprise models of hydraulic and electrical components depending on the fidelity of the model and type of PTO system. This is out of scope of this thesis. Instead we will employ simplified PTO models, and in particular a linear, frequency independent damping model. Idealized reactive PTO systems will also be considered by frequency domain analysis, but this will not be a main topic. The numerical optimization schemes that will be suggested in Chapter 2 only optimize the parameters of the simplified PTO system. Optimization of the geometry of the device will not be considered.

Analysis techniques that can be useful for reducing the computational time for systems comprising a large number of floating bodies, such as the wide-spacing approximation, will not be addressed. A range of these techniques have recently been reviewed by Folley et al. (2012), focusing on large arrays of WECs. Arrays of widely spaced bodies and the interaction between them will however be treated, mainly as a mean to assess the wall effects in the conducted model tests. The equivalence between the problem of a single body in a channel, and that of an infinite (or large enough) array of bodies, enables such a study.

The important topic of behavior and survivability in extreme sea states will not be investigated. It is however believed that the numerical models developed as part of the thesis will be an important first step in such investigations. The nonlinearities included in the numerical models presented in this thesis will be increasingly important in more severe sea states. Still, other nonlinearities, which is not included, may also be important and such investigations should therefore be accompanied by dedicated model tests.

1.5 Outline

Chapter 2 deals with the linear frequency domain analysis of power absorption by oscillating bodies with one or more degrees of freedom. Firstly, the formula for wave energy transport in regular and irregular waves on infinite and finite water depths are given. Then, the well known theory of power absorption by a WEC oscillating in one DOF is introduced. The theory is exemplified by a numerical example using a spherical buoy oscillating in a sloped mode of motion, a case study that motivates the design of the hinged 5-body WEC. The theory is then extended to systems oscillating in multiple DOFs. The lack of a closed form solution for the optimal power absorption under amplitude constraints on individual modes of motion motivates the formulation of a numerical optimization problem for regular waves (for a fixed geometry). Due to the convexity of this optimization problem, the global optimum can be found using well established numerical tools. A different (non-convex) optimization problem for irregular waves, assuming a linear resistive PTO model is then suggested. Moreover, a two-objective optimization problem that accounts for the short term variability of the absorbed power is also suggested. This latter problem rests on an expression for the variance of the absorbed power of a MDOF WEC under the assumption of Gaussian body motions and a linear resistive PTO system. Chapter 2 also introduce the hinged 5-body WEC as a case study, and the different optimization methods are applied to this WEC.

Chapter 3 discuss wave radiation forces in the time and frequency domains and suggests a new approach for identification of a state space representation of these forces. The new approach is particularly suited for the high order models needed to represent problems with strongly frequency dependent added mass and damping. Although the considered radiation forces are linear, such a representation is an important first step in the development of the nonlinear simulation model, since it enables time domain simulation with inclusion of external nonlinearities. The chapter starts with introducing Cummin's equation and the retardation function, and discuss inherent properties of the radiation forces (in both time and frequency domain) that should be retained in the state space approximation. Then, rational transfer functions and transfer matrices on different forms are discussed. The time domain representation of these transfer matrices, either as a set of first order differential equations (the state space model), a set of second order differential equations, or finally, as impulse response (retardation) functions, are also given. The identification procedure is then described. The passivity assessment and enforcement steps of the identification procedure are described in more detail, since these steps have been modified to suit wave radiation problems (as opposed to the electrical problems the method was originally developed for). Finally, the identification procedure

is demonstrated for the hinged 5-body WEC and an array of 17 circular cylinders, the latter problem possessing particularly strong frequency dependency. The case of a single circular cylinder is also included for comparison.

Chapter 4 derive equations of motion for the hinged 5 body WEC. Important steps in doing so is the definition of a suitable set of independent parameters describing the displacements and velocities of the system, and the formulation of exact (large-angle) kinematic relationships that relate these independent parameters to the description of the motions of each individual body. The importance of the inertia nonlinearities included in the equations of motion are assessed by simulating the hinged 5-body WEC in one irregular sea-state and a regular wave.

Chapter 5 describe the nonlinear Froude-Krylov and hydrostatic forces that are part of the simulation model. The chapter starts with giving a motivation for such a model and a discussion of its limitations. An account of previous work on the topic is also given. Then, the mathematical definition and numerical implementation is described. This rests to a large extent on the multibody kinematic relationships described above. Since the relative importance of the Froude-Krylov forces relative to the diffraction forces are important for the success of the method, these force components (in terms of linear transfer functions) are plotted as a function of frequency for the hinged 5-body WEC.

Chapter 6 presents the results of the conducted model tests and compare these with two different simulation models, one that include nonlinear Froude-Krylov and hydrostatic forces and one that linearize these forces in the traditional manner. The experimental setup is described with particular emphasis to the PTO system. The importance of beach and side-wall reflections are assessed by simplified analysis. The mathematical models are also summarized and given a more specific description, with emphasis on the aspects that are relevant for the scale model, such as the representation of PTO, mooring etc.

2 Linear analysis of power absorption

2.1 Wave energy transport and capture width

The energy in ocean waves consists of an equal amount of kinetic and potential energy. According to linear wave theory, the average stored energy under a regular wave can be written (Falnes, 2002):

$$E = E_p + E_k = 2E_p = \frac{1}{2}\rho g \xi_A^2 \tag{2.1}$$

Here, ρ is the density of the sea water, g is the acceleration of gravity and ξ_A is the wave amplitude. E have SI unit J/m^2 and corresponds to the average energy content in a vertical water column of unit cross sectional area extending from the free surface down to the sea bottom. It's worth noting that E is independent of the water depth.

When wave energy is to be harvested, it is more relevant to consider the (average) wave energy transport p_w, expressing the amount of energy that is transported past a unit width control surface per second. The control surface is taken perpendicular to the wave propagation direction and extends all the way down to the sea bottom. p_w can be obtained by integrating the product of pressure and horizontal velocity over the control surface, and averaging over a wave period. Assuming unidirectional waves (no standing wave component), the following expression is obtained,

$$p_w = Ec_g = \frac{1}{2}\rho g \xi_A^2 c_g \tag{2.2}$$

showing that the wave energy travel with the group velocity c_g. The wave energy transport have SI unit W/m.

The group velocity is given by the expression,

$$c_g = \frac{1}{2}c_p\left(1 + \frac{kh - kh\tanh^2(kh)}{\tanh(kh)}\right) \tag{2.3}$$

where c_p is the phase velocity of the waves, given as:

$$c_p = \frac{\lambda}{T} = \frac{\omega}{k}\,,\ \omega = \frac{2\pi}{T}\,,\ k = \frac{2\pi}{\lambda} \tag{2.4}$$

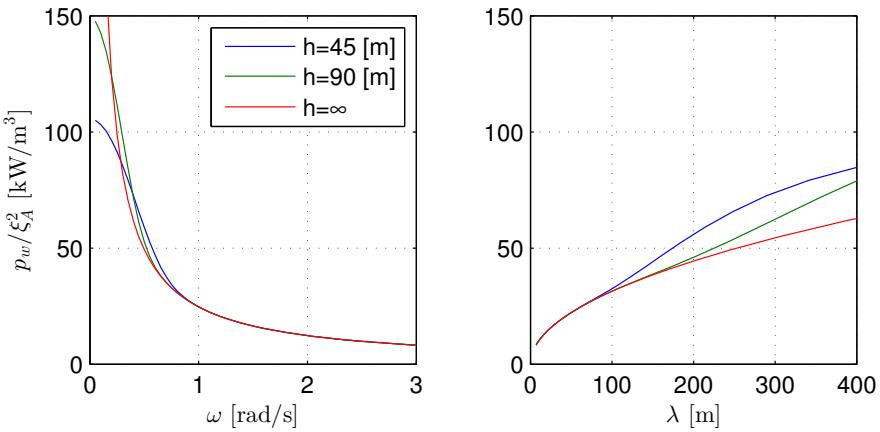

Figure 2.1: Mean energy transport in regular waves

Here, ω is the angular frequency, T is the period, k is the wave number, λ is the wave length and h is the water depth. The phase velocity is governed by the dispersion relation, relating k and ω:

$$\omega^2 = kg \tanh(kh) \tag{2.5}$$

When the water depth is much larger than the wave length, we can use that $\tanh(kh) \to 1$ when $kh \to \infty$ and write $\omega^2 = kg$ and $c_g = c_p/2$.

Figure 2.1 shows the energy transport in regular waves for different frequencies and water depths. The case of 45 meter depth is included because it correspond to the full-scale equivalent of the depth in the towing tank used in the experiments that will be presented in Chapter 6.

In unidirectional irregular (random) waves, the wave energy transport becomes,

$$p_w = \rho g \int_0^\infty S(\omega)\, c_g(\omega)\, d\omega = 2 \int_0^\infty S(\omega)\, p_{unit}(\omega)\, d\omega \tag{2.6}$$

where the wave spectrum $S(\omega)$ is related to the (infinitesimal) wave amplitudes of the regular wave components as $S(\omega)\, d\omega = \xi_A^2/2$. In the latter expression, we let $p_{unit}(\omega)$ mean the energy transport in a regular wave with unit amplitude.

The wave spectrum $S(\omega)$ expresses the power spectral density of the surface elevation in a short term stationary sea state. A particular model for $S(\omega)$ is

the JONSWAP model, expressed as (e.g. DNV, 2007):

$$S_J(\omega) = A(\gamma) S_{PM}(\omega) \gamma^{\exp\left(-\frac{1}{2}\left(\frac{\omega-\omega_p}{\sigma\omega_p}\right)\right)} \tag{2.7}$$

Here, $S_{PM}(\omega)$ is the Pierson-Moskowitz (PM) spectrum and γ is a non-dimensional peak shape parameter. The spectral width parameter σ can be taken as 0.07 for $\omega \leq \omega_p$ and 0.09 for $\omega > \omega_p$. $A(\gamma)$ is a normalizing factor ensuring that $\int_0^\infty S_J(\omega)\, d\omega = \int_0^\infty S_{PM}(\omega)\, d\omega$. When $\gamma = 1$, the JONSWAP spectrum is identical to the PM spectrum:

$$S_{PM}(\omega) = \frac{5}{16} H_s^2 \omega_p^4 \omega^{-5} \exp\left(-\frac{5}{4}\left(\frac{\omega}{\omega_p}\right)^{-4}\right) \tag{2.8}$$

Here, $\omega_p = 2\pi/T_p$ is the peak frequency and H_s is the significant wave height (of both S_J and S_{PM}), defined as four times the standard deviation of the random sea surface:

$$H_s = 4\sigma_\xi = 4\sqrt{\int_0^\infty S(\omega)\, d\omega} \tag{2.9}$$

The PM model is applicable for wind generated fully developed seas whereas the JONSWAP model extends the applicability to developing seas (e.g. DNV, 2007).

The non-dimensional JONSWAP spectrum $S_J\omega_p/H_s^2$ as a function of non-dimensional frequency ω/ω_p, have γ as it's only parameter and is illustrated in Figure 2.2 for different γ.

Unless site-specific data is available, DNV (2007) recommends to relate γ to the parameter $T_p/\sqrt{H_s}$ in the following manner,

$$\gamma = \begin{cases} 5 & T_p/\sqrt{H_s} \leq 3.6 \\ \exp\left(5.75 - 1.15\dfrac{T_p}{\sqrt{H_s}}\right) & 3.6 < T_p/\sqrt{H_s} \leq 5 \\ 1 & 5 \leq T_p/\sqrt{H_s} \end{cases} \tag{2.10}$$

expressing the fact that steep waves tend to have a more peaked spectrum.

$S(\omega)$ describe the distribution of stored wave energy over frequencies. The total stored energy is thus proportional to H_s^2 and independent of ω_p, γ and the water depth h. The distribution of wave energy *transport* is however described by $S(\omega) c_g(\omega)$, as seen by eq. (2.6). The total wave energy transport p_w will therefore depend on all spectral parameters H_s, ω_p and γ in addition to the water depth h. In Figure (2.3), it is seen that p_w is proportional to H_s^2 and

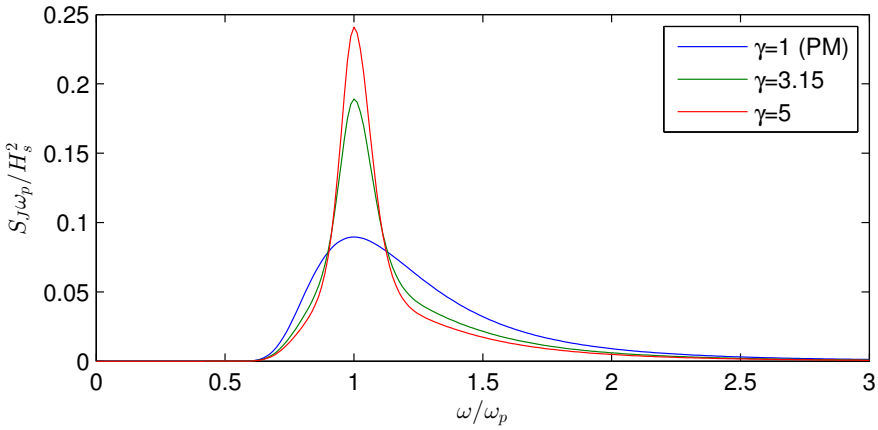

Figure 2.2: Non-dimensional JONSWAP spectra for different γ. The area under all curves is 1/16.

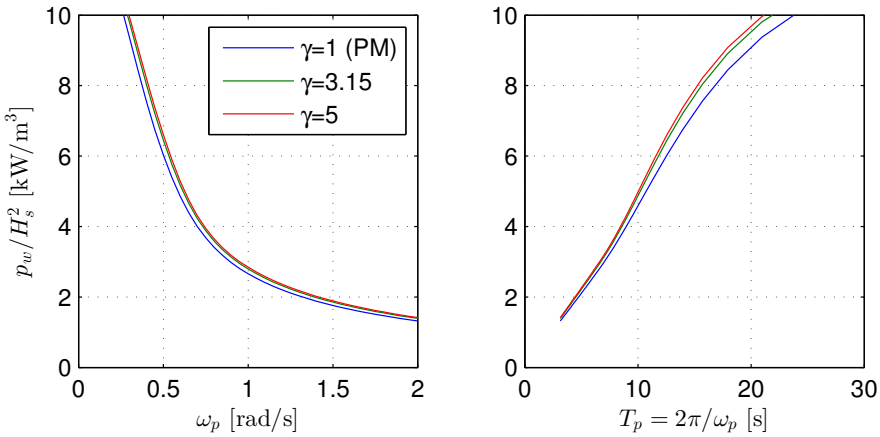

Figure 2.3: Mean energy transport in irregular waves with a JONSWAP spectrum and 45 m water depth

have in addition a strong dependency on ω_p and a relatively weak dependency on γ.

In deep water, the wave energy transport becomes:

$$p_w = \frac{1}{2}\rho g^2 \int_0^\infty \frac{S(\omega)}{\omega} d\omega \approx \frac{1}{2}\rho g^2 \frac{H_s^2 (4.2+\gamma)}{16\omega_p (5+\gamma)} \tag{2.11}$$

Here, the last expression is an approximation suggested by DNV (2007), only applicable for JONSWAP spectra. The first expression holds for all spectral models.

It is customary in the wave energy community to describe the power absorption of a wave energy converter (WEC) in terms of its *capture width*, defined as the ratio p_m/p_w (SI unit m) where p_m is the mean absorbed power. Since the capture width will often be used to present numerical result in this thesis, Figure (2.1) and (2.3) will be useful in translating the capture widths into the actual absorbed power. We will also sometimes use the non-dimensional *relative capture width,* $p_m/(Dp_w)$, where D is a characteristic dimension of the WEC.

2.2 Single degree of freedom (SDOF) WECs

The most widely studied type of WECs are those assumed to oscillate in only one degree of freedom. The *linear* dynamic behavior of such a WEC is similar to that of the classical mass-damper-spring oscillator treated in most textbooks on dynamics. One important difference is that the added mass and damping coefficients of a floating body is frequency dependent, resulting in a time domain representation involving a convolution integral. This fact makes frequency domain analysis particularly useful. In the frequency domain, the temporal variables are harmonic in time and form a basis for more general solutions expressed as a superposition of harmonics.

It is convenient to express a harmonic quantity $v(t)$ in terms of its complex amplitude $\tilde{v}$. For an angular frequency ω, their relation can be expressed in various ways:

$$\begin{aligned} v(t) &= \frac{1}{2}\tilde{v}\exp(j\omega t) + \frac{1}{2}\tilde{v}^*\exp(-j\omega t) && \text{(2.12a)}\\ &= \Re[\tilde{v}\exp(j\omega t)] && \text{(2.12b)}\\ &= \Re[\tilde{v}]\cos(\omega t) - \Im[\tilde{v}]\sin(\omega t) && \text{(2.12c)}\\ &= |\tilde{v}|\cos(\omega t + \arg(\tilde{v})) && \text{(2.12d)} \end{aligned}$$

Here, $j = \sqrt{-1}$ is the imaginary unit. The complex amplitude have a real and imaginary part, $\tilde{v} = \Re[\tilde{v}] + j\Im[\tilde{v}]$, and a complex conjugate, $\tilde{v}^* = \Re[\tilde{v}] -$

$j\Im[\tilde{v}]$. A polar representation is given by the magnitude, $|\tilde{v}| \equiv \sqrt{\Re[\tilde{v}]^2 + \Im[\tilde{v}]^2}$, and phase, $\arg(\tilde{v}) \equiv \arctan(\Im[\tilde{v}]/\Re[\tilde{v}])$. In the following, we will take $\tilde{v}$ as the complex amplitude of the velocity of the WEC, although we will frequently refer to it simply as the velocity.

In the frequency domain, differentiation with time reduces to multiplication with $j\omega$. Hence, the displacement becomes $\tilde{q} = \tilde{v}/(j\omega) = -j\tilde{v}/\omega$ and the acceleration becomes $j\omega\tilde{v}$. The equation of motion can now be formulated as,

$$\left[B(\omega) + j\omega(m + A(\omega)) - j\frac{G}{\omega}\right]\tilde{v}(\omega) = \tilde{f}_{exc}(\omega) \tag{2.13a}$$

$$Z_i(\omega)\,\tilde{v}(\omega) = \tilde{f}_{exc}(\omega) \tag{2.13b}$$

where we also indicate which quantities that are functions of frequency. Here, m is the mass of the WEC, A is the added mass, B is the radiation damping, G is the restoring coefficient and $\tilde{f}_{exc}$ is the wave excitation force. Following Falnes (2002), we also define the intrinsic impedance Z_i, in analogy with similar system descriptions in other branches of physics (electronics, acoustics etc). The imaginary part $\Im[Z_i]$ is called the intrinsic reactance. Falnes refer to the real part $\Re[Z_i]$ as a radiation resistance, whereas we will use the term radiation damping, in line with the usual terminology in marine hydrodynamics.

In order to convert the wave energy into useful energy, the WEC has to work against a power take-off (PTO) force. In a linear analysis, we assume an harmonic PTO force expressed in terms of an impedance, $\tilde{f}_u = -Z_u\tilde{v}$. Hence, there is generally one force component in phase with velocity, and one force component out of phase with the velocity. Including the linear PTO system, the equation of motion becomes:

$$(Z_i + Z_u)\,\tilde{v} = \tilde{f}_{exc} \tag{2.14a}$$

$$Z\tilde{v} = \tilde{f}_{exc} \tag{2.14b}$$

The power converted by the PTO system is the product of PTO force and velocity. Using eq. (2.12) we can write the absorbed power as a function of time as:

$$
\begin{aligned}
p_u(t) &= -f_u(t)\, v(t) && \text{(2.15a)}\\
&= -\frac{1}{4}\left(\tilde{f}_u\tilde{v}^* + \tilde{f}_u^*\tilde{v} + \tilde{f}_u\tilde{v}\exp(2j\omega t) + \tilde{f}_u^*\tilde{v}^*\exp(-2j\omega t)\right) && \text{(2.15b)}\\
&= -\frac{1}{2}\left(\Re\left[\tilde{f}_u\tilde{v}^*\right] + \Re\left[\tilde{f}_u\tilde{v}\exp(2j\omega t)\right]\right) && \text{(2.15c)}\\
&= \frac{1}{2}\left(\Re\left[Z_u\tilde{v}\tilde{v}^*\right] + \Re\left[Z_u\tilde{v}^2\exp(2j\omega t)\right]\right) && \text{(2.15d)}\\
&= \underbrace{\frac{1}{2}\Re\left[Z_u\right]|\tilde{v}|^2}_{p_m} + \frac{1}{2}|Z_u|\,|\tilde{v}|^2\cos\left(2\omega t + \arg\left(Z_u\tilde{v}^2\right)\right) && \text{(2.15e)}
\end{aligned}
$$

Here, p_m is the active or mean absorbed power, which is seen to be constant in time and dependent only on the real part of the PTO impedance. The time varying term is called the reactive power and oscillate with a frequency twice that of the body motion. The reactive power has zero time average and is proportional to the absolute value of the PTO impedance. By solving the equation of motion (2.14) for $\tilde{v}$, we can write the mean absorbed power,

$$
\begin{aligned}
p_m &= \frac{\Re\left[Z_u\right]\left|\tilde{f}_{exc}\right|^2}{2\left|Z_i + Z_u\right|^2} && \text{(2.16a)}\\
&= \frac{\frac{1}{2}b_u\left|\tilde{f}_{exc}\right|^2}{\left(B + b_u\right)^2 + \left(\omega\left(m + A\right) - \frac{G}{\omega} + \Im\left[Z_u\right]\right)^2} && \text{(2.16b)}
\end{aligned}
$$

where we in eq. (2.16b) introduce the PTO damping coefficient $b_u \equiv \Re\left[Z_u\right]$. Looking at eq. (2.16b), it is evident that $\left|\tilde{f}_{exc}\right|$ should be maximized. To minimize the denominator and thus maximize the absorbed power, we should also bring the total reactance to zero, which is the same as attaining resonance. Apparently, the radiation damping B should also be minimized. This is however an incorrect conclusion since it is in conflict with the goal of maximizing $\left|\tilde{f}_{exc}\right|$. This is because $\tilde{f}_{exc}$ and B are related by the Haskind relation (see Newman (1977) or Falnes (2002), for instance). Falnes emphasizes that power absorption should be understood as a wave interference phenomena where the incoming waves are reduced by the radiated waves far away from the body. Since B is associated with the radiated waves far away, a non-zero B is in fact a premise for power absorption.

In order to achieve resonance, the PTO system should provide an impedance of equal size, but of opposite sign, as the intrinsic impedance:

$$
\Im\left[Z_{u,opt}\right] = -\Im\left[Z_i\right] \tag{2.17}
$$

There is also a unique value of b_u that maximizes the absorbed power (Falnes, 2002):

$$b_{u,opt} = \sqrt{B^2 + \left(\omega\left(m + A\right) - \frac{G}{\omega} + \Im\left[Z_u\right]\right)^2} \tag{2.18}$$

If both eq. (2.17) and eq. (2.18) are satisfied, we have that:

$$Z_{u,opt} = Z_i^* \tag{2.19}$$

$$= B - j\omega\left(m + A\right) + j\frac{G}{\omega} \tag{2.20}$$

A WEC that achieves this optimum is sometimes said to be under complex conjugate control. Then, the mean absorbed power becomes,

$$p_{m,opt} = \frac{\left|\tilde{f}_{exc}\right|^2}{8B} \tag{2.21}$$

achieved when the body have a velocity:

$$\tilde{v}_{opt} = \frac{\tilde{f}_{exc}}{2B} \tag{2.22}$$

It is seen that optimum absorption requires that $\tilde{v}$ and $\tilde{f}_{exc}$ are in phase.

For a heaving axisymmetric WEC, eq. (2.16) reduce to,

$$p_{m,opt} = \frac{\lambda}{2\pi} p_w \tag{2.23}$$

$$= \frac{\rho g^3 \left|\tilde{\xi}\right|^2}{4\omega^3} \tag{2.24}$$

where λ and $\left|\tilde{\xi}\right|$ is the length and amplitude of the incoming waves and p_w is the energy transport per meter wave front (SI unit W/m), in deep water given by $p_w = \rho g^2 \left|\tilde{\xi}\right|^2 / \left(4\omega\right)$. According to Falnes (2002), this result was derived independently by Budal and Falnes (1975), Evans (1976) and Newman (1976). It is a remarkable result, since it shows that the maximum absorbed power is a function only of the incoming waves, and independent of the size and (axisymmetric) geometry of the absorbing body. The result thus indicates that economical WECs should be very small in order to save material cost. However, a small body has to move with a larger motion amplitude $|\tilde{q}|$ than a similar large body in order to absorb the same amount of energy. Then one must remember that linear theory is only valid when $|\tilde{q}| \ll D$ where D is the diameter or other characteristic length of the WEC. It is therefore necessary to impose a constraint on the displacement amplitude such that $|\tilde{q}| < q_{max}$.

This can be done by using an increased value of b_u, obtained by solving the equation of motion for b_u rather than for the motions, using the maximum allowed motion amplitude as input. Evans (1981) showed that the maximum absorbed power respecting a amplitude constraint can be written as,

$$p_{m,opt,c} = p_{m,opt}\left(1 - (1-\alpha)^2 H(1-\alpha)\right) \tag{2.25}$$

corresponding to a PTO damping coefficient,

$$b_{u,opt,c} = b_{u,opt}\left(1 + \frac{2(1-\alpha)}{\alpha} H(1-\alpha)\right) \tag{2.26}$$

where α is a reduction factor on the velocity amplitude and $H(x)$ is the unit step function, defined as:

$$\alpha = \frac{\omega q_{max}}{|\tilde{v}_{opt}|}, \; H(x) = \begin{cases} 1 & , x \geq 0 \\ 0 & , x < 0 \end{cases} \tag{2.27}$$

There is no obvious choice for q_{max}. For a heaving body, Budal and Falnes (1980) suggested that the volume swept by the waterplane area during a full oscillation cycle should be less than the total volume of the body, giving the amplitude constraint $|\tilde{q}| < V/(2A_{WL})$. By neglecting the radiated power and taking the low frequency asymptote of excitation force as an upper limit, $\tilde{f}_{exc} < \rho g A_{WL} \tilde{\xi}$, they arrived at the following upper bound for the ratio between absorbed power and absorber volume V:

$$\frac{p_m}{V} < \frac{\rho g \omega \left|\tilde{\xi}\right|}{4} \tag{2.28}$$

This upper limit as a function of frequency is known as the Budal curve. An important note is that V is the total volume of the body, including the part above the mean waterline. This upper limit can only be approached for low frequencies, when the low frequency excitation force is relatively accurate and the maximum allowed motion amplitude is much smaller than the optimal amplitude, so that the neglected radiated power is small.

2.2.1 Case study: Spherical WEC translating along a slope

Figure 2.4 shows a semi-submerged spherical WEC translating along a rod inclined at an angle of θ relative to the vertical. The rod is fixed in space so the system have only 1 DOF. In this case, the hydrodynamic coefficients needed in the equation of motion (2.13) can be found from the horizontal and

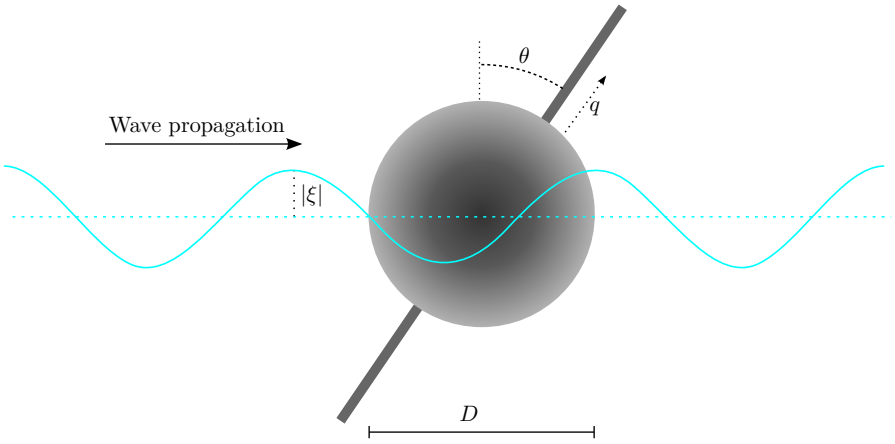

Figure 2.4: Sloped WEC

vertical coefficients by a transformation of coordinates,

$$\tilde{f}_{exc} = \sin(\theta)\,\tilde{f}_{exc,1} + \cos(\theta)\,\tilde{f}_{exc,3} \tag{2.29}$$

$$A = \sin^2(\theta)\,A_{11} + \cos^2(\theta)\,A_{33} \tag{2.30}$$

$$B = \sin^2(\theta)\,B_{11} + \cos^2(\theta)\,B_{33} \tag{2.31}$$

$$G = \cos^2(\theta)\,\rho g A_{WL} \tag{2.32}$$

where subscripts 1 and 3 designate the surge (x-direction) and heave (z-direction) modes, defined relative to the center of the sphere. There is no hydrodynamic coupling between the surge and heave mode for this choice of reference point. We note in particular that the restoring coefficient approaches zero as θ approaches $\pm 90°$, which means that the natural period approaches infinity in the same limit.

Figure 2.5 shows the hydrodynamic coefficients needed to solve the equation of motion, here expressed as contour lines in the ω-θ plane. Infinite water depth is assumed. The excitation force is normalized with respect to its low frequency asymptotic value for heave, which is also the upper limit used in the derivation of the Budal curve, eq. (2.28). Note in particular the contour line for zero reactance, indicating the combinations of slope angle and frequency where resonance occurs for a WEC without PTO reactance.

We first investigate the performance for the case $\theta = 0$, corresponding to a pure heave motion. We consider regular waves with steepness $H/\lambda = 1/30$ and $H/\lambda = 1/60$ (with $H = 2\left|\tilde{\xi}\right|$) and impose a displacement amplitude constraint $|\tilde{q}| < V/(2A_{WL}) = D/3$, which is the same constraint used in the derivation of

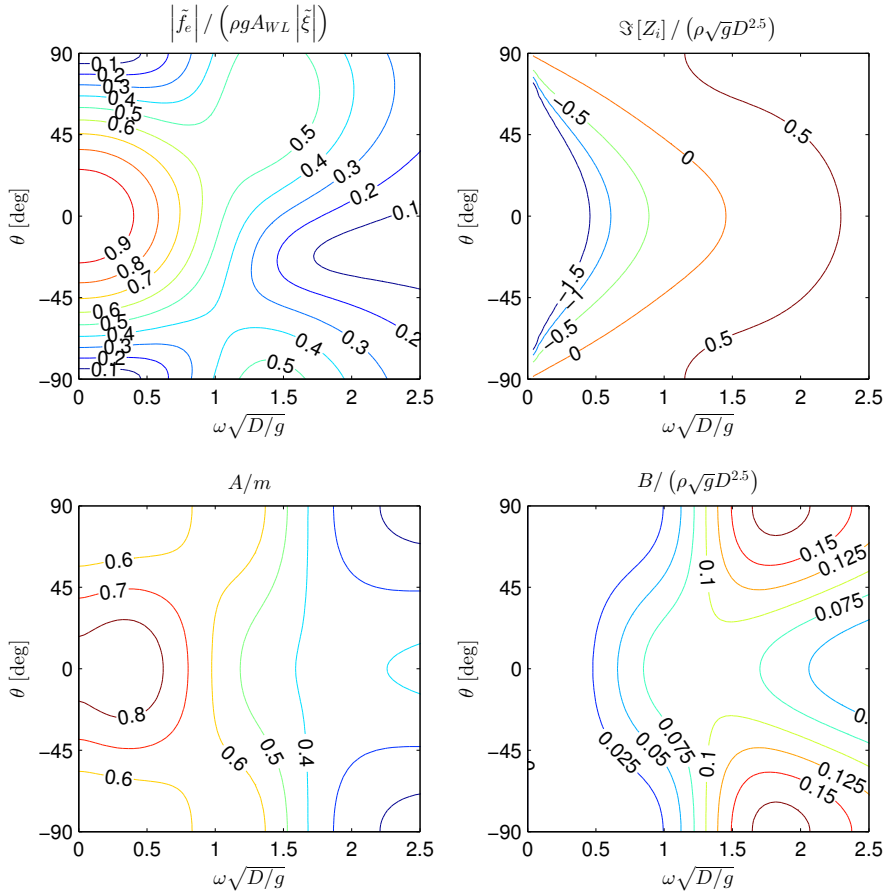

Figure 2.5: Non-dimensional hydrodynamic coefficients of the sloped WEC for different slope angles and wave frequencies. Excitation force (top-left), intrinsic reactance (top-right), added mass (bottom-left) and radiation damping (bottom-right). The diameter D, waterplane area $A_{WL} = \pi D^2/4$ and mass $m = \rho\pi D^3/12$ are used in the normalization.

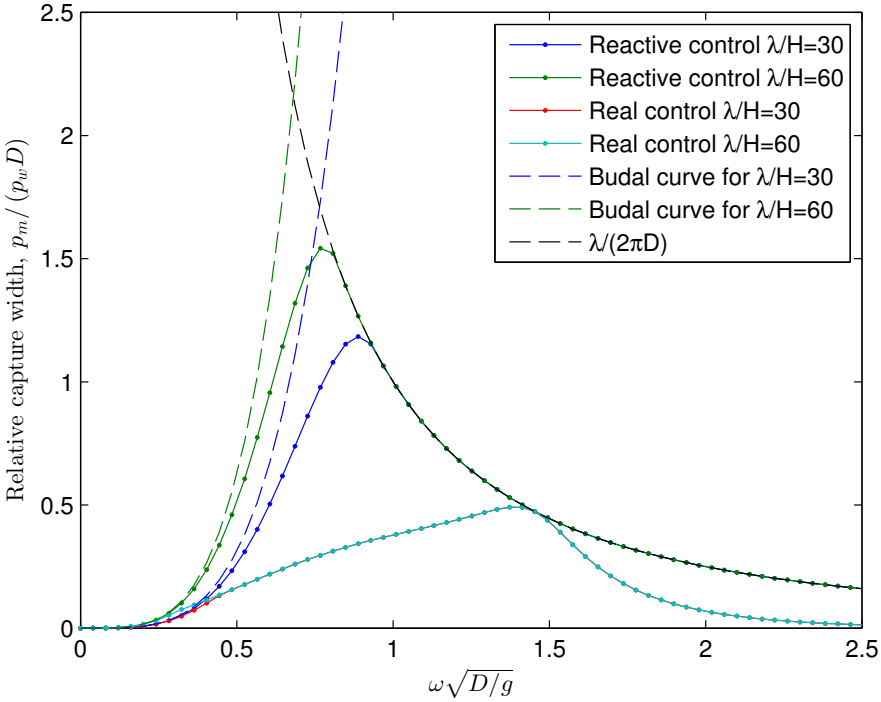

Figure 2.6: Relative capture width of a heaving semi-submerged sphere exposed to regular waves of steepness $H/\lambda = 1/30$ and $H/\lambda = 1/60$ in infinite water depth. A displacement amplitude constraint $|\tilde{q}| \leq D/3$ is imposed.

the Budal curve. Since we plot relative capture width for regular waves of fixed steepness, it is useful to re-express the Budal curve (2.28) for a semi-submerged spherical WEC as follows:

$$\frac{p_m}{p_w D} < \frac{D^2\omega^4}{6g^2}\left(\frac{\lambda}{H}\right) \tag{2.33}$$

Figure 2.6 shows the relative capture width for the heave case. As expected, the efficiency of the WEC under reactive control approaches the Budal curve for low frequencies and is identical to the unconstrained analytical result $p_m/p_w = \lambda/2\pi$ when the amplitude constraint has no effect. When the constraint has an effect, the efficiency increases with decreasing wave steepness. For the case of real control, both the efficiency and the motion amplitudes are low, and the constraint only has a slight effect at very low frequencies.

Figure 2.7 shows the performance and response of the WEC as a function of

both θ and ω for regular waves with $H/\lambda = 1/30$. Although the Budal curve is only valid for heave motion, we use the constraint $|\tilde{q}| < D/3$ also when $\theta \neq 0$. It is seen that high efficiency can be achieved without the aid of PTO reactance for ω,θ combinations where a large excitation force is combined with small intrinsic reactance (near resonance). This is seen to happen for $\theta \approx 45°$ and $\omega\sqrt{D/g} \approx 1$. The benefit of this sloped mode of motion have previously been noted by other authors as well, see for instance (Pizer, 1994).

Also the WEC under reactive control can benefit from having $\theta \neq 0$. However, the bottom right diagram of the figure shows that full reactive control involves huge negative power flowing out of the PTO system during part of the oscillation cycle, many times as high as the mean absorbed power. The maximum negative power flow is here found as (ref. eq. (2.15)):

$$p_{neg} = \frac{1}{2}\left|\tilde{v}\right|^2 \left(\left|Z_u\right| - \Re\left[Z_u\right]\right) \tag{2.34}$$

PTO systems with large negative power flow is believed to be expensive and impractical. As noted by Falnes (2002), even small losses in the conversion of instantaneous power will lead to large losses in the mean absorbed power when negative power is present.

2.3 Multiple degrees of freedom (MDOF) WECs

WECs oscillating in multiple degrees of freedom (MDOF) are conveniently described using matrix notation and we will in the following use bold upright font to denote vectors and matrices. The MDOF equivalent of the equation of motion (2.14) then becomes,

$$\left(\mathbf{Z}_i + \mathbf{Z}_u\right)\tilde{\mathbf{V}} = \tilde{\mathbf{F}}_{exc} \tag{2.35}$$

where $\tilde{\mathbf{V}}, \tilde{\mathbf{F}}_{exc} \in \mathbb{C}^{n\times 1}$ and $\mathbf{Z}_i, \mathbf{Z}_u \in \mathbb{C}^{n\times n}$ for the case of n degrees of freedom. The intrinsic impedance matrix $\mathbf{Z}_i$ is composed of the mass and added mass matrices, the radiation damping matrix and the hydrostatic restoring matrix:

$$\mathbf{Z}_i = \mathbf{B} + j\omega\left(\mathbf{M} + \mathbf{A}\right) - \frac{j}{\omega}\mathbf{G} \tag{2.36}$$

In analogy with eq. (2.15), we can find the total power absorbed by the PTO system as the inner product of the PTO force vector with the velocity vector:

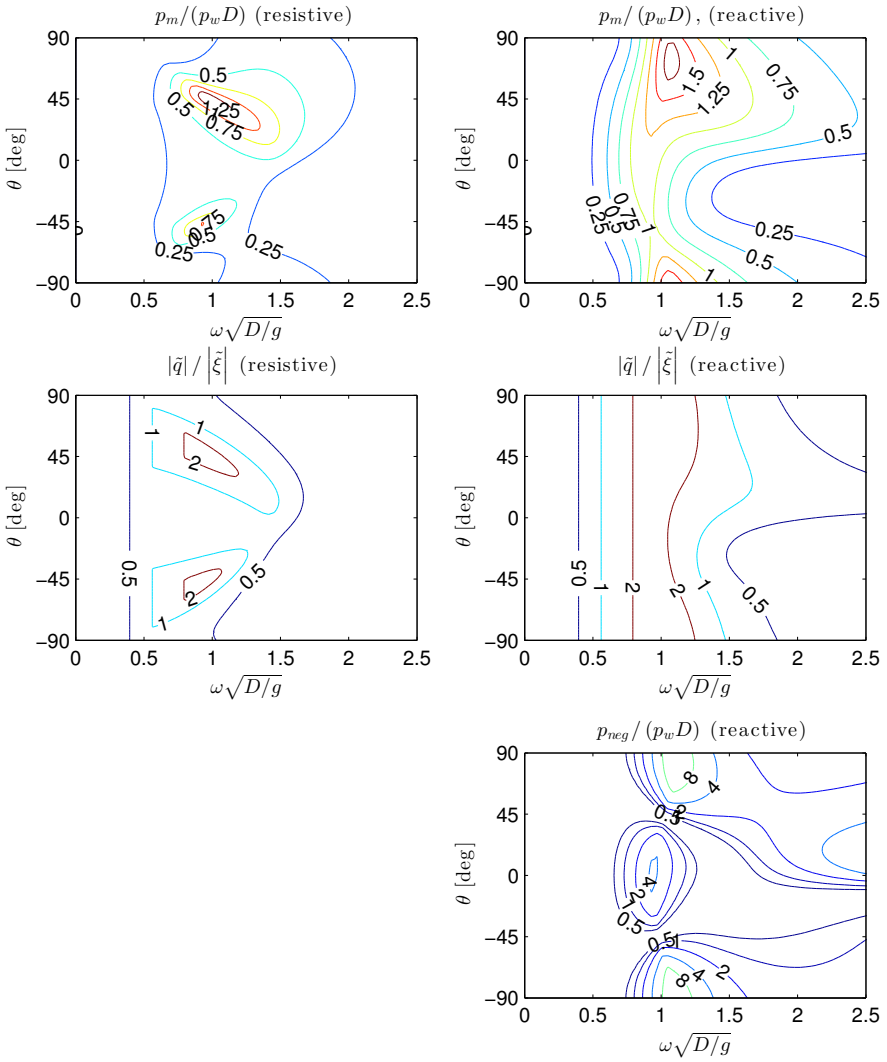

Figure 2.7: Performance of the sloped WEC in regular waves as a function of the slope angle and frequency under both resistive (diagrams to the left) and reactive (diagrams to the right) control. A displacement amplitude constraint $|\tilde{q}| \leq D/3$ is imposed based on a wave steepness $H/\lambda = 1/30$. The upper diagrams show relative capture width. The diagrams in the middle show the (constrained) displacement amplitudes. The bottom diagrams show the maximum negative power flowing out of the PTO system under reactive control, here expressed as a "relative capture width" for easy comparison with mean absorbed power.

$$
\begin{aligned}
p_u(t) &= -\mathbf{F}_u(t)^T \mathbf{V}(t) && \text{(2.37a)}\\
&= -\frac{1}{2}\left(\Re\left[\tilde{\mathbf{V}}^\dagger \tilde{\mathbf{F}}_u\right] + \Re\left[\tilde{\mathbf{V}}^T \tilde{\mathbf{F}}_u \exp(2j\omega t)\right]\right) && \text{(2.37b)}\\
&= \underbrace{\frac{1}{2}\Re\left[\tilde{\mathbf{V}}^\dagger \mathbf{Z}_u \tilde{\mathbf{V}}\right]}_{p_m} + \frac{1}{2}\Re\left[\tilde{\mathbf{V}}^T \mathbf{Z}_u \tilde{\mathbf{V}} \exp(2j\omega t)\right] && \text{(2.37c)}
\end{aligned}
$$

Here, ^{T} mean transpose and † means complex conjugate transpose. If $\Im[\mathbf{Z}_u]$ is symmetric, which is typically the case, we can write the mean absorbed power as,

$$
p_m = \frac{1}{2}\Re\left[\tilde{\mathbf{V}}^\dagger \Re[\mathbf{Z}_u]\, \tilde{\mathbf{V}}\right] \tag{2.38}
$$

showing that it is only the real part of $\mathbf{Z}_u$ that contributes to the mean power. Moreover, if $\Re[\mathbf{Z}_u]$ is diagonal, we can write:

$$
p_m = \frac{1}{2}\sum_{i=1}^{n} \Re[Z_{ii,u}] \left|\tilde{V}_i\right|^2 \tag{2.39}
$$

A WEC that extracts energy from the relative motion between bodies will typically have off-diagonal terms in $\mathbf{Z}_u$. However, by expressing the equation of motion in terms of relative rather than absolute modes of motion, it is possible to obtain a diagonal $\mathbf{Z}_u$ also in this case. This is exemplified by a case study in Section 2.5.

Eq. (2.37) expresses the instantaneous power absorbed by the PTO system. It is also relevant to consider the power absorbed from the waves by the oscillating bodies, $p_f(t) = \mathbf{F}_f(t)^T \mathbf{V}(t)$, where $\mathbf{F}_f(t)$ is the fluid forces obtained by integrating the fluid pressure over the wetted surface of the bodies. The complex amplitudes of these fluid forces be written as,

$$
\begin{aligned}
\tilde{\mathbf{F}}_f &= \tilde{\mathbf{F}}_{exc} - \left(\mathbf{B} + j\omega\mathbf{A} - \frac{j}{\omega}\mathbf{G}\right)\tilde{\mathbf{V}}\\
&= \tilde{\mathbf{F}}_{exc} - \mathbf{Z}_f \tilde{\mathbf{V}} && \text{(2.40)}
\end{aligned}
$$

This power can be written as,

$$
\begin{aligned}
p_f(t) &= \mathbf{F}_f(t)^T \mathbf{V}(t)\\
&= \frac{1}{2}\left(\Re\left[\tilde{\mathbf{V}}^\dagger\left(\tilde{\mathbf{F}}_{exc} - \mathbf{Z}_f\tilde{\mathbf{V}}\right)\right] + \Re\left[\tilde{\mathbf{V}}^T \tilde{\mathbf{F}}_f \exp(2j\omega t)\right]\right)\\
&= \underbrace{\frac{1}{2}\Re\left[\tilde{\mathbf{V}}^\dagger \tilde{\mathbf{F}}_{exc}\right]}_{p_e} - \underbrace{\frac{1}{2}\Re\left[\tilde{\mathbf{V}}^\dagger \mathbf{B}\tilde{\mathbf{V}}\right]}_{p_r} + \frac{1}{2}\Re\left[\tilde{\mathbf{V}}^T \tilde{\mathbf{F}}_f \exp(2j\omega t)\right] && \text{(2.41)}
\end{aligned}
$$

where p_e is called the excitation power and p_r is the radiated power (Falnes, 2002). The time varying part of p_u and p_f will differ, and the difference $p_u(t) - p_f(t)$ is due to the kinetic and potential energy storage associated with the mass, added mass and hydrostatic restoring. However, if we take a time average over an integer number of periods, we have from conservation of energy that $\overline{p_u(t)} = \overline{p_f(t)}$. Or,

$$p_m = p_e - p_r \tag{2.42}$$

It is seen that maximization of the mean absorbed power p_m is the same as maximization of p_e and minimization of p_r. However, since the two are related (Haskind relation), these are conflicting goals. This was also discussed for the SDOF case in connection with eq. (2.16). The radiated power p_r is always non-negative (and positive in most practical applications). This fact follows from the positive (semi) definiteness of $\mathbf{B}$, which is an inherent property of radiation damping matrices (Falnes, 2002).

Starting from the expressions for excitation and radiated power, Falnes shows that the maximum mean absorbed power becomes,

$$p_{m,opt} = \frac{1}{4}\tilde{\mathbf{F}}_{exc}^{\dagger}\tilde{\mathbf{V}}_{opt} \tag{2.43}$$

where the optimal velocities is a solution of:

$$\mathbf{B}\tilde{\mathbf{V}}_{opt} = \frac{1}{2}\tilde{\mathbf{F}}_{exc} \tag{2.44}$$

In the case that $\mathbf{B}$ is singular, there may exist many $\tilde{\mathbf{V}}_{opt}$, all producing the same optimal power. If $\mathbf{B}$ is non-singular, it can be inverted to give an expression analogous to eq. (2.21):

$$p_{m,opt} = \frac{1}{8}\tilde{\mathbf{F}}_{exc}^{\dagger}\mathbf{B}^{-1}\tilde{\mathbf{F}}_{exc} \tag{2.45}$$

It should be noted that $\mathbf{B}$ is non-singular in most practical applications, and in all problems studied in this thesis. Assuming $\mathbf{B}$ to be non-singular, the PTO forces associated with $\tilde{\mathbf{V}}_{opt}$ can be written:

$$\tilde{\mathbf{F}}_{u,opt} = \frac{1}{2}j\Im\left[\mathbf{Z}_i\right]\mathbf{B}^{-1}\tilde{\mathbf{F}}_{exc} - \frac{1}{2}\tilde{\mathbf{F}}_{exc} \tag{2.46}$$

One way to achieve this is by setting $\mathbf{Z}_u = \mathbf{Z}_i^*$, analogous to the SDOF case, although there are many possible $\mathbf{Z}_u$ that solve the equation $\tilde{\mathbf{F}}_{u,opt} = \mathbf{Z}_u\tilde{\mathbf{V}}_{opt}$.

2.3.1 Convex optimization problem for maximum mean power with velocity constraints and released modes

The velocities (and thus displacement amplitudes) needed to achieve the optimal power given by eq. (2.45) will often be unrealistically large, violating

both linear theory and physical constraints present in the system. For the SDOF case, we used eq. (2.25) to compute the maximum power respecting an amplitude constraint. This is actually a SDOF special case of a MDOF formula suggested by Evans (1981). However, in the MDOF case, the velocity constraint considered by Evans only limits the norm of the velocity vector such that $\tilde{\mathbf{V}}^{\dagger}\tilde{\mathbf{V}} \leq V_{max}^2$. With this type of constraint, an analytical expression for the constrained optimal power is obtained. In the following, we will instead use an amplitude constraint on the individual velocity components such that $\left|\tilde{V}_i\right| \leq V_{max,i}$, and show how we can use established numerical optimization techniques to find the constrained maximum power absorption.

A general optimization problem is formulated as,

$$\text{minimize } f_0(\mathbf{x}) \tag{2.47a}$$

$$\text{subject to } f_i(\mathbf{x}) \leq 0,\ i = 1, .., m \tag{2.47b}$$

for a problem with m inequality constraints. The functions $f_i(\mathbf{x})$ take a set of optimization variables collected in the vector $\mathbf{x}$ as input and return a scalar output. The function to be minimized, $f_0(\mathbf{x})$, is called the objective function. It can be noted that this formulation also encompasses equality constraints of the form $f(\mathbf{x}) = c$, since this can be replaced by the two inequality constraints $f(\mathbf{x}) - c \leq 0$ and $c - f(\mathbf{x}) \leq 0$.

The general optimization problem is difficult to solve. If however the functions $f_i(\mathbf{x})$ possess certain properties, the problem can be manageable in many cases. If, for instance,

$$f_i(a\mathbf{x} + b\mathbf{y}) \leq af_i(\mathbf{x}) + bf_i(\mathbf{y})\ i = 0, .., m \tag{2.48}$$

holds for all $\mathbf{x}, \mathbf{y} \in \mathbb{R}^n$ and all $a, b \in \mathbb{R}$ with $a + b = 1$, $a \geq 0$, $b \geq 0$, the functions $f_i(\mathbf{x})$ are said to be convex, and the optimization problem is a convex optimization problem (Boyd and Vandenberghe, 2004, available online). One of the advantages of convex optimization problems is that if a local minimum exist, then it is a global minimum.

The problem of maximizing the absorbed power of an MDOF WEC subject to velocity constraints of the type $|V_i| \leq V_{max,i}$, is in fact a convex optimization problem if we choose the real and imaginary parts of the velocities $\mathbf{V}$ as the optimization variables. The objective function can then be written,

$$f_0(\mathbf{x}) = -p_m = \mathbf{x}^T \begin{bmatrix} \mathbf{B} & \mathbf{0} \\ \mathbf{0} & \mathbf{B} \end{bmatrix} \mathbf{x} - \begin{bmatrix} \Re\left[\tilde{\mathbf{F}}_{exc}\right] \\ \Im\left[\tilde{\mathbf{F}}_{exc}\right] \end{bmatrix}^T \mathbf{x},\ \mathbf{x} = \begin{bmatrix} \Re\left[\tilde{\mathbf{V}}\right] \\ \Im\left[\tilde{\mathbf{V}}\right] \end{bmatrix} \tag{2.49}$$

which is a convex function of $\mathbf{x}$ if $\mathbf{B}$ is a positive semi-definite matrix, which we have already stated is the case. The constraint functions can be formulated as,

$$f_i(\mathbf{x}) = \Re\left[\tilde{V}_i\right]^2 + \Im\left[\tilde{V}_i\right]^2 - V_{max,i}^2 \tag{2.50}$$

which are also convex functions of $\mathbf{x}$. From the quadratic form of both the objective function and the constraint functions, it follows that our optimization problem can be categorized as a quadratically constrained quadratic programming (QCQP) problem. An alternative is to replace each of the quadratic constraints with a number of linear constraints:

$$f_{ik}(\mathbf{x}) = \Re\left[\tilde{V}_i\right]\cos(\omega t_k) - \Im\left[\tilde{V}_i\right]\sin(\omega t_k) - V_{max,i} \tag{2.51}$$

That is, we replace the amplitude constraint with constraints on the velocity at discrete times t_k. Choosing a relatively large number of times between $t = 0$ and $t = 2\pi/\omega$, the amplitude constraint will be approximately enforced. With these linear constraints, the optimization problem becomes a quadratic programming (QP) problem.

The solution obtained by solving the above optimization problem assumes that we have a PTO system that can prescribe the velocities (phase and magnitude) in all modes of motion. This corresponds to imposing PTO forces in all modes of motion. Some WECs are designed to only impose PTO forces in some modes of motion, referred to as the controlled modes, as opposed to the released modes. If mode i is a released mode, row i of the PTO impedance matrix $\mathbf{Z}_u$ consists of only zeros. From eq. (2.35), we can then write the force equilibrium in mode i as:

$$\sum_j Z_{i,ij}\tilde{V}_j = \tilde{F}_{exc,i} \tag{2.52}$$

Note here that the first i in $Z_{i,ij}$ stands for "intrinsic" and is not a integer. If we have n_r released modes, there will be $2n_r$ equality constraints since the forces have a real and imaginary part.

We have already mentioned that an equality constraint $f(\mathbf{x}) = 0$ is equivalent to the two inequality constraints $f(\mathbf{x}) \leq 0$ and $-f(\mathbf{x}) \leq 0$. The optimization problem is therefore convex only if both $f(\mathbf{x})$ and $-f(\mathbf{x})$ is convex functions, which is the same as requiring that $f(\mathbf{x})$ is a linear function. Hence, convex optimization problems always have linear equality constraints, if any. Since eq. (2.52) is linear in $\mathbf{x}$, accounting for released modes does not destroy the convexity of the optimization problem.

Although the formulation of equality constraints as two inequality constraints is useful conceptually, it is normally not done numerically. Many solvers accept equality constraints formulated explicitly and treats these differently from the inequality constraints. In fact, the standard solvers utilize linear equality constraints to reduce the number of unknowns and thus the computational time.

2.3.2 Non-convex optimization problem for maximum mean power with zero or limited reactive power

The optimal PTO system requires reactive power and thus a PTO system that do work during part of the oscillation cycle. Since this is considered difficult in practice, it is relevant to limit the required negative power of the PTO system. The instantaneous power absorbed by the PTO system in mode i is $p_{u,i}(t) = -F_{u,i}(t)\, V_i(t)$. We can say that this power is absorbed by a PTO subsystem absorbing from mode i only. This is not the same as the power absorbed from the waves by the same mode, since we have kinetic and potential energy storage and redistribution of power between modes due to cross coupling in the intrinsic impedance matrix. Negative $p_{u,i}(t)$ is undesirable, and we therefore want to impose a lower bound on $p_{u,i}(t)$. We start by expressing the minimum value of $p_{u,i}(t)$, written as,

$$\begin{aligned} p_{min,i} &\equiv \min\left(p_{u,i}(t)\right) \\ &= \frac{1}{2}\Re\left[\tilde{V}_i^*\left(\tilde{F}_{exc,i} - \sum_j Z_{i,ij}\tilde{V}_j\right)\right] - \frac{1}{2}\left|\tilde{V}_i\left(\tilde{F}_{exc,i} - \sum_j Z_{i,ij}\tilde{V}_j\right)\right| \end{aligned} \tag{2.53}$$

$p_{min,i}$ is always non-positive, and the case $p_{min,i} = 0$ corresponds to the case where $F_{u,i}(t)$ and $V_i(t)$ are in counter-phase (real control). If we require $p_{min,i} \geq p_{min,lim,i}$, we can include this in the optimization problem by including the following constraint for all i:

$$\frac{1}{2}\left|\tilde{V}_i\left(\tilde{F}_{exc,i} - \sum_j Z_{i,ij}\tilde{V}_j\right)\right| - \frac{1}{2}\Re\left[\tilde{V}_i^*\left(\tilde{F}_{exc,i} - \sum_j Z_{i,ij}\tilde{V}_j\right)\right] + p_{min,lim,i} \leq 0 \tag{2.54}$$

One hitch in this approach is that the introduced constraint function is non-convex. Thus, if a nonlinear optimization algorithm finds a local minimum, there may exist a "better" global minimum. Moreover, setting $p_{min,lim,i}$ to zero as a mean to enforce real control, effectively introduces a non-linear equality constraint since $p_{min,i}$ is always non-positive. Non-linear equality constraints are difficult to handle, but can be included approximately by giving $p_{min,lim,i}$ a small negative value.

Since constraining the minimum power destroys the convexity of the problem, we can just as well formulate a different optimization problem that enforces real control exactly. This can be done by requiring $\mathbf{Z}_u$ to be a real diagonal matrix, and choose the diagonal elements $b_{u,i} = Z_{u,ii}$ as the optimization variables so that $\mathbf{x} = \begin{bmatrix} b_{u,1} & \cdots & b_{u,n} \end{bmatrix}$ in the optimization problem, eqs. (2.47). Released modes can now be handled simply by removing some elements from $\mathbf{x}$. Since both the objective function and the constraint functions

expressing the amplitude constraints involve solving the equation of motion by matrix inversion, the convexity of this optimization problem is difficult to assess. This approach is particularly beneficial in irregular waves, which will be discussed in Section 2.4.

For a MDOF WEC that has limited energy storage capabilities, but that is able to transfer energy almost instantly between the PTO sub-systems, it is relevant to formulate a lower limit on the total power rather than on the individual powers of the subsystems. That is, we put a lower bound on $p_u(t) = -\mathbf{F}_u(t)^T \mathbf{V}(t)$ rather than on the individual $p_{u,i}(t) = -F_{u,i}(t) V_i(t)$. This corresponds to introducing the (non-convex) inequality constraint,

$$\frac{1}{2}\left|\tilde{\mathbf{V}}^T\left(\tilde{\mathbf{F}}_{exc} - \mathbf{Z}_i\tilde{\mathbf{V}}\right)\right| - \frac{1}{2}\Re\left[\tilde{\mathbf{V}}^\dagger\left(\tilde{\mathbf{F}}_{exc} - \mathbf{Z}_i\tilde{\mathbf{V}}\right)\right] + p_{min,lim} \leq 0 \tag{2.55}$$

in the optimization problem. The minimum total power can be both positive and negative, and it is therefore relevant to give $p_{min,lim}$ a positive value as a mean to limit the variability of the absorbed power.

2.4 Energy absorption in irregular waves

The discussion so far has been limited to regular waves. The principle of superposition for linear systems makes the extension to irregular waves relatively straightforward. However, the constraints on the motion amplitudes and negative power suggested for the optimization problem will take a different meaning (and perhaps be less meaningful) in irregular waves. Hence, we will suggest other constraints to be used with irregular waves.

In this section, we will derive the statistical mean and variability of the absorbed power in irregular waves. Then we will try to give a time domain interpretation of a PTO model with frequency dependent coefficients, and describe the difference between passivity and non-negative power absorption. Finally, we will suggest a formulation for the optimization of a simple resistive PTO model for irregular waves, and show how the variability of power can be included in the optimization problem.

2.4.1 Mean power

In eq. (2.12a), we wrote the harmonic velocity $v(t)$ in terms of its complex amplitude $\tilde{v}$. We will now allow $v(t)$ to be non-harmonic and assume that its

Fourier transform $V(\omega)$ exist, so that:

$$V(\omega) = \frac{1}{2\pi} \int_{-\infty}^{\infty} v(t) \exp(-j\omega t)\, dt \tag{2.56a}$$

$$v(t) = \int_{-\infty}^{\infty} V(\omega) \exp(j\omega t)\, d\omega \tag{2.56b}$$

Using that $V(-\omega) = V(\omega)^*$ and comparing with eq. (2.12a), we see that the complex amplitude $\tilde{v}$ and the Fourier transform $V(\omega)$ are closely related as $\tilde{v} = 2V(\omega)\, d\omega$. Using the inverse Fourier transform of velocity and PTO force, and allowing more than one mode of motion, the absorbed power signal can be written:

$$p(t) = -\mathbf{f}(t)^T \mathbf{v}(t) \tag{2.57a}$$

$$= -\left(\int_{-\infty}^{\infty} \mathbf{F}(\omega)^T \exp(j\omega t)\, d\omega \right) \left(\int_{-\infty}^{\infty} \mathbf{V}(\omega) \exp(j\omega t)\, d\omega \right) \tag{2.57b}$$

$$= -\int_{-\infty}^{\infty} \int_{-\infty}^{\infty} \mathbf{F}(\omega_1)^T \mathbf{V}(\omega_2) \exp(jt(\omega_1 + \omega_2))\, d\omega_1 d\omega_2 \tag{2.57c}$$

Here, the integrand only contributes a mean when $\omega_1 + \omega_2 = 0$. Hence, when we are only interested in the mean power, we can replace the double integral with a single integral over ω, inserting $\omega_1 = -\omega$ and $\omega_2 = \omega$. Using that $\mathbf{F}(-\omega) = \mathbf{F}(\omega)^*$ and likewise for $\mathbf{V}(\omega)$, we only have to integrate over positive ω:

$$p_m = -2 \int_0^{\infty} \Re\left[\mathbf{V}(\omega)^\dagger \mathbf{F}(\omega) \right] d\omega \tag{2.58a}$$

$$= -\int_0^{\infty} \int_{-\pi}^{\pi} \Re\left[\mathbf{H}_V(\omega, \beta)^\dagger \mathbf{H}_F(\omega, \beta) \right] S(\omega, \beta)\, d\beta d\omega \tag{2.58b}$$

$$= \int_0^{\infty} \int_{-\pi}^{\pi} \Re\left[\mathbf{H}_V(\omega, \beta)^\dagger \mathbf{Z}_u(\omega) \mathbf{H}_V(\omega, \beta) \right] S(\omega, \beta)\, d\beta d\omega \tag{2.58c}$$

$$= \int_0^{\infty} \int_{-\pi}^{\pi} 2p_{unit}(\omega, \beta)\, S(\omega, \beta)\, d\beta d\omega \tag{2.58d}$$

Here, $S(\omega, \beta)$ is the single-sided wave spectrum for short crested waves, with β representing wave heading angle. $\mathbf{H}_V(\omega, \beta)$ and $\mathbf{H}_F(\omega, \beta)$ are wave-to-velocity

and wave-to-PTO force transfer function vectors. p_{unit} is taken as the mean absorbed power in a unit amplitude regular wave.

When $\Re\left[\mathbf{Z}_u\left(\omega\right)\right] = \mathrm{diag}\left(b_{u,1}, \ldots, b_{u,n}\right)$, the mean power becomes:

$$p_m = \sum_i b_{u,i}\sigma_{V,i}^2 \tag{2.59}$$

Here, the variance of velocity, $\sigma_{V,i}^2$, can be calculated either from the velocity spectrum in the case of a frequency domain analysis, or from time series of velocity in the case of time domain simulation.

2.4.2 Short term variability of absorbed power

The short term variability of absorbed power is important for the short term energy storage requirements of the WEC and the quality of the delivered power. In the following, we will derive an expression for the variance of the absorbed power of a linear MDOF WEC in steady state response to random Gaussian short crested waves. The derivation is based on (Rogne, 2007). We will assume a frequency independent, real and diagonal PTO damping matrix (real control), so that the mean absorbed power is given by eq. (2.59). We will further introduce the notation $\mathrm{E}\left[p\left(t\right)\right]$ for the expected value, or ensemble average, of the random signal $p\left(t\right)$. All variables are assumed to be ergodic, which implies that the ensemble variance and average is the same as variance and average over time. Hence, we will simply use the words variance and average in the following. For the power signal, for instance, ergodicity implies that $\mathrm{E}\left[p\left(t\right)\right] = p_m$.

The variance of power can be written as:

$$\sigma_p^2 = \mathrm{E}\left[p\left(t\right)^2\right] - \mathrm{E}\left[p\left(t\right)\right]^2 \tag{2.60}$$

Here, the second term is simply eq. (2.59) squared. The first term can be written:

$$\mathrm{E}\left[p\left(t\right)^2\right] = \mathrm{E}\left[\left(\sum_i b_{u,i}v_i\left(t\right)^2\right)^2\right] \tag{2.61}$$

$$= \sum_i \sum_j b_{u,i}b_{u,j}\mathrm{E}\left[v_i\left(t\right)^2 v_j\left(t\right)^2\right] \tag{2.62}$$

At this point we will assume $v_i\left(t\right)$ to be a zero mean Gaussian signal and make use of an identity given by (Bendat, 1998),

$$\begin{aligned}\mathrm{E}\left[X_1X_2X_3X_4\right] = {} & \mathrm{E}\left[X_1X_2\right]\mathrm{E}\left[X_3X_4\right] + \mathrm{E}\left[X_1X_3\right]\mathrm{E}\left[X_2X_4\right] \\ & + \mathrm{E}\left[X_1X_4\right]\mathrm{E}\left[X_2X_3\right]\end{aligned} \tag{2.63}$$

which holds for zero mean Gaussian variables X_i. Using this, we have that:

$$\mathrm{E}\left[v_i\left(t\right)^2 v_j\left(t\right)^2\right] = \mathrm{E}\left[v_i\left(t\right)^2\right]\mathrm{E}\left[v_j\left(t\right)^2\right] + 2\mathrm{E}\left[v_i\left(t\right)v_j\left(t\right)\right]^2 \tag{2.64}$$

Here, the term $\mathrm{E}\left[v_i\left(t\right)v_j\left(t\right)\right]$ can be re-expressed by using a derivation similar to that leading to the mean power, eqs. (2.58) and (2.59). We then get:

$$\mathrm{E}\left[v_i\left(t\right)v_j\left(t\right)\right] = 2\int_0^\infty \Re\left[V_i\left(\omega\right)^* V_j\left(\omega\right)\right] d\omega \tag{2.65}$$

$$= \int_0^\infty \int_{-\pi}^{\pi} \Re\left[H_{Vi}\left(\omega,\beta\right)^* H_{Vj}\left(\omega,\beta\right)\right] S\left(\omega,\beta\right) d\beta d\omega \tag{2.66}$$

Combing these results, we finally arrive at an expression for the variance,

$$\sigma_p^2 = 2\sum_i \sum_j b_{u,i} b_{u,j} \sigma_{Vi,Vj}^2 \tag{2.67}$$

where $\sigma_{Vi,Vj}$ is the covariance of $v_i\left(t\right)$ and $v_j\left(t\right)$, written as:

$$\sigma_{Vi,Vj} = \int_0^\infty \int_{-\pi}^{\pi} \Re\left[H_{Vi}\left(\omega,\beta\right)^* H_{Vj}\left(\omega,\beta\right)\right] S\left(\omega,\beta\right) d\beta d\omega \tag{2.68}$$

Note here that $\sigma_{Vi,Vj}$ and $\sigma_{Vi,Vj}^2$ have the dimension of velocity squared and velocity to the power of four, respectively.

The dimensionless coefficient of variation is defined as:

$$\rho_p = \frac{\sigma_p}{p_m} \tag{2.69}$$

An interesting result appears for the special case of a WEC absorbing energy from only one mode of motion (or a SDOF WEC). We then have:

$$\rho_p = \sqrt{2} \tag{2.70}$$

For the MDOF case, we want ρ_p to be as low as possible. To achieve this, it is beneficial to have many energy absorbing modes of motion with comparable power contributions and velocities out of phase with each other.

2.4.3 PTO forces in the time and frequency domains

The PTO impedance $Z_u\left(\omega\right)$ corresponding to optimal absorption will be frequency dependent. It is therefore important to understand how this frequency dependency should be interpreted in the time domain.

It is always possible to write the PTO force in the time domain as:

$$f_u(t) = b(t)\, v(t) \tag{2.71}$$

If $b(t)$ can be chosen freely, and is allowed to approach $-\infty$ and ∞, this PTO model is completely general, possibly non-linear. A linear PTO force is one that can be written as,

$$f_u(t) = \mathcal{F}^{-1}\left[Z_u(\omega)\, H_V(\omega)\right] \tag{2.72}$$

$$= \int_{-\infty}^{\infty} z_u(t-\tau)\, v(\tau)\, d\tau \tag{2.73}$$

where the PTO impulse response function $z_u(\tau)$ is the inverse Fourier transform of the PTO impedance $Z_u(\omega)$. It is seen that the PTO force generally depend on the velocity in both the past and in the future. Casting this linear PTO model into the form in eq. (2.71), we understand that $b_u(t)$ have to vary with time. In this case, $f_u(t)$ is linear because it is linear in the velocity *at all times*, whereas a constant b_u will suffice only when $f_u(t)$ is linear in the *instantaneous* velocity.

The optimal unconstrained PTO impedance of a SDOF WEC was shown in Section 2.2 to be written $Z_{u,opt}(\omega) = Z_i(\omega)^*$. Here, the intrinsic impedance $Z_i(\omega)$ is known to be causal, meaning that the associated impulse response $z_i(t)$ is zero for $t \leq 0$. A consequence of this is that the optimal PTO impulse response is anti-causal, meaning that $z_{u,opt}(t)$ is zero for $t \geq 0$. Using this, we can write the optimal PTO force as:

$$f_{opt}(t) = \int_{t}^{\infty} z_{u,opt}(t-\tau)\, v(\tau)\, d\tau \tag{2.74}$$

Hence, the controller that sets the PTO force in this case would not utilize information about the velocity history, but would require accurate prediction of the velocity some seconds into the future. Not only does this require accurate prediction of the future incoming waves, it also requires an accurate mathematical model of the WEC dynamics to turn the wave predictions into a velocity prediction. The required prediction horizon will depend on $z_{u,opt}(t)$. If $z_{u,opt}(t)$ is approximately zero for $t < -t_{mem}$, the upper integration limit (ideally infinity) can be taken as $t + t_{mem}$.

Another challenge with the optimal PTO impedance is the need for negative power flow during parts of the oscillation cycle. For the case of harmonic velocity (linear, steady-state response to a regular wave), the negative power

flow can be avoided by requiring $\Im\left[Z_u\left(\omega\right)\right] = 0$ and $\Re\left[Z_u\left(\omega\right)\right] \geq 0$. In this case, the WEC is said to be under real control. Some authors say that a WEC under real control is a passive WEC. This is however not in line with the definition of passivity used in this thesis. Khalil (2002) defines a passive system as a system with a positive real transfer function, i.e. $\Re\left[Z_u\left(\omega\right)\right] \geq 0$, regardless of the imaginary part $\Im\left[Z_u\left(\omega\right)\right]$. With this definition, passivity is the same as positive mean absorbed power and thus all meaningful WECs have a passive PTO system. For a MDOF WEC, passivity implies that the real part of the impedance matrix is positive semi-definite, often written as $\Re\left[\mathbf{Z}_u\left(\omega\right)\right] \geq 0$. If in addition $\Im\left[\mathbf{Z}_u\left(\omega\right)\right] = \mathbf{0}$, the total absorbed power is always non-negative for harmonic velocities. A stricter requirement is that the power absorbed by each PTO subsystem, associated with each PTO force component, should be non-negative. This is achieved if in addition $\Re\left[\mathbf{Z}_u\left(\omega\right)\right]$ is diagonal.

For non-harmonic velocities, such as in irregular waves, the requirement of non-negative instantaneous power is not easy to formulate in the frequency domain. An obvious requirement is that $b_u\left(t\right) \geq 0$ in eq. (2.71). Requiring non-negative instantaneous power of each PTO subsystem of a MDOF WEC is the same as requiring $f_{u,i}\left(t\right) = b_{u,i}\left(t\right) v_i\left(t\right)$ with $b_{u,i}\left(t\right) \geq 0$ for all i. This is a stricter requirement than only requiring the *total* absorbed power to be non-negative at all times. An obvious MDOF PTO model that satisfies this strict non-negative power requirement is,

$$F_{u,i}\left(\omega\right) = b_{u,i} V_i\left(\omega\right) \tag{2.75a}$$

$$f_{u,i}\left(t\right) = b_{u,i} v_i\left(t\right) \tag{2.75b}$$

corresponding to a real, diagonal, frequency independent $\mathbf{Z}_u$. Here, $b_{u,i}$ is a constant and thus becomes a coefficient of proportionality between forces and velocities in both the time and frequency domains. This is the simple PTO model that will be the main focus in this thesis. When we allow $b_{u,i}$ to take different values in different sea states, we are loosely saying that $b_{u,i}$ vary slowly with time, slowly enough to be regarded as a constant during a sea state. This approach compares well with the traditional approach used in describing ocean waves, where a *sea state* is defined to have a duration of a few hours (sometimes less) where sea state parameters such as significant wave height and peak period can be regarded as constants. This approach allows us to use linear frequency domain methods and to optimize $b_{u,i}$ for each individual sea state.

Not all PTO systems with frequency dependent impedance will require knowledge of future or past velocity. The most natural example of this is

the following PTO model:

$$F_u(\omega) = \underbrace{\left[b_u + j\left(\omega I - \frac{k}{\omega}\right)\right]}_{Z_u(\omega)} V(\omega) \tag{2.76}$$

$$f_u(t) = I\dot{v}(t) + bv(t) + kq(t)\ ,\ \dot{q}(t) = v(t) \tag{2.77}$$

Here, the controller would only need measurements of the instantaneous acceleration, velocity and displacement. If I is a physical inertia and k the stiffness of a physical spring, nature will of course take care of the "measurement" of displacement and acceleration. Using a physical inertia and/or spring of course rules out the choices $I < 0$ and $k < 0$. When this is beneficial, it is important to ensure that the total mass and stiffness is positive in order to ensure a stable system (Hals et al., 2011).

A last PTO model which is worth a brief mentioning is the one referred to as latching control (Budal and Falnes, 1980). The formulation in eq. (2.71) also includes latching control if we allow $b_u(t)$ to go to infinity during the latching periods. The main principle of latching is to stop (latch) the velocity during parts of the oscillation cycle (by letting $b_u(t) \to \infty$) in order to bring the excitation force and velocity into phase with each other. Since latching delays the motion, it is best suited for systems with high natural frequency, having an intrinsic reactance being too low compared to the optimal. One advantage of latching control is that $b_u(t) \geq 0$, and thus no negative power flow is needed. A disadvantage is the large forces involved, which can lead to excessive strain on the components. It is also difficult to determine the optimal de-latching instants, as well as the optimal $b_u(t)$ between the latching periods. A latching control strategy would benefit from having predictions of future incoming waves (non-causal), although causal latching strategies have also been proposed (Lopes et al., 2009; Falcão, 2008). A recent, extensive study of latching control and other non-linear (and linear) control strategies is provided by Hals (2010).

2.4.4 Optimal resistive PTO in irregular waves

In Section 2.3.1 we introduced a convex optimization problem for optimal power absorption in regular waves with amplitude constraints and released modes. Here, we used the velocities as optimization variables. In principle, it is possible to extend this approach to irregular waves with a finite number of harmonic components by extending the optimization vector to include the velocity components at all frequencies (the Fourier coefficients). In addition, motion constraints similar to eq. 2.51 must then be enforced at discrete times over the full duration of the sea state realization. The resulting optimization

problem would be very time consuming with a large number of unknowns and constraints. The obtained optimal velocity signals would correspond to non-causal PTO forces and reactive power flow.

In order to optimize the more simple and realizable PTO model given in eq. (2.75) for irregular waves, we turn the optimization problem around, using a small number of damping coefficients $b_{u,1}, \cdots, b_{u,n}$ as optimization variables rather than the large number of velocity Fourier coefficients. The objective function then becomes the negative of eq. (2.59):

$$f_{obj} = -p_m = -\sum_i b_{u,i}\sigma_{V,i}^2 \tag{2.78}$$

To avoid dependence on sea state realization, constraints are placed on the displacement standard deviation σ_{q_i} rather than on the global extreme values, $\max_t(|q_i(t)|)$. If the maximum allowable σ_{q_i} is chosen significantly lower than physical end stops in the system, the end stop events will occur rarely and affect the mean absorbed power to a limited extent. The disadvantage of this approach is that both the objective function and the constraint functions involves solving the equation of motion by matrix inversion, and the convexity of the optimization problem is difficult to assess. Hence, we can obtain a good solution, but have no guarantees for having found the best solution.

One of the challenges of wave energy conversion is the short term variability of the absorbed power, associated with individual waves and wave groups, as well as the long term variability, associated with changing sea states. In order to account for the first type of variability, which is discussed in Section 2.4.2, we suggest the following dimensionless multi-objective objective function:

$$f_{obj} = (1-\alpha)\,\rho_p - \alpha\frac{p_m}{p_{ref}} \tag{2.79}$$

Here, ρ_p is the coefficient of variation, p_{ref} is a fixed power reference and α is a trade-off factor, chosen close to 1 if mean power is most important, and close to 0 if the variability is most important.

A perhaps intuitive alternative to this objective function is $f_{obj} = (1-\alpha)\,\sigma_p - \alpha p_m$. This is however a bad choice, since the "optimal" in this case easily ends up being the case of zero power absorption! Using the coefficient of variation, $\rho_p = \sigma_p/p_m$, instead, we avoid this since zero absorbed power now corresponds to the objective function approaching infinity.

2.5 Case study: Hinged 5 body WEC

Figure 2.8 shows a 5-body WEC consisting of a cylindrical center floater hinged to 4 semi-submerged spherical buoys. This WEC is the main case study in this

thesis and will be used as an example in this section and also in the following chapters. Accounting for the kinematic constraints imposed by the hinges, the WEC has 10 degrees of freedom. We choose the following generalized displacement coordinates:

- q_k, $k = 1..6$ are the displacements in surge (x), sway (y), heave (z), roll (rx), pitch (ry) and yaw (rz) of the center floater with the buoys rigidly attached. Referred to as the collective modes.
- q_k, $k = 7..10$ are the hinge angles, describing relative rotation between the center floater and the buoys.

Since this chapter deals with linear analysis we will apply the small angle approximation, so that $\sin(q_k) \approx q_k$ and $\cos(q_k) \approx 1$ for $k = 4..10$. We will assume that we have the generalized excitation force vector $\tilde{\mathbf{F}}_{exc}(\omega) \in \mathbb{C}^{10\times 1}$ and generalized intrinsic impedance matrix $\mathbf{Z}_i(\omega) \in \mathbb{C}^{10\times 10}$ available. In Chapter 4, we will show how these generalized matrices, describing the dynamic behavior of the hinged WEC, can be found from a description of the WEC without the hinges. The added mass and damping (in terms of a complex transfer matrix) are shown in Figure 3.1 and the excitation forces in Figure 5.1. Table 2.1 describes the hydrostatic parameters needed to construct the mass and restoring matrices.

One advantage of the choice of displacement coordinates used here is that the PTO impedance matrix will be diagonal for the case where the PTO system consists of independent subsystems, each imposing a hinge moment based on measurements of hinge angular velocity. Assuming resistive PTO forces, we have the following PTO impedance:

$$\mathbf{Z}_u = \Re[\mathbf{Z}_u] = \mathrm{diag}(0, 0, 0, 0, 0, 0, b_{u,1}, b_{u,2}, b_{u,3}, b_{u,4}) \tag{2.80}$$

This is the assumption we will use for this WEC in all subsequent chapters. In this chapter however, we will in addition consider the case of reactive control and controlled collective modes. For simplicity, only regular and long-crested irregular waves propagating along one of the symmetry axes of the WEC have been considered.

When we allow power absorption from all modes of motion, we use the following constraints on the displacement standard deviation $\sigma_{q,i}$:

$$\sqrt{2}\sigma_{q,i} \leq \begin{cases} D_{CF}/2 & \text{, Surge, Sway [m]} \\ T_{CF} & \text{, Heave [m]} \\ \arctan(2T_{CF}/D_{CF}) & \text{, Roll, Pitch, Yaw [rad]} \\ D_{BUOY}/(3L_{BUOY}) & \text{, Hinge angles [rad]} \end{cases} \tag{2.81}$$

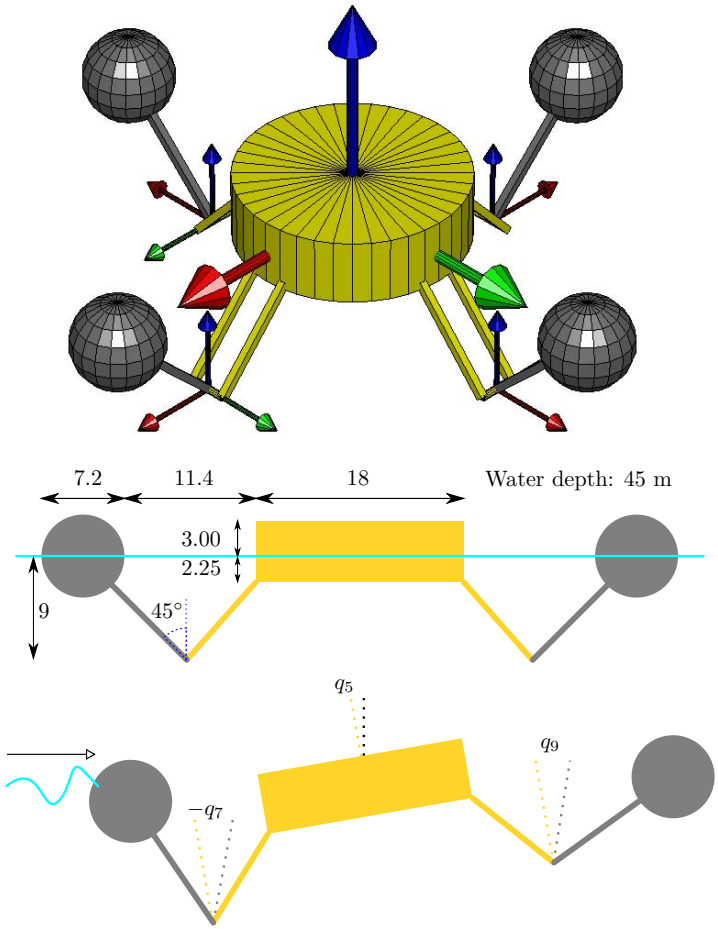

Figure 2.8: Hinged 5 body WEC. 3D view (top), XZ-intersection showing dimensions in meters and degrees (middle) and the same intersection showing a displaced state with definition of angular generalized coordinates (bottom). The intersection is in the coordinate frame of the center floater. Due to symmetry, the XZ (shown) and YZ (not shown) intersections are identical. The x/y/z axes of the body fixed frames are drawn as red/green/blue arrows. The y axes of the buoys are the hinge axis. Note that the slender beams are neglected in the hydrodynamic analysis.

Table 2.1: Hydrostatic parameters of the hinged 5-body WEC. All values are taken relative to the body fixed coordinate frames shown in Figure 2.8. The inertia tensors are diagonal with $I_{jj} = mr_{jj}^2$. The parameters corresponds to the full-scale equivalent (using Froude scaling) of the scale model shown in Figure 6.1, including the effect of the slender elements. Note that all bodies are neutrally buoyant (i.e. no forces in the hinges in still water).

	CF	Buoys		CF	Buoys	
m	631	103	$\rho\forall$	631	103	[tonne]
x_G	0	8.78	x_B	0	8.78	[m]
y_G	0	0	y_B	0	0	[m]
z_G	0.96	8.79	z_B	-1.28	7.47	[m]
r_{xx}	8.88	9.33				[m]
r_{yy}	8.88	13.05				[m]
r_{zz}	7.45	9.27				[m]

Here, D_{CF} is the diameter of the center floater, T_{CF} is the draft of the center floater, D_{BUOY} is the diameter of the buoy and $L_{BUOY} = \sqrt{2} \cdot 9$ [m] is the distance between the hinge and the center of the buoy, as shown in Figure 2.8. Note here that in the case of regular waves, $\sqrt{2}\sigma_{q,i}$ corresponds to the displacement amplitude.

When we allow power absorption only from the hinge modes, we use the following constraints:

$$\sqrt{2}\sigma_{q,i} \leq \begin{cases} D_{BUOY}/\left(3L_{BUOY}\right) & \text{, Hinge angles [rad]} \\ \infty & \text{, Other modes} \end{cases} \tag{2.82}$$

Since the constraints are imposed on the hinge angle, which is a relative angle, it is only loosely related to the amplitude constraint used in the SDOF case study in Section 2.2.1 and the Budal curve, eq. (2.28). In principle, it would have been possible to impose a constraint on the absolute motion of the buoys. However, this would have been less relevant as a physical constraint. In addition, the motion amplitude would not necessarily be a uniformly decreasing function of the damping coefficient, meaning that we have the possibility that the motion constraint are violated regardless of the value of the damping coefficient. In optimization theory, this means that there is a possibility that the optimization problem have no feasible point.

The intention of the amplitude constraints is partly to avoid stretching linear theory too far. The choice of appropriate motion constraints is as such more an art than science, and model testing clearly has a role in determining how well linear theory works in predicting large amplitude motion. Model tests of the hinged 5-body WEC is presented in Section 6.

It should be noted that the amplitude constraints above are only used in the frequency domain analysis presented in this section. In the time domain simulations presented in later chapters, we employ non-linear end stop forces to limit the instantaneous hinge amplitudes rather than its standard deviation.

The numerical optimization presented in the following has been carried out with the function *fmincon,* available in Matlab's optimization toolbox. This is a function intended for general non-linear optimization, supporting both inequality constraints and equality constraints. The sequential quadratic programming (SQP) algorithm was used, which is only one of the alternatives in fmincon. Several options that govern accuracy and iteration stopping criteria can be set. In this example, the default options were accepted, which is suitable if both the objective function and the optimization variables are scaled to have an order of 1.

Figure 2.9 shows the optimal power absorption in regular waves with various control strategies and constraints described in the table embedded in the figure. It's seen that quite a lot of extra energy can be absorbed by having a PTO system that harvest from the collective modes in addition to the hinge modes. Such a PTO system would however have to work in six degrees of freedom and would also need the sea-bed as a force reference. This is not believed to be an economical solution and is not considered any further. Comparing real and reactive control, it is seen that the difference almost vanish for a frequency just below $\omega = 1$. This is associated with eigenfrequencies and eigenmodes involving the hinge motion in this range of frequencies. For higher frequencies, the difference is significant. The most feasible PTO system will be a trade-off between efficiency and cost. It is interesting to note that the case of reactive control of a PTO constrained to always deliver positive power is almost as efficient as the unconstrained reactive control case. This is of course only possible for MDOF WECs with controlled modes oscillating out of phase with each other.

A constraint that is present in all results is the kinematic constraint imposed by the hinges. Even higher power absorption can be reached if also this constraint is removed. This would however correspond to a conceptually different WEC absorbing energy from up to 5*6 modes of motion and is not considered any further.

Figure 2.10 shows more realistic results for long-crested irregular waves and real control with frequency independent PTO damping optimized for each sea state (wave spectrum). This optimization problem is described in Section 2.4.4. The irregular waves are represented by a three parameter JONSWAP spectrum (eq. (2.7)). The γ parameter in the JONSWAP spectrum is related to the bandwidth of the spectrum. It is seen that an decrease in γ will distribute the power absorption more evenly over the peak frequencies, as expected. γ also

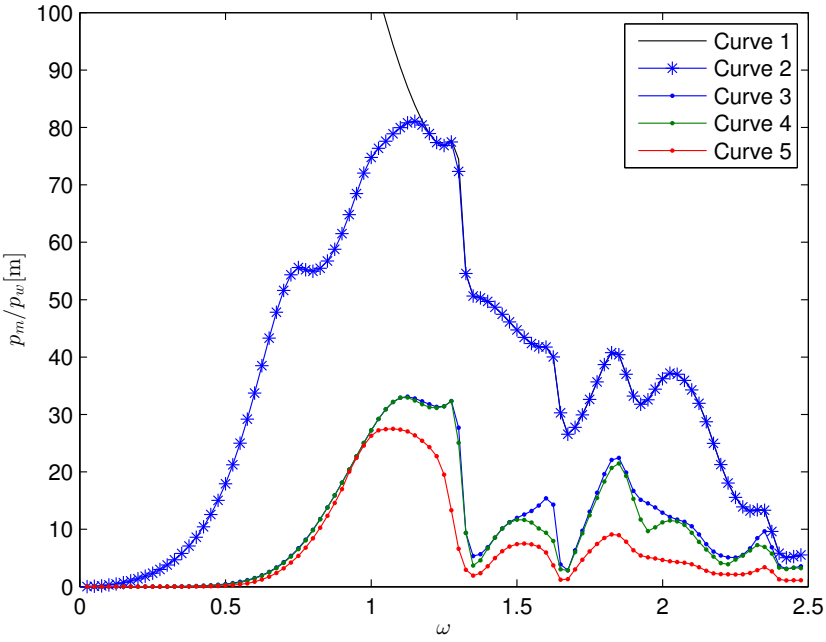

Curve	Variables	Constraints	Convex prob.?
1	Analytical sol.	None	Yes
2	$\Re\{\check{\mathbf{V}}\}$,$\Im\{\check{\mathbf{V}}\}$	Eq. (2.81)	Yes
3	$\Re\{\check{\mathbf{V}}\}$,$\Im\{\check{\mathbf{V}}\}$	Eqs. (2.82), (2.52)	Yes
4	$\Re\{\check{\mathbf{V}}\}$,$\Im\{\check{\mathbf{V}}\}$	Eqs. (2.82), (2.52), (2.55) with $p_{min,lim} = 0$	No
5	$b_{u,7}, \cdots, b_{u,10}$	Eq. (2.82)	No

Figure 2.9: Optimal power absorption in regular waves of steepness 1/30 with various control strategies and constraints. Curve 1 present the unconstrained maximum with absorption in all 10 modes (eq. (2.45)). Curve 2 introduce motion amplitude constraints. Curve 3 only allow power absorption from the hinge modes. Curve 4 constrain the instantaneous absorbed power to be non-negative. Curve 5 consider real control with diagonal PTO damping matrix.

have implications on the optimality of a frequency independent PTO system. With a small γ, the adverse effect of restraining the PTO damping to be frequency independent will be more severe, since more energy is present on frequencies where the PTO is sub-optimal.

Figure 2.11 shows the optimal PTO damping coefficients in irregular waves. It is seen that $b_{u,2}$ and $b_{u,4}$ are always identical, ensuring that the WEC is symmetrical about the wave propagation axis also in a displaced state. This could have been included as a-priori information in the optimization problem, reducing the number of unknowns from 4 to 3. Another interesting observation is that the optimal damping coefficient of the down-wave buoy, $b_{u,3}$, is zero for the range of frequencies where the capture width is largest.

Figure 2.12 shows the trade-offs between a large mean power and small variability of power, as described in Sections 2.4.2 and 2.4.4. There seems to be no obvious trade-off, as a significant reduction in variability is associated with a significant reduction in absorbed power. It should be noted that long crested waves are assumed. In more realistic short crested waves, the variability is believed to be smaller, since the relative contribution from the buoys will be more even in this case.

A more extensive optimization of the WEC should include optimization of geometry parameters. Since geometry parameters cannot (normally) be changed with changing wave conditions, a long term approach accounting for the joint probability of sea state parameters should be made. This type of optimization will normally be very time consuming, since changes in geometry parameters generally require the hydrodynamic coefficients to be re-calculated. For this particular WEC, changes in the hinge locations can be made without having to re-run the hydrodynamic code provided that the hydrodynamic coefficients are available in all 6*5 modes of motion, which is the number of degrees of freedom in the case without hinge constraints. This is described in Section 4. A uniform scaling of all lengths can also be made without re-running the hydrodynamic code by applying the Froude scaling law on the hydrodynamic coefficients. Geometry optimization is outside the scope of this thesis.

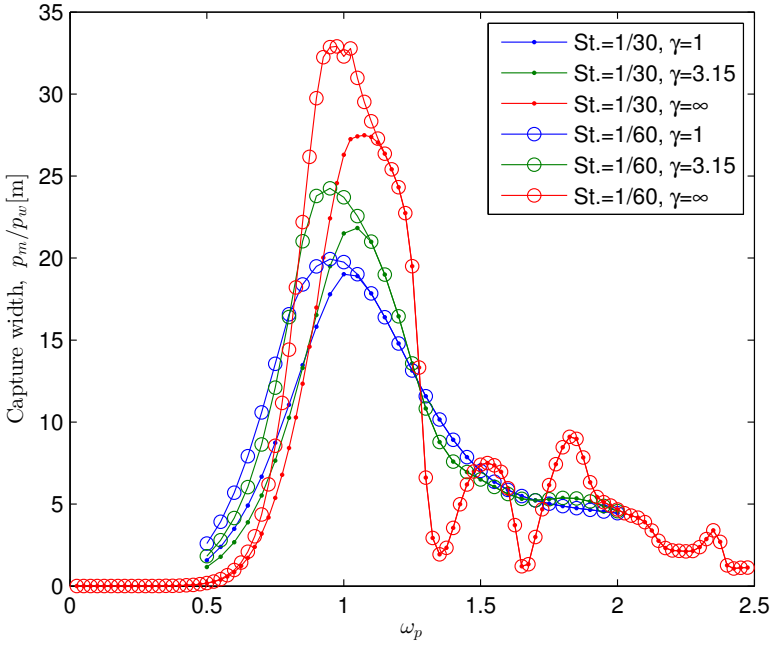

Figure 2.10: Optimal power absorption under real control in irregular waves including amplitude constraints. The frequency independent PTO damping coefficients are optimized in each sea state, and shown in Figure 2.11. Sensitivity to the JONSWAP spectrum peakedness parameter γ is shown. The case $\gamma = \infty$ should here be interpreted as a regular wave with angular frequency $\omega = \omega_p$ and height $H = \sqrt{1/2}H_s$ (matching surface elevation variance). The dependency on significant wave height H_s is due to the constraint on the standard deviation of the hinge angle, $\sqrt{2}\sigma_q \leq 14$ [deg]. Therefore, capture width is presented for wave steepness 1/30 and 1/60. Steepness is defined as $\sqrt{1/2}H_s/\lambda_p$ with λ_p being the (finite depth) wave length corresponding to the peak frequency.

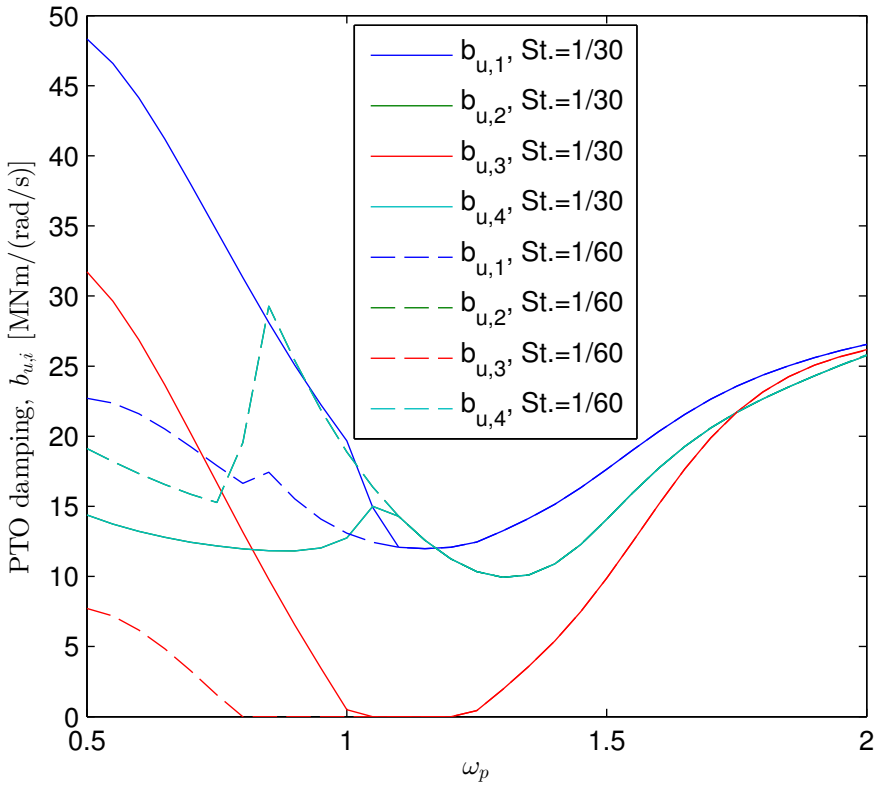

Figure 2.11: Optimal PTO damping coefficients in irregular waves of steepness 1/30 and 1/60. Only JONSWAP spectra with $\gamma = 1$ is considered. $b_{u,1}$ and $b_{u,3}$ are the damping coefficients of the up-wave and down-wave buoys, respectively. Note that $b_{u,2}$ and $b_{u,4}$ are always identical. The corresponding power absorption is given in Figure 2.10.

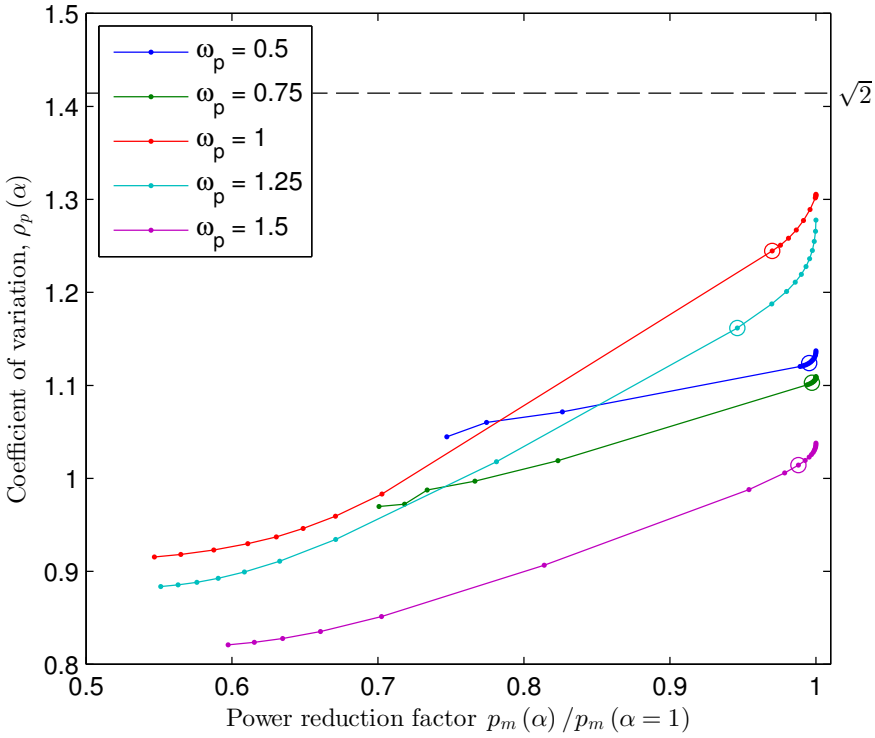

Figure 2.12: Multi-objective optimization of PTO damping for different sea states. The optimization tries to maximize the mean absorbed power p_m while at the same time minimizing the coefficient of variation of the power, ρ_p. The curves (one for each sea state) show the variation with the α parameter in the objective function (eq. (2.79)), expressing different trade-offs between large mean power and small variability. The small dots shows the values $\alpha = 0.1, 0.15, \ldots, 1$ whereas the large O shows the value $\alpha = 0.5$. The reference power p_{ref} in the objective function is taken as the optimal power without regard to the variability, such that p_m/p_{ref} represent a reduction factor. The amplitude constraint is given by eq. (2.82). The significant wave height is $H_s = \sqrt{2}\lambda_p/30$ with λ_p being the (finite depth) wave length corresponding to the peak frequency.

3 Wave radiation forces in the time domain

3.1 Introduction

Linear potential flow theory is still an important tool in the analysis of wave-body interactions. For linear equations of motion, a frequency domain analysis is the preferred choice since statistical response quantities is then readily obtained from the frequency response functions and the wave spectrum. Moreover, the frequency dependency of the added mass and damping is straightforward to incorporate in a frequency domain analysis. If the equations of motion includes nonlinear forces in addition to the linear hydrodynamic ones, a time-domain approach is needed. In this case, the motions can be obtained using Cummin's equation (Cummins, 1962), which includes a convolution integral representing the fluid memory effect. The kernel of the convolution integral is the retardation function, which can either be obtained directly from time domain potential flow solvers (Babarit et al., 2005) or, (more often) from its frequency domain counterparts, the added mass and damping, using the Ogilvie relations (Ogilvie, 1964).

Cummin's equation is inconvenient to implement in standard simulation packages and the convolution integral is time consuming to evaluate. Moreover, it is not convenient for analysis and design of control systems (Taghipour et al., 2008). For these reasons, many authors have sought a replacement of the convolution integral by an approximate state space model, with the advantage that the equations of motion are reduced to a set of ordinary differential equations. The task of finding the approximate state space model based on another type of system description can be seen as a system identification problem. Taghipour et al. (2008) reviews and compares different system identification approaches in a hydrodynamic context. The three approaches considered are time domain identification (referred to as impulse response curve fitting), realization theory and frequency domain identification (referred to as regression in the frequency domain). They demonstrate that both frequency domain identification and realization theory work well for identification of a radiation force model of a modern container-ship with zero forward speed in open sea conditions, and that they imply a significant reduction in computational

time compared to the direct application of Cummin's equation. Time domain identification was only considered for a generic rational transfer function.

A single body in open sea conditions, such as the container-ship considered by Taghipour et al. (2008), is characterized by an added mass and damping that have only a few peaks along the frequency axis. The corresponding retardation function has typically a short memory. Multibody systems, single bodies in confined water volumes (e.g. towing tanks) and other cases where resonant liquid motion occur are on the contrary characterized by added mass and damping curves with a large number of peaks along the frequency axis and a retardation function with a long memory.

This chapter deals with a frequency domain identification method based on fitting of rational transfer functions written on a pole-residue form, which is particularly well suited for problems with strongly frequency dependent added mass and damping. The method will be demonstrated for the hinged 5 body WEC presented in Section 2.5, and for an array of upright circular cylinders with equal spacing, closely related to the channel problem. The method has been developed through a series of papers (Gustavsen and Semlyen, 1999; Gustavsen, 2006; Deschrijver et al., 2008) and implemented in a package of Matlab routines made available on the internet (Gustavsen, 2012). The method was originally intended for analysis of electrical power systems, and to the author's knowledge, it has not been reported in the hydrodynamic literature.

For large multibody systems, the evaluation of added mass and damping for high frequencies can easily become infeasible since the panel size used in the boundary element solvers should be taken as a fraction of the wave length associated with the highest frequency. For this reason, the effect of the high frequency truncation is investigated and parameter constraints governing the behavior of the high frequency tail, above the fitting range, is suggested.

Passivity is a fundamental property of wave radiation forces which we want to retain in the approximating state space model in order to guarantee stability of the equations of motion. For the high order models needed to represent strongly frequency dependent added mass and damping, small passivity violations is hard to avoid. An accompanying method for passivity enforcement is developed in the papers (Gustavsen, 2008; Semlyen and Gustavsen, 2009). In this thesis, the method for passivity enforcement has been modified and re-implemented to suit systems where the added mass and damping matrices are sparse and structured, which is typical for multibody systems with geometrical symmetry. With the modified method, this sparsity and structure is retained after the passivity enforcement. A modification to the passivity assessment method, which is necessary for systems with vanishing damping in the low frequency limit, is also suggested.

It is widely recognized that WECs should be placed in arrays, or farms, in

order to be economically viable. In that case, the hydrodynamic interaction between the WECs in the farm is important, even when they have relatively large spacing. The large added mass and damping matrix representing a whole farm of WECs will typically be strongly frequency dependent. The VF method can then be an important tool if the farm performance should be analyzed in the time domain and a state space representation is desired. A state space representation will in this case reduce the computational time greatly as compared to a retardation function representation. A state space representation will also enlarge the "toolbox" of methods available for analyzing the system, especially if automatic control is part of the problem.

The work presented in this chapter have resulted in a paper which have been submitted to the journal Ocean Engineering (Rogne et al., 2013).

3.2 Important properties of wave radiation forces

Cummins equation (Cummins, 1962) governs the motions of a floating body at zero forward speed in the time domain and can be written as,

$$\left(\mathbf{M}+\mathbf{A}_{\infty}\right)\ddot{\mathbf{q}}\left(t\right)+\int_{0}^{t}\mathbf{k}\left(t-\tau\right)\dot{\mathbf{q}}\left(\tau\right)d\tau+\mathbf{G}\mathbf{q}\left(t\right)=\mathbf{f}_{exc}\left(t\right)+\mathbf{f}_{nl}\left(t,\mathbf{q},\dot{\mathbf{q}}\right) \quad (3.1)$$

where we have included an additional term, $\mathbf{f}_{nl}\left(t,\mathbf{q},\dot{\mathbf{q}}\right)$, representing external, generally non-linear forces. $\mathbf{f}_{exc}\left(t\right)$ is the linear wave excitation forces and $\mathbf{A}_{\infty}$ is the added mass matrix in the high frequency limit. Instead of representing $\mathbf{A}_{\infty}$ by a high frequency approximation, which would require a very fine discretization of the body geometry, one should find $\mathbf{A}_{\infty}$ by solving a modified boundary value problem where the usual free surface condition is replaced with the condition of vanishing velocity potential on the free surface. The commercial BEM code WAMIT, which is used in this study, includes this feature.

The retardation function $\mathbf{k}\left(t\right)$ can be found from frequency domain data using the inverse Fourier transform:

$$\mathbf{k}\left(t\right)=\mathcal{F}^{-1}\left[\mathbf{K}\left(j\omega\right)\right]=\mathcal{F}^{-1}\left[\mathbf{B}\left(\omega\right)+j\omega\left(\mathbf{A}\left(\omega\right)-\mathbf{A}_{\infty}\right)\right] \quad (3.2)$$

Here, $\mathbf{B}\left(\omega\right)$ and $\mathbf{A}\left(\omega\right)$ is the damping and added mass, respectively. The retardation function $\mathbf{k}\left(t\right)$ is causal, implying that $\mathbf{k}\left(t\right)=\mathbf{0}$ for $t<0$ (i.e. there is no force due to future motions). A consequence of this is that we can find $\mathbf{k}\left(t\right)$ with knowledge only about the damping,

$$\mathbf{k}\left(t\right)=\frac{2}{\pi}\int_{0}^{\infty}\mathbf{B}\left(\omega\right)\cos\left(\omega t\right)d\omega \quad (3.3)$$

, or only the added mass:

$$\mathbf{k}(t) = -\frac{2}{\pi}\int_0^\infty \omega\left(\mathbf{A}(\omega) - \mathbf{A}_\infty\right)\sin(\omega t)\, d\omega \tag{3.4}$$

These are often referred to as the Ogilvie relations (Ogilvie, 1964). Falnes (2002) gives a thorough discussion about impulse response functions in hydrodynamics and their causality properties.

The asymptotic values of the retardation function $\mathbf{k}(t)$ as $t \to 0$ and as $t \to \infty$, and its Fourier transform $\mathbf{K}(j\omega)$ as $\omega \to 0$ and as $\omega \to \infty$ are given by e.g. Taghipour et al. (2008):

$$\mathbf{k}(0) = \frac{2}{\pi}\int_0^\infty \mathbf{B}(\omega)\, d\omega \tag{3.5}$$

$$\lim_{t\to\infty} \mathbf{k}(t) = \mathbf{0} \tag{3.6}$$

$$\mathbf{K}(0) = \mathbf{0} \tag{3.7}$$

$$\lim_{\omega\to\infty} \mathbf{K}(j\omega) = \mathbf{0} \tag{3.8}$$

It's worth noting that although $\mathbf{K}(0) = \mathbf{0}$, we have that $\mathbf{A}(0) \neq \mathbf{0}$. Further, both the real and imaginary part of $\mathbf{K}(j\omega)$ are symmetric:

$$K_{ij}(j\omega) = K_{ji}(j\omega) \tag{3.9}$$

The derivation of this symmetry property can be found in e.g. Falnes (2002) and Newman (1977).

The wave radiation forces are passive. This is a fundamental property which implies that the *time averaged* energy transport from the body (or system of bodies) is non-negative. The mathematical condition for passive wave radiation forces is that the damping matrix is positive semi-definite, meaning that,

$$\mathbf{x}^T\mathbf{B}\mathbf{x} \geq 0 \tag{3.10}$$

holds for any $\mathbf{x}$ (Falnes, 2002, p. 213) . A necessary (but not sufficient) condition for positive semi-definiteness is non-negative diagonal entries. When $\mathbf{B} = \Re[\mathbf{K}]$ is positive semi-definite, we say that $\mathbf{K}$ is positive real. An equivalent condition for positive semi-definite $\mathbf{B}$ is,

$$\mathrm{eig}(\mathbf{B}) \geq \mathbf{0} \tag{3.11}$$

where $\mathrm{eig}(\mathbf{B})$ is a vector containing the eigenvalues of $\mathbf{B}$ and the inequality should be understood element-wise. Since $\mathbf{B}$ is symmetric, its eigenvalues will be real.

Khalil (2002) defines a passive system to be one that satisfies $\mathbf{f}(t)^T \dot{\mathbf{q}}(t) \geq \dot{V}(t)$, where $\dot{\mathbf{q}}(t)$ is the system inputs (here velocities), $\mathbf{f}(t)$ is the system outputs (here radiation forces) and $\dot{V}(t)$ is the rate of change of some scalar storage function (here stored energy). The added mass is associated with kinetic and potential energy stored in the body's near field, whereas the damping is associated with energy radiated into the far-field (Falnes, 2002). Thus, if we define $V(t)$ to be the kinetic and potential energy in the near field, the condition of positive semi-definite damping matrix comply with Khalil's definition of passivity.

3.3 Utilizing geometrical symmetries

Bodies (or multibody systems) with geometrical symmetries will have added mass and damping matrices with a special structure. One example is an axisymmetric body with the vertical z-axis as the symmetry axis. For this case, we have that $B_{11} = B_{22}$, $B_{44} = B_{55}$, $B_{51} = B_{15} = -B_{42} = -B_{24}$ and that all other matrix entries except B_{33} are uniformly zero (zero for all frequencies). That is, the full damping matrix can be constructed by multiplying 4 independent parameters with either 1 or -1. The same structure appears for the added mass matrix. For a single body without geometrical symmetry the number of independent parameters will be at most 21, since $\mathbf{A}$ and $\mathbf{B}$ are symmetric matrices.

It is desirable to retain this structure in a rational approximation of the radiation forces, and it will be useful to have a methodology to identify the structure and number of independent parameters of the added mass and damping matrices. For geometries that produce added mass and damping matrices that are uniformly zero in some matrix entries, we can calculate the number of non-zero independent matrix entries as,

$$n_i = \text{rank}\left[\begin{array}{ccc} \text{col}(\mathbf{B}(\omega_1)) & \cdots & \text{col}(\mathbf{B}(\omega_n)) \end{array}\right] - 1 \tag{3.12}$$

where ω_j are discrete frequencies and the $\text{col}(.)$ operator stacks the columns of a matrix on top of each other to form a single column. We subtract by 1 since we do not count the entries which are uniformly zero. In practice, we must include a small tolerance in the calculation of the matrix rank due to numerical inaccuracies. If we make sure that the panel model possess the same symmetries as the ideal geometry, we can choose a very small tolerance.

If we collect the independent matrix entries of $\mathbf{A}$ and $\mathbf{B}$ in the column vectors $\mathbf{a}$ and $\mathbf{b}$, we have the relations,

$$\text{col}(\mathbf{A}(\omega)) = \mathbf{Q}\mathbf{a}(\omega) \tag{3.13}$$

$$\text{col}(\mathbf{B}(\omega)) = \mathbf{Q}\mathbf{b}(\omega) \tag{3.14}$$

For a n_d degree of freedom system with n_i independent matrix entries, the matrix $\mathbf{Q}$ will have size $n_d^2 \times n_i$ and be populated by the numbers -1, 0 and 1. In Section 3.8.1 we are able to plot the hydrodynamic coefficients of a wave energy converter with 10 degrees of freedom on a single page, because only 11 of the 100 matrix entries are non-zero and independent. The motivation here for identifying the independent coupling terms in the radiation matrices is not only to increase clarity and reduce the computational time. In Section (3.7.5) about passivity enforcement we implicitly use the matrix $\mathbf{Q}$ to retain the sparsity and structure of the radiation matrices that would otherwise be lost.

3.4 Rational transfer functions

It is well known that a linear single-input single-output (SISO) system, $Y(s) = H(s)\,U(s)$, where the transfer function is rational,

$$H(s) = \frac{b_r s^r + b_{r-1} s^{r-1} + \cdots + b_0}{s^n + a_{n-1} s^{n-1} + \cdots + a_0} \tag{3.15}$$

has a representation in the time domain by a state space model:

$$\dot{\boldsymbol{\mathcal{X}}}(t) = \boldsymbol{\mathcal{A}}\boldsymbol{\mathcal{X}}(t) + \boldsymbol{\mathcal{B}}u(t) \tag{3.16}$$

$$y(t) = \boldsymbol{\mathcal{C}}\boldsymbol{\mathcal{X}}(t) + \boldsymbol{\mathcal{D}}u(t) \tag{3.17}$$

The matrices $\boldsymbol{\mathcal{A}}$, $\boldsymbol{\mathcal{B}}$, $\boldsymbol{\mathcal{C}}$ and $\boldsymbol{\mathcal{D}}$ are not unique, meaning that several sets of matrices will realize a given system. Some canonical forms expressing these matrices in terms of the real coefficients $b_1, \cdots, b_m$, $a_1, \cdots, a_n$ are given by e.g. Chen (1998) and Kailath (1980). The extension to MIMO systems is straightforward. The transfer function $H(s)$ is the (one-sided) Laplace transform of the corresponding impulse response $h(\tau)$. For causal systems, such as all systems with a state space representation, $H(s = j\omega)$ corresponds also to the Fourier transform of $h(\tau)$.

Non-rational transfer functions can be approximated by eq. (3.15) using complex curve fitting, often based on measurements or numerical calculations at discrete frequencies. Perez and Fossen (2011) used complex curve fitting to fit the entries of the frequency response $\mathbf{K}(j\omega)$ and emphasize the importance of using *a priori* information about the hydrodynamic system in the identification. They state that the relative degree $(n - r)$ of the rational function, eq. (3.15), should be one or higher to retain a strictly proper $\mathbf{K}(j\omega)$, i.e. $\lim_{\omega\to\infty} \mathbf{K}(j\omega) = \mathbf{0}$ and $\boldsymbol{\mathcal{D}} = \mathbf{0}$. A further constraint is imposed by considering the requirement $\lim_{t\to 0^+} \mathbf{k}(t) \neq \mathbf{0}$ which imply that the relative degree

must be exactly one. Further, the requirement $\lim_{\omega\to 0}\mathbf{K}(j\omega)=\mathbf{0}$ imply that the coefficient b_0 must be zero.

If we let $\hat{\mathbf{K}}(s)$ denote the rational transfer matrix which approximates $\mathbf{K}(j\omega)$ for $s=j\omega$, we can write its entries as,

$$\hat{K}_{ij}(s)=\frac{P_{ij}(s)}{Q_{ij}(s)}=\frac{b_{n-1}s^{n-1}+\cdots+b_1 s}{s^n+a_{n-1}s^{n-1}+\cdots+a_0} \tag{3.18}$$

The non-proper part of the radiation forces, i.e. the infinite frequency added mass $\mathbf{A}_\infty$, is also a-priori information which is subtracted from the added mass dataset before the fitting in order to make $\hat{\mathbf{K}}(j\omega)$ strictly proper.

The identification method considered by Perez and Fossen use the coefficients $b_{n-1},b_{n-2},\cdots,b_1,a_n,a_{n-1},\cdots,a_0$ as free variables in the fitting. The method considered here rewrite the rational transfer functions on a pole-residue form. This is achieved by first expressing the denominator polynomial in terms of its complex roots:

$$\hat{K}_{ij}(s)=\frac{P_{ij}(s)}{Q_{ij}(s)}=\frac{b_{n-1}s^{n-1}+\cdots+b_1 s}{(s-p_1)(s-p_2)\cdots(s-p_n)} \tag{3.19}$$

The complex roots $p_1,\cdots,p_n$ of the denominator corresponds to the poles of the transfer function, which is also the eigenvalues of the $\boldsymbol{\mathcal{A}}$ matrix in the state space model. If these poles are distinct, we can carry out a partial fraction expansion and write the transfer function in yet another form (Kailath, 1980),

$$\hat{K}_{ij}(s)=\frac{r_1}{(s-p_1)}+\frac{r_2}{(s-p_2)}+\cdots+\frac{r_n}{(s-p_n)} \tag{3.20}$$

where r_k is the residue corresponding to the pole p_k. Because the coefficients $b_{n-1},b_{n-2},\cdots,b_1,a_n,a_{n-1},\cdots,a_0$ are real, the poles are either real or come in complex conjugate pairs. That is, if p_k is real, r_k is also real. If p_k is complex, r_k is also complex and there is an integer q such that $p_k=p_q^*$ and $r_k=r_q^*$.

Gustavsen and Semlyen (1999) suggest to use these residues and poles as free variables in the fitting of rational transfer function approximations of admittance matrices, relating voltage to current in electrical power systems. They also suggest to use the same set of poles for all elements in the transfer matrix so that the full matrix can be written:

$$\hat{\mathbf{K}}(s)=\sum_{k=1}^{n}\frac{\mathbf{R}_k}{s-p_k} \tag{3.21}$$

The choice of using a common set of poles may seem like an unnecessary restriction. However, as will become evident in Section 3.5.1, this leads to compact state space models which justify the need for a somewhat higher number of common poles.

If the number of poles is even, we can reverse the partial fraction expansion for each pair of poles and write,

$$\hat{\mathbf{K}}(s) = \sum_{q=1}^{n/2} \frac{\mathbf{a}_q s + \mathbf{b}_q}{s^2 + 2\xi_q \Omega_q s + \Omega_q^2} \tag{3.22}$$

where $\mathbf{a}_q$, $\mathbf{b}_q \in \mathbb{R}^{n_d \times n_d}$ and ξ_q and Ω_q is real positive scalars. The requirement $\xi_q > 0$ and $\Omega_q > 0$ ensures that the corresponding poles in eq. (3.21) has negative real part (i.e. that the transfer function is stable). It is worth noting that the parameters ξ_q and Ω_q is analogous to the damping ratio and undamped natural frequency of the one degree of freedom mass-damper-spring oscillator.

If we sort the poles and residues so that p_k and p_{k+1} is either both real or constitute a complex conjugate pair (and likewise for the residuals), we can relate ξ_q, Ω_q to the poles, and $\mathbf{a}_q$, $\mathbf{b}_q$ to the residues as,

$$p_k = -\Omega_q \left(\xi_q - \sqrt{\xi_q^2 - 1}\right) \tag{3.23}$$

$$p_{k+1} = -\Omega_q \left(\xi_q + \sqrt{\xi_q^2 - 1}\right) \tag{3.24}$$

$$\mathbf{R}_k = \frac{\mathbf{a}_q p_k + \mathbf{b}_q}{p_k - p_{k+1}} \tag{3.25}$$

$$\mathbf{R}_{k+1} = -\frac{\mathbf{a}_q p_{k+1} + \mathbf{b}_q}{p_k - p_{k+1}} \tag{3.26}$$

from which we see that $\xi_q > 1$ yields real distinct poles, $\xi_q = 1$ yields real repeated poles, and $\xi_q < 1$ yields complex conjugate (and thus distinct) poles. We also see that the residues goes to infinity when $\xi_q \to 1$ which explains why the partial fraction decomposition of eq. (3.19) is only possible for distinct poles. The inverse relations become:

$$\Omega_q = \sqrt{p_k p_{k+1}} \tag{3.27a}$$

$$\xi_q = \frac{-p_k - p_{k+1}}{\sqrt{p_k p_{k+1}}} \tag{3.27b}$$

$$\mathbf{a}_q = \mathbf{R}_k + \mathbf{R}_{k+1} \tag{3.27c}$$

$$\mathbf{b}_q = -p_{k+1}\mathbf{R}_k - p_k \mathbf{R}_{k+1} \tag{3.27d}$$

Damaren (2000) used the rational approximation in eq. (3.22) with $\mathbf{b}_q = \mathbf{0}$ to study the (water) wave radiation problem, and pointed out that by setting $\mathbf{b}_q = \mathbf{0}$ for all q, the property $\hat{\mathbf{K}}(s = 0) = 0$ would automatically by satisfied. The parameters ξ_q and Ω_q was estimated by first fitting the parameters of eq. (3.18) to the diagonal entries $K_{ii}(s)$ using an similar approach as Perez and Fossen (2011). The denominator coefficients a_k was then converted into ξ_q and Ω_q. $\mathbf{a}_q$ was determined with standard least squares methods.

Damaren states that a sufficient condition for $\hat{\mathbf{K}}(s)$ to represent a passive system is that $\mathbf{a}_q$ is positive definite for all q. This passivity requirement is sufficient but also too restrictive, and can impair the accuracy of the fit. Omitting the constant term in the nominator as a mean to enforce $\hat{\mathbf{K}}(s=0) = \mathbf{0}$ is also too restrictive.

3.5 Time domain representation of pole-residue models

3.5.1 State space representation

In Section 3.4 we stated that the convolution integral in Cummin's equation can be approximated by a state space model without a feed-through term:

$$\begin{aligned} \dot{\boldsymbol{\mathcal{X}}}(t) &= \boldsymbol{\mathcal{A}}\boldsymbol{\mathcal{X}}(t) + \boldsymbol{\mathcal{B}}\dot{\mathbf{q}}(t) \\ \mathbf{f}_{SPR}(t) &= \boldsymbol{\mathcal{C}}\boldsymbol{\mathcal{X}}(t) \end{aligned} \tag{3.28}$$

Here, $\mathbf{f}_{SPR}$ denote the strictly proper (SP) portion of the radiation forces, such that the total radiation force becomes $\mathbf{f}_R = \mathbf{f}_{SPR} - \mathbf{A}_\infty \ddot{\mathbf{q}}$. If we take the Laplace transform of the above state space model, we can find the corresponding transfer matrix as:

$$\hat{\mathbf{K}}(s) = \boldsymbol{\mathcal{C}}(s\mathbf{I} - \boldsymbol{\mathcal{A}})^{-1}\boldsymbol{\mathcal{B}} \tag{3.29}$$

An alternative form of this transfer matrix results from a reformulation of pole-residue form of eq. (3.21),

$$\hat{\mathbf{K}}(s) = \begin{bmatrix} \mathbf{R}_1 & \cdots & \mathbf{R}_n \end{bmatrix} \begin{bmatrix} \frac{\mathbf{I}}{s-p_1} & & \\ & \ddots & \\ & & \frac{\mathbf{I}}{s-p_n} \end{bmatrix} \begin{bmatrix} \mathbf{I} \\ \vdots \\ \mathbf{I} \end{bmatrix} \tag{3.30}$$

where $\mathbf{I}$ is the identity matrix of the same size as $\mathbf{R}_k$. By a direct comparison of these two forms we see that one choice of state space matrices is,

$$\boldsymbol{\mathcal{A}}' = \operatorname{diag}(p_1\mathbf{I}, \ldots, p_n\mathbf{I}) \tag{3.31}$$

$$\boldsymbol{\mathcal{B}}' = \begin{bmatrix} \mathbf{I} & \cdots & \mathbf{I} \end{bmatrix}^T \tag{3.32}$$

$$\boldsymbol{\mathcal{C}}' = \begin{bmatrix} \mathbf{R}_1 & \cdots & \mathbf{R}_n \end{bmatrix} \tag{3.33}$$

where $\boldsymbol{\mathcal{A}}'$ and $\boldsymbol{\mathcal{C}}'$ are complex valued. Because the poles and residues come in complex conjugate pairs, it is possible to find a special similarity transform,

$$\boldsymbol{\mathcal{A}} = \mathbf{T}^{-1}\boldsymbol{\mathcal{A}}'\mathbf{T} \tag{3.34}$$

$$\boldsymbol{\mathcal{B}} = \mathbf{T}^{-1}\boldsymbol{\mathcal{B}}' \tag{3.35}$$

$$\boldsymbol{\mathcal{C}} = \boldsymbol{\mathcal{C}}'\mathbf{T} \tag{3.36}$$

that yields real valued matrices (Semlyen and Gustavsen, 2009). Moreover, if we express the transformation matrix as a product $\mathbf{T} = \mathbf{P}\tilde{\mathbf{T}}$, where $\mathbf{P}$ is a suitable permutation matrix, the real only system matrix $\boldsymbol{\mathcal{A}}$ can be brought to a block diagonal form with 2-by-2 blocks corresponding to complex conjugate pairs of poles and scalar "blocks" corresponding to the real poles.

It is worth noting that the order of the state space model is only linear in the number of degrees of freedom n_d, at least if we disregard the effect of n_d on the required number of poles. This is a consequence of the choice of using a common set of poles for all elements in $\hat{\mathbf{K}}(s)$. If individual pole sets had been used for each coupling term, the order would have been proportional to n_d^2. Yet another alternative would have been to use a set of poles for each column in $\hat{\mathbf{K}}(s)$. This would also give an order proportional to n_d, but with the drawback that $\hat{\mathbf{K}}(s)$ would be slightly unsymmetric. Gustavsen and Semlyen (2004) give a thorough discussion of the state space realization of pole-residue models and the topic of model order reduction, which is not treated here.

Using the state space representation of the convolution integral, we can express Cummin's equation as a system of first order differential equations:

$$\begin{bmatrix} \ddot{\mathbf{q}} \\ \dot{\mathbf{q}} \\ \dot{\boldsymbol{\mathcal{X}}} \end{bmatrix} = \underbrace{\begin{bmatrix} \mathbf{0} & -\mathbf{M}_T^{-1}\mathbf{G} & -\mathbf{M}_T^{-1}\boldsymbol{\mathcal{C}} \\ \mathbf{I} & \mathbf{0} & \mathbf{0} \\ \boldsymbol{\mathcal{B}} & \mathbf{0} & \boldsymbol{\mathcal{A}} \end{bmatrix}}_{\boldsymbol{\mathcal{A}}_{FM}} \begin{bmatrix} \dot{\mathbf{q}} \\ \mathbf{q} \\ \boldsymbol{\mathcal{X}} \end{bmatrix} + \begin{bmatrix} \mathbf{f}_{exc} + \mathbf{f}_{nl} \\ \mathbf{0} \\ \mathbf{0} \end{bmatrix} \tag{3.37}$$

We have here included the non-proper portion of the wave radiation forces, $\mathbf{A}_\infty$, as part of the "total" mass matrix $\mathbf{M}_T = \mathbf{M} + \mathbf{A}_\infty$.

3.5.2 Second order ODE representation

In the following we will show that there is an alternative to the state space form of the equations of motion, eq. (3.37), when the number of poles in the rational model is even. In that case it is possible to use the oscillator formulation, eq. (3.22), with parameters obtained from the poles and residues using eqs. (3.27). The SP radiation forces can then be written as a sum,

$$\mathbf{F}_{SPR}(s) = \sum_q \mathbf{F}_{SPR,q}(s) \tag{3.38}$$

with contributions given by the equation:

$$\left(s^2 + 2\xi_q\Omega_q s + \Omega_q^2\right)\mathbf{F}_{SPR,q}(s) = \left(\mathbf{a}_q s + \mathbf{b}_q\right) s\mathbf{q}(s) \tag{3.39}$$

If we let $\mathbf{Y}_q(s)$ designate the Laplace transform of a signal $\boldsymbol{\mathcal{Y}}_q(t)$ and define $\mathbf{F}_{SPR,q}(s) = s\mathbf{Y}_q(s)$, we can divide eq. (3.39) by s and obtain the following system of second order ordinary differential equations (ODE) in the time

domain:

$$\ddot{\boldsymbol{\mathcal{Y}}}_q(t) + 2\xi_q\Omega_q\dot{\boldsymbol{\mathcal{Y}}}_q(t) + \Omega_q^2\boldsymbol{\mathcal{Y}}_q(t) = \mathbf{a}_q\dot{\mathbf{q}}(t) + \mathbf{b}_q\mathbf{q}(t) \tag{3.40}$$

We can then write the strictly proper portion of the radiation forces as,

$$\mathbf{f}_{SPR}(t) = \sum_q \dot{\boldsymbol{\mathcal{Y}}}_q(t) \tag{3.41}$$

and formulate the equations of motion of the coupled wave-body system as a set of second order ODEs with constant coefficients:

$$\underbrace{\begin{bmatrix} \mathbf{M}_T & \mathbf{0} \\ \mathbf{0} & \mathbf{I} \end{bmatrix}}_{\check{\mathbf{M}}} \begin{bmatrix} \ddot{\mathbf{q}} \\ \ddot{\boldsymbol{\mathcal{Y}}} \end{bmatrix} + \underbrace{\begin{bmatrix} \mathbf{0} & \check{\mathbf{B}}_{12} \\ \check{\mathbf{B}}_{21} & \check{\mathbf{B}}_{22} \end{bmatrix}}_{\check{\mathbf{B}}} \begin{bmatrix} \dot{\mathbf{q}} \\ \dot{\boldsymbol{\mathcal{Y}}} \end{bmatrix} + \underbrace{\begin{bmatrix} \mathbf{G} & \mathbf{0} \\ \check{\mathbf{G}}_{21} & \check{\mathbf{G}}_{22} \end{bmatrix}}_{\check{\mathbf{G}}} \begin{bmatrix} \mathbf{q} \\ \boldsymbol{\mathcal{Y}} \end{bmatrix} = \begin{bmatrix} \mathbf{f} \\ \mathbf{0} \end{bmatrix} \tag{3.42}$$

Here, we have:

$$\boldsymbol{\mathcal{Y}} = \begin{bmatrix} \boldsymbol{\mathcal{Y}}_1^T & \cdots & \boldsymbol{\mathcal{Y}}_m^T \end{bmatrix}^T \tag{3.43a}$$

$$\mathbf{M}_T = \mathbf{M} + \mathbf{A}_\infty \tag{3.43b}$$

$$\mathbf{f} = \mathbf{f}_{exc} + \mathbf{f}_{nl} \tag{3.43c}$$

$$\check{\mathbf{B}}_{21} = \begin{bmatrix} -\mathbf{a}_1 & \cdots & -\mathbf{a}_m \end{bmatrix}^T,\ \mathbf{a}_q = \mathbf{a}_q^T \tag{3.43d}$$

$$\check{\mathbf{B}}_{12} = \begin{bmatrix} \mathbf{I} & \cdots & \mathbf{I} \end{bmatrix} \tag{3.43e}$$

$$\check{\mathbf{B}}_{22} = \operatorname{diag}\left(2\xi_1\Omega_1\mathbf{I}, \ldots, 2\xi_m\Omega_m\mathbf{I}\right) \tag{3.43f}$$

$$\check{\mathbf{G}}_{21} = \begin{bmatrix} -\mathbf{b}_1 & \cdots & -\mathbf{b}_m \end{bmatrix}^T,\ \mathbf{b}_q = \mathbf{b}_q^T \tag{3.43g}$$

$$\check{\mathbf{G}}_{22} = \operatorname{diag}\left(\Omega_1^2\mathbf{I}, \ldots, \Omega_m^2\mathbf{I}\right) \tag{3.43h}$$

Note here that $\check{\mathbf{B}}$ and $\check{\mathbf{G}}$ are non-symmetric matrices. Damaren (2000) obtain a similar second order form with symmetric $\check{\mathbf{B}}$ and $\check{\mathbf{G}}$. This symmetry is possible because he assumes that $\mathbf{b}_q = \mathbf{0}$ and that $\mathbf{a}_q$ is positive definite, enabling a factoring of the type $\mathbf{a}_q = \mathbf{c}_q^T\mathbf{c}_q$.

The second order form can be useful because it enables the use of time stepping algorithms such as e.g. the Newmark-beta method, which is applicable only for second order differential equations. This has however not been implemented here, and the second order realization will not be considered any further in this thesis.

3.5.3 Impulse response functions

The rational approximation of the wave radiation forces makes it possible to obtain time domain models without convolutions terms. Still, it is worthwhile to compute the corresponding impulse response (retardation) functions,

as these gives useful insight into the system dynamics. When the rational approximation is brought to a pole-residue form, the associated retardation functions take a particularly simple form. If we take the inverse Laplace transform of eq. (3.21) we get:

$$\begin{aligned}\hat{\mathbf{k}}(t) &= H(t) \sum_{k=1}^{n} \mathbf{R}_k \exp(p_k t) \\ &= H(t) \sum_{k=1}^{n} \exp(\Re[p_k] t) (\Re[\mathbf{R}_k] \cos(\Im[p_k] t) - \Im[\mathbf{R}_k] \sin(\Im[p_k] t))\end{aligned} \tag{3.44}$$

The Heaviside step function, defined here as $H(t<0) = 0$, $H(t \geq 0) = 1$, ensures that $\hat{\mathbf{k}}(t)$ is causal. In the last equality, we have used that the poles and residues are real or come in complex conjugate pairs, with the result that the imaginary parts cancel out and we obtain a real expression for $\hat{\mathbf{k}}(t)$. The exponential term in eq. (3.44) clearly displays the well known stability criterion stating that the poles must be in the left half-plane (i.e. that $\Re[p_k] < 0$) for the response to be bounded.

In this work, we identify the poles and residues by frequency domain identification, meaning that we aim at matching $\mathbf{K}(j\omega)$ with $\hat{\mathbf{K}}(j\omega)$. The simple form of the retardation functions in eq. (3.44) shows that the selection of poles and residues as the free variables is suitable for identification also in the time domain, where the aim is to match $\mathbf{k}(t)$ with $\hat{\mathbf{k}}(t)$. Babarit et al. (2005) and others have used Prony's method to fit eq. (3.44) to the impulse response calculated at discrete times using a time domain potential flow solver. However, in the recent work by Folley et al. (2012), reviewing modeling of WEC arrays, it is noted that the method does not work well for multibody systems because of a requirement that the impulse response function should decrease sufficiently quickly to zero as time increases. This is a restriction that we want to remove in this work. Prony's method has been described by Duclos et al. (2001).

3.6 Properties of the rational approximations

3.6.1 High and low frequency asymptotic behavior

In Section 3.2 we established that $\mathbf{K}(j\omega) \to \mathbf{0}$ as $\omega \to 0$. For the rational approximation in the form considered by Perez and Fossen (2011), eq. (3.18), this property is satisfied simply by setting the constant term in the nominator

b_0 equal to zero. For the pole-residue form, this corresponds to requiring:

$$\sum_{k=1}^{n} \frac{\mathbf{R}_k}{p_k} = \mathbf{0} \tag{3.45}$$

Since, $\mathbf{R}_k$ and p_k are real or come in complex conjugate pairs this is automatically satisfied for the imaginary part, but not for the real part. In principle, one could enforce the property by reducing the number of independent parameters in the fitting by expressing one $\mathbf{R}_k$ as a function of the others. However, for the relatively high order models considered here, this has shown to produce passivity violations for small nonzero frequencies, and poor fit in the low frequency range after passivity enforcement. For this reason we choose to satisfy $\mathbf{K}(0) = \mathbf{0}$ only approximately by including $\mathbf{K}(0) = \mathbf{0}$ as a part of the dataset in the fitting. The exact enforcement of $\mathbf{K}(0) = \mathbf{0}$ is of little practical importance. The property that $\mathbf{K}(j\omega) \to \mathbf{0}$ as $\omega \to \infty$ is automatically satisfied when we employ the pole residue form.

The high- and low frequency behavior is best explored with the oscillator formulation, eq. (3.22). By setting $s = j\omega$ and rewriting $\hat{\mathbf{K}}(j\omega)$ in terms of added mass and damping, this formulation can be expressed:

$$\hat{\mathbf{B}}(\omega) = \sum_{q=1}^{n/2} \frac{\mathbf{b}_q \left(\Omega_q^2 - \omega^2\right) + 2\mathbf{a}_q \xi_q \Omega_q \omega^2}{\left(\Omega_q^2 - \omega^2\right)^2 + 4\xi_q^2 \Omega_q^2 \omega^2} \tag{3.46a}$$

$$\hat{\mathbf{B}}(0) = \sum_{q=1}^{n/2} \frac{\mathbf{b}_q}{\Omega_q^2} \tag{3.46b}$$

$$\hat{\mathbf{A}}(\omega) = \mathbf{A}_\infty + \sum_{q=1}^{n/2} \frac{\mathbf{a}_q \left(\Omega_q^2 - \omega^2\right) - 2\mathbf{b}_q \xi_q \Omega_q}{\left(\Omega_q^2 - \omega^2\right)^2 + 4\xi_q^2 \Omega_q^2 \omega^2} \tag{3.46c}$$

$$\hat{\mathbf{A}}(0) = \mathbf{A}_\infty + \sum_{q=1}^{n/2} \left(\frac{\mathbf{a}_q}{\Omega_q^2} - 2\frac{\mathbf{b}_q \xi_q}{\Omega_q^3} \right) \tag{3.46d}$$

Greenhow (1986) showed that both $\mathbf{A}(\omega) - \mathbf{A}_\infty$ and $\mathbf{B}(\omega)$ behaves like $\beta'\omega^{-2} + \beta''\omega^{-4}$ for sufficiently high frequency. In the limit $\omega \to \infty$, $\beta'\omega^{-2}$ will be the leading term. Keeping only the leading term in the nominator and denominator of eqs. (3.46a) and (3.46c), we can conclude that the rational approximation will approach the asymptotic values at the correct rate for sufficiently high frequencies. This was also showed by Perez and Fossen (2008) using the formulation of eq. (3.18). It is also seen that $\hat{\mathbf{A}}(0) \neq 0$, as it should, although $\Im\left[\hat{\mathbf{K}}(0)\right] = 0$. $\hat{\mathbf{B}}(0)$ should be zero but is only approximately so for reasons mentioned above.

3.6.2 Stability and passivity

The rational transfer matrix $\hat{\mathbf{K}}(s)$ represent a stable system if all of its poles have negative real part. Most often, the goal is to determine the body motions for given excitation forces and we are therefore interested in the stability of the force-to-motion system as well. If we temporarily let the external forces in Cummin's equation (3.1) be represented by a linear, frequency independent damping term $\mathbf{f}_{nl} = -\mathbf{B}_e\dot{\mathbf{q}}$, we can express its frequency domain counterpart as,

$$\dot{\mathbf{q}}(s) = \left[s(\mathbf{M} + \mathbf{A}_\infty) + \mathbf{B}_e + \frac{1}{s}\mathbf{G} + \hat{\mathbf{K}}(s)\right]^{-1} \mathbf{F}_{exc}(s) \tag{3.47}$$

$$= \left[\mathbf{H}(s)^{-1} + \hat{\mathbf{K}}(s)\right]^{-1} \mathbf{F}_{exc}(s) \tag{3.48}$$

$$= \hat{\mathbf{H}}_{FQ}(s)\,\mathbf{F}_{exc}(s) \tag{3.49}$$

where we use the notation $\dot{\mathbf{q}}(s) = s\mathbf{q}(s)$ so that $\dot{\mathbf{q}}(s)$ represent the Laplace transform of velocities. Note that $\mathbf{H}(s)$ equals $\hat{\mathbf{H}}_{FQ}(s)$ when $\hat{\mathbf{K}}(s) = \mathbf{0}$. The stability properties of $\hat{\mathbf{H}}_{FQ}(s)$ can be determined by calculating the eigenvalues of the system matrix $\boldsymbol{\mathcal{A}}_{FM}$ in eq. (3.37), which corresponds to the poles of $\hat{\mathbf{H}}_{FQ}(s)$. Since $\hat{\mathbf{H}}_{FQ}(s)$ relates excitation forces and body velocities, whose product is power, it is also meaningful to talk about the passivity of $\hat{\mathbf{H}}_{FQ}(s)$. One important result from control theory is that the negative feedback interconnection of a passive system is itself passive (Khalil, 2002; Perez and Fossen, 2011). This means that $\hat{\mathbf{H}}_{FQ}(s)$ represents a passive system provided that $\mathbf{H}(s)$ and $\hat{\mathbf{K}}(s)$ represents passive systems.

Moreover, if $\mathbf{H}(s)$ and $\mathbf{K}(s)$ represent *strictly* passive systems, $\hat{\mathbf{H}}_{FQ}(s)$ will be asymptotically stable (Khalil, 2002). $\mathbf{H}(s)$ represents a strictly passive system provided that $\mathbf{B}_e$ is positive definite (e.g. as in the case where $\mathbf{B}_e$ is made diagonal with arbitrary small positive diagonal elements). $\hat{\mathbf{K}}(s)$ is only passive since $\hat{\mathbf{K}}(s=0) = \mathbf{0}$. This is however of little practical importance since the excess of passivity in $\mathbf{B}_e$ compensates the lack of passivity in $\hat{\mathbf{K}}(s)$ for $s = 0$. The assumption of linear external forces is made here to simplify the discussion. However, the passivity theorems given by Khalil (2002) are not restricted to linear systems and the same conclusion carries over to the case where $\mathbf{f}_{nl}$ represent nonlinear dissipative forces with or without memory. A highly relevant example of memoryless dissipative nonlinear forces is quadratic drag arising from viscous effects, often determined by experiments. External forces with memory can represent a power take-off system (with internal states) of a wave energy converter.

Passivity of $\hat{\mathbf{K}}(s)$ is a sufficient but not necessary condition for stability of the force-to-motion system (Perez and Fossen, 2011). This will be further investigated in the numerical examples in Section 3.8 for the case $\mathbf{f}_{nl} = \mathbf{0}$.

3.7 Identification of pole-residue model

3.7.1 Vector fitting (VF)

The transfer function in eq. (3.21) is linear in the residues. Hence, the fitting of residues is facilitated by standard linear least squares methods and can be performed independently for each coupling term in the transfer matrix. The challenge lies in fitting the common set of poles, having a non-linear relation to the transfer function. Gustavsen and Semlyen (1999) developed the VF method for identification of residues and poles given transfer function data at discrete frequencies. Further improvements to the method is described in Gustavsen (2006) and Deschrijver et al. (2008) and implemented in a Matlab toolbox made available on the internet (Gustavsen, 2012). VF can be seen as a robust reformulation of the Sanathanan–Koerner iteration (Gustavsen, 2006). See also Sanathanan and Koerner (1963).

It is emphasized that the pole-residue formulation used in VF is better suited for approximations of high order models covering wide frequency ranges compared to the standard rational model, eq. (3.15). This is related to the large difference in scale of the different powers of s, which makes the transfer function very sensitive to its parameters and the curve fitting problem numerically ill-conditioned. Gustavsen and Semlyen (1999) successfully fitted a rational model using as much as 120 poles to data of a complex electrical network.

This work suggests parameter constraints not handled by the VF algorithm. For this reason, the poles found by VF is here used as initial poles in a more general nonlinear optimization, presented briefly in Section 3.7.6, which account for these parameter constraints. Due to the superior CPU-efficiency of the more specialized VF algorithm, an obvious improvement to the current approach would be to modify VF to account for the constraints.

Readers are referred to the references above for details about the VF algorithm. Since the accompanying passivity assessment and enforcement methods are modified and re-implemented in this work, a more thorough treatment of these topics is given in sections 3.7.4 and 3.7.5.

3.7.2 Weighting and scaling

The term vector fitting comes from the fact that several transfer functions (elements in the transfer matrix) are fitted to the same set of poles. Thus, the error to be minimized is a sum over all matrix elements and frequencies:

$$\epsilon^2 = \frac{\sum_q \sum_i \sum_k w_q \left| \hat{K}^s_{ik}(j\omega_q) - K^s_{ik}(j\omega_q) \right|^2}{\sum_q \sum_i \sum_k w_q \left| K^s_{ik}(j\omega_q) \right|^2} \tag{3.50}$$

The frequency weights w_q are here chosen to reflect the spacings in the frequency vector according to the trapezoidal integration rule. The relative weighting of the different matrix elements is taken care of by a pre-scaling step (thus the superscript s on K^s_{ik}). We here choose the following power conservative scaling transformation,

$$\begin{aligned} K^s_{ik}(j\omega) &= \alpha_i \alpha_k K_{ik}(j\omega) \\ \mathbf{K}^s(j\omega) &= \boldsymbol{\alpha}^T \mathbf{K}(j\omega)\,\boldsymbol{\alpha} \end{aligned} \tag{3.51}$$

with $\boldsymbol{\alpha} = \mathrm{diag}(\alpha_1, \ldots, \alpha_n)$. The coupling term weights α_i is chosen such that the mean (over frequencies) magnitude of the diagonal elements of the scaled matrix is unity. This weighting scheme reflects the fact that the degrees of freedom associated with small radiation forces is not necessarily less important and should thus be given a larger weight to compensate (i.e. the radiation pitch moment of a ship will be much larger than the radiation roll moment, although the latter is often more interesting than the former). At the same time, insignificant off-diagonal elements are given less weight. It is worth noting that since the scaling transformation is power conservative, $\hat{\mathbf{K}}$ will be passive provided that $\hat{\mathbf{K}}^s$ is passive. We can therefore use the scaled transfer matrix in the passivity enforcement as well. After the fitting and passivity enforcement, the correct residue matrices is found by the inverse scaling transformation, $R_{ik,j} = R^s_{ik,j}/(\alpha_i \alpha_k)$.

The weighting scheme presented above will be used in the numerical examples in Section 3.8.1 and 3.8.2. This is just a choice and other weighting schemes is of course possible.

3.7.3 Parameter constraints

Since we showed in Section 3.6.1 that the rational approximation have correct behavior for sufficiently high frequency, it is natural to ask how high frequency is high enough. This largely depends on ξ_q and it is seen that terms with very large ξ_q tends slowly to zero (see eq. (3.46)). To avoid that $\hat{\mathbf{K}}(j\omega)$ tends too slowly to zero above the frequency range of the dataset, we here employ the following parameter constraint,

$$0 < \xi_q < 0.98 \tag{3.52}$$

for all q, with the consequence that the number of poles have to be even and that all poles are complex and appear in conjugate pairs. We choose the upper limit slightly below 1 to avoid the singularity in the residues seen in eq. (3.25) and (3.26). The lower limit of zero is necessary for the poles to be stable. One consequence of forcing the poles to be complex is that the retardation

function will be composed of only oscillatory components (see eq. (3.44)). Forcing the poles to be complex also comply with the multivariable example given by Damaren (2000) where it was reported that two stable real poles was discarded.

To avoid abrupt changes in $\hat{\mathbf{K}}(j\omega)$ above the data range, we also suggest the constraint,

$$0 < \Omega_q < \omega_{max} \tag{3.53}$$

for all q. Here, ω_{max} is the largest frequency in the dataset. The latter parameter constraint rarely has an effect, since the best fit most often obeys the inequality.

In Section 3.5.3 we showed that residues and poles can be used as parameters also in a time domain identification. It is also possible to think of a hybrid approach, where a pole-residue model is fitted to match both frequency- and time-domain data. This would require a time domain potential flow solver, which is not as widely available as its frequency domain counterparts. However, we have one piece of information about the retardation functions that we can utilize without having to run a time domain potential flow solver. If we take the time derivative of eq. (3.3) we get the following initial time condition:

$$\frac{d}{d\tau}\mathbf{k}(\tau)\bigg|_{\tau=0} = \mathbf{0} \tag{3.54}$$

If we do the same for the rational approximation we get the parameter constraint:

$$\sum_{k=1}^{n} \Re[p_k]\,\Re[\mathbf{R}_k] = \sum_{k=1}^{n} \Im[p_k]\,\Im[\mathbf{R}_k] \tag{3.55}$$

This has the consequence that the number of independent parameters needed to construct $\mathbf{R}_k$ is reduced. Finding the residues for a given set of poles is a standard least squares problem. For a given coupling term $K_{ij}(j\omega)$, this means that we find $\mathbf{x} = \arg\min_{\mathbf{x}} \|\mathbf{A}\mathbf{x} - \mathbf{b}\|$, where the real vector $\mathbf{x}$ contains the independent parameters of $R_{k,ij}$ for all k, $\mathbf{b}$ contains the corresponding data and $\mathbf{A}$ contains information about the poles. Using these variables, the constraint in eq. (3.55) can be written on the form $\mathbf{x} = \mathbf{T}\mathbf{x}'$ where $\mathbf{x}'$ contains the new independent parameters, reduced in number due to the constraint. We can now find the residues obeying the constraint as $\mathbf{x}' = \arg\min_{\mathbf{x}'} \|\mathbf{A}\mathbf{T}\mathbf{x}' - \mathbf{b}\|$.

The initial time parameter constraint is also first and foremost important in the absence of high frequency data, since we otherwise have all the information we need to represent $\mathbf{k}(t)$ accurately without the support of the constraint.

3.7.4 Passivity assessment

Small inaccuracies in the fitting of residues and poles can introduce small passivity violations in the radiation forces. Above the frequencies in the dataset, larger passivity violations can sometimes occur. We will here present a methodology for determining whether or not a given transfer matrix represent a passive system, and to identify the frequency intervals of non-passivity.

The passivity condition (3.11) is not practical since it can only be checked at discrete frequencies. For a MIMO system $\mathbf{Y}(s) = \bar{\mathbf{H}}(s)\mathbf{U}(s)$ that can be realized in the time domain by a state space model,

$$\dot{\boldsymbol{\mathcal{X}}}(t) = \bar{\boldsymbol{\mathcal{A}}}\boldsymbol{\mathcal{X}}(t) + \bar{\boldsymbol{\mathcal{B}}}\mathbf{u}(t) \tag{3.56}$$

$$\mathbf{y}(t) = \bar{\boldsymbol{\mathcal{C}}}\boldsymbol{\mathcal{X}}(t) + \bar{\boldsymbol{\mathcal{D}}}\mathbf{u}(t) \tag{3.57}$$

we can use the Hamiltonian matrix,

$$\bar{\boldsymbol{\mathcal{H}}} = \begin{bmatrix} \bar{\boldsymbol{\mathcal{A}}} - \bar{\boldsymbol{\mathcal{B}}}\left(\bar{\boldsymbol{\mathcal{D}}} + \bar{\boldsymbol{\mathcal{D}}}^{\dagger}\right)^{-1}\bar{\boldsymbol{\mathcal{C}}} & \bar{\boldsymbol{\mathcal{B}}}\left(\bar{\boldsymbol{\mathcal{D}}} + \bar{\boldsymbol{\mathcal{D}}}^{\dagger}\right)^{-1}\bar{\boldsymbol{\mathcal{B}}}^{\dagger} \\ \bar{\boldsymbol{\mathcal{C}}}^{\dagger}\left(\bar{\boldsymbol{\mathcal{D}}} + \bar{\boldsymbol{\mathcal{D}}}^{\dagger}\right)^{-1}\bar{\boldsymbol{\mathcal{C}}} & -\bar{\boldsymbol{\mathcal{A}}}^{\dagger} + \bar{\boldsymbol{\mathcal{C}}}^{\dagger}\left(\bar{\boldsymbol{\mathcal{D}}} + \bar{\boldsymbol{\mathcal{D}}}^{\dagger}\right)^{-1}\bar{\boldsymbol{\mathcal{B}}}^{\dagger} \end{bmatrix} \tag{3.58}$$

to check for passivity. Here, we allow complex valued state space matrices and † means complex conjugate transpose. The transfer matrix $\bar{\mathbf{H}}(s)$ is SPR (strict positive real) if $\bar{\boldsymbol{\mathcal{H}}}$ has no eigenvalues on the imaginary axis (Gustavsen, 2008). Moreover, if the system is non-SPR, the eigenvalues on the imaginary axis represents frequencies where the eigenvalues of the transfer function $\bar{\mathbf{H}}(s)$ changes sign. Hence, $\bar{\boldsymbol{\mathcal{H}}}$ can be used to identify frequency intervals of non-passivity.

This passivity test relies on $\left(\bar{\boldsymbol{\mathcal{D}}} + \bar{\boldsymbol{\mathcal{D}}}^{\dagger}\right)$ to be invertible and cannot be used for strictly proper transfer matrices (i.e. when $\bar{\boldsymbol{\mathcal{D}}} = \mathbf{0}$). Shorten et al. (2008) showed that this problem can be managed by considering a transformation of the frequency variable. If we write the transfer matrix $\hat{\mathbf{K}}(s)$ as,

$$\hat{\mathbf{K}}(j\omega) = \bar{\mathbf{H}}(j\bar{\omega}) = \bar{\mathbf{H}}\left(\frac{1}{j\omega - j\omega_0}\right) \tag{3.59}$$

we can write the state-space matrices of $\bar{\mathbf{H}}(j\omega)$ in terms of the state space matrices of $\hat{\mathbf{K}}(j\omega)$:

$$\bar{\boldsymbol{\mathcal{A}}} = (\boldsymbol{\mathcal{A}} - j\omega_0\mathbf{I})^{-1} \tag{3.60}$$

$$\bar{\boldsymbol{\mathcal{B}}} = -(\boldsymbol{\mathcal{A}} - j\omega_0\mathbf{I})^{-1}\boldsymbol{\mathcal{B}} \tag{3.61}$$

$$\bar{\boldsymbol{\mathcal{C}}} = \boldsymbol{\mathcal{C}}(\boldsymbol{\mathcal{A}} - j\omega_0\mathbf{I})^{-1} \tag{3.62}$$

$$\bar{\boldsymbol{\mathcal{D}}} = \boldsymbol{\mathcal{C}}(\boldsymbol{\mathcal{A}} - j\omega_0\mathbf{I})^{-1}\boldsymbol{\mathcal{B}} \tag{3.63}$$

The matrix $\boldsymbol{\mathcal{A}} - j\omega_0 \mathbf{I}$ will be diagonal if we choose the realization of eqs. (3.31) and can thus be easily inverted. If $\bar{\lambda}_k$ is a purely imaginary eigenvalue of $\bar{\boldsymbol{\mathcal{H}}}$, then $\bar{\omega}_k = \bar{\lambda}_k / j$ is a frequency where an eigenvalue of $\Re\left[\bar{\mathbf{H}}\right]$ changes sign. Then we can use the mapping in eq. (3.59) to find the corresponding frequency ω_k where an eigenvalue of $\Re\left[\hat{\mathbf{K}}\right]$ changes sign:

$$\omega_k = \omega_0 - \frac{1}{\bar{\omega}_k} \tag{3.64}$$

In practice $\bar{\lambda}_k$ will have a small real part due to round-off errors. Hence, it is treated as purely imaginary when $\Re\left[\bar{\lambda}_k\right] / \Im\left[\bar{\lambda}_k\right] < \epsilon$, where ϵ is a small tolerance.

The matrices $\bar{\boldsymbol{\mathcal{D}}}$ and $\bar{\boldsymbol{\mathcal{D}}} + \bar{\boldsymbol{\mathcal{D}}}^{\dagger}$ can be written:

$$\bar{\boldsymbol{\mathcal{D}}} = \lim_{\bar{\omega}\to\infty} \bar{\mathbf{H}}\left(j\bar{\omega}\right) = \hat{\mathbf{K}}\left(j\omega_0\right) \tag{3.65}$$

$$\bar{\boldsymbol{\mathcal{D}}} + \bar{\boldsymbol{\mathcal{D}}}^{\dagger} = 2\hat{\mathbf{B}}\left(\omega_0\right) \tag{3.66}$$

Hence, we should choose ω_0 such that $\hat{\mathbf{B}}\left(\omega_0\right)$ is non-singular, which rules out the choice $\omega_0 = 0$. A consequence of $\omega_0 \neq 0$ is that $\bar{\boldsymbol{\mathcal{A}}}$, $\bar{\boldsymbol{\mathcal{B}}}$,$\bar{\boldsymbol{\mathcal{C}}}$ and $\bar{\boldsymbol{\mathcal{D}}}$ have to be complex valued.

The Matlab toolbox (Gustavsen, 2012) implements a different passivity test matrix which was introduced by Semlyen and Gustavsen (2009) and has half the size of $\bar{\boldsymbol{\mathcal{H}}}$. This test matrix is only applicable when either $\mathbf{B}\left(\omega = 0\right)$ or $\mathbf{B}\left(\omega \to \infty\right)$ are non-singular and thus cannot be used for wave radiation forces.

3.7.5 Passivity enforcement

In Section 3.2 (eq. (3.11)) we stated that the radiation damping matrix must have non-negative eigenvalues for the radiation forces to be passive. This can be stated as,

$$\mathbf{W}_i^T\left(\omega\right) \mathbf{B}\left(\omega\right) \mathbf{W}_i\left(\omega\right) \geq 0 \tag{3.67}$$

for all i. $\mathbf{W}_i\left(\omega\right)$ is here the ith eigenvector of $\mathbf{B}$. If we take $\hat{\mathbf{K}}$ (with $\hat{\mathbf{B}} = \Re\left[\hat{\mathbf{K}}\right]$) as the rational approximation fitted without regard to passivity, we can enforce passivity by adding a small term $\Delta\hat{\mathbf{K}}$ such that $\hat{\mathbf{K}} + \Delta\hat{\mathbf{K}}$ is positive real. We can then require,

$$\hat{\mathbf{W}}_i^T\left(\omega\right) \left[\hat{\mathbf{B}}\left(\omega\right) + \Delta\hat{\mathbf{B}}\left(\omega\right)\right] \hat{\mathbf{W}}_i\left(\omega\right) > \delta \tag{3.68}$$

where δ is a small safety factor which ideally should be zero. $\hat{\mathbf{W}}_i$ is the i'th eigenvector of $\hat{\mathbf{B}}$. We implicitly assume that $\Delta\hat{\mathbf{B}}$ is small enough for $\hat{\mathbf{W}}_i$ to be a reasonable approximation to the i'th eigenvector of $\hat{\mathbf{B}} + \Delta\hat{\mathbf{B}}$ as well. This

represents a linearization of the inequality (3.67) with respect to $\hat{\mathbf{B}}$. Gustavsen (2008) suggested enforcing this inequality at a set of discrete frequencies,

$$< \omega_1, \cdots, \omega_{n_e} >=< \frac{\acute{\omega}_1}{2}, \frac{\acute{\omega}_1 + \acute{\omega}_2}{2}, \cdots, \frac{\acute{\omega}_{n_e-2} + \acute{\omega}_{n_e-1}}{2}, 2\acute{\omega}_{n_e-1} > \tag{3.69}$$

where $\acute{\omega}_k$ is a frequency where one of the eigenvalues of $\hat{\mathbf{B}}$ changes sign, identified using the Hamiltonian matrix of eq. (3.58).

The addition $\Delta\hat{\mathbf{K}}(j\omega)$ can be expressed as a linear combination of residue additions $\Delta\mathbf{R}_k$ from all k. Since $\hat{\mathbf{K}}$ is non-linear in the poles p_k, no modifications to the poles are made. Not all entries of $\mathbf{R}_k$ can be changed independently. First of all, $\mathbf{R}_k$ is a symmetric matrix, and the modification also needs to be symmetric. Gustavsen (2008) suggested two methods for perturbing the elements of $\mathbf{R}_k$. Residue perturbation (RP) refers to the perturbation of the upper or lower triangular part of $\mathbf{R}_k$ (hence retaining the matrix symmetry) whereas Fast Residue Perturbation (FRP) refers to the perturbation of the eigenvalues of $\mathbf{R}_k$. In both cases, any sparsity and structure of $\hat{\mathbf{K}}$ (and thus $\mathbf{R}_k$) resulting from geometrical symmetry of the floating bodies will be lost. For this reason, we here suggest a new version of the method where only the independent matrix entries in $\mathbf{R}_k$ are perturbed. The independent matrix entries in $\mathbf{R}_k$ will correspond to the independent matrix entries of the added mass and damping matrices, as discussed in Section 3.3.

Taking all n_d eigenvectors and n_e passivity violating frequencies into account, the scalar inequalities (3.68) can be reformulated as a matrix inequality,

$$\mathbf{A}_{QP}\Delta\mathbf{x} < \mathbf{b}_{QP} \tag{3.70}$$

where $\Delta\mathbf{x}$ is a column vector consisting of the minimal set of parameters needed to reconstruct $\Delta\mathbf{R}_k$ for all k (all poles). The eigenvectors $\mathbf{W}_i$, needed to construct $\mathbf{A}_{QP}$ and $\mathbf{b}_{QP}$, are independent of $\Delta\mathbf{x}$ as a consequence of the linearization.

Since the transfer matrix $\hat{\mathbf{K}}$ represent the best fit to $\mathbf{K}$ without regard to passivity, we want to satisfy these inequalities with as little perturbation as possible. That is, we want to minimize a sum of weighted squares which can be written on a non-dimensional form similar to eq. (3.50):

$$\epsilon_\Delta = \frac{\sum_q \sum_i \sum_k w_q \left|\Delta\hat{K}^s_{ik}(j\omega_q)\right|^2}{\sum_q \sum_i \sum_k w_q \left|\hat{K}^s_{ik}(j\omega_q)\right|^2} \tag{3.71}$$

Here, the superscript s means that we use the scaled matrix, eq. (3.51). Note that we here minimize the perturbation instead of the fitting error. Because

$\Delta\hat{\mathbf{K}}$ is linear in $\Delta\mathbf{R}_k$, and thus in the independent parameters $\Delta\mathbf{x}$, we can reformulate the sum of weighted squares as:

$$\epsilon_\Delta = \Delta\mathbf{x}^T\mathbf{H}_{QP}\Delta\mathbf{x},\ \mathbf{H}_{QP} = \mathbf{H}_{QP}^T \tag{3.72}$$

The minimization of ϵ_Δ in this form, subject to the inequalities (3.70), is a quadratic programming problem (QP) which has tailor-made solution algorithms. In this study, the *quadprog* routine in Matlab's optimization toolbox is used.

If we let n_d, n_i, n_p and n_e designate the number of degrees of freedom, number of independent matrix entries in $\mathbf{K}$, number of poles and number of passivity violating frequencies, respectively, we have the following matrix dimensions:

$$\hat{\mathbf{K}},\ \mathbf{R}_k \in \mathbb{C}^{n_d\times n_d} \tag{3.73}$$
$$\mathbf{A}_{QP} \in \mathbb{R}^{n_d n_e\times n_p n_i} \tag{3.74}$$
$$\Delta\mathbf{x} \in \mathbb{R}^{n_p n_i\times 1} \tag{3.75}$$
$$\mathbf{H}_{QP} \in \mathbb{R}^{n_p n_i\times n_p n_i} \tag{3.76}$$

It should be mentioned that n_p can also be the number of poles minus one, if the equality constraint, eq. (3.55), is used. Although $\Delta\mathbf{x}$ is a real vector containing both the real and imaginary parts of $\Delta\mathbf{R}_k$, $k = 1,\ldots,n_p$, the number of elements in $\Delta\mathbf{x}$ is only $n_p n_i$. The reason for this is that one complex conjugate pair has only two independent parameters. Note also that the size of $\mathbf{H}_{QP}$ is independent of the number of frequencies used in the error summation in eq. (3.71). Instead, $\mathbf{H}_{QP}$ can be written as the sum of contributions from all frequencies. Moreover, $\mathbf{H}_{QP}$ is a symmetric, block-diagonal matrix with n_i diagonal blocks of size $n_p \times n_p$.

Solving the quadratic programming problem only once does not guarantee a passive model because of the approximation implied by the linearization of the inequalities. An iterative approach is therefore necessary. In each new iteration, $\mathbf{A}_{QP}$ and $\mathbf{b}_{QP}$ are updated based on the new eigenvectors and remaining passivity violating frequencies. The number of inequalities (number of rows in $\mathbf{A}_{QP}$) is also updated in each iteration, reflecting the new prediction of zero-crossing frequencies, eq. (3.69), from the updated Hamiltonian matrix (eq. (3.58)). When the Hamiltonian matrix has no eigenvalues on the imaginary axis, we are guaranteed that $\hat{\mathbf{K}}$ is positive real at all frequencies and the iteration is stopped.

As seen from eq. (3.69), we choose the midpoint between the zero crossing frequencies, in addition to one low and one high frequency, as the frequencies of passivity enforcement. Not all of these frequencies will have negative eigenvalues. Gustavsen (2008) suggest several means to remove unnecessary

inequalities, motivated by the fact that the computational load of solving the quadratic programming problem is approximately linear in the number of inequalities. This is not implemented since the total CPU time of the passivity enforcement (all iteration loops) is typically a few seconds for the problems presented here.

3.7.6 Modified identification procedure

The vector fitting algorithm does not include all parameter constraints discussed in Section 3.7.3. For this reason, we here suggest a modified fitting procedure which uses vector fitting to obtain the starting poles in a nonlinear optimization. Including passivity assessment, -enforcement, search for required model order and conversion to state space form, we can describe a modified identification procedure in multiple stages as:

1. Select an even number of starting poles.
2. Improve the location of these poles using the iterative VF method, *without* regard to the parameter constraints described in Section 3.7.3.
3. Express the poles from stage 2 in terms of the parameters ξ_q and Ω_q using eq. (3.27a) and (3.27b). Modify these parameters to obey the constraints $\xi_q < 0.98$ and $\Omega_q < \omega_{max}$.
4. a) Use ξ_q and Ω_q (for all q) as parameters in a constrained nonlinear optimization with initial values taken from stage 3, constraints described in Section 3.7.3 and ϵ^2 from eq. (3.50) as the quantity to minimize. Each iteration in this optimization involves a linear least squares problem to find the residues $\mathbf{R}_k$, expressed in such a way that the initial time condition, eq. (3.55), is satisfied. The poles can now be found from the optimal ξ_q and Ω_q using eqs. (3.23) and (3.24).

   b) Or, same as (a), except that the initial values of ξ_q and Ω_q are retained, eliminating the need for a nonlinear optimization.
5. Compare the fitting error ϵ^2 to some selected tolerance. If the error is too large, increase the number of poles by 2 and go back to stage 1.
6. Assess the passivity of the model using the procedure described in Section 3.7.4. If the model is passive, proceed to stage 9.
7. Perturb the residues $\mathbf{R}_k$ to obtain a passive model using the procedure of Section 3.7.5. The residue perturbations is also here expressed in such a way that the initial time condition, eq. (3.55), is satisfied.

8. Same as stage 5.

9. Convert the pole residue model to state space form using the procedure of Section 3.5.1

We have here included two alternatives for stage 4. The first alternative includes constrained nonlinear optimization to improve the pole locations, whereas the more CPU efficient second alternative omits the nonlinear optimization, although still respecting the constraints. The *lsqnonlin* routine of the Matlab optimization toolbox is used in the constrained nonlinear optimization. This routine is tailored for constrained minimization problems where the objective function is a sum of squares.

An even more CPU efficient approach is also possible by simply omitting stage 3 and 4, which is the same as allowing all stable poles (i.e. to skip the additional pole constraints) and neglecting the initial time constraint on the residues. This is not considered any further, but is believed to work fine when there is no significant high frequency truncation. In this case, the constraints should be reflected in the data, and there would be less need for imposing them explicitly. The lower bounds $\xi_q > 0$ and $\Omega_q > 0$, necessary for stability, is respected in the VF routine by sign flipping during the iterations. See Gustavsen and Semlyen (1999).

3.8 Case studies

This section presents three numerical examples; the hinged 5-body WEC, an array of 17 circular cylinders and a single circular cylinder. The two first mentioned examples are characterized by strongly frequency dependent added mass and damping. The commercial boundary element code WAMIT v6.4 is used to obtain the hydrodynamic coefficients and the option for removing irregular frequencies is enabled in WAMIT. All dimensional results are presented in SI units with a prefix kilo- on mass (and thus forces and moments as well).

Vector fitting (VF) requires a set of starting poles. In the numerical examples given below, starting poles with linearly distributed imaginary parts spanning the frequency range of the data, and a small proportional real part, are taken as $0.01\Delta\omega + j\Delta\omega$, $0.01\Delta\omega - j\Delta\omega$, $0.02\Delta\omega + 2j\Delta\omega$, $0.02\Delta\omega - 2j\Delta\omega$, etc.

Previous publications dealing with the hinged 5-body WEC (Rogne and Pedersen, 2012; Rogne et al., 2012) used a different identification method using the nominator and denominator coefficients of eq. (3.18) as the free variables in the fitting (Perez and Fossen, 2009). The numerical implementation were based on the *invfreqs* function in Matlab's signal processing toolbox. This method also treats the different elements in the matrix as independent SISO systems, as opposed to the present method, where a common set of poles is used

for all matrix elements. Although the identification of a state space model of the hinged 5-body WEC was successful using the old approach, the numerical problems that motivated the development of the vector fitting algorithm was experienced, causing *invfreqs* to warn about a nearly singular matrix when solving a linear system of equations. Due to these problems, it was necessary to exclude the highest frequencies in the dataset and select the model order with care. It was also impossible to get a passive model, except when the model order was very low, with associated compromise on the accuracy (although the non-passivity did not lead to unstable equations of motion). With the new method, no such problems are experienced. The use of a common set of poles also gives better accuracy for a given model order.

The 17 body array case is even more challenging, and attempts to fit a state space model using *invfreqs* was unsuccessful for this case.

3.8.1 Hinged 5-body WEC

This hinged 5 body WEC is presented in Section 2.5 and the geometry is shown in Figure 2.8. Here, we also defined the 10 generalized displacement coordinates describing the admissible motions of the WEC. The methodology for obtaining the corresponding 10-by-10 generalized added mass and damping matrices $\mathbf{A}$ and $\mathbf{B}$ will be presented in Section 4.4. Here, we will assume that these matrices are available (including $\mathbf{A}_\infty$) and combined to give the radiation transfer matrix $\mathbf{K}(j\omega)$.

When we investigate the stability of the equations on motions we have to include some restoring from the soft moorings in the three horizontal degrees of freedom. This is done in a very simplified manner by setting $G_{11} = G_{22} = 0.01 \cdot G_{33}$ and $G_{66} = 0.01 \cdot G_{44}$, with G_{33} and G_{44} calculated from the hydrostatics. No viscous or other external forces are included.

Evaluating the added mass and damping for high frequencies is computationally intensive since the panel size should be taken as a fraction of the shortest wave length. In principle, transient radiation forces depend on the damping (or added mass) for all frequencies, as seen in the Ogilvie relations (e.g. eq. (3.3)). This motivates us to investigate the effect of the truncation frequency. For this purpose, we include rational fits for two sets of discrete frequencies. The full dataset includes the 241 linearly spaced angular frequencies 0, 0.025, ..., 6 rad/s, whereas the economical dataset includes 41 linearly spaced angular frequencies; 0, 0.05, ..., 2 rad/s. Note that both spacing and truncation frequency differs. The identification procedure of Section 3.7.6 have been used and resulted in rational models with 72 and 16 poles for the full and economical datasets respectively, both corresponding to the lowest number of poles satisfying the error tolerance $\epsilon = 0.02$. The order of the state space

models is the number of poles multiplied by the number of degrees of freedom.

Running the vector fitting routine implemented by Gustavsen (2012) took $\approx$ 4 seconds for the high order model and $\approx$ 0.3 seconds for the low order model. The pole improvement using nonlinear constrained optimization (stage 4a in the procedure in Section 3.7.6) was prohibitively slow for the high order model and was aborted. Thus, alternative 4b was chosen instead, eliminating the need for nonlinear optimization while still respecting the constraints of Section 3.7.3. For the low order model, stage 4a finished in $\approx$ 0.6 seconds which resulted in a model with fitting error $\epsilon \approx 0.016$. Choosing alternative 4b instead resulted in a fitting error $\epsilon \approx 0.032$. The passivity enforcement of the high order model required 5 iterations and took 41 seconds. However, only about 3.6 seconds was spent solving the quadratic programming problem (5 times) and the majority of the CPU time was associated with finding the eigenvalues of the Hamiltonian matrix, eq. (3.58). This indicates that although the passivity assessment method of Section 3.7.4 is robust, faster alternatives could be considered for high order models. Passivity enforcement of the low order model required 4 iterations and took $\approx$ 1.6 seconds of which only $\approx$ 0.3 seconds was spent solving the quadratic programming problem 4 times. These CPU time indications is based on the use of a modern laptop computer and the stopwatch functions tic() and toc() in Matlab.

The geometrical symmetries of the system imply that the added mass and damping matrices (and thus the $\mathbf{K}$ matrix) are described by only 11 independent matrix entries. These are plotted in Figure 3.1, showing both sets of WAMIT data with corresponding rational fits. It is seen that the rational approximation is very good in the fitting range. The ability of the low order model, fitted only with knowledge of low frequency data, to predict the high frequency data, is also shown to be surprisingly good. This extrapolation has importance for the area under the $\Re\left[\hat{K}_{ij}(\omega)\right]$ curves, and thus the initial value of the corresponding retardation function $\hat{k}_{ij}(\tau)$.

The retardation functions are shown in Figure 3.2. It is observed here that the correspondence between the retardation functions of the high and low order rational models is largely related to the low order model's ability to predict the high frequency data. The retardation function obtained by integrating eq. (3.3) using Filon's integration scheme (without any type of truncation correction) on the full dataset is also included, and produce results almost indistinguishable from the high order rational model.

Figure 3.6 shows the effect of the truncation frequency and different parameter constraints on the retardation function of the hinge modes. The term "pole constraint" in the legend of the figure refers here to the bound constraint expressed by the inequalities (3.52) and (3.53), the first one ensuring complex poles. The term "residual constraint" refers to the equality constraint of eq.

(3.55), ensuring the correct zero-slope of $\hat{k}_{ij}(\tau)$ at $\tau = 0$. It is observed that a large error is introduced in the retardation function if Filon's integration is used on the economical dataset without any form of truncation correction. The corresponding rational model produces a more trustworthy retardation function. We know that the retardation functions calculated using Filon's integration has a too small initial value $k_{ii}(0)$, since the diagonal elements of the damping matrix is positive for all frequencies. Hence, it is promising that $\hat{k}_{e,ii}(0) > k_{f,ii}(0)$ for all combinations of parameter constraints.

Figure 3.4 presents a free decay test, showing the motion and the strictly proper portion of the radiation force of the four buoys after an initial unit angular displacement in hinge 1. The center floater is fixed to prevent mechanical coupling between the remaining four degrees of freedom. The free decay response results from integrating eq. (3.37) in time with reduced number of degrees of freedom and nonzero initial angle in hinge 1. The simulation is carried out for both the low- and high order radiation models, with indistinguishable results. This is perhaps surprising considering the differences in the retardation functions, especially for the coupling terms. Although the motions are dominated by the natural frequency, the problem is a transient one and in principle dependent on the radiation forces at all frequencies. The fact that the buoy motion are insensitive to inaccuracies in the transient radiation force (the retardation function) can partly be attributed to the body inertia. The inertia acts as a filter that reduces high frequency motion and prevents discontinuous velocity, even when the exciting force is discontinuous, such as in a free decay test. The small difference in the free decay tests indicates that lower order models will often suffice in practical applications. This is also commented by Perez and Fossen (2011) based on the frequency response of the force-to-motion system.

Floating bodies with catenary mooring typically experience low frequency resonant motions in the horizontal plane excited by second order wave loads, wind and current. The added mass is non-zero in the low frequency asymptote, and the ability of the rational models to represent the low frequency added mass will have importance for these resonant motions. Figure 3.5 shows the added mass in surge for the collection of bodies of the WEC. The added mass corresponding to the rational models is found using eq. (3.46c). An accurate representation of the added mass by the rational models is shown, also in the low frequency range. An interesting observation is that the added mass is negative for frequencies around 2 rad/s, corresponding to a wave length a little longer than the space between the center floater and the buoys.

Figure 3.6 shows the effect of the passivity enforcement on the stability and fitting error for various model orders, based only on the economical dataset. The "passivity indicator", which is positive for a passive model, is here taken

as,

$$\lambda_{K^s} = \min_{\omega} \left(\text{eig}_1 \left(\Re \left[\hat{\mathbf{K}}^s (\omega) \right] \right) \right) \tag{3.77}$$

where the $\text{eig}_1(.)$ operator returns the smallest eigenvalue and the minimization is taken over a very large number of frequencies between 0 and $5 \cdot \omega_{max}$, ω_{max} being the largest frequency in the dataset. Note that the scaled transfer matrix of eq. (3.51) is used. It is seen that increasing the model order does not increase the passivity indicator of the non-passivated model. This is because we have no control of the fit for frequencies above the data range.

The stability of the equation of motion is expressed by the quantity,

$$\lambda_M = \max_i \left(\text{Re} \left[\text{eig}_i \left(\boldsymbol{\mathcal{A}}_{FM} \right) \right] \right) \tag{3.78}$$

where $\boldsymbol{\mathcal{A}}_{FM}$ is the system matrix in eq. (3.37). A stable system is characterized by a negative λ_M. It is seen that the passivity enforcement ensures stable equations of motions for all model orders, as it should according to theory (see Section 3.6.2). Without passivity enforcement, only the use of 14 and 26 poles gives stable equations of motions. It should be emphasized that no external dissipative forces are included in this example, and that doing so will often change this conclusion. It is also seen from the figure that the passivity enforcement only introduce a slight worsening of the fitting error.

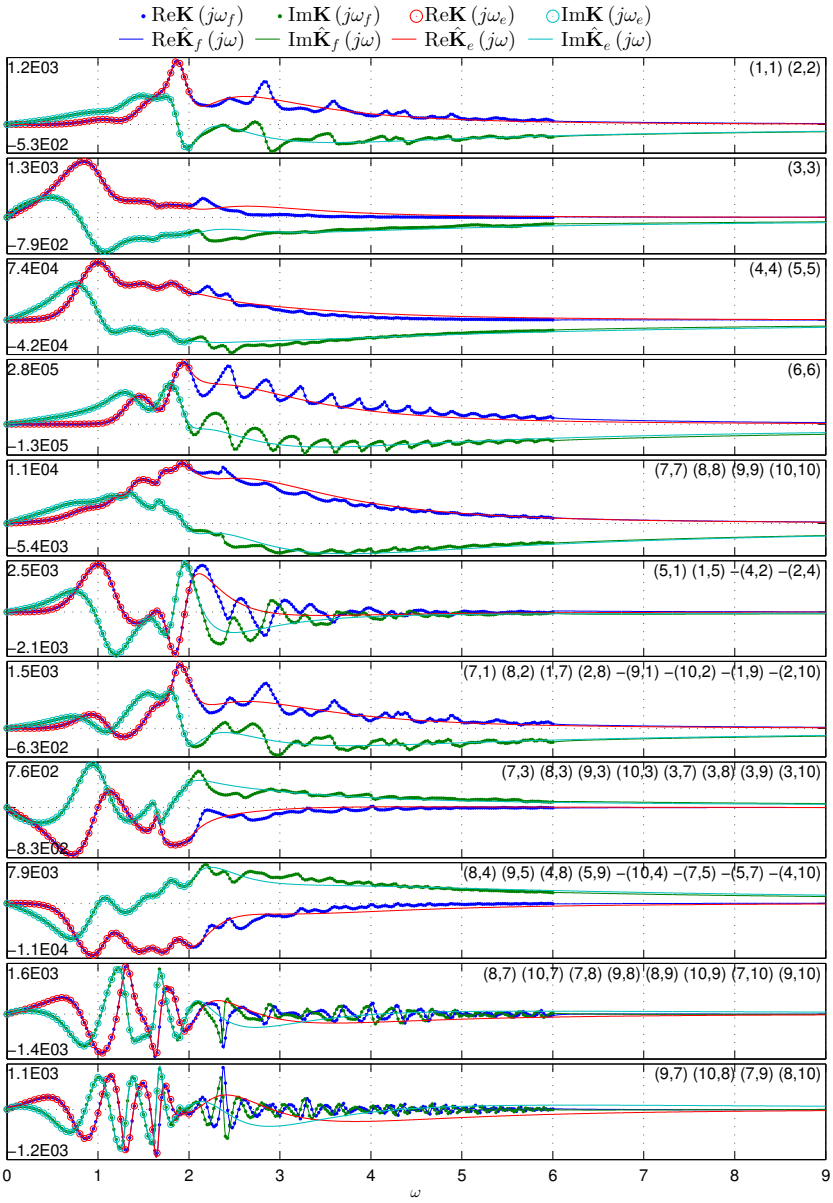

Figure 3.1: Radiation force transfer matrix of hinged 5-body WEC. As indicated above the topmost diagram, the small dots shows the full set of WAMIT data whereas the larger o's shows the economical subset. The lines with matching color shows the corresponding rational fits, using 72 poles for the full dataset, and 16 poles for the economical subset. The 11 independent matrix entries populate the matrix as indicated in the top-right corner of each diagram. Here, a minus before the index doublet (i,j) means that a sign shift applies in the interpretation.

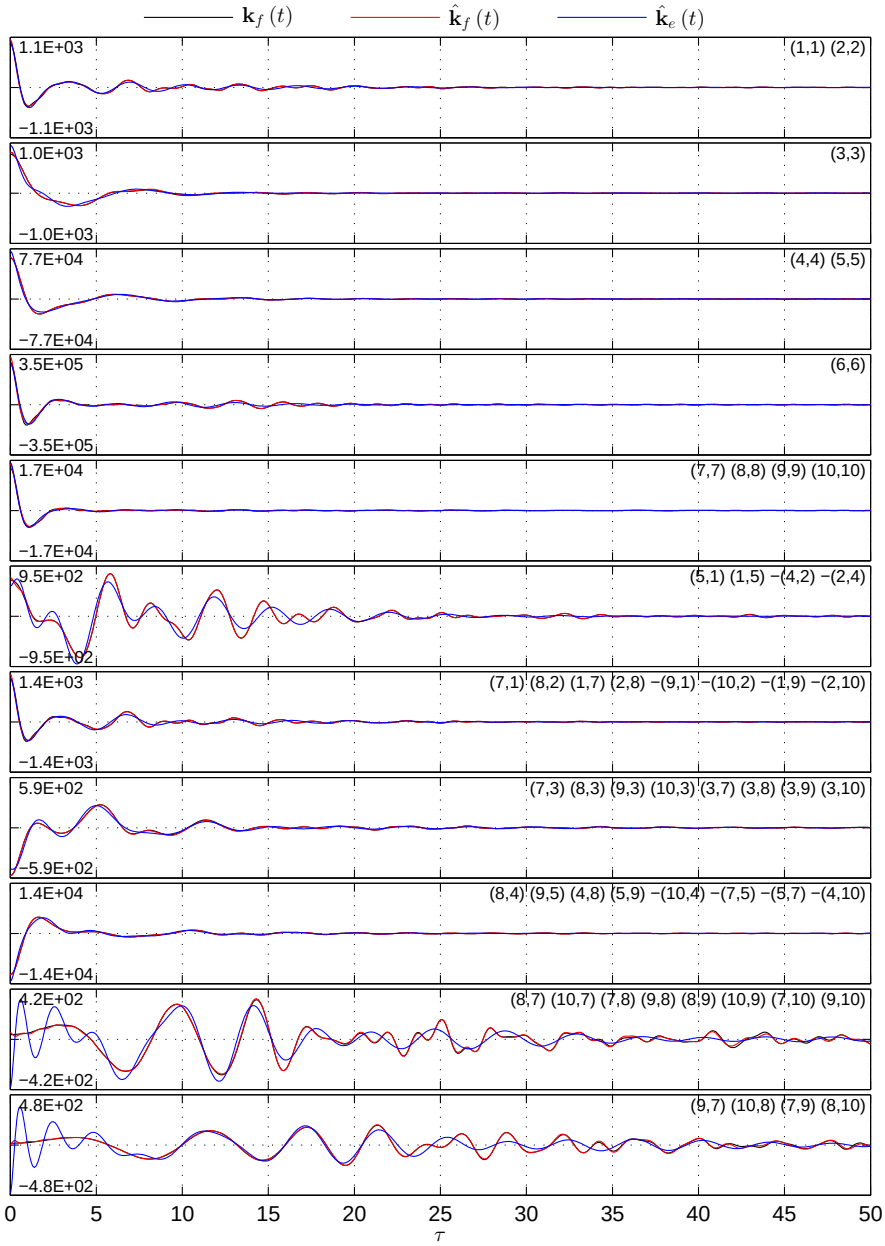

Figure 3.2: Retardation functions of 5 body WEC. $\mathbf{k}_f(t)$ (black line) is calculated from the full dataset using Filon's integration scheme, $\hat{\mathbf{k}}_f(t)$ (red line) is calculated from the rational fit of the full dataset and $\hat{\mathbf{k}}_e(t)$ (blue line) is calculated from the rational fit of the economical subset. Note that the black line is mostly hidden behind the red line.

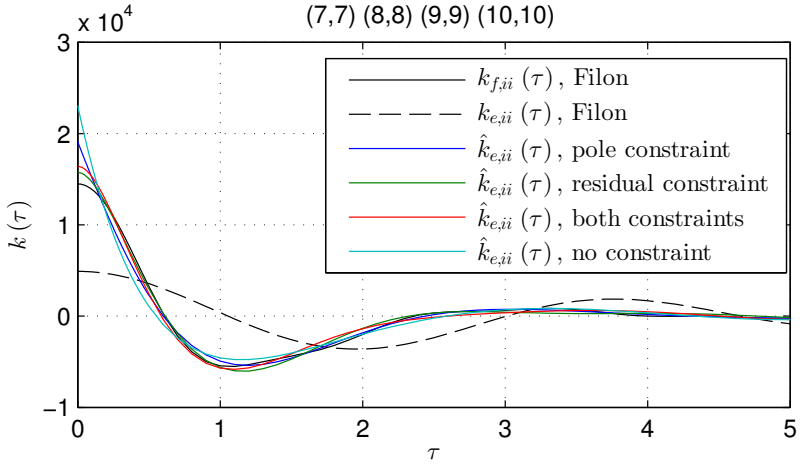

Figure 3.3: Effect of parameter constraints and truncation frequency on the retardation function for the hinge modes. Subscript f and e on the annotations refers to the full and economical dataset, respectively.

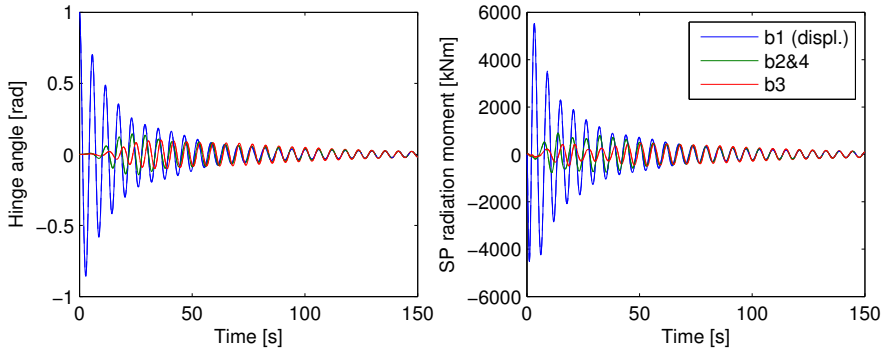

Figure 3.4: Free decay after unit initial angle in hinge 1 with center floater fixed (four degrees of freedom). The blue/green/red whole line shows response in hinge 1/2/3 with high order model. Hinge 4 moves synchronously with hinge 2 due to symmetry. Dotted lines show corresponding result for the low order model (but is hidden behind the whole lines). Despite the difference in the retardation functions (especially for the cross coupling), the high and low order models show indistinguishable results. Note that it is only the strictly proper (SP) part of the radiation moment that is plotted.

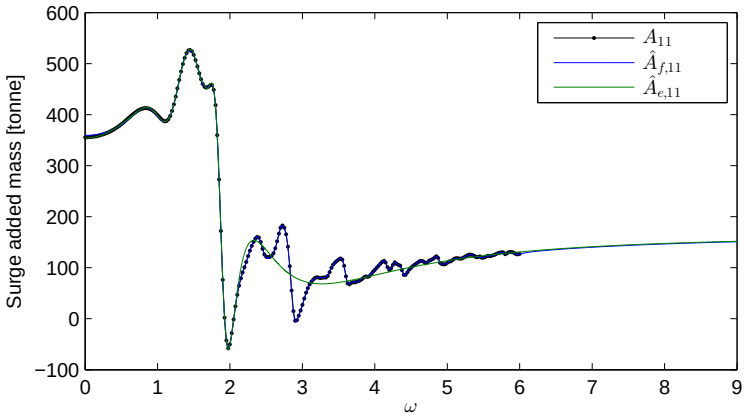

Figure 3.5: Added mass in collective surge for the WEC. WAMIT data is shown in black. The high order rational fit is shown in blue (hidden behind the black line) and low order rational fit is shown in green.

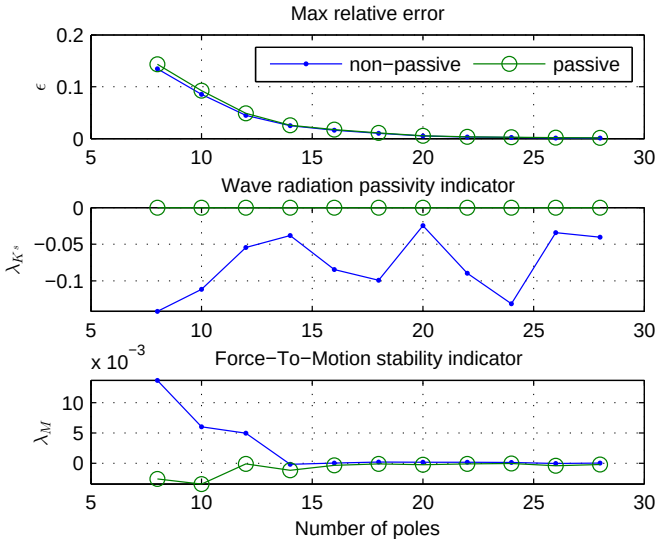

Figure 3.6: Relative fitting error and passivity and stability measures for the WEC as a function of model order, before (-.-) and after (-o-) passivity enforcement.

3.8.2 Array of 17 circular cylinders

This example concerns a uniform array of upright circular cylinders with the same dimensions as the center floater of the hinged 5-body WEC shown in Figure 2.8 (18 meter diameter, 2.25 meter draft). The array includes 17 cylinders with a spacing of 193.5 meters. This problem can be seen as an approximation to the infinite array problem, which is equivalent to the channel problem with channel width corresponding to body spacing. For the finite array considered here, the condition of no flow through the channels walls (imagined to be on each side of the middle cylinder) will be approximately satisfied if the bodies move synchronously in a plane perpendicular to the array. Hence, we only consider surge, heave and pitch of the collection of bodies as if they were rigidly connected. To further emphasize the equivalence to the channel problem, all hydrodynamic coefficients are divided by the number of bodies. The water depth is also here taken to be 45 meters. Both water depth and channel width comply with the experiments that is reported in Chapter 6. The case of a single cylinder is included for comparison.

The identification procedure of Section 3.7.6 using an error tolerance $\epsilon = 0.02$ resulted in a 8 pole model for the single body case and a 32 pole model for the cylinder array. The entries of the radiation transfer matrix $\mathbf{K}$ and its rational approximation $\hat{\mathbf{K}}$ for both the single body and the array is shown in Figure 3.7. The dataset includes the 302 linearly spaced angular frequencies 0, 0.01, . . . , 3.01 rad/s.

The rational approximation for the array demonstrate that using a common set of poles works well even though the different matrix elements have very different behavior. The use of 32 poles gives a very close approximation. It is seen that the transfer function for heave-heave of the array ($K_{a,22}$) have strong frequency dependency and large deviation from the corresponding single body case. The other elements in the transfer matrix have a more regular behavior with very little difference between the array and the single body case. The irregularities of $K_{a,22}$ appear as strong spikes or jumps at frequencies corresponding to wave lengths of an integer multiple of the spacing/tank width, and are related to transverse sloshing modes in the channel. This characteristic agrees with the results of Linton and Evans (1992), which considered a cylinder in a channel and solved the problem using a multipole method. They showed that the spiky behavior appears for modes that are symmetrical about a plane perpendicular to the channel walls (such as heave), but not for modes that are anti-symmetric about the same plane (surge and pitch).

The corresponding impulse response functions is shown in Figure 3.8. It is seen that the interaction between the cylinders only influence the heave-heave retardation function significantly for high values of τ. This is related to the time a wave use to travel between the cylinders. The interaction greatly

increases the memory of the retardation function. The calculation of the surge-surge retardation function is subject to a significant truncation error, with the consequence that Filon's integration gives erroneous results and too long memory.

Figure 3.9 shows the upper half of the pole-plot of both the single body and the array. The 15 lowest natural sloshing frequencies, corresponding to wave lengths of an integer multiple of the spacing, is also indicated on the imaginary axis. It is seen that 24 out of the 32 poles of the array model can be associated with the 12 lowest natural sloshing frequencies. In fact, the fitting algorithm predicts these 12 sloshing frequencies to within graphical precision. Since these modes are so lightly damped, we have that $\Im[p] \approx \Omega$, where Ω is the natural frequency of the oscillator formulation, eq. (3.22).

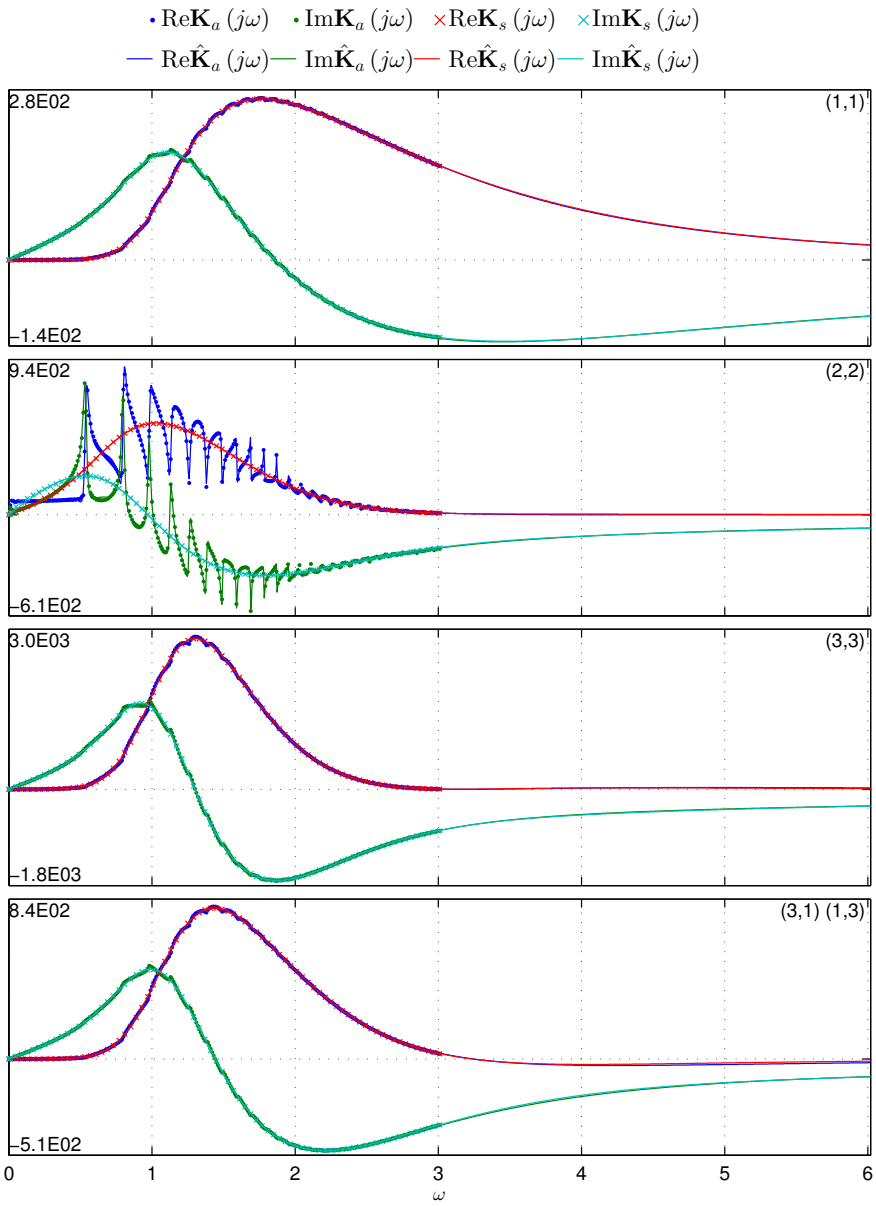

Figure 3.7: Radiation force transfer matrix of the array of circular cylinders ($\mathbf{K}_a$) and single cylinder ($\mathbf{K}_s$). As indicated above the topmost diagram, the small dots (array) and crosses (single cylinder) shows the WAMIT data whereas the lines show the rational fits using 32 poles for the array and 8 poles for the single cylinder.

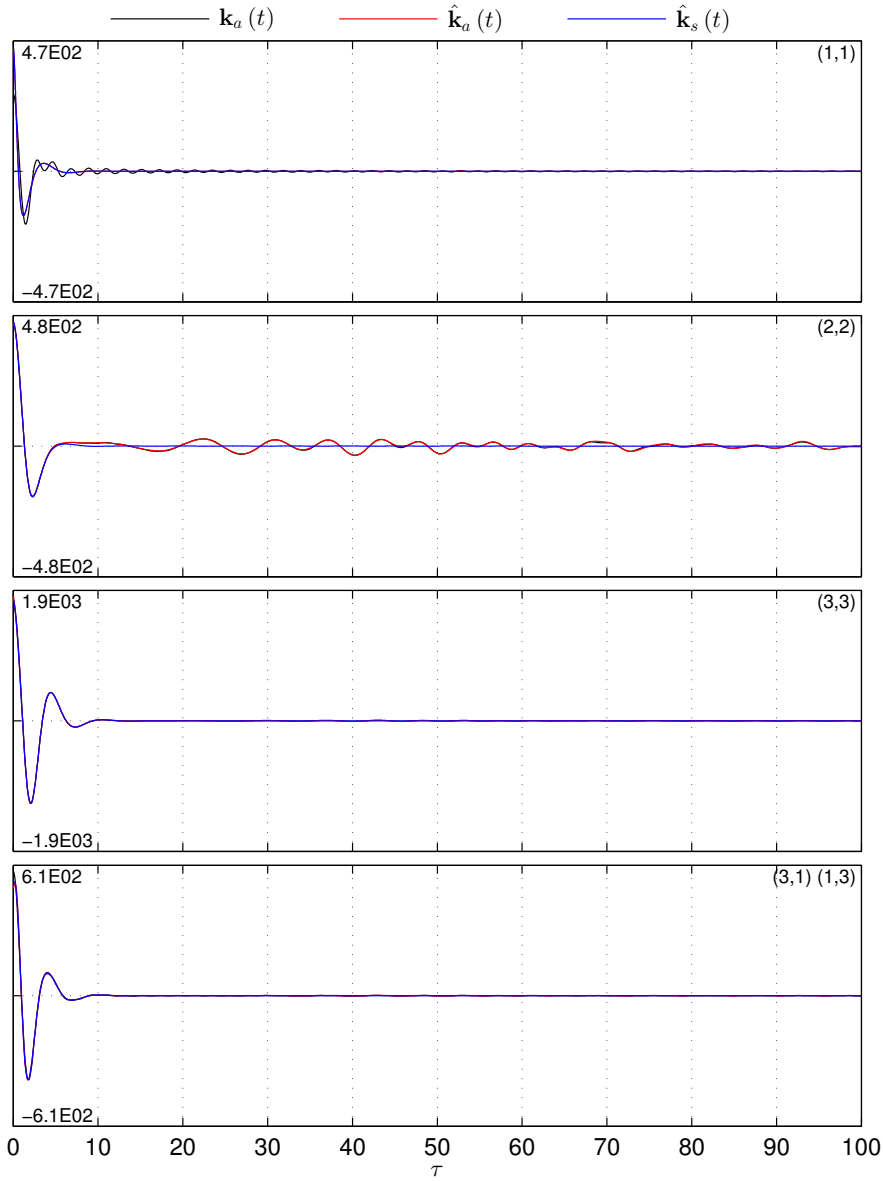

Figure 3.8: Retardation functions of the array of circular cylinders and the single cylinder. $\mathbf{k}_a(t)$ represents the cylinder array and is calculated from the full dataset using Filon's integration scheme. $\hat{\mathbf{k}}_a(t)$ is calculated from the rational fit. $\hat{\mathbf{k}}_s(t)$ represents the single cylinder and is calculated from the rational fit.

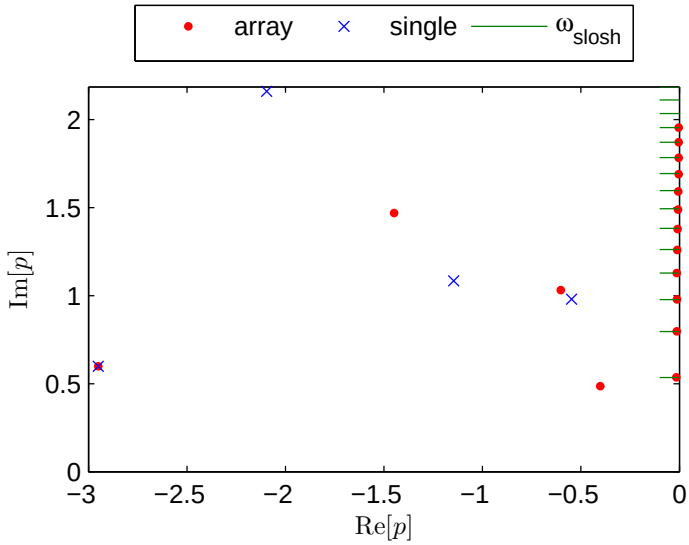

Figure 3.9: Pole locations for a single cylinder, represented by 8 poles, and an array of 17 cylinders, represented by 32 poles. Each pole has a complex conjugate not shown. The 15 lowest natural sloshing frequencies, corresponding to wave lengths of an integer multiple of the tank spacing, is also indicated on the imaginary axis.

4 Equations of motion for hinged bodies

4.1 Introduction

There are several possible approaches for obtaining equations of motion for multiple rigid bodies with rigid constraints (e.g. hinges) between them. One approach is to replace the rigid constraints (infinitely stiff) with springs of finite stiffness. With this approach, a system of N bodies will have $6N$ degrees of freedom (DOF), meaning that the constraints does not reduce the number of DOFs as compared to the unconstrained case. This procedure is perhaps the easiest to formulate and implement since we can employ the commonly used displacement coordinates for each body, referred to as surge, sway, heave, roll, pitch and yaw. One can argue that rigid constraints are an idealization, and that replacing them with springs of finite stiffness, and perhaps also a damper, would be more correct from a physical viewpoint. Karnopp et al. (2006) discuss this modeling approach and note that the introduction of stiff springs will introduce fast dynamics that would require a very small time step in the time domain simulations .

In this thesis we will instead use a formulation where the physical constraints (imposed by the hinges) are infinitely stiff, and thus the number of DOFs are reduced as compared to the unconstrained case. The motions of the bodies can then be described using a minimal set of generalized (displacement) coordinates and corresponding velocities, and the fast, "spurious" dynamics are eliminated. The reduction of the number of DOFs is in itself an advantage, in terms of simulation efficiency, but also because it reduces complexity and makes it easier to study the system. This was clearly observed in Section 3.8.1 where the hydrodynamic radiation forces of the hinged 5-body WEC are presented, and seen to be represented by an manageable amount of information.

The equations of motion rely on a description of the kinematics of the system. Section 4.2 deals with the exact kinematic descriptions of the hinged 5-body WEC. The term "Kinematic description" here encompasses the definition of generalized coordinates, velocities and the relation between them. The term "exact" means that we remove the usual assumption of small angles. We will use a minimal number of generalized coordinates (i.e. equal to the number

of DOFs), and independent velocities. Emphasis is placed on the selection of generalized coordinates and independent velocities with the aim to simplify the equations of motion. We will see that this implies a choice of independent velocities where each velocity is not necessarily the time derivative of the corresponding generalized coordinate.

The kinematic descriptions will be exemplified by a generic hinged 2-body system and the hinged 5-body WEC, although it is noted that generalization to other similar systems will be straight-forward. "Similar systems" here means N-body systems where body 1 acts as a common link, so that body $2, 3, ..., N$ are all hinged to body 1.

The equations of motion will be developed in Section 4.3 and will include geometric nonlinearities represented by Coriolis-centrifugal forces and a mass matrix that is a function of the hinge angles. Two different approaches will be discussed. Numerical simulations will be presented in Section 4.6. Here, emphasis is placed on the importance of the nonlinearities in the inertia forces, and all other forces are linearized.

The non-linear restoring and Froude-Krylov forces that will be presented in Chapter 5 also relies on the exact kinematic relations developed in this chapter. It turns out that this non-linearity will be much more important than the nonlinearity in the inertia forces.

The bulk of the material in this chapter have previously been published by Rogne and Pedersen (2012). This paper emphasize how the equations of motion can be represented using the Bond-graph formalism. For a WEC, this can for instance be useful when the dynamic model includes a complex sub-model of the PTO system, which may include electrical and hydraulic components. The strength of the Bond-Graph method lies in the systematic treatment of this type of multi energy domain models. The Bond-Graph method will not be employed in this thesis, and the material in the aforementioned paper is here rewritten in order to be accessible for readers without knowledge of the Bond-graph method. The treatment here is also more extensive and detailed.

4.2 Exact kinematics

4.2.1 Coordinate frames and notation

In the following we will use several Cartesian coordinate frames. The body fixed frame of body number j is denoted "frame j" or O_jxyz. Its axes are O_jx, O_jy and O_jz. When natural, we will use the word "body", and take it to mean the body fixed frame. The position of a body is then taken to mean the position of the origin of its frame. Frame 0 will be fixed to the earth, which can be assumed inertial for our purpose. When the index j is dropped, $j = 0$

shall be assumed, meaning that $Oxyz$ denote the inertial frame.

The position of body j is described by the vector $\mathbf{r}_j \in \mathbb{R}^3$. The unit vectors of its axes are $\mathbf{i}_j$, $\mathbf{j}_j$, $\mathbf{k}_j \in \mathbb{R}^3$, for the x, y and z directions, respectively. Note that there is an important distinction between O_jx and $\mathbf{i}_j$. O_jx is an axis; a line that goes through the point $\mathbf{r}_j$ and have a direction $\mathbf{i}_j$. Hence, O_jx contains information about both $\mathbf{r}_j$ and $\mathbf{i}_j$. In mathematical expressions, we prefer to use the vectors $\mathbf{r}_j$ and $\mathbf{i}_j$ to express O_jx whereas we will use the notation O_jx to make statements such as "body i is rotated about axis O_jx". The same goes for the y and z axes.

The vector pointing from body i to body j is:

$$\mathbf{r}_{j/i} \equiv \mathbf{r}_j - \mathbf{r}_i \tag{4.1}$$

When $i = 0$, we drop the index i and write $\mathbf{r}_{j/0} \equiv \mathbf{r}_j$, complying with the notation already used. Generalizing further, we take $\mathbf{r}_{j/i}^{(k)}$ to mean the vector pointing from body i to body j decomposed in the frame of body k. Again, when the superscript is dropped, we implicitly assume a decomposition in the inertial frame, meaning that we define $\mathbf{r}_{j/i}^{(0)} \equiv \mathbf{r}_{j/i}$. The position vector components of a hinged two-body system is illustrated in Figure 4.1.

A vector $\mathbf{r}^{(k)} = \begin{bmatrix} x^{(k)} & y^{(k)} & z^{(k)} \end{bmatrix}^T$ (decomposed in frame k) can be transformed to a decomposition in frame q by a vector summation involving the unit vectors of frame k decomposed in frame q:

$$\begin{aligned} \mathbf{r}^{(q)} &= x^{(k)}\mathbf{i}_k^{(q)} + y^{(k)}\mathbf{j}_k^{(q)} + y^{(k)}\mathbf{k}_k^{(q)} && (4.2) \\ &= \mathbf{R}_k^{(q)}\mathbf{r}^{(k)} && (4.3) \end{aligned}$$

Here, we introduce the rotation matrix (see e.g. Sciavicco and Siciliano, 2000):

$$\mathbf{R}_k^{(q)} \equiv \begin{bmatrix} \mathbf{i}_k^{(q)} & \mathbf{j}_k^{(q)} & \mathbf{k}_k^{(q)} \end{bmatrix} \in \mathbb{R}^{3\times 3} \tag{4.4}$$

Rotation matrices have a number of useful properties. We have for instance that their inverse equals their transpose:

$$\mathbf{R}_j^{(i)} = \left(\mathbf{R}_i^{(j)}\right)^{-1} = \left(\mathbf{R}_i^{(j)}\right)^T \tag{4.5}$$

4.2.2 The hinged two-body system

The linear velocity of body 1 is the rate of change of its position:

$$\mathbf{v}_1 = \dot{\mathbf{r}}_1 \tag{4.6}$$

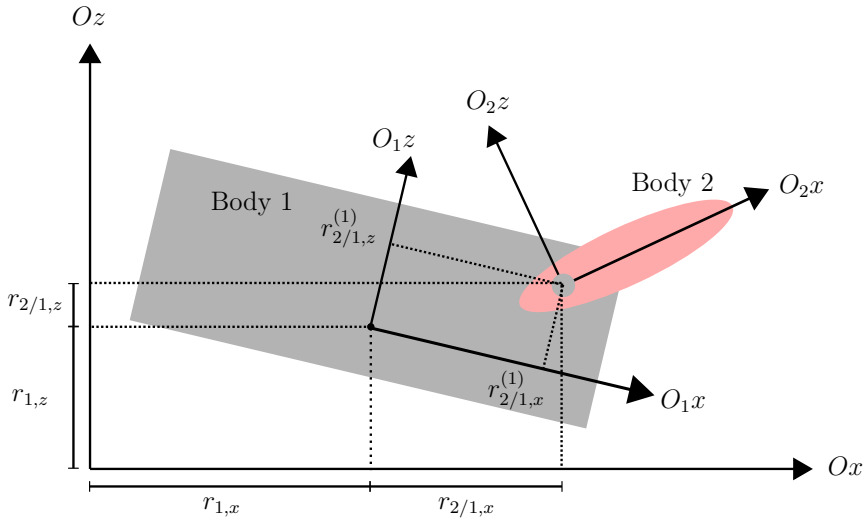

Figure 4.1: Illustration of the hinged two-body system and body fixed frames showing the notation used for the position vector components with different decompositions. We have here that $\mathbf{r}^{(k)}_{j/i} = \begin{bmatrix} x^{(k)}_{j/i} & y^{(k)}_{j/i} & z^{(k)}_{j/i} \end{bmatrix}^T$.

Since $\mathbf{r}_1$ is decomposed in the inertial frame, $\mathbf{v}_1$ is an absolute velocity. In dynamic analysis, it is particularly useful to decompose the velocity of a body in its own frame, writing:

$$\mathbf{v}^{(1)}_1 = \mathbf{R}^{(1)}\mathbf{v}_1 \tag{4.7}$$

We will now express the location of body 2 by the location of body 1 and their relative position:

$$\mathbf{r}_2 = \mathbf{r}_1 + \mathbf{r}_{2/1} \tag{4.8}$$

$$= \mathbf{r}_1 + \mathbf{R}_1\mathbf{r}^{(1)}_{2/1} \tag{4.9}$$

Here, the last expression is useful if $\mathbf{r}^{(1)}_{2/1}$ is time invariant (constant in time). This is the case when body 1 and body 2 are hinged together with $\mathbf{r}_2$ located on the hinge axis. This is the situation illustrated in Figure 4.1. With time invariant $\mathbf{r}^{(1)}_{2/1}$, the velocity of body 2 becomes,

$$\mathbf{v}_2 = \mathbf{v}_1 + \dot{\mathbf{R}}_1\mathbf{r}^{(1)}_{2/1} \tag{4.10}$$

where we note that we take the time derivative of the rotation matrix. Decomposing $\mathbf{v}_2$ in frame 1 we can write:

$$\mathbf{v}_2^{(1)} = \mathbf{v}_1^{(1)} + \mathbf{R}^{(1)}\dot{\mathbf{R}}_1\mathbf{r}_{2/1}^{(1)} \tag{4.11}$$

$$= \mathbf{v}_1^{(1)} + \mathbf{S}\left(\boldsymbol{\omega}_1^{(1)}\right)\mathbf{r}_{2/1}^{(1)} \tag{4.12}$$

$$= \mathbf{v}_1^{(1)} + \boldsymbol{\omega}_1^{(1)} \times \mathbf{r}_{2/1}^{(1)} \tag{4.13}$$

Here, $\boldsymbol{\omega}_j^{(j)}$ is the angular velocity vector of body j decomposed in its own frame. The matrix operator $\mathbf{S}(.)$ is defined by its equivalence to the vector cross product of arbitrary vectors $\mathbf{a}$ and $\mathbf{b}$:

$$\mathbf{S}(\mathbf{a})\,\mathbf{b} \equiv \mathbf{a} \times \mathbf{b}\,,\ \mathbf{S}(\mathbf{a}) = \begin{bmatrix} 0 & -a_3 & a_2 \\ a_3 & 0 & -a_1 \\ -a_2 & a_1 & 0 \end{bmatrix} \tag{4.14}$$

We note that $\mathbf{S}(.)$ possess the properties $\mathbf{S}(\mathbf{a})\,\mathbf{b} = -\mathbf{S}(\mathbf{b})\,\mathbf{a}$ and $\mathbf{S}(\mathbf{a}) = -\mathbf{S}(\mathbf{a})^T = -\mathbf{S}(-\mathbf{a})$, i.e. it is skew-symmetric. The result $\mathbf{R}^{(j)}\dot{\mathbf{R}}_j = \mathbf{R}_j^T\dot{\mathbf{R}}_j = \mathbf{S}\left(\boldsymbol{\omega}_j^{(j)}\right)$ is shown by Perez and Fossen (2007) (in a somewhat different form).

Making use of the property $\mathbf{S}(\mathbf{a})\,\mathbf{b} = -\mathbf{S}(\mathbf{b})\,\mathbf{a}$, we can write $\mathbf{v}_2^{(1)}$ using compact matrix notation, collecting linear and angular velocities in a vector:

$$\mathbf{v}_2^{(1)} = \begin{bmatrix} \mathbf{I} & -\mathbf{S}\left(\mathbf{r}_{2/1}^{(1)}\right) \end{bmatrix} \begin{bmatrix} \mathbf{v}_1^{(1)} \\ \boldsymbol{\omega}_1^{(1)} \end{bmatrix} \tag{4.15}$$

We note here that the 3-by-6 matrix premultiplying the velocity vector is time invariant. This formula is useful in the case that we have only one body, and $\mathbf{v}_2^{(1)}$ represents a velocity of a fixed point on that body. If however $\mathbf{v}_2$ is the velocity of a second body, it is more useful to decompose the velocity of body 2 in its own frame. Premultiplying with $\mathbf{R}_1^{(2)}$ we obtain:

$$\mathbf{v}_2^{(2)} = \begin{bmatrix} \mathbf{R}_1^{(2)} & -\mathbf{R}_1^{(2)}\mathbf{S}\left(\mathbf{r}_{2/1}^{(1)}\right) \end{bmatrix} \begin{bmatrix} \mathbf{v}_1^{(1)} \\ \boldsymbol{\omega}_1^{(1)} \end{bmatrix} \tag{4.16}$$

Note here that $\mathbf{R}_1^{(2)}$ will in general vary with time.

The orientation and angular velocity of body 1 are given by the rotation matrix $\mathbf{R}_1$ and the angular velocity $\boldsymbol{\omega}_1^{(1)}$, respectively. As already stated, they are related by the expression:

$$\mathbf{S}\left(\boldsymbol{\omega}_1^{(1)}\right) = \mathbf{R}_1^T\dot{\mathbf{R}}_1 \tag{4.17}$$

When we seek an expression for the angular velocity of body 2, we make use of a result shown by Perez and Fossen (2007):

$$\boldsymbol{\omega}_2 = \boldsymbol{\omega}_1 + \boldsymbol{\omega}_{2/1} \tag{4.18}$$

Here, $\boldsymbol{\omega}_{2/1}$ express the angular velocity of body 2 relative to body 1. Decomposing the vectors differently, we have:

$$\boldsymbol{\omega}_2^{(2)} = \mathbf{R}_1^{(2)} \boldsymbol{\omega}_1^{(1)} + \boldsymbol{\omega}_{2/1}^{(2)} \tag{4.19}$$

Now, the vector $\boldsymbol{\omega}_{2/1}^{(2)}$ have a clear physical interpretation when body 2 and body 1 are hinged together. If the hinge axis is parallel to (or identical to) O_2y, we can write,

$$\boldsymbol{\omega}_{2/1}^{(2)} = \begin{bmatrix} 0 & \dot{q}_7 & 0 \end{bmatrix}^T \tag{4.20}$$

where q_7 is the hinge angle, describing a relative angle between the bodies.

4.2.3 Euler angles

Up to this point, we have used 3 parameters to describe the position of a body, 3 parameters to describe the translational velocity and 3 parameters to describe the angular velocity. We have however used the 9 numbers occupying the 3-by-3 rotation matrix to describe the orientation of a body. These 9 numbers are not independent and can be related to only 3 independent parameters, as expected. There are however numerous different conventions in use, each leading to different angular displacement coordinates (and causing a lot of confusion). One choice is to use Euler angles and employ a yaw-pitch-roll sequence of rotations, where it should be noted that the order of the rotations matter. This is the definition used in e.g. Perez and Fossen (2007). Sciavicco and Siciliano (2000) includes an extensive treatment of rotation matrices and provide formula for a few conventions, including the convention used here. Note however that they define roll as a rotation about the z axis and yaw as a rotation about the x axis. For this reason, our convention is named "roll-pitch-yaw" in the latter reference.

Employing the yaw-pitch-roll convention and considering only body 1 ($j = 1$), we can write the rotation matrix as a product of three elementary rotation matrices,

$$\mathbf{R}_1 = \mathbf{R}_z(q_6)\,\mathbf{R}_y(q_5)\,\mathbf{R}_x(q_4) \tag{4.21}$$

where q_4, q_5 and q_6 are the roll, pitch and yaw Euler angles. The elementary rotation matrices are,

$$\begin{aligned} \mathbf{R}_x(\alpha) &= \begin{bmatrix} 1 & 0 & 0 \\ 0 & c_\alpha & -s_\alpha \\ 0 & s_\alpha & c_\alpha \end{bmatrix}, \quad \mathbf{R}_y(\alpha) = \begin{bmatrix} c_\alpha & 0 & s_\alpha \\ 0 & 1 & 0 \\ -s_\alpha & 0 & c_\alpha \end{bmatrix} \\ \mathbf{R}_z(\alpha) &= \begin{bmatrix} c_\alpha & -s_\alpha & 0 \\ s_\alpha & c_\alpha & 0 \\ 0 & 0 & 1 \end{bmatrix}, \qquad \begin{aligned} c_\alpha &= \cos(\alpha) \\ s_\alpha &= \sin(\alpha) \end{aligned} \end{aligned} \tag{4.22}$$

giving:

$$\mathbf{R}_1 = \begin{bmatrix} c_6c_5 & -s_6c_4 + c_6s_5s_4 & s_6s_4 + c_6s_5c_4 \\ s_6c_5 & c_6c_4 + s_6s_5s_4 & -c_6s_4 + s_6s_5c_4 \\ -s_5 & c_5s_4 & c_5c_4 \end{bmatrix}, \quad \begin{matrix} c_i = \cos(q_i) \\ s_i = \sin(q_i) \end{matrix} \tag{4.23}$$

With this convention, the position and orientation of body 1 can be obtained by a sequence of three rotations followed by a translation, starting from a state where O_1xyz and $Oxyz$ coincides. The following sequence apply:

- A rotation of $Oxyz$ an angle q_6 about its z axis, defining the temporary frame O_axyz
- A rotation of O_axyz an angle q_5 about its y axis, defining the temporary frame O_bxyz
- A rotation of O_bxyz an angle q_4 about its x axis, defining the temporary frame O_cxyz
- A translation of O_cxyz by $\mathbf{r}_1$, defining the body fixed frame O_1xyz

Note again that the order of the rotations matter. With the order used here, yaw is always a rotation about a vertical axis, pitch is always a rotation about a horizontal axis, but roll is a rotation about a horizontal axis only if the pitch angle is zero.

It must be emphasized that $\boldsymbol{\omega}_1^{(1)}$ is not the time derivative of the Euler angles, $\mathbf{q}_r = \begin{bmatrix} q_4 & q_5 & q_6 \end{bmatrix}^T$. When we relate $\dot{\mathbf{q}}_r$ and $\boldsymbol{\omega}_1^{(1)}$, we make use of a generalization of eq. (4.18):

$$\boldsymbol{\omega}_1 = \boldsymbol{\omega}_a + \boldsymbol{\omega}_{b/a} + \boldsymbol{\omega}_{1/b} \tag{4.24}$$

Here, O_axyz and O_bxyz are the temporary frames involved in the yaw-pitch-roll sequence of rotations as defined above. Since q_6 is a rotation about Oz, which is identical to O_az, we have that $\boldsymbol{\omega}_a = \boldsymbol{\omega}_a^{(a)} = \begin{bmatrix} 0 & 0 & \dot{q}_6 \end{bmatrix}^T$. Similarly, we have $\boldsymbol{\omega}_{b/a}^{(a)} = \boldsymbol{\omega}_{b/a}^{(b)} = \begin{bmatrix} 0 & \dot{q}_5 & 0 \end{bmatrix}^T$ and $\boldsymbol{\omega}_{1/b}^{(b)} = \boldsymbol{\omega}_{1/b}^{(1)} = \begin{bmatrix} \dot{q}_4 & 0 & 0 \end{bmatrix}^T$. Using this, we can write:

$$\begin{aligned} \boldsymbol{\omega}_1^{(1)} &= \boldsymbol{\omega}_{1/b}^{(1)} + \mathbf{R}_x^T(q_4)\,\boldsymbol{\omega}_{b/a}^{(b)} + \mathbf{R}_x^T(q_4)\,\mathbf{R}_y^T(q_5)\,\boldsymbol{\omega}_{1/b}^{(1)} \\ &= \begin{bmatrix} 1 & 0 & -\sin(q_5) \\ 0 & \cos(q_4) & \sin(q_4)\cos(q_5) \\ 0 & -\sin(q_4) & \cos(q_4)\cos(q_5) \end{bmatrix} \begin{bmatrix} \dot{q}_4 \\ \dot{q}_5 \\ \dot{q}_6 \end{bmatrix} \\ &= \mathbf{T}_r\dot{\mathbf{q}}_r \end{aligned} \tag{4.25}$$

Note here that $\mathbf{T}_r$ is not a rotation matrix since the angular velocities $\dot{q}_4$, $\dot{q}_5$ and $\dot{q}_6$ are taken about axes which are not orthogonal. The inverse transformation is provided by the matrix,

$$\mathbf{T}_r^{-1} = \begin{bmatrix} 1 & \frac{\sin(q_5)\sin(q_4)}{\cos(q_5)} & \frac{\sin(q_5)\cos(q_4)}{\cos(q_5)} \\ 0 & \cos(q_4) & -\sin(q_4) \\ 0 & \frac{\sin(q_4)}{\cos(q_5)} & \frac{\cos(q_4)}{\cos(q_5)} \end{bmatrix} \tag{4.26}$$

which reveals a kinematic singularity for $\cos(q_5) = 0$ (which should be of no concern for the system studied here).

The orientation of body 2 is specified by the rotation matrix $\mathbf{R}_2$. Assuming again that body 2 is hinged to body 1 with O_2y as the hinge axis, it is more relevant to describe the orientation of body 2 by its relative orientation to body 1:

$$\begin{aligned} \mathbf{R}_2 &= \mathbf{R}_1 \mathbf{R}_2^{(1)} \\ &= \mathbf{R}_1 \mathbf{R}_z(\gamma_z)\, \mathbf{R}_x(\gamma_x)\, \mathbf{R}_y(q_7) \end{aligned} \tag{4.27}$$

Here, we take q_7 to be the time varying hinge angle (with time derivative $\dot{q}_7$ appearing in eq. (4.20)). The angles γ_z and γ_x are time invariant parameters determining the orientation of the hinge axis relative to body 1. Note that we use a yaw-roll-pitch sequence to parametrize $\mathbf{R}_2^{(1)}$, as opposed to the yaw-pitch-roll sequence used to parametrize $\mathbf{R}_1$.

For the hinged 5-body WEC described in the next section, we assume that the hinge axes are parallel to the xy-plane of O_1xyz. This imply the slight simplification $\gamma_x = 0$ and thus $\mathbf{R}_2^{(1)} = \mathbf{R}_z(\gamma_z)\, \mathbf{R}_y(q_7)$. With $\gamma_x = 0$, γ_z can be interpreted as the angle between O_1y and O_2y.

4.2.4 Kinematics of the hinged 5-body WEC

Figure 4.2 shows a principal sketch of the hinged 5-body WEC and the different body fixed frames used in the analysis. In the following, we will use the methodology and notation introduced in this chapter to describe relationships between the velocities of the bodies and their relative orientation, respecting the kinematic constraints imposed by the hinges. The WEC consist of four buoys (body 2-5), all hinged to the same center floater (body 1), having the y axis of the buoys as hinge axes. It turns out that this system is a straightforward generalization of the hinged two body system discussed so far in this chapter.

The position and orientation of the rigid bodies are uniquely determined by 10 generalized coordinates, $\mathbf{q} = \begin{bmatrix} q_1 & \cdots & q_{10} \end{bmatrix}^T$, defined as follows:

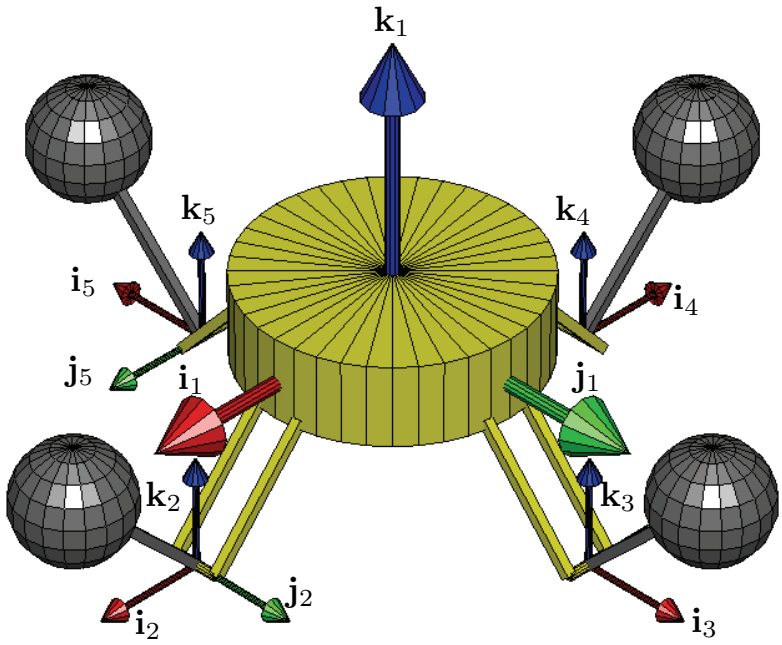

Figure 4.2: Body fixed coordinate frames. The red/green/blue arrows indicate the body fixed x/y/z axes.

- q_1, q_2 and q_3 are the components of $\mathbf{r}_1$, giving the position of the center floater.
- q_4, q_5 and q_6 are the roll, pitch and yaw Euler angles of O_1xyz, employing a yaw-pitch-roll rotation sequence, as defined in Section 4.2.3.
- q_k where $k = 7..10$ are the hinge angles. The hinge axes are assumed to be parallel to the xy-plane of O_1xyz. Thus, q_k can be interpreted as the angle between O_1z and O_kz. A positive hinge angle is defined as a positive rotation about O_ky following the right hand rule (see Figure 2.8).

Changes in $q_1, ..., q_6$ with all hinges fixed will cause the collection of bodies to move as if they were one rigid body. These modes of motion will therefore sometimes be referenced as the collective modes. The coordinates q_k, $k > 6$ express relative rotations and will be referenced as the hinge modes.

The inertial frame have Oz pointing upwards and its origin in the mean free water surface. When the system is in static equilibrium, $\mathbf{q} = \mathbf{0}$, and thus O_1xyz coincides with $Oxyz$.

Equations of motion are most conveniently expressed using linear and angular velocity vectors decomposed in body fixed frames. We define the vector of dependent velocities to be:

$$\bar{\mathbf{V}} = \begin{bmatrix} \mathbf{v}_1^{(1)T} & \boldsymbol{\omega}_1^{(1)T} & \cdots & \mathbf{v}_5^{(5)T} & \boldsymbol{\omega}_5^{(5)T} \end{bmatrix}^T \in \mathbb{R}^{30} \tag{4.28}$$

The dependent velocities can be related to the time derivative of $\mathbf{q}$ with the linear transformation:

$$\begin{aligned} \bar{\mathbf{V}} &= \mathbf{J}\left(q_7, \ldots, q_{10}\right) \mathbf{T}\left(q_4, q_5, q_6\right) \dot{\mathbf{q}} \\ &= \mathbf{J}\left(q_7, \ldots, q_{10}\right) \mathbf{V} \\ \mathbf{J} &\in \mathbb{R}^{30\times 10}, \mathbf{T} \in \mathbb{R}^{10\times 10} \end{aligned} \tag{4.29}$$

This type of transformation is sometimes called a displacement modulated velocity transformation. We factor the total transformation matrix into two parts, a non-square transformation matrix $\mathbf{J}$ only dependent on the hinge angles, and a square and invertible transformation matrix $\mathbf{T}$ only dependent on the Euler angles of the center floater. This factoring turns out to be highly beneficial and will show to simplify the equations of motions significantly. The product $\mathbf{T}\left(q_4, q_5, q_6\right) \dot{\mathbf{q}}$ defines the independent velocities $\mathbf{V}$. The matrix $\mathbf{T}$ can be partitioned as:

$$\mathbf{T} = \begin{bmatrix} \mathbf{R}^{(1)} & \mathbf{0} & \mathbf{0} \\ \mathbf{0} & \mathbf{T}_r & \mathbf{0} \\ \mathbf{0} & \mathbf{0} & \mathbf{I}_{4\times 4} \end{bmatrix} \tag{4.30}$$

Here, $\mathbf{R}^{(1)}$ is the transpose (or inverse) of the rotation matrix given in eq. (4.23), $\mathbf{T}_r$ is the angular velocity transformation matrix given in eq. (4.25) and $\mathbf{I}_{4\times4}$ is a identity matrix. It follows that the independent velocities can be written:

$$\mathbf{V} = \begin{bmatrix} \mathbf{v}_1^{(1)T} & \boldsymbol{\omega}_1^{(1)T} & \dot{q}_7 & \cdots & \dot{q}_{10} \end{bmatrix}^T \in \mathbb{R}^{10} \tag{4.31}$$

The matrix $\mathbf{J}$ can be partitioned as,

$$\mathbf{J} = \begin{bmatrix} \mathbf{I}_{6\times6} & \mathbf{0} & \mathbf{0} & \mathbf{0} & \mathbf{0} \\ \mathbf{J}_{21} & \mathbf{J}_d & \mathbf{0} & \mathbf{0} & \mathbf{0} \\ \mathbf{J}_{31} & \mathbf{0} & \mathbf{J}_d & \mathbf{0} & \mathbf{0} \\ \mathbf{J}_{41} & \mathbf{0} & \mathbf{0} & \mathbf{J}_d & \mathbf{0} \\ \mathbf{J}_{51} & \mathbf{0} & \mathbf{0} & \mathbf{0} & \mathbf{J}_d \end{bmatrix} \tag{4.32}$$

with partitions given by:

$$\mathbf{J}_{j1}(q_k) = \begin{bmatrix} \mathbf{R}_1^{(j)} & -\mathbf{R}_1^{(j)}\mathbf{S}\left(\mathbf{r}_{j/1}^{(1)}\right) \\ \mathbf{0} & \mathbf{R}_1^{(j)} \end{bmatrix}, k = 5 + j \tag{4.33}$$

$$\mathbf{J}_d = \begin{bmatrix} 0 & 0 & 0 & 0 & 1 & 0 \end{bmatrix}^T \tag{4.34}$$

Here, $\mathbf{r}_{j/1}^{(1)}$ express the position of body j relative to body 1 in O_1xyz. The matrix $\mathbf{J}$ express the relationships given in eqs. (4.16) and (4.19).

One of the advantages of this formulation is that each partition in $\mathbf{J}$ does not depend on more than one angle. This is greatly simplifying the task of finding an analytical time derivative of $\mathbf{J}$. It is only the lower left 24-by-6 partition of $\mathbf{J}$ that has a non-zero time derivative. For the non-zero partitions we have,

$$\begin{aligned} \frac{d\mathbf{J}_{j1}(q_k)}{dt} &= V_k \frac{d\mathbf{J}_{j1}(q_k)}{dq_k} \\ &= V_k \begin{bmatrix} \frac{d\mathbf{R}_1^{(j)}}{dq_k} & -\frac{d\mathbf{R}_1^{(j)}}{dq_k}\mathbf{S}\left(\mathbf{r}_{j/1}^{(1)}\right) \\ \mathbf{0} & \frac{d\mathbf{R}_1^{(j)}}{dq_k} \end{bmatrix}, \; k = 5 + j \end{aligned} \tag{4.35}$$

with,

$$\frac{d\mathbf{R}_1^{(j)}}{dq_k} = \begin{bmatrix} -\sin(q_k) & \cos(q_k) & 0 \\ -\cos(q_k) & -\sin(q_k) & 0 \\ 0 & 0 & 0 \end{bmatrix} \mathbf{R}_z(-\gamma_z) \tag{4.36}$$

Recall here that γ_x in eq. (4.27) is zero for this WEC. We have also used that $\dot{q}_k = V_k$ for $k > 6$.

4.3 Equations of motion

4.3.1 Newton-Euler equations with eliminated constraint forces

Ó'Catháin et al. (2008) demonstrates a methodology for obtaining equations of motion for floating systems with kinematic constraints. Their methodology is based on the Newton-Euler equations of motion and the elimination of constraint forces using independent velocities and the principle of virtual work. Their derivation is based on Egeland and Gravdahl (2002, pp. 339), which refer to the obtained equations as the *Newton-Euler equations of motion with eliminated constraint forces*, and cite several sources presenting the same equations, under various names. The matrix form used here follow more closely the work by Ó'Catháin et al. (2008). Note however that we will use different symbols.

The classical Newton-Euler equations of motion for a rigid body in six degrees of freedom express an equilibrium of external- and inertia forces and moments decomposed in a body fixed frame. Formulated for body j it can be written:

$$\bar{\mathbf{M}}_{jj}\dot{\bar{\mathbf{V}}}_j + \bar{\mathbf{C}}_{jj}\left(\bar{\mathbf{V}}_j\right)\bar{\mathbf{V}}_j = \bar{\mathbf{F}}_j + \bar{\mathbf{F}}_{c,j} \tag{4.37}$$

We have here separated the external forces on the r.h.s. in two parts with $\bar{\mathbf{F}}_{c,j}$ representing the constraint forces acting in the hinges. We have here,

$$\bar{\mathbf{V}}_j = \begin{bmatrix} \mathbf{v}_j^{(j)} \\ \boldsymbol{\omega}_j^{(j)} \end{bmatrix}, \bar{\mathbf{F}}_j = \begin{bmatrix} \mathbf{f}_j^{(j)} \\ \boldsymbol{\tau}_j^{(j)} \end{bmatrix} \tag{4.38}$$

$$\bar{\mathbf{M}}_{jj} = \begin{bmatrix} m_j\mathbf{I}_{3\times 3} & m_j\mathbf{S}\left(\mathbf{r}_{Gj/j}^{(j)}\right)^T \\ m_j\mathbf{S}\left(\mathbf{r}_{Gj/j}^{(j)}\right) & \boldsymbol{I} \end{bmatrix} \tag{4.39}$$

$$\bar{\mathbf{C}}_{jj}\left(\bar{\mathbf{V}}_j\right) = \begin{bmatrix} \mathbf{S}\left(\boldsymbol{\omega}_j^{(j)}\right) & \mathbf{0} \\ \mathbf{S}\left(\mathbf{v}_j^{(j)}\right) & \mathbf{S}\left(\boldsymbol{\omega}_j^{(j)}\right) \end{bmatrix} \bar{\mathbf{M}}_{jj} \tag{4.40}$$

$\mathbf{f}_j^{(j)}$ and $\boldsymbol{\tau}_j^{(j)}$ are here Cartesian vectors representing force and moment. The mass matrix $\bar{\mathbf{M}}_{jj}$ is symmetric and time invariant and the Coriolis-centrifugal matrix $\bar{\mathbf{C}}_{jj}\left(\bar{\mathbf{V}}_j\right)$ is skew symmetric. m_j is the mass of the body. Recall the cross-product operator $\mathbf{S}(.)$ from eq. (4.14). The forces $\bar{\mathbf{C}}_{jj}\left(\bar{\mathbf{V}}_j\right)\bar{\mathbf{V}}_j$ is sometimes called fictitious forces, needed only because we decompose velocities and forces in a body fixed (non-inertial) frame. Using a body fixed frame is necessary in order to have a time invariant $\bar{\mathbf{M}}_{jj}$.

The hydrodynamic forces have a component which is proportional to the accelerations and can therefore be represented by an added mass matrix. Because the calculation of added mass is based on linear hydrodynamic theory, in

which small perturbations around the mean position of the bodies is assumed, we do not include the added mass effect in $\bar{\mathbf{M}}_{jj}$, but rather include it as part of the external forces $\bar{\mathbf{F}}_j$. A treatment of the generalized hydrodynamic forces is presented in Section 4.4.

The inertia tensor $\boldsymbol{I}_j$ (not to be confused with the identity matrix $\mathbf{I}$) must be taken relative to O_jx, O_jy and O_jz which may not correspond to the principle axis of the body. In the case where the principle axes of a body is identical to the body fixed coordinate axes, $\bar{\mathbf{M}}_{jj}$ becomes a diagonal matrix, and the equations of motions of a *single* body will simplify greatly. In a multibody system with hinged bodies, the simplest equations are obtained when the hinge axes are aligned with one of the body fixed axes. We therefore formulate the most general form of the Newton-Euler equations here.

If we define the block diagonal mass matrix $\bar{\mathbf{M}} = \text{diag}\left(\bar{\mathbf{M}}_{11}, \cdots, \bar{\mathbf{M}}_{55}\right) \in \mathbb{R}^{30\times 30}$, and similarly for the Coriolis-centrifugal matrices, we can express the equations of motion for all 5 bodies simultaneously,

$$\bar{\mathbf{M}}\dot{\bar{\mathbf{V}}} + \bar{\mathbf{C}}\left(\bar{\mathbf{V}}\right)\bar{\mathbf{V}} = \bar{\mathbf{F}} + \bar{\mathbf{F}}_c \tag{4.41}$$

with obvious definition of $\bar{\mathbf{F}}$ and $\bar{\mathbf{F}}_c$.

We want to eliminate the constraint forces and formulate equations of motions in terms of the independent velocities. To do so, we introduce a vector $\delta\mathbf{X}$ representing virtual displacements respecting the kinematic constraints expressed by eq. (4.29). This means that they can be written as a linear combination of the *independent* virtual displacements $\delta\boldsymbol{\eta}$:

$$\delta\mathbf{X} = \mathbf{J}\delta\boldsymbol{\eta}\,, \in \mathbb{R}^{30} \tag{4.42}$$

The principle of virtual work states that the virtual work associated with a constraint force and a virtual displacement respecting the constraint is zero. This can be expressed:

$$\delta W = \delta\mathbf{X}^T\bar{\mathbf{F}}_c = \delta\boldsymbol{\eta}^T\mathbf{J}^T\bar{\mathbf{F}}_c = 0 \tag{4.43}$$

The independent virtual displacements $\delta\boldsymbol{\eta}$ can be chosen arbitrarily. The above equation hold for arbitrary $\delta\boldsymbol{\eta}$ only if:

$$\mathbf{J}^T\bar{\mathbf{F}}_c = 0 \tag{4.44}$$

This shows that also the physical power $\mathbf{V}^T\mathbf{J}^T\bar{\mathbf{F}}_c$ associated with the constraint forces is zero. Solving eq. (4.41) for $\bar{\mathbf{F}}_c$ and inserting into eq. (4.44) we obtain,

$$\mathbf{J}^T\bar{\mathbf{M}}\dot{\bar{\mathbf{V}}} + \mathbf{J}^T\bar{\mathbf{C}}\left(\bar{\mathbf{V}}\right)\bar{\mathbf{V}} = \mathbf{J}^T\bar{\mathbf{F}} \tag{4.45}$$

Moreover, by using eq. (4.29) we can insert $\bar{\mathbf{V}} = \mathbf{J}\mathbf{V}$ and $\dot{\bar{\mathbf{V}}} = \mathbf{J}\dot{\mathbf{V}} + \dot{\mathbf{J}}\mathbf{V}$ and write the equations of motions in its final form:

$$\mathbf{M}\left(q_7, ..., q_{10}\right)\dot{\mathbf{V}} + \mathbf{C}\left(\mathbf{V}, q_7, ..., q_{10}\right)\mathbf{V} = \mathbf{F} \tag{4.46}$$

Here, the symmetric, hinge angle dependent generalized mass matrix can be written:

$$\mathbf{M}\left(q_7, ..., q_{10}\right) = \mathbf{J}^T\bar{\mathbf{M}}\mathbf{J}\,, \in \mathbb{R}^{10\times 10} \tag{4.47}$$

The generalized Coriolis-centrifugal matrix becomes,

$$\mathbf{C}\left(\mathbf{V}, q_7, ..., q_{10}\right) = \mathbf{J}^T\bar{\mathbf{M}}\dot{\mathbf{J}} + \mathbf{J}^T\bar{\mathbf{C}}\mathbf{J} \tag{4.48}$$

and the generalized external forces are:

$$\mathbf{F} = \mathbf{J}^T\bar{\mathbf{F}} \tag{4.49}$$

The generalized forces have a clear physical interpretation. $F_1, \ldots, F_6$ are the sum of forces and moments acting on the collection of bodies, decomposed in O_1xyz. $F_k, k > 6$ are the moments acting in the hinges. We note also that the generalized Coriolis-centrifugal matrix have two contributions. One skew-symmetric contribution $\mathbf{J}^T\bar{\mathbf{C}}\mathbf{J}$ where $\bar{\mathbf{C}}$ appear also in the Newton-Euler equations for a single body, and one non-skew-symmetric contribution due to the time derivative of $\mathbf{J}$, which is given by an analytical expression in Section 4.2.4. $\mathbf{J}$ is dependent on the hinge angles, $\dot{\mathbf{J}}$ is dependent on the hinge angles and hinge velocities whereas $\bar{\mathbf{C}}$ depend on all independent velocities.

4.3.2 Lagrange's equation for quasi-coordinates

We will here show an alternative approach for obtaining equations of motion for the hinged 5-body WEC (and similar systems) based on Lagrange's equation. Lagrange's equations of motion can be formulated as,

$$\frac{d}{dt}\left(\frac{\partial \mathcal{T}}{\partial \dot{q}_k}\right) - \frac{\partial \mathcal{T}}{\partial q_k} = \check{F}_k,\ k = 1, 2, .., n \tag{4.50}$$

where the index k runs from 1 to n, the number of generalized coordinates. For the choice of generalized coordinates used here, n is also the number of degrees of freedom. The scalar $\mathcal{T}$ is the kinetic energy of the system. In some formulations of Lagrange's equation, the Lagrangian $\mathcal{L}$, defined as the difference between kinetic and potential energy, is used in place of the kinetic energy. Here, it is found more convenient to include the generalized forces derivable from the potential energy in the generalized force $\check{F}_k$ on the right hand side of the equation. Note that we put a $\check{}$ on $\check{F}_k$ to indicate that its definition differ from that of F_k, that will appear in the final equation.

The kinetic energy of the system can be written:

$$\mathcal{T} = \frac{1}{2}\bar{\mathbf{V}}^T\bar{\mathbf{M}}\bar{\mathbf{V}} \tag{4.51}$$

Here, $\bar{\mathbf{M}} \in \mathbb{R}^{30\times30}$ is the block diagonal mass matrix comprising the 6-by-6 mass matrices of all bodies (see eq. (4.41)) and $\bar{\mathbf{V}}$ is the dependent velocities, eq. (4.28).

The transformation of $\dot{\mathbf{q}}$ into $\bar{\mathbf{V}}$, eq. (4.29), involves all rotational coordinates $q_4..q_{10}$. In order to separate the dependence on the Euler angles q_4, q_5, q_6 from the hinge angles $q_7..q_{10}$, we factored the total transformation matrix as a product of two matrices, $\mathbf{J}(q_7, \ldots, q_{10}) \in \mathbb{R}^{30\times10}$ and $\mathbf{T}(q_4, q_5, q_6) \in \mathbb{R}^{10\times10}$, defining the independent velocities $\mathbf{V} = \mathbf{T}(q_4, q_5, q_6)\,\dot{\mathbf{q}}$ (recall Section 4.2.4).

Lagrange's equation of motion, as it is written in eq. (4.50), is only valid if the generalized coordinates q_k is true coordinates in the sense that they uniquely describe the configuration of the system in inertial space (Meirovitch, 2004). The choice of generalized coordinates applied here certainly fulfill this requirement. However, a direct application of eq. (4.50) will lead to rather complicated and computationally inefficient equations of motion, involving a generalized mass matrix dependent on all rotational generalized coordinates $q_4..q_n$, in addition to the derivative of this generalized mass matrix with respect to the same coordinates. This complication is because the Euler angles appear in products of sines and cosines, as in eq. (4.23). Taking the time derivative of such expressions using the chain rule of derivation yields long expressions of cosines and sines. The different hinge angles on the other hand, appear in different entries of the transformation matrix $\mathbf{J}(q_7, \ldots, q_{10})$, yielding a relatively simple expression for the time derivative of $\mathbf{J}$, as seen in eq. (4.35). We therefore seek an expression where the generalized mass matrix only depend on the hinge angles.

Meirovitch (2004) shows that Lagrange's equation can be rewritten with $\mathbf{V}$ representing velocities rather than $\dot{\mathbf{q}}$. The components of $\mathbf{V}$ are independent and are taken as a linear combination of the components of $\dot{\mathbf{q}}$. The velocities $\mathbf{V}$ are seen as being time derivatives of quasi-coordinates, which itself is not defined, and that do not have to be true coordinates.

We start by noting that the kinetic energy can be written as an explicit function of $\dot{\mathbf{q}}$ and $\mathbf{q}$,

$$\mathcal{T}(\dot{\mathbf{q}}, \mathbf{q}) = \frac{1}{2}\dot{\mathbf{q}}^T\mathbf{T}(q_4, q_5, q_6)^T\,\mathbf{J}(q_7, \ldots, q_{10})^T\,\bar{\mathbf{M}}\mathbf{J}(q_7, \ldots, q_{10})\,\mathbf{T}(q_4, q_5, q_6)\,\dot{\mathbf{q}} \tag{4.52}$$

or as an explicit function of $\mathbf{V}$ and $\mathbf{q}$:

$$\hat{\mathcal{T}}(\mathbf{V},\mathbf{q}) = \frac{1}{2}\mathbf{V}^T\mathbf{J}(q_7,\ldots,q_{10})^T\bar{\mathbf{M}}\mathbf{J}(q_7,\ldots,q_{10})\mathbf{V} \tag{4.53}$$

$$= \frac{1}{2}\mathbf{V}^T\mathbf{M}(q_7,\ldots,q_{10})\mathbf{V} \tag{4.54}$$

Obviously, $\hat{\mathcal{T}} = \mathcal{T}$. We will however let their partial derivatives take different meanings so that $\partial\hat{\mathcal{T}}/d\dot{\mathbf{q}} = \mathbf{0}$, for instance. By writing the terms $\partial\mathcal{T}/\partial\dot{q}$ and $\partial\mathcal{T}/\partial q$ appearing in the standard Lagrange equations using the partial derivatives,

$$\frac{\partial\mathcal{T}}{\partial\dot{q}_k} = \sum_{i=1}^{n}\frac{\partial\hat{\mathcal{T}}}{\partial V_i}\frac{\partial V_i}{\partial\dot{q}_k} \tag{4.55}$$

$$\frac{\partial\mathcal{T}}{\partial q_k} = \frac{\partial\hat{\mathcal{T}}}{\partial q_k} + \sum_{i=1}^{n}\frac{\partial\hat{\mathcal{T}}}{\partial V_i}\frac{\partial V_i}{\partial q_k} \tag{4.56}$$

followed by a series of algebraic manipulations, Meirovitch (2004) shows that Lagrange equation can be written,

$$\frac{d}{dt}\left(\frac{\partial\hat{\mathcal{T}}}{\partial\mathbf{V}}\right) + \boldsymbol{\beta}^T\boldsymbol{\gamma}\frac{\partial\hat{\mathcal{T}}}{\partial\mathbf{V}} - \boldsymbol{\beta}^T\frac{\partial\hat{\mathcal{T}}}{\partial\mathbf{q}} = \boldsymbol{\beta}^T\check{\mathbf{F}}\,,\ \boldsymbol{\beta} \equiv \mathbf{T}^{-1} \tag{4.57}$$

which he refer to as the *Lagrange equations for quasi-coordinates*. Here, the matrix $\boldsymbol{\gamma}$ have entries,

$$\gamma_{ij} = \sum_{p=1}^{n}\left[\mathbf{V}^T\boldsymbol{\beta}^T\right]_p\left(\frac{\partial T_{ji}}{\partial q_p} - \frac{\partial T_{jp}}{\partial q_i}\right) \tag{4.58}$$

where the scalar $\left[\mathbf{V}^T\boldsymbol{\beta}^T\right]_p$ should be interpreted as the p'th element in the row vector $\mathbf{V}^T\boldsymbol{\beta}^T$.

Eqs. (4.57) and (4.58) are valid for any $\mathbf{V}$ that is a linear combination of $\dot{\mathbf{q}}$. For the hinged N-body WEC and the definition of $\mathbf{V}$ given in Section 4.2.4, we can make several simplifications. We note first that $\boldsymbol{\beta}^T\partial\hat{\mathcal{T}}/\partial\mathbf{q} = \partial\hat{\mathcal{T}}/\partial\mathbf{q}$, which is true because $\partial\hat{\mathcal{T}}/\partial q_j$ is only non-zero for $j > 6$ and the lower-right partition of $\boldsymbol{\beta}$ is equal to the identity matrix. The evaluation of the matrix product $\boldsymbol{\beta}^T\boldsymbol{\gamma}$ is rather involved, and the symbolic mathematical software Maple is used for this task. The result is remarkably simple:

$$\boldsymbol{\beta}^T\boldsymbol{\gamma} = \begin{bmatrix} \mathbf{S}\left(\boldsymbol{\omega}_1^{(1)}\right) & \mathbf{0} & \mathbf{0} \\ \mathbf{S}\left(\mathbf{v}_1^{(1)}\right) & \mathbf{S}\left(\boldsymbol{\omega}_1^{(1)}\right) & \mathbf{0} \\ \mathbf{0} & \mathbf{0} & \mathbf{0} \end{bmatrix} \tag{4.59}$$

Because the generalized mass matrix $\mathbf{M}$ is symmetric, we can write $\partial\hat{\mathcal{T}}/\partial\mathbf{V} = \mathbf{MV}$, and reformulate eq. (4.57) in the form,

$$\mathbf{M}\left(q_7, ..., q_n\right)\dot{\mathbf{V}} + \mathbf{C}_L\left(\mathbf{V}, q_7, ..., q_n\right)\mathbf{V} \quad = \quad \mathbf{F} \tag{4.60}$$

which corresponds to the equations of motion given by eq. (4.46), obtained using the Newton-Euler approach.

Note however that we add a subscript L on the Coriolis-centrifugal matrix. The reason for this is that the Newton-Euler approach and the Lagrangian approach lead to different but equivalent Coriolis-centrifugal matrices. That is, we have $\mathbf{C}_L\left(\mathbf{V}, \mathbf{q}\right) \neq \mathbf{C}\left(\mathbf{V}, \mathbf{q}\right)$, but the resulting forces are identical, i.e. $\mathbf{C}_L\left(\mathbf{V}, \mathbf{q}\right)\mathbf{V} = \mathbf{C}\left(\mathbf{V}, \mathbf{q}\right)\mathbf{V}$. This holds for arbitrary $\mathbf{V}$ and $\mathbf{q}$. The key in understanding that this is possible is that $\mathbf{C}$ is a function of $\mathbf{V}$ (as noted by Sciavicco and Siciliano (2000)). It is not attempted here to show (in a mathematical sense) that the Newton-Euler approach and the Lagrangian approach are equivalent. It is instead "shown" by experimenting on the numerical implementations of the two methods, drawing a number of random vectors $\mathbf{q}$ and $\mathbf{V}$ and comparing the resulting Coriolis-centrifugal forces, which turn out to be identical to within the expected numerical accuracy.

The Coriolis-centrifugal matrix resulting from the Lagrangian approach can be written:

$$\mathbf{C}_L = \mathbf{C}_A + \mathbf{C}_A^T + \mathbf{C}_B + \mathbf{C}_C \tag{4.61}$$

$$\mathbf{C}_A = \mathbf{J}^T\bar{\mathbf{M}}\dot{\mathbf{J}} \tag{4.62}$$

$$\mathbf{C}_B = \boldsymbol{\beta}^T\boldsymbol{\gamma}\mathbf{M} \tag{4.63}$$

$$C_{C,ij} = -\frac{1}{2}\sum_{k=1}^{n}\frac{\partial M_{jk}}{\partial q_i}V_k \tag{4.64}$$

We note that the first six columns of $\mathbf{C}_A$ are the only which is non-zero. Further, the first six rows of $\mathbf{C}_B$ are the only non-zero, meaning that it will induce forces only in the collective modes. The matrix $\mathbf{C}_C$, arising from the term $\partial\hat{\mathcal{T}}/\partial\mathbf{q}$, will only induce hinge moments.

The equations of motion as it is written in eq. (4.60) can easily be put in a (non-linear) state space form with $\mathbf{q}$ and $\mathbf{V}$ as the system states (this will be treated in Section 4.5). Defining the generalized momenta $\mathbf{p} = \mathbf{MV}$, we can also choose a different state space form with $\mathbf{q}$ and $\mathbf{p}$ as the system states. This is the choice of state variables compatible with the Bond-graph method (see e.g. Karnopp et al., 2006). Writing $\mathbf{p}_t = \begin{bmatrix} p_1 & p_2 & p_3 \end{bmatrix}^T$, $\mathbf{p}_r = \begin{bmatrix} p_4 & p_5 & p_6 \end{bmatrix}^T$

and likewise for $\mathbf{F}$, we have:

$$\begin{aligned}
\dot{\mathbf{q}} &= \mathbf{T}^{-1}\mathbf{V} \\
\dot{\mathbf{p}}_t &= -\boldsymbol{\omega}_1^{(1)} \times \mathbf{p}_t + \mathbf{F}_t \\
\dot{\mathbf{p}}_r &= -\mathbf{v}_1^{(1)} \times \mathbf{p}_t - \boldsymbol{\omega}_1^{(1)} \times \mathbf{p}_r + \mathbf{F}_r \\
\dot{p}_i &= \sum_{k=1}^{n} C_{C,ik} V_k + F_i,\ i = 7..n
\end{aligned} \tag{4.65}$$

with,

$$\mathbf{V} = \mathbf{M}^{-1}\mathbf{p} \tag{4.66}$$

In this form, the contribution to the Coriolis-centrifugal forces arising from $\mathbf{C}_A$ will be "hidden" because $\dot{\mathbf{p}} = \mathbf{M}\dot{\mathbf{V}} + \left(\mathbf{C}_A + \mathbf{C}_A^T\right)\mathbf{V}$.

4.3.3 Conservation of energy

In Sections 4.3.2 and 4.3.1 we obtained equations of motion using two different approaches. We noted that the Coriolis-centrifugal matrix $\mathbf{C}$ obtained by the Newton-Euler approach differ from that obtained using the Lagrangian approach, although resulting in identical forces, showing that the two approaches are equivalent. This type of comparison is a useful aid in the process of debugging the numerical implementation. Another useful aid is to study the energy in the system.

Inertia forces are conservative. This implies that the time derivative of kinetic energy must be balanced by the power generated by the external generalized forces. Hence, we require that $\dot{\mathcal{T}} = \mathbf{F}^T\mathbf{V}$. This is equivalent to (Sciavicco and Siciliano, 2000),

$$\mathbf{V}^T \underbrace{\left(\dot{\mathbf{M}} - 2\mathbf{C}\right)}_{\mathbf{N}(\mathbf{V},\mathbf{q})} \mathbf{V} = 0 \tag{4.67}$$

where we note that we take the time derivative of the generalized mass matrix. This requirement is satisfied if $\mathbf{N}$ is skew symmetric. However, because $\mathbf{N}$ is a function of $\mathbf{V}$, skew symmetry is not a necessary property (Sciavicco and Siciliano, 2000). The matrix $\mathbf{N}$ and $\mathbf{N}_L$, obtained using the Newton-Euler approach and the Lagrange approach, respectively, turn out not to be skew-symmetric. In this case it is more difficult to show energy conservativeness. Still, calculating $\mathbf{V}^T\mathbf{N}\left(\mathbf{V},\mathbf{q}\right)\mathbf{V}$ with $\mathbf{V}$ and $\mathbf{q}$ found by computer simulation (or drawn randomly) and requiring the product to be zero within expected numerical precision at least increase the confidence in that we have a implementation free of bugs.

4.4 Linearization of hydrodynamic forces

In this chapter, we have formulated accurate non-linear equations of motion for the hinged 5-body WEC. These equations have the inertia forces on the left hand side, balanced by the external forces on the right hand side. The external forces have several contributions, including the power take-off forces and the hydrodynamic forces. The hydrodynamic radiation and diffraction forces in this work rely on linear hydrodynamic theory, in which the forces are calculated assuming small perturbations around the mean position of the bodies. For the linear hydrodynamic forces, it is therefore not possible to take advantage of the exact kinematics in a consistent manner. We will therefore show how we can linearize the kinematic relationships needed to obtain linear generalized forces from the linear forces and moments of each body.

In this work we use the commercial BEM code WAMIT to calculate the added mass, damping and excitation forces in all 5*6=30 modes of motion. That is, we have available the added mass matrix $\bar{\mathbf{A}}(\omega) \in \mathbb{R}^{30\times 30}$, the radiation damping matrix $\bar{\mathbf{B}}(\omega) \in \mathbb{R}^{30\times 30}$ and the wave-to-excitation force transfer function $\bar{\mathbf{H}}_F(\omega) \in \mathbb{R}^{30}$. We also have the added mass at infinite frequency $\bar{\mathbf{A}}_\infty \in \mathbb{R}^{30\times 30}$. In the time domain, radiation forces are represented by the infinite frequency added mass $\bar{\mathbf{A}}_\infty$ and the retardation function matrix $\bar{\mathbf{K}}(\tau) \in \mathbb{R}^{30\times 30}$,or alternatively, $\bar{\mathbf{A}}_\infty$ and an equivalent state space model $\{\boldsymbol{\mathcal{A}}, \boldsymbol{\mathcal{B}}, \boldsymbol{\mathcal{C}}\}$, as shown in Chapter 3. The excitation forces can be pre-generated using the inverse Fourier transform, $\bar{\mathbf{F}}_{exc}(t) = \mathcal{F}^{-1}\left(\bar{\mathbf{H}}_{exc}(\omega)\,\xi(\omega)\right)$. Some consequences of the assumption of periodicity inherent in discrete Fourier transforms will be discussed in Section 5.3.1 (where we also treat the diffraction and Froude-Krylov components of $\bar{\mathbf{F}}_{exc}$ somewhat different than here).

Using the exact kinematic relationships to obtain generalized equivalents of these forces will have some odd consequences. All forces and matrices will for instance depend on the hinge angles. A more consistent approach is to linearize also the kinematic relationships by assuming small angles. This is the same as keeping only the 0'th order approximation of the transformation matrices. Assuming that $\mathbf{q} = \mathbf{0}$ is a reasonable linearization point, the linearized version of (4.29) becomes:

$$\bar{\mathbf{V}} \approx \mathbf{J}_0\mathbf{V}\,,\ \mathbf{J}_0 = \mathbf{J}(\mathbf{q} = \mathbf{0}) \tag{4.68}$$

We also disregard the Coriolis-centrifugal effect associated with the added mass, since these are quadratic in the velocities. With this linearization, we can obtain the generalized forces and matrices in the frequency domain rather

than in the time domain:

$$\mathbf{A}(\omega) = \mathbf{J}_0^T \bar{\mathbf{A}}(\omega) \mathbf{J}_0, \in \mathbb{R}^{10\times 10} \tag{4.69a}$$
$$\mathbf{A}_\infty = \mathbf{J}_0^T \bar{\mathbf{A}}_\infty \mathbf{J}_0, \in \mathbb{R}^{10\times 10} \tag{4.69b}$$
$$\mathbf{B}(\omega) = \mathbf{J}_0^T \bar{\mathbf{B}}(\omega) \mathbf{J}_0, \in \mathbb{R}^{10\times 10} \tag{4.69c}$$
$$\mathbf{H}_{exc}(\omega) = \mathbf{J}_0^T \bar{\mathbf{H}}_{exc}(\omega), \in \mathbb{R}^{10} \tag{4.69d}$$

and transform these into a time domain representation following the approach described in Chapter 3.

4.5 Non-linear state space representation

The equations of motion, eq. (4.46) (or eq. (4.60)), can be written on a non-linear state space form, tractable for computer simulation:

$$\dot{\mathbf{V}} = \left(\mathbf{M}(\mathbf{q}) + \mathbf{A}_\infty\right)^{-1} \left(\mathbf{F}(\mathbf{V}, \mathbf{q}, t) - \mathbf{C}(\mathbf{V}, \mathbf{q})\mathbf{V} - \boldsymbol{\mathcal{C}}\boldsymbol{\mathcal{X}}\right) \tag{4.70a}$$
$$\dot{\mathbf{q}} = \mathbf{T}(q_4, q_5, q_6)^{-1} \mathbf{V} \tag{4.70b}$$
$$\dot{\boldsymbol{\mathcal{X}}} = \boldsymbol{\mathcal{A}}\boldsymbol{\mathcal{X}} + \boldsymbol{\mathcal{B}}\mathbf{V} \tag{4.70c}$$

We have here redefined $\mathbf{F}$ not to include the radiation forces. The radiation forces are instead given by the expression $-\mathbf{A}_\infty\dot{\mathbf{V}} - \boldsymbol{\mathcal{C}}\boldsymbol{\mathcal{X}}$ where $\boldsymbol{\mathcal{X}} \in \mathbb{R}^{10N}$ is the radiation states and N is the number of common poles in the rational model (recall Chapter 3). We indicate that the remaining generalized force $\mathbf{F}(\mathbf{V}, \mathbf{q}, t)$ generally have a dependence on velocity, displacement and also an explicit dependence on time. The explicit time dependence is due to the incoming waves, causing excitation forces on the system. The dependence on displacement is due to restoring forces from gravity, hydrostatic pressure and the mooring system. The dependence on velocity is typically due to PTO-forces and viscous drag. These forces will be discussed in more detail in Chapter 6. Note that an alternative state space form using generalized momenta and displacements as system states was presented in Section 4.3.2. This form will not be considered any further.

A linear time domain model can be obtained by using the small angle velocity transformation matrix $\mathbf{J}_0 = \mathbf{J}(\mathbf{q} = \mathbf{0})$ in obtaining all generalized forces and matrices. We also linearize the relationship between $\dot{\mathbf{q}}$ and $\mathbf{V}$, yielding simply $\dot{\mathbf{q}} \approx \mathbf{V}$. The linear state space model becomes,

$$\begin{bmatrix} \ddot{\mathbf{q}} \\ \dot{\mathbf{q}} \\ \dot{\boldsymbol{\mathcal{X}}} \end{bmatrix} = \begin{bmatrix} -\mathbf{M}_{0,T}^{-1}\mathbf{B}_u & -\mathbf{M}_{0,T}^{-1}\mathbf{G} & -\mathbf{M}_{0,T}^{-1}\boldsymbol{\mathcal{C}} \\ \mathbf{I} & \mathbf{0} & \mathbf{0} \\ \boldsymbol{\mathcal{B}} & \mathbf{0} & \boldsymbol{\mathcal{A}} \end{bmatrix} \begin{bmatrix} \dot{\mathbf{q}} \\ \mathbf{q} \\ \boldsymbol{\mathcal{X}} \end{bmatrix} + \begin{bmatrix} \mathbf{F}_{exc}(t) \\ \mathbf{0} \\ \mathbf{0} \end{bmatrix} \tag{4.71}$$

where $\mathbf{M}_{0,T} = \mathbf{J}_0^T \bar{\mathbf{M}} \mathbf{J}_0 + \mathbf{A}_\infty$. The matrices $\mathbf{G}$ and $\mathbf{B}_u$ represent linear restoring forces and linear PTO damping, respectively.

4.6 Case study: Effect of inertia nonlinearity on the hinged 5-body WEC

The simulation results presented here aims at highlighting the effect of the inertia force nonlinearities by comparison with a linear model. Therefore, all other force terms are linearized, meaning for instance that we do not include viscous drag. Note that more realistic simulation results will be presented in Chapter 6, along with experimental results. The nonlinear simulation results implement eqs. (4.70) with,

$$\mathbf{F}(\mathbf{V}, \mathbf{q}, t) = \mathbf{F}_{exc}(t) - \mathbf{B}_u \mathbf{V} - \mathbf{G}\mathbf{q} \tag{4.72}$$

where $\mathbf{F}_{exc}$ is the linear wave excitation forces, $\mathbf{B}_u$ is the diagonal PTO damping matrix and $\mathbf{G}$ is the hydrostatic restoring matrix. The non-zero diagonal entries in the PTO damping matrix is $B_{u,jj} = b_u$, $j = 7..10$ with $b_u = 12777$ [kNm/(rad/s)]. This is somewhat above the value that maximizes the power absorption. The nonlinearity is due to the time varying mass matrix, the Coriolis-centrifugal forces and the transformation $\dot{\mathbf{q}} = \mathbf{T}(q_4, q_5, q_6)^{-1} \mathbf{V}$. The linear simulation results implement eq. (4.71). Because we linearize the hydrodynamic forces in both the linear and nonlinear simulations (see section 4.4), the infinite frequency added mass matrix will be time invariant and does not contribute to the Coriolis-centrifugal forces.

We will consider a sea-state with intermediate severity, believed to be of importance for the annual mean power production of the WEC. Long-crested waves are assumed and the propagation direction is in the negative x direction such that buoy 1 meets the waves first. The significant wave height is 3.1 meters and the spectrum peak period is 7.1 seconds. The wave spectrum is of the JONSWAP type with the γ parameter chosen as 3.15 (see Section 2.1). We will also consider a regular wave. The geometry and dimensions of the WEC is shown in Figure 2.8.

Table 4.1 shows the power in kilowatts absorbed by PTO damping in the four hinges and the corresponding standard deviation of the hinge rotations, based on a three hour realization of the irregular sea state. It is seen that the power prediction by the linear model is almost identical to the non-linear prediction. It is also seen that hinge 1, which belongs to the up-wave buoy, contributes about 75% of the total power absorption.

Figure 4.3 shows the power spectra of collective pitch velocity V_5 and angular velocity in hinge 1, V_7. The spectra are calculated with the discrete Fourier

Table 4.1: Mean absorbed power and standard deviation of hinge rotation with and without inertia force nonlinearities. Irregular waves with a JONSWAP spectrum with $H_s = 3.1$ [m] and $T_p = 7.1$ [s] are used.

	H-1	H-2	H-3	H-4	Total
p_m [kW] , nonlinear	373.3	35.3	59.4	35.3	503.4
p_m [kW] , linear	373.0	35.3	60.0	35.3	503.7
STD(q_j) [deg] , nonlinear	10.5	3.2	4.4	3.2	
STD(q_j) [deg] , linear	10.5	3.2	4.2	3.2	

transform (using FFT) of the steady state portion of the measured time series using a single rectangular window function. Spectral smoothing is applied using a Gaussian (bell) function of width $2\delta = 0.05$ rad/s and "standard deviation" $\sigma = \delta/3$ as the averaging function (Stansberg, 1997). This means that the smoothed spectrum is calculated from the raw spectrum as:

$$S_{smooth}(\omega) = \frac{\int_{-\delta}^{\delta} S_{raw}(\omega - \bar{\omega}) \exp\left(\frac{-\bar{\omega}^2}{2\sigma^2}\right) d\bar{\omega}}{\int_{-\delta}^{\delta} \exp\left(\frac{-\bar{\omega}^2}{2\sigma^2}\right) d\bar{\omega}} \tag{4.73}$$

The collective pitch is a mode of motion which intuitively should be affected by the non-linearity, since the inertia associated with this mode will depend on the hinge angles. In the spectrum, the nonlinearity is shown to contribute to wave frequency peak and the high frequency end of the spectrum. Obviously, this high frequency component will be higher in the corresponding acceleration spectrum and smaller in the displacement spectrum.

Since the Coriolis-centrifugal forces are quadratic and bi-linear forces proportional to $V_i V_j$, one should expect that they affect the larger amplitudes more than the integrated quantities, such as the mean power absorption. This is confirmed by Figure 4.4, which shows the cumulative distribution of maxima and minima of collective pitch angle q_5 and rotation in hinge 1, q_7. Maxima and minima are here defined as the maximum and minimum response between subsequent up-crossings of the mean level. The y-axis is scaled such that the data-points will form a straight line if the maxima and minima happen to be Rayleigh distributed, as is the case if the process is Gaussian and narrow-banded (Naess and Moan, 2012). It is seen that the largest excursions are larger in the non-linear model, at least for the collective pitch. It should be mentioned here that the largest observed values should only be regarded as indicative as they are considerably influenced by randomness. The three-hour realization of the wave spectrum is generated as a sum of cosines with random, evenly distributed phases and deterministic amplitudes (determined by the wave spectrum). Hence, to obtain a good estimate of the extreme values, more realizations are generally required. However, the trend that the

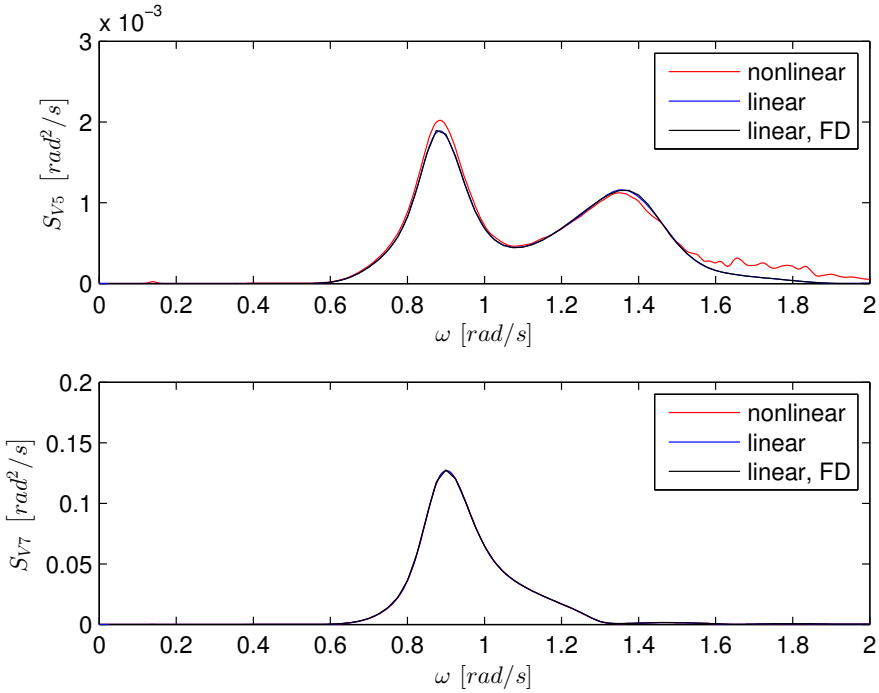

Figure 4.3: Power specter of collective pitch velocity (top) and hinge-1 velocity (bottom). Linear results are obtained both by time and frequency domain methods. The spectra obtained in the time domain have been smoothed using eq. (4.73) with $2\delta = 0.05$ rad/s and $\sigma = \delta/3$.

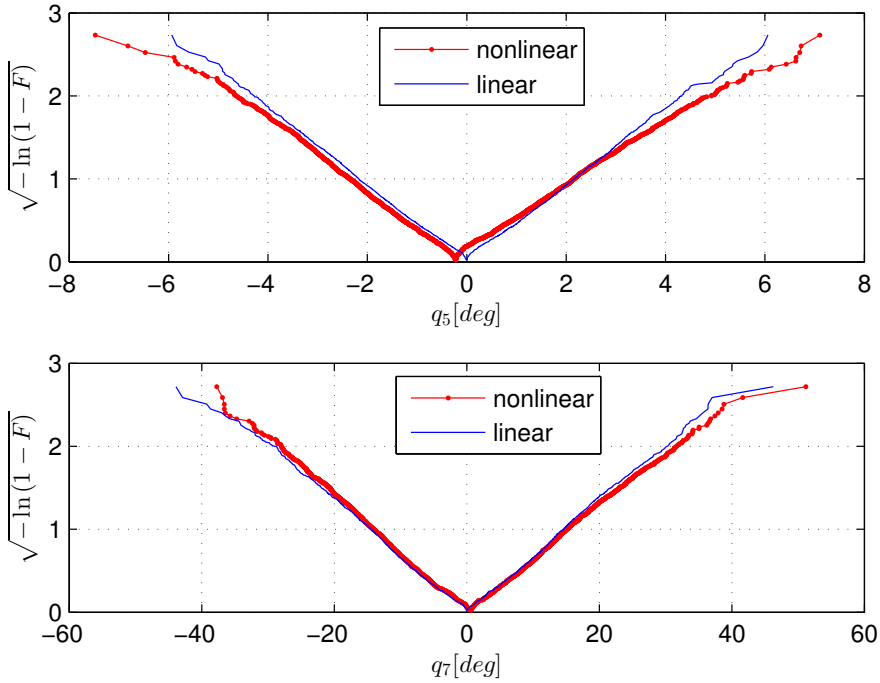

Figure 4.4: Cumulative distribution of maxima and minima of $q_5(t)$ and $q_7(t)$ plotted on Rayleigh-scale

non-linear model gives larger extrema is seen to repeat for new realizations, although this is not shown here.

Figure 4.5 shows a steady-state portion of the time series of collective pitch angle, along with the absolute value of its discrete Fourier transform, when the WEC is exposed to a regular wave of height of 4.1 meter and a period of 9 seconds. The Fourier transform shows that the energy is concentrated at frequencies which are multiples of the wave frequency ω_w, where only the $0 \cdot \omega_w$, $1 \cdot \omega_w$ and $2 \cdot \omega_w$ components have significant energy. The largest hinge response in this regular wave is for hinge 1, on the up-wave side, and shows steady state amplitudes of about 20 degrees.

The overall conclusion is that a linearized model is sufficient to estimate the power production of the WEC, whereas the inertia force nonlinearities can have some importance for the collective pitch mode. Since the nonlinearities are associated with high frequency motions, accelerations on-board the center floater are especially affected by this feature. With regard to the discrepancies

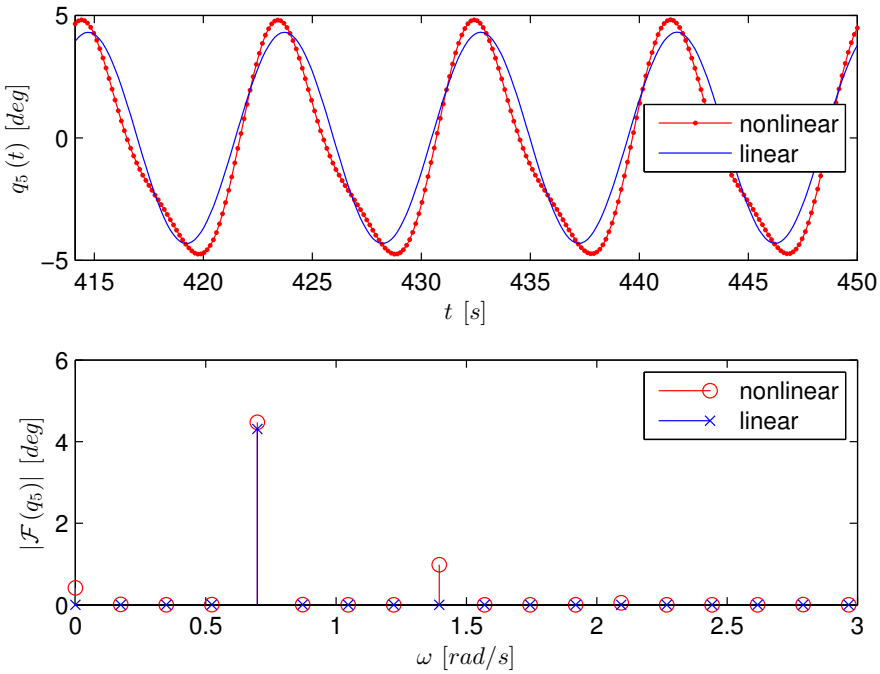

Figure 4.5: Pitch displacement time series (top) and absolute value of its discrete Fourier transform (bottom) in a regular wave, H=4.1 m, T=9 s.

shown in Chapter 6 between the experimental and numerical results of this WEC, it is fair to say that other non-linear effects associated with hydrodynamic and restoring forces are more important.

5 Non-linear restoring and Froude-Krylov forces

5.1 Introduction

The goal of a wave energy developer generally is to minimize the cost of the delivered power. This is a difficult measure to work with, and in an early design stage one typically work with simplified cost indicators. Babarit et al. (2012) suggest four such cost indicators: 1) Annual absorbed energy (AAE) 2) AAE per characteristic mass 3) AAE per characteristic surface area. 4) AAE per unit of characteristic PTO force. The power absorption, belonging to the income side of the cost indicators, is related to the WECs ability to generate waves that interfere destructively with the incoming waves (Falnes, 2002). A small body would have to move with larger motion amplitudes than a larger (similar) body in order to generate waves of the same amplitude. Thus, if cost indicator number 2) and 3) are relevant, the optimal would typically be a quite small device having a characteristic length small compared to its motion amplitudes and the length and height of the incoming waves. The device also have to move out of phase with the ambient water particles in order to displace water and generate waves, giving a greatly varying wetted area. In such a situation the validity of linear hydrodynamic theory, where the water pressure is integrated over the mean wetted area of the body, can be questioned. On the other hand, it is hard to find alternatives (e.g. CFD) that are computationally fast enough for the parameter variations that are required in an early design stage.

For these reasons we will here explore an approach where the undisturbed hydrostatic and dynamic pressure is integrated over a time varying wetted surface, taken as the surface underneath the undisturbed incoming waves. This pressure integration results in nonlinear hydrostatic and Froude-Krylov forces, while we still rely on linear diffraction and radiation forces calculated with industry standard computer codes, in our case by using WAMIT. This is a simplified approach which is believed to give accurate results in cases where the Froude-Krylov component of the excitation forces are large compared to the diffraction component, and where the body surface portion below the undisturbed waves is not too far from the true wetted surface.

The accuracy of the method is largely related to the relative importance of the Froude-Krylov forces in comparison to the diffraction forces. We know that the diffraction forces, which we linearize, go to zero in the low frequency limit and therefore expect good results in waves that are much longer than the size of the device. Figure 5.1 shows the Froude-Krylov and diffraction parts of the excitation (generalized) forces on the hinged 5-body WEC, represented by the modulus of the wave-to-force transfer function. Note here that the Froude-Krylov component is linearized. An important difference between $|H_{F7}|$ (hinge 1, up-wave buoy) and $|H_{F9}|$ (hinge 2, down-wave buoy) is seen. In short waves, the down-wave buoy is sheltered by the center floater, which appears as a near cancellation of the Froude-Krylov forces by the diffraction forces. It is also worth noting that the magnitude of the Froude-Krylov forces on the two hinges are identical.

It perhaps seems like a contradiction to assume small disturbance from a floating body that need to disturb the waves in order to fulfill its purpose (absorb power). The success of the method is related to the fact that we consider devices that maximize the power absorption per unit displacement (or surface area) and not the power absorption itself. Thus, the small sized body disturbs the waves the most at frequencies significantly higher than the peak frequency of the incoming waves, meaning that the total wave field consists of radiated and diffracted waves of relatively low amplitude and length riding on top of the longer and higher undisturbed waves. This situation is observed in the photograph in Figure 6.2, where the waves propagate from left to right and the leftmost body, having the largest motion amplitudes, generate noticeable circular waves of shorter length and amplitude than the incoming waves.

The current modeling assumption is not new. Babarit et al. (2009) showed that this type of model was able to predict the parametric roll instability of the SEAREV WEC. Gilloteaux et al. (2008) used a similar model to perform non-linear regular wave simulations of the WAVEBOB WEC. Their model also included nonlinearities resulting from the quadratic pressure term in Bernoulli's equation and some second order terms from a Taylor expansion of the radiation-diffraction potential around the mean wetted body surface. However, the study concludes that the hydrostatic and Froude-Krylov forces are dominating, and that the quadratic pressure terms were insignificant. A very similar paper by Merigaud et al. (2012) considered a heaving spherical WEC with a diameter of 2 meters exposed to regular waves of 6 s period and wave amplitudes in the range 0.8-2.0 meters. Here it was shown that the effect of nonlinear hydrostatic and Froude-Krylov forces were important and that the linearized model gave more than twice as large power absorption than the nonlinear model for wave amplitudes larger than 1.4 meters. The latter paper also concluded that the contributions from the quadratic pressure term and the nonlinear correction

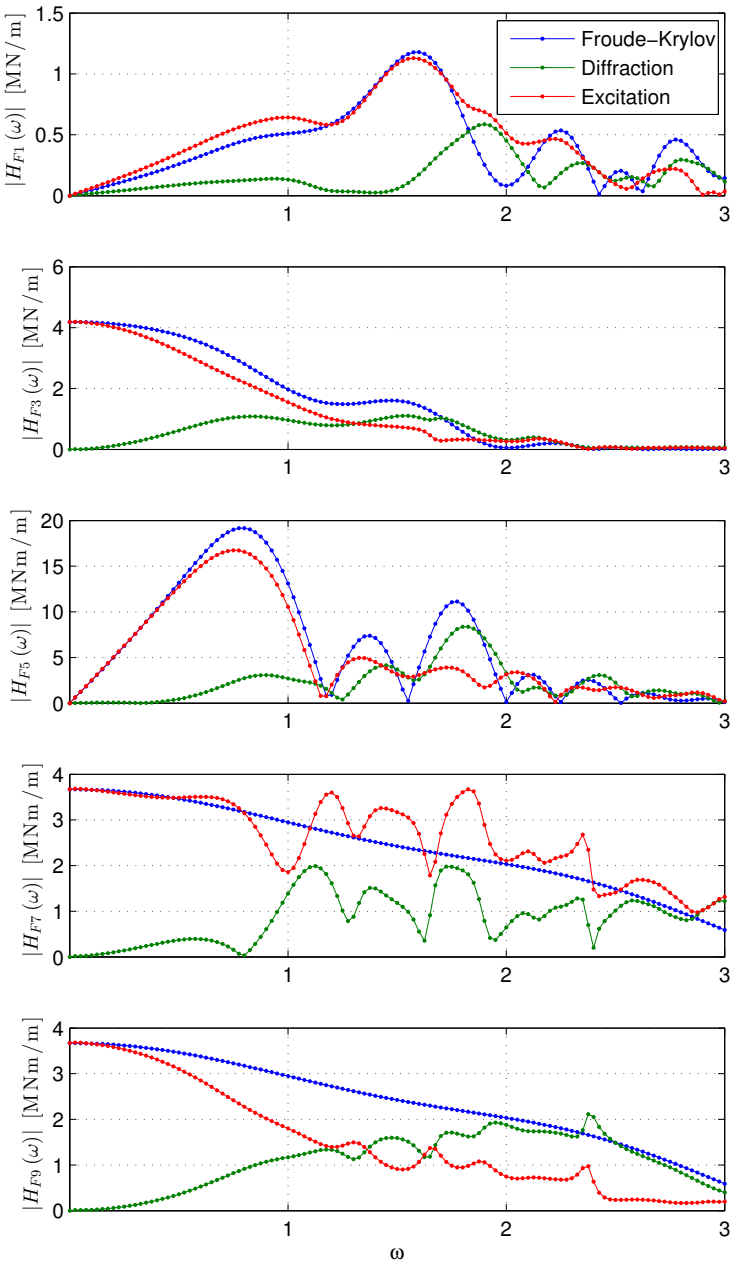

Figure 5.1: Linear excitation (generalized) forces and their diffraction and Froude-Krylov components for the hinged 5-body WEC. The curves show the modulus of the wave elevation to force transfer function in collective surge (F_1), heave(F_3) and pitch (F_5) and for the up-wave hinge (F_7) and the down-wave hinge (F_9).

to the diffraction-radiation forces were small in comparison and did not justify the large increase (factor of 10) in simulation time.

Among the three mentioned references, only the paper by Babarit et al. (2009) included comparison with experimental data. In Chapter 6, we will therefore present comparisons between experiments and a numerical model for the hinged 5-body WEC in typical operating conditions, with emphasis on the effect of including non-linear restoring and Froude-Krylov forces. The experimental data have previously been presented by Rogne et al. (2012), which included comparison with a numerical model. The large discrepancies between simulations and experiments presented in that paper motivated the development of the more advanced numerical model presented here. The present chapter deals with the mathematical formulation and numerical implementation. Here, the treatment we will be largely device independent, except that we restrict ourselves to WECs consisting of one or more rigid bodies.

5.2 Mathematical formulation

In Chapter 4 we developed equations of motions for the hinged 5-body WEC. Here, little was said about the generalized external forces $\mathbf{F}$. These forces can be decomposed as,

$$\mathbf{F} = \overbrace{\mathbf{F}_{HS} + \underbrace{\mathbf{F}_{FK} + \mathbf{F}_{D}}_{\mathbf{F}_{exc}}}^{\mathbf{F}_{HSFK}} + \mathbf{F}_{R} + \mathbf{F}_{other} \tag{5.1}$$

where,

- $\mathbf{F}_{HS}$ is restoring forces due to hydrostatic pressure and the body weight. Linearized, we have $\mathbf{F}_{HS} = -\mathbf{G}_{HS}\mathbf{q}$ where $\mathbf{G}_{HS}$ is the hydrostatic restoring matrix.
- $\mathbf{F}_{FK}$ is the Froude-Krylov force, due to the dynamic pressure under the undisturbed wave.
- $\mathbf{F}_{D}$ is the linear diffraction force.
- $\mathbf{F}_{R}$ is the wave radiation forces.

In linear analysis, it is relevant to treat $\mathbf{F}_{exc}(t) = \mathbf{F}_{FK}(t) + \mathbf{F}_{D}(t)$ as an excitation force since both contributions only have an explicit time dependence. On the other hand, when the undisturbed pressure is integrated over the instantaneous wetted body surface, $\mathbf{F}_{FK}$ will also depend on the position and orientation of the bodies. The hydrostatic pressure force will also depend on the incoming waves since we integrate the hydrostatic component to the

undisturbed free surface. Then it is more relevant to combine $\mathbf{F}_{HS}$ and $\mathbf{F}_{FK}$ and write $\mathbf{F}_{HSFK}(\mathbf{q},t) = \mathbf{F}_{HS}(\mathbf{q},t) + \mathbf{F}_{FK}(\mathbf{q},t)$.

A nonlinear model as the one considered here requires time domain analysis. This enables use of nonlinear wave theories in the evaluation of undisturbed pressure. This is not considered further herein. Instead, we use linear (Airy) wave theory and assume constant (no depth variation) dynamic pressure above the mean water level. To simplify further, we neglect the quadratic velocity term in Bernoulli's equation. The latter assumption is very accurate, considering that the time varying part of the quadratic term is very small for typical ocean waves and in fact zero for deep water waves (because $\cos^2(\omega t) + \sin^2(\omega t) = 1$). The undisturbed pressure (taken relative to the atmospheric pressure) can then be written as:

$$p_u = -\rho g z - \rho \frac{\partial \phi_0}{\partial t} \tag{5.2a}$$

$$\frac{\partial \phi_0}{\partial t} = -g \sum_{i=1}^{n} \Re \left[\zeta(\omega_i) \Delta\omega \frac{\cosh(k_i z' + k_i h)}{\cosh(k_i h)} \exp(-j k_i x) \exp(j \omega_i t) \right] \tag{5.2b}$$

$$z' = \min(0, z) \tag{5.2c}$$

Here, $\zeta(\omega_i)$ is the Fourier transform of the surface elevation in $x = 0$, sampled at frequencies $\omega_i = i\Delta\omega$, $i = 1..n$. Figure 5.2 illustrates the surface elevation and pressure based on this simple model. It is seen that the isobar for zero pressure coincides with the surface elevation above the mean water level (MVL) whereas the pressure in the surface below MVL is somewhat too high. A similar illustration and discussion for regular waves is provided by Faltinsen (1990, p. 20).

The six force components for each body in body fixed frames are found by integrating the undisturbed pressure over the wetted surface and including the weight of the bodies:

$$\bar{\mathbf{F}}^{(i)}_{HSFK,i} = \oiint_{S_i(t)} p_u(\mathbf{r}_{s"}) \begin{bmatrix} \mathbf{n}_s^{(i)} \\ \mathbf{r}_s^{(i)} \times \mathbf{n}_s^{(i)} \end{bmatrix} ds - m_i g \begin{bmatrix} \mathbf{k}^{(i)} \\ \mathbf{r}_{CG,i}^{(i)} \times \mathbf{k}^{(i)} \end{bmatrix} \tag{5.3}$$

Here, the first term represents the pressure force and the second term represents the weight acting in CG. $\mathbf{r}_s$ and $\mathbf{n}_s$ represent a point on the wetted surface and the unit length inward surface normal in the same point. $\mathbf{r}_{CG,i}$ and $\mathbf{k}$ represent the center of gravity of body i and the upward unit vector. Recall from Section 4.2 that a superscript (i) on a Cartesian vector signifies that the vector is decomposed in the body fixed frame. Hence, $\mathbf{k} = \begin{bmatrix} 0 & 0 & 1 \end{bmatrix}^T$ whereas $\mathbf{k}^{(i)}$ will change with time and have generally 3 nonzero elements. Moreover, $\mathbf{r}_s^{(i)}$

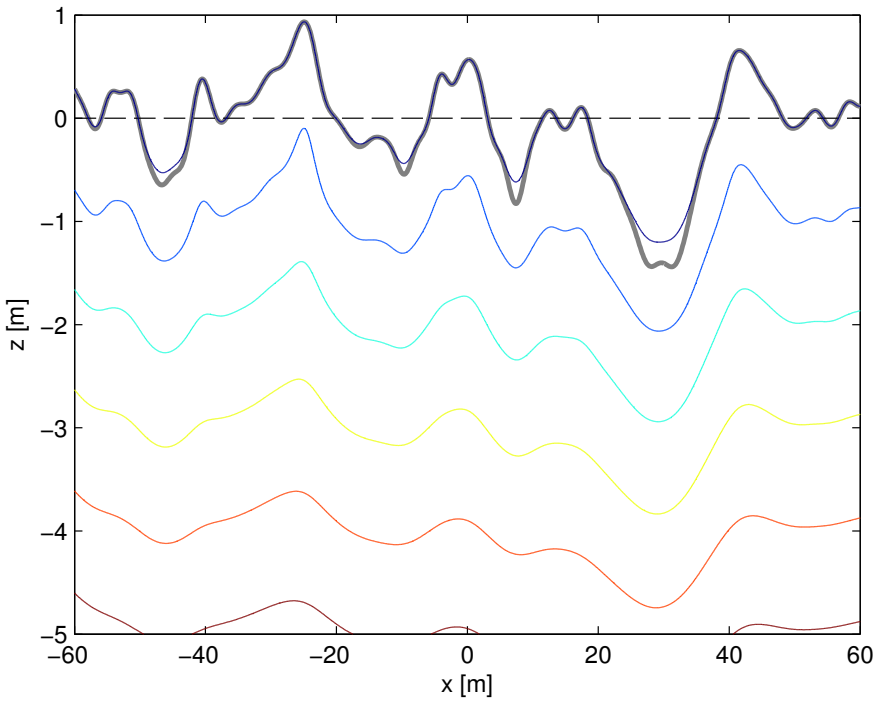

Figure 5.2: Spacial plot of wave elevation and isobars of static+dynamic wave pressure in a sea state with $H_S = 3.1$ m and $T_P = 7.1$ s at a random time instant. The thick gray line shows the linear wave elevation, whereas the colored lines show the isobars for $p_u/\rho g = 0, 1, \ldots, 5$, calculated using eq. 5.2.

and $\mathbf{n}_s^{(i)}$ will be time invariant, whereas $\mathbf{r}_s$ and $\mathbf{n}_s$ will change with the motion of body i, containing the point s. The pressure integration is taken over the wetted surface S_i which will change with time and be a function of both the undisturbed wave and the body displacements.

For n-body systems with less than $6n$ degrees of freedom, the generalized force becomes (ref. Section 4.3.1):

$$\mathbf{F}_{HSFK} = \mathbf{J}\left(\mathbf{q}\right)^T \begin{bmatrix} \bar{\mathbf{F}}_{HSFK,1}^{(1)} \\ \vdots \\ \bar{\mathbf{F}}_{HSFK,n}^{(n)} \end{bmatrix} \tag{5.4}$$

Accurate large-angle expressions is used both in the relation between $\mathbf{k}$ and $\mathbf{k}^{(i)}$and in the formulation of the kinematic transformation matrix $\mathbf{J}\left(\mathbf{q}\right)$, contributing to the nonlinearity together with the time varying wetted surfaces S_i.

In eq. (5.3), we evaluate the pressure in a point $\mathbf{r}_{s''}$, defined as,

$$\mathbf{r}_{s''} = \begin{bmatrix} (x_s - x_{CG,1}) & (y_s - y_{CG,1}) & z_s \end{bmatrix}^T \tag{5.5}$$

rather than in $\mathbf{r}_s$. That is, we subtract the horizontal position of the center of gravity of body 1, for all points on all bodies. This choice is a pragmatic one and is made to try to resolve the incompatibility in phasing between the undisturbed pressure forces and the diffraction forces when the system of bodies undergoes large horizontal excursions. Since the linear diffraction forces are evaluated in the equilibrium position of the bodies, the phase of these forces will be 90 degree wrong when the system of bodies is offset a quarter wavelength, for instance. With the approach adopted herein, the phase of both the undisturbed pressure force and the diffraction force will be "wrong" with respect to the waves, but consistent with each other. That the two phases are consistent is very important since we otherwise can have an erroneous cancellation or magnification of the total force. It should be mentioned that the effect of such a phase correction is relatively minor in the numerical examples presented here. This is because the horizontal motion amplitude is small compared to the length of the wave components with significant energy. Still, it is important to judge the importance of this type of incompatibility between linear and nonlinear force terms in new applications of the method.

5.3 Numerical implementation

The surface integral of eq. (5.3) is evaluated by discretisation of the body geometry into flat triangular panels and assuming a linearly varying pressure

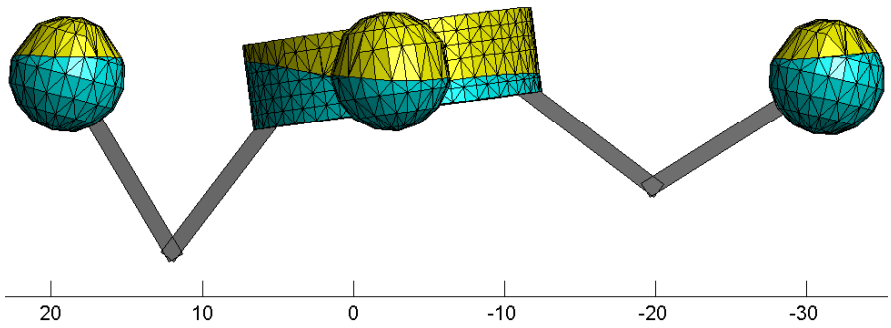

Figure 5.3: Discretisation of the wetted surface, shown in light blue color.

over each panel. An efficient and robust geometry processing routine has been developed that identifies the submerged panels and modifies partly submerged panels by translating their "dry" nodes to the free surface in each time step. The translation of dry nodes to the free surface always takes place along a panel edge towards a neighboring wet node to preserve the original geometry and avoid flipping the surface normal. By using nodes that is shared between neighboring panels, we are assured that no "holes" will be made in the body surface as a consequence of the node translation.

The accurate capturing of the wetted surface in each time step assures that the pressure force becomes a continuous function of time. This is a requirement when using high order time integrators that rely on the states (i.e. body velocities) to have a continuous time derivative. Figure 5.3 illustrates the discretisation of the body geometry and the capturing of the wetted surface.

The slender elements of the hinged 5-body WEC (shown in gray in Figure 5.3), are assumed not to contribute diffraction, Froude-Krylov and radiation forces. Still, the buoyancy of these elements will have a small effect on the stability of the bodies. This effect is included by using an equivalent mass and center of gravity in eq. (5.3). The equivalent mass will be somewhat lower than the actual mass. Since the slender elements will lower the center of buoyancy, the equivalent center of gravity will have a slightly higher vertical component than the actual center of gravity. This approach is justified as long as the slender elements never leave the water.

5.3.1 Pre-generated time series of pressures and diffraction forces

The direct summation of the large number of harmonic components in eq. (5.2b) for all time steps and body points will be very time consuming. A more efficient approach is to use pre-generated time series of pressures, employing the inverse fast Fourier transform (IFFT). The IFFT have to be taken in a fixed point in space. In order to "follow" the instantaneous position of the wetted surface in time, it is therefore necessary to generate pressure time series in a number of spatial points forming a grid, and to interpolate in the grid to find the pressures on the instantaneous body surface. In long crested waves, it is sufficient to consider spatial points in the $x-z$ plane. In that case, a 3-dimensional lookup table of pressures p_{ijk} for discrete values x_i, z_j and t_k is required. The numerical results presented here only refer to long crested waves and the use of tri-linear interpolation on the look-up table to calculate the pressure on the body surface. Yet it is described in the following how the pressure can be evaluated efficiently in the case of short crested waves as well. The straightforward solution is to use a 4-dimensional lookup table extending also in the y direction. This would however require a large amount of computer memory. Because a reasonable short-crested surface elevation can be represented with a relatively small number of wave headings, it is better to use a 3-dimensional lookup table for each heading in this case, taking x as a local coordinate aligned with the wave headings.

The time domain diffraction forces for long crested waves are given by,

$$\mathbf{F}_D(t) = \sum_{i=1}^{n} \Re\left[\mathbf{H}_{F_D}(\omega_i)\,\xi(\omega_i)\,\Delta\omega \exp(j\omega_i t)\right] \tag{5.6}$$

analogous to the calculation of pressure, eq. (5.2b). Section 6.6 contains comparisons with model test results where the Fourier transform of the wave, $\zeta(\omega)$, is obtained by using the fast Fourier transform (FFT) algorithm on the measured time series of the undisturbed wave (measured without the WEC present in the towing tank). Strictly speaking, eq. (5.2) and eq. (5.6) express the pressure and diffraction force corresponding to a *periodic* irregular wave repeating itself with a period of $T = T_{dur} + \Delta t = 2\pi/\Delta\omega$, with T_{dur} representing the duration of the measurement and Δt and $\Delta\omega$ being time and frequency resolutions. Because the measured wave does not normally exhibit a periodic behavior, the time series of pressure and diffraction force will be contaminated in the beginning and in the end. This contamination is both due to so-called spectral leakage and because the impulse response functions associated with the transfer functions have a memory of the past and influence from the future. The latter effect occurs because the pressure and diffraction

forces are a-causal responses, at least when evaluated in a point up-wave of the probe measuring the wave (see discussion by Falnes (2002), for instance). A non-physical consequence of this is that the calculated pressure in the beginning of the time series will have a memory of the wave measured in the end of the time series. As a consequence of the a-causality, the calculated pressure in the end of the time series will also be influenced by the wave measured in the beginning of the time series. A more correct approach for non-periodic waves is to convolve the measured wave elevation with the impulse response function associated with the wave-to-pressure transfer function. However, since we use measurements of rather long duration, the FFT-IFFT approach is accurate provided that we exclude the beginning and end of the time series from the statistical post-processing. Omitting the convolution will also reduce the time it takes to pre-generate the large 3D lookup table of pressures significantly.

One important aspect of Fourier analysis of sampled time series is the presence of aliasing. A consequence of aliasing is that the Fourier transform of the wave elevation, $\zeta(\omega)$, only contains meaningful information for frequencies lower than the Nyquist frequency $\omega_N = \omega_S/2$, where ω_S is the sampling frequency of the wave measurement. FFT algorithms normally result in Fourier transforms with information up to ω_S, where the information above ω_N is redundant. In fact, $\Re[\zeta(\omega)]$ will be symmetric about ω_N, whereas $\Im[\zeta(\omega)]$ will be anti-symmetric about ω_N. Care must then be taken when $\zeta(\omega)$ is to be multiplied with a transfer function. For $y(t) = \mathrm{IFFT}(H(\omega)\zeta(\omega))$ to return a meaningful result, $\zeta(\omega_i)$ should be replaced with 0's for frequencies above ω_N, and only the real part of $y(t)$ should be interpreted as the time domain counterpart of $Y(\omega)$. It should also be mentioned that the Fourier transform returned by FFT algorithms normally has a slightly different definition than the one used here, so that a scaling normally applies. Here, we define $\zeta(\omega_i)$ such that the surface elevation can be written as $\xi(t) = \sum_{i=1}^{n} |\xi(i\Delta\omega)| \Delta\omega \cos(i\Delta\omega t + \arg(\xi(i\Delta\omega)))$ with $i\Delta\omega \leq \omega_N$. That is, we interpret $|\xi(i\Delta\omega)| \Delta\omega$ as the amplitude of the regular wave component number i, and only take the summation over frequencies lower than (or equal to) the Nyquist frequency.

6 Comparison between simulations and experimental results

This chapter deals with the experimental results for the hinged 5-body WEC, and a comparison with the results from two different numerical models, one including non-linear Froude-Krylov and restoring forces, and one more traditional model that linearize these force terms. The model tests were carried out in a towing tank at the Marine Technology Center in Trondheim with dimensions L x B x D = 40m x 6.45m x 1.5m. A model scale of 1:30 was employed in the tests. The experimental data have previously been presented by Rogne et al. (2012).

6.1 Experimental setup

Four two-way pneumatic cylinders were chosen to represent the power take-off in the scale model, as shown in Figure 6.1. The pneumatic cylinders dissipate energy by friction and by forcing an air flow through two nozzles, one in each end. The level of damping was tuned by using nozzles with different inlet diameter, and by using two different cylinder configurations having different lever arms. Figure 6.1 shows the cylinder configuration used in the tests with ID<110. All other tests used a configuration shown in Figure 6.2, which mounted the cylinders between the lower bearing on the buoy beams and the lower bearing of the center floater mast.

The axial force in the cylinders were measured by a force transducer mounted in the connection between the cylinder and the center platform. The instantaneous length of the cylinders were measured by a spring with stiffness coefficient small enough not to affect the dynamics of the system significantly.

In addition to measuring the force and time varying length of the cylinders, sufficient to estimate the power absorption, the position and orientation of the central platform was measured in 6 DOFs by an optical positioning system using four position markers on the top of the center mast (see Figure 6.2). A mooring system with four horizontal mooring lines mounted to the side walls of the basin was used, designed to be soft enough not to magnify any wave frequency motions, and to have an essentially linear behavior over the operating range of displacements. The resulting natural period in surge of the

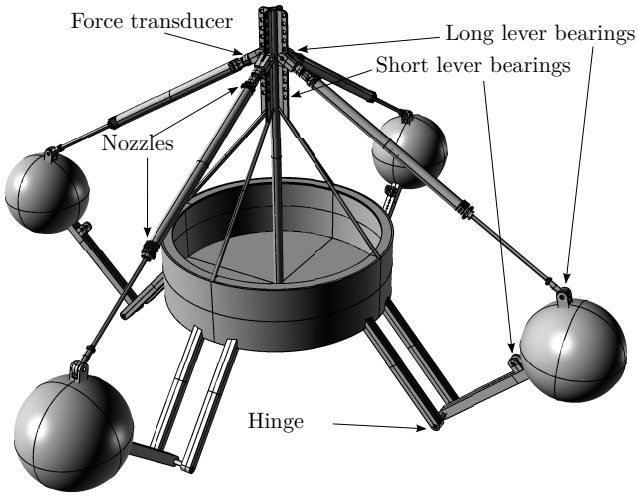

Figure 6.1: As-built CAD drawing of the scale model WEC with pneumatic cylinders mounted in a long lever arm configuration

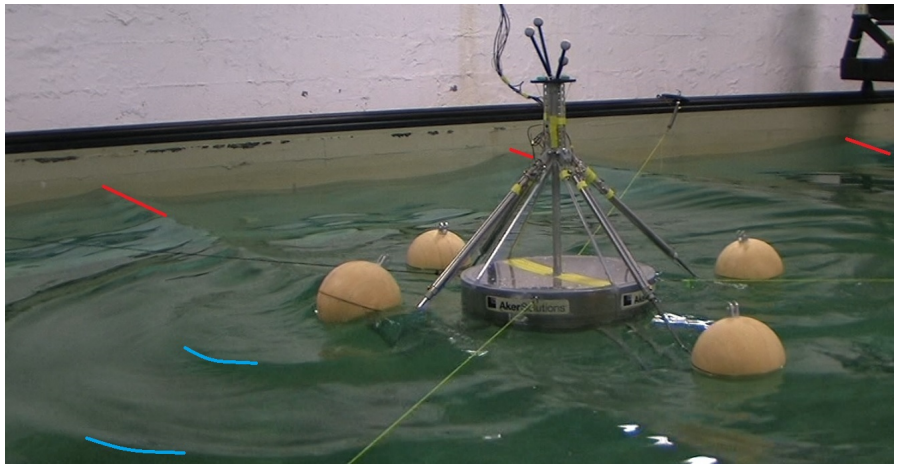

Figure 6.2: Photograph taken during test run 112, showing the WEC with pneumatic cylinders mounted in a short lever arm configuration. The incoming waves propagate from left to right. Based on visual inspection, red lines are drawn on the crests of the incoming waves whereas blue lines are drawn on the crests of the radiation+diffraction component.

Table 6.1: Full scale sea state parameters. T_p is the peak period, T_z is the zero-upcrossing period, H_s is the significant wave height, $2\pi H_s/\left(gT_z^2\right)$ is a steepness measure, γ is the peakedness parameter in the applied JONSWAP spectra and p_w is the mean energy transport per meter wave front. A single realization of each spectrum is generated. The portion of the wave record assumed to produce steady state response has a full scale duration of ≈ 78 minutes.

ID	T_p [s]	T_z [s]	H_s [m]	$\frac{2\pi}{g}\frac{H_s}{T_z^2}$	γ	p_w [kW/m]
1	7.7	5.5	1.6	1/30	1.00	8.4
2	9.3	6.6	2.2	1/30	1.00	20.3
3	10.8	7.7	3.1	1/30	1.00	46.1
4	5.6	4.4	2.0	1/15	3.15	9.8
5	7.1	5.5	3.1	1/15	3.15	30.4

collection of bodies was 45 seconds in full scale. The moorings also induce a weak coupling between surge and pitch that is represented in the numerical model. However, this coupling does not have any important consequences for the response.

The irregular sea states used in the tests are summarized in Table 6.1. Only a single realization from each wave spectrum was generated and repeated with different PTO characteristics. Table 6.2 summarize all test runs showing the variation of the PTO parameters. The selection of sea states was subject to numerous constraints. Wave height and length was limited by the available stroke length and velocity of the wavemaker. Moreover, small sea states with small hinge excitation caused stiction (static friction) in the pneumatic cylinders to become a dominating effect, making it difficult to study the other, more interesting nonlinear effects. For this reason, some smaller sea states are not included. For the long lever arm configuration, resulting in the largest stiction effects, only the sea state resulting in the largest hinge excitation is included.

6.2 Scaling of results

Full scale equivalent results (1:30 scale) will be presented unless stated otherwise. Since inertial and gravitational forces are dominating, Froude's scaling law will be used. There are two effects of some importance that does not follow Froude's scaling law; 1) the characteristics of the pneumatic cylinders used as PTO system (in particular friction and air compressibility), and 2) the viscous forces on the bodies.

We are not concerned with scaling issues regarding the pneumatic cylinders, simply because pneumatic cylinders are not relevant technology in full scale. The linear model we use to represent the PTO system in the simulations is

Table 6.2: Description of test runs. Corresponding sea state parameters are given in Table 6.1. $D_{nozz,CF}$ is the model scale nozzle diameter used in the center floater end of all cylinders. $D_{nozz,buoy}$ is the corresponding nozzle diameter in the buoy end. $L_{\perp}(0)$ is the lever arm (model scale) evaluated at zero hinge angle.

ID	Sea state	$D_{nozz,CF}$ [mm]	$D_{nozz,buoy}$ [mm]	$L_{\perp}(q=0)$ [mm]
92	5	2.0	2.0	510
93	5	2.0	2.0	510
110	5	1.6	1.6	280
111	5	1.6	1.2	280
112	5	1.2	1.2	280
113	4	1.2	1.2	280
114	1	1.2	1.2	280
115	2	1.2	1.2	280
116	3	1.2	1.2	280
117	1	1.6	1.2	280
118	2	1.6	1.2	280
119	3	1.6	1.2	280
120	4	1.6	1.2	280

highly idealized, and does not attempt to include those non-scalable effects. As such, we are more concerned with the applicability of the linear model, and this will be investigated in Section 6.3.

There is always an uncertainty associated with scaling when the scale-model is governed by viscous forces in addition to the inertial and gravitational ones. Still, it is generally accepted that Froude's scaling law can be applied when the viscous forces are caused by vortex shedding around sharp corners (see e.g. DNV, 2007, chapter 10), and especially if those viscous forces are of secondary importance. The estimation of drag coefficients for use in the simulation model will be discussed in Section 6.5.3. This estimation is based on the model tests and does not attempt to account for scaling effects.

6.3 Measured and idealized power take-off (PTO) characteristics

A linear PTO model was applied in the simulations. The dominant neglected nonlinear effect is the occurrence of stiction. This is clearly observed in Figure 6.3, illustrating the measured PTO characteristics (in the form of a probability distribution) and fitted linear model for test run 92, 112 and 114. Stiction is here observed as a large probability of having close to zero velocity in combi-

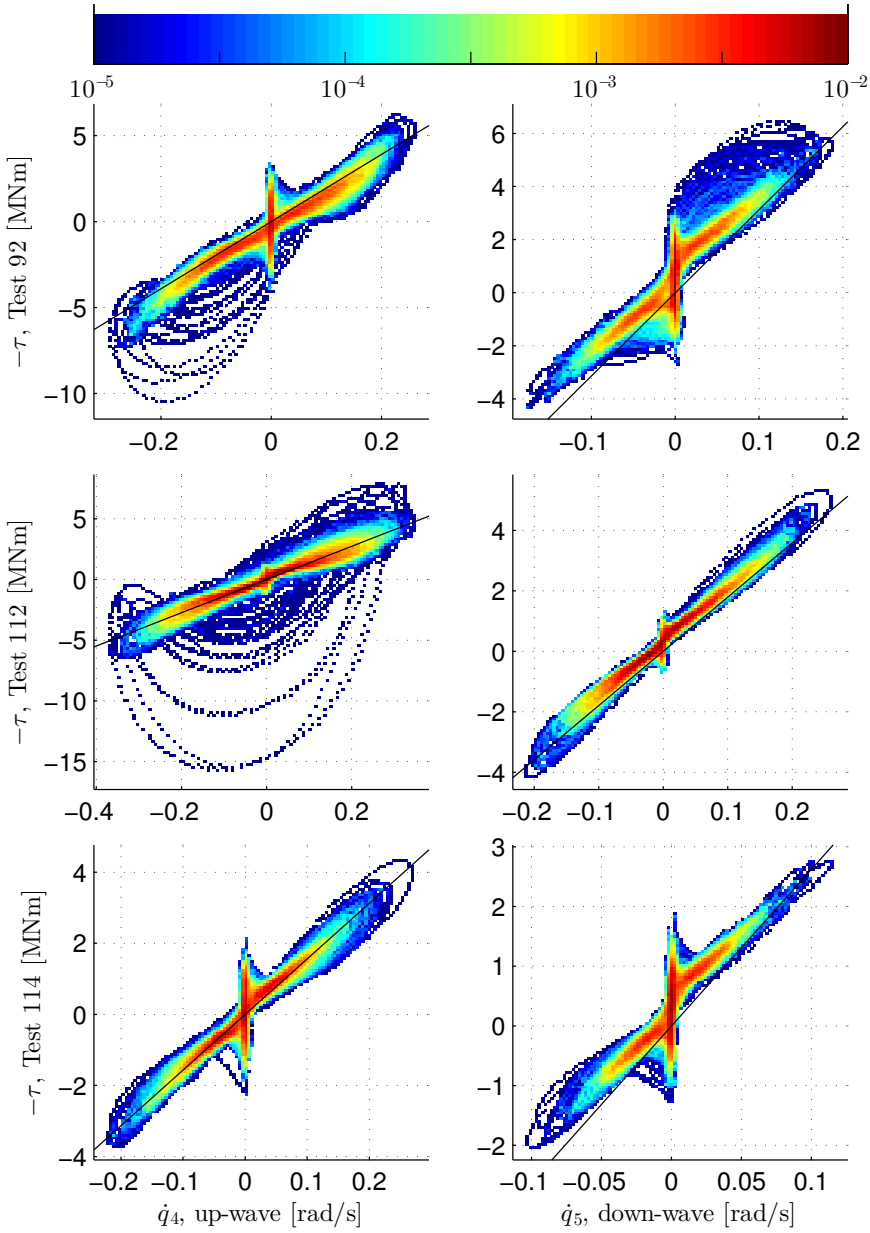

Figure 6.3: Measured PTO characteristics and fitted linear model. The measured characteristic is illustrated as a discrete joint probability distribution of angular velocity $\dot{q}$ and moment τ in a 100-by-100 grid.

nation with relatively large moment, τ. Test 92 was based on the configuration with a long lever arm, which increases the effect of stiction. Tests 112 and 114 are included because they are the tests with the largest and smallest power absorption, respectively.

Another effect not captured by the linear model is the compressibility of the air in the chambers, observed as narrow "loops" in the $\dot{q}, \tau$-plane for all tests. In addition, test 112 includes several end-stop events where the up-wave cylinder reaches its minimal length and becomes an air-spring as the nozzles are blocked by the piston head. These events are observed as larger loops deviating greatly from the linear law.

The stiction prevented motion completely in all sea states for the two buoys located perpendicular to the incoming waves, since these buoys experience very little wave excitation. For this reason, results will only be presented for the up-wave and down-wave buoys. A further consequence of this fact is that the 5 body system can be modeled mathematically as a 3 body system, considering the center floater plus two of the buoys as a single rigid body.

Since stiction mainly occurs in calm periods where very little energy is extracted anyway, a linear model can be justified (see also Figure 6.10). The damping coefficients is determined from the measured PTO force and velocity, requiring that the absorbed energy from the idealized PTO should equal absorbed energy from the scale models PTO, given the same velocity time series. This results in the following estimates of the angular damping coefficients,

$$b_u = \frac{\int_{t_s}^{t_e} \tau_m \dot{q}_m dt}{\int_{t_s}^{t_e} \dot{q}_m^2 dt} \tag{6.1a}$$

$$\dot{q}_m = v_m / L_\perp (q_m) \tag{6.1b}$$

$$\tau_m = f_m L_\perp (q_m) \tag{6.1c}$$

where τ_m is the measured PTO moment and q_m and $\dot{q}_m$ is the hinge angular displacement and velocity. These quantities are derived from the measured time series of cylinder length (with time derivative v_m) and axial force f_m using the lever arm $L_\perp (q_m)$, which is a function of hinge angle q_m. The integration is taken over the time span considered steady state. It should be noted that this procedure is not affected by any time invariant error in the measured PTO moment (a vertical shift of the $\dot{q}, \tau$-curve), since such a shift will not change the *mean* absorbed power.

The nozzle diameters used in both the CF-end and buoy-end of all cylinders, and the resulting damping coefficients, are shown in Figure 6.4. It is seen that the down-wave cylinder produces more damping than the up-wave cylinder with the same nozzle diameter. This can be partly due to the nonlinearity and the lower velocities in the down-wave hinge, and partly because the cylinders were of different model type, although from the same fabricator.

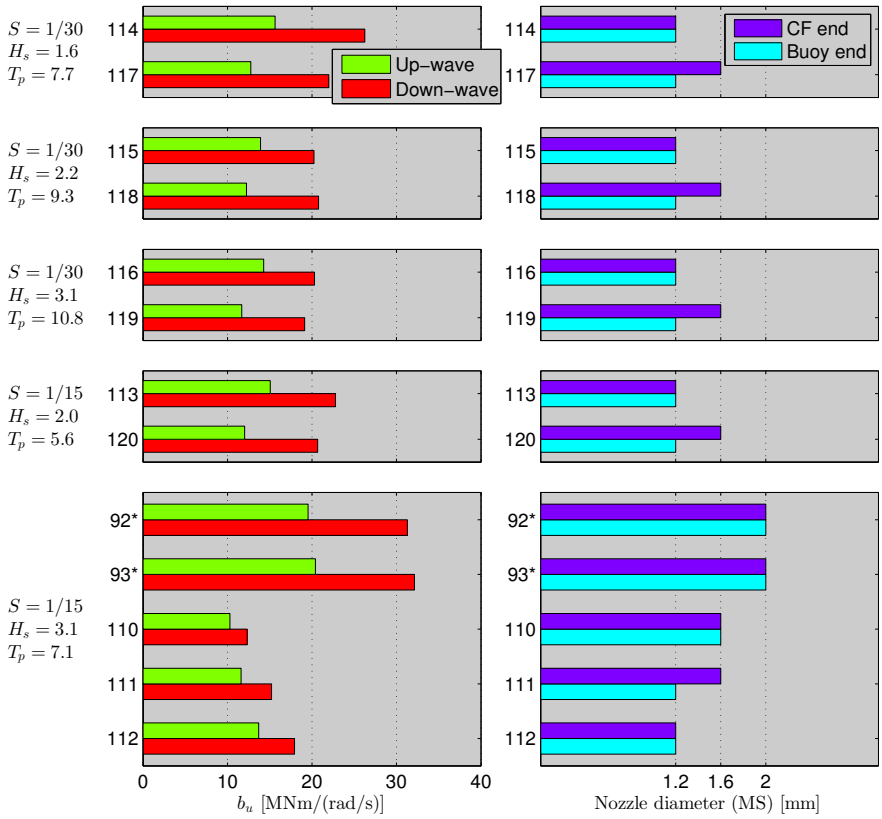

Figure 6.4: Angular linearized PTO damping and model scale nozzle diameter of the pneumatic cylinders. Each cylinder have two nozzles (CF-end and Bouy-end) and the same nozzle pair is used in all cylinders. Test 92 and 93 were based on the configuration shown in Figure 6.1, with a lever arm of 0.51 meters (model scale) at $q = 0$. In all other tests, the cylinders are mounted on the lower bearing, as shown in Figure 6.2, creating a lever arm of 0.28 meters. The damping coefficients are applied in all presented simulation cases.

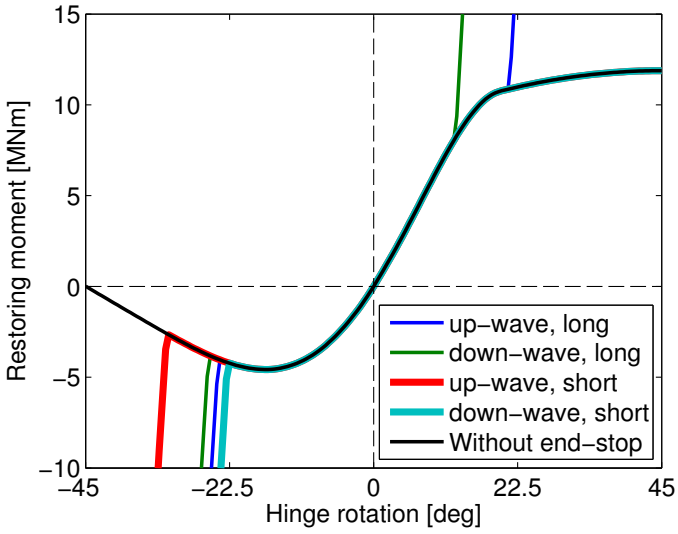

Figure 6.5: Hinge restoring moment with end-stop spring effect for the long and short lever arm configurations.

When the cylinders reach their maximum and minimum length, the piston head blocks the nozzles and the cylinders start to behave like an air spring. This is included in the mathematical model as stiff end-stop springs, represented as bi-linear hinge restoring being zero between the min and max hinge angle corresponding to min and max cylinder length. This effect is illustrated in Figure 6.5 where the end-stop spring effect have been superimposed onto the nonlinear hydrostatic restoring moment. It is seen that the end-stop spring prevents an unstable equilibrium point for -45 degree hinge angle, which corresponds to the case where the center of gravity of the buoy is positioned directly above the hinge axis. The stiffness of the end-stop springs is taken as 10 times the linearized hydrostatic restoring (the slope at zero hinge angle). The nonlinear hydrostatic restoring curve has been calculated using eq. (5.3) without the presence of waves and center floater motion.

6.4 Open sea assumption

Open sea conditions are assumed in the numerical simulations. This means that the wall boundary condition is imposed only on the bottom of the tank, and not on the two side walls. It also mean that reflections from the absorbing beach and re-reflections from the wavemaker (and so on) are not accounted

for. Some implications of this assumption will be discussed in this section. Since the interpretation of the wave measurements for the calibration waves (without the WEC in the tank) are affected by the reflections from the beach, the relationship between measured wave elevation and applied waves in the numerical models are also discussed.

6.4.1 Wave measurements and beach reflection analysis

The wave elevation was measured using two probes with different locations. The up-wave probe was located on the center line of the tank, 8.62 meters (model scale) from the wavemaker. The down-wave probe was located 0.8 meters from one of the walls and 11.05 meters from the wavemaker. For comparison, the center floater of the WEC was located 11 meters from the wavemaker in calm water. The surface elevation measured by the up-wave and down-wave probe will be referred to as $\xi_u(t)$ and $\xi_d(t)$.

When the waves from the wave maker reach the end of the tank, most of the energy is absorbed by the beach. The absorbing beach have a parabolic shape with a length of 5.5 meters (165 meter full scale), with a slope varying between $\approx 20°$ near the bottom and $\approx 5°$ near the water line. The beach is open underneath to allow water from the over-topping waves to run back into the basin without generating waves.

The reflected waves will create partially standing waves and thus inhomogeneous significant wave height along the length of the tank. This fact implies that the assumption of ergodicity no longer holds (Jefferys, 1987). In this study, the method of Goda and Suzuki (1976) is used to assess the importance of beach reflection. The basis of this method is to express the surface elevation in two alternative ways:

$$\xi = A\cos(\omega t + \theta) \tag{6.2}$$

$$\xi = A_I\cos(\omega t - kx + \theta_I) + A_R\cos(\omega t + kx + \theta_R) \tag{6.3}$$

Here, A and θ are the amplitude and phase of the elevation measured by one of the probes, extracted from each frequency using Fourier analysis in the case of an irregular sea. As shown by Isaacson (1991), it is possible to use elevation measurements at two locations to construct three equations which can be solved for the amplitude of the incident wave A_I, the reflected wave A_R, and the phase difference $\theta_I - \theta_R$. The two amplitudes are written,

$$A_I = \frac{\sqrt{A_u^2 + A_d^2 - 2A_u A_d \cos\left(kd + \theta_u - \theta_d\right)}}{2\left|\sin\left(kd\right)\right|} \tag{6.4a}$$

$$A_R = \frac{\sqrt{A_u^2 + A_d^2 - 2A_u A_d \cos\left(kd + \theta_d - \theta_u\right)}}{2\left|\sin\left(kd\right)\right|} \tag{6.4b}$$

where d is the distance (along the longitudinal axis) between the wave probes, here $11.05 - 8.62 = 2.43$ meters in model scale. Subscript u is used on quantities measured by the up-wave probe, and subscript d is used for the down-wave probe. The reflection coefficient can then be defined as,

$$K_R = \frac{A_R}{A_I} = \sqrt{\frac{1 + \left(\frac{A_u}{A_d}\right)^2 - 2\frac{A_u}{A_d}\cos\left(kd + \theta_d - \theta_u\right)}{1 + \left(\frac{A_u}{A_d}\right)^2 - 2\frac{A_u}{A_d}\cos\left(kd + \theta_u - \theta_d\right)}} \tag{6.5}$$

here written in a form making it explicit that it is the ratio between the amplitudes at the two probes and the phase difference that determine the reflection. The method breaks down when there is an integer number of half waves between the wave probes, signified by $k = n\pi/d$, $n = 0, 1, ...$, where the denominator of eqs. (6.4) becomes zero. In practice, we will also have large inaccuracies close to these singularities due to magnification of measurement error.

Figure 6.6 shows the wave elevation spectrum measured at the two probes and the spectrum of incident and reflected waves for the largest of the steep sea states. The spectra are calculated with the discrete Fourier transform (using FFT) of the steady state portion of the measured time series using a single rectangular window function. Spectral smoothing is applied using eq. (4.73). We use a Gaussian (bell) function of width $2\delta = 0.05$ rad/s and "standard deviation" $\sigma = \delta/3$ as the averaging function (Stansberg, 1997).

For frequencies above the singularity at $\omega = 1.15$, the incident spectrum seems to be governed more by the singularities than by the target wave spectrum, which indicates that the reflection analysis is incorrect for these frequencies. One source of error for the high frequencies can be the nonlinear bounded waves that do not follow the linear dispersion relation which the reflection analysis is based on, and that inevitably is present in this steep sea state. If the measured distance between the probes are slightly wrong, the resulting error will also be magnified for large wave numbers. It should also be mentioned that the location of the wave probes was not optimized for wave reflection analysis. Especially the difference in distance from the tank wall between the two probes is not beneficial since it implies that any small 3D effect in the tank will erroneously be attributed as a beach reflection effect. Better

accuracy and fewer singular frequencies can clearly be achieved by using more than two probes (Isaacson, 1991).

Figure 6.7 shows the estimated reflection coefficients for all considered sea states. The inaccuracies described above makes it difficult to conclude on the importance of beach reflections. Still, if we only include frequencies around the peak frequencies in the various target spectra, and in addition exclude the spikes around the singularities, it is likely that the reflection is below 15% in amplitude with 10% as a typical value. This is somewhat higher than what is reported by Cruz (2008) for comparable wave length to beach length ratio.

It should be emphasized that 10% reflection in amplitude implies that only 1% of the wave energy is reflected. However, the uncertainty in the reflection implies an uncertainty in the incoming waves as well. Measuring wave elevation in a single point and assuming zero reflection while you in reality have 10% reflection, implies that the error in the measured incoming amplitude is between -10% and 10% whereas the error in incoming power is between -19% and 21%, depending on the location of the probe. In an irregular sea, this effect will even out when integrating over frequencies to produce a standard deviation that is more accurate than the spectral shape.

The reflection analysis above is not accurate enough to produce time series of incoming and reflected waves for input to the simulation model. Instead, we disregard reflection and use,

$$\xi(t) = \frac{\mathrm{var}\left[\xi_u(t)\right] + \mathrm{var}\left[\xi_d(t)\right]}{2\mathrm{var}\left[\xi_d(t)\right]}\xi_d(t) \tag{6.6}$$

as the assumed unidirectional wave input to the simulation model. This assures that the variance of the applied elevation equals the average of the two measured variances. The correction factor is between 1.009 and 1.044 in the various sea states. The down-wave probe is used as basis because this probe has almost the same distance from the wave maker as the origin of the center floater, thus giving correct phasing. An important note is that the wave measurements are taken in a dedicated test run, without the WEC present in the tank.

In the simulation models, $\xi(t)$ is assumed to be composed of harmonic components all following the linear dispersion relation. This is a simplification and not strictly true, especially for steep sea states.

6.4.2 Assessment of wall effects on a single hemisphere

The effect of the tank walls can be accounted for approximately by including several mirror bodies having prescribed motions (method of images). This was done in Section 3.8.2 for a circular cylinder identical to the center floater of

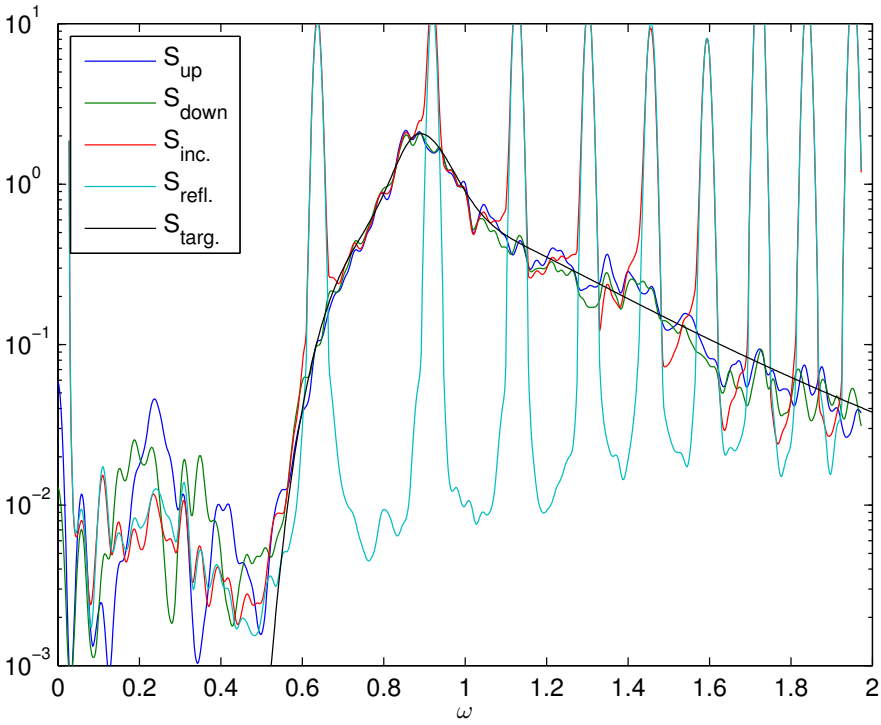

Figure 6.6: Spectrum of wave elevation at up-wave (S_{up}) and down wave (S_{down}) probes, the resolved incident (S_{inc}) and reflected (S_{refl}) waves as well as the target JONSWAP wave spectrum (S_{targ}) with parameters $T_p = 7.1$ s, $H_s = 3.1$ m and $\gamma = 3.15$. The strong peaks deviating greatly from the target spectrum is due to magnification of measurement errors close to the singular wave numbers $k = n\pi/d$, $n = 0, 1, ...$

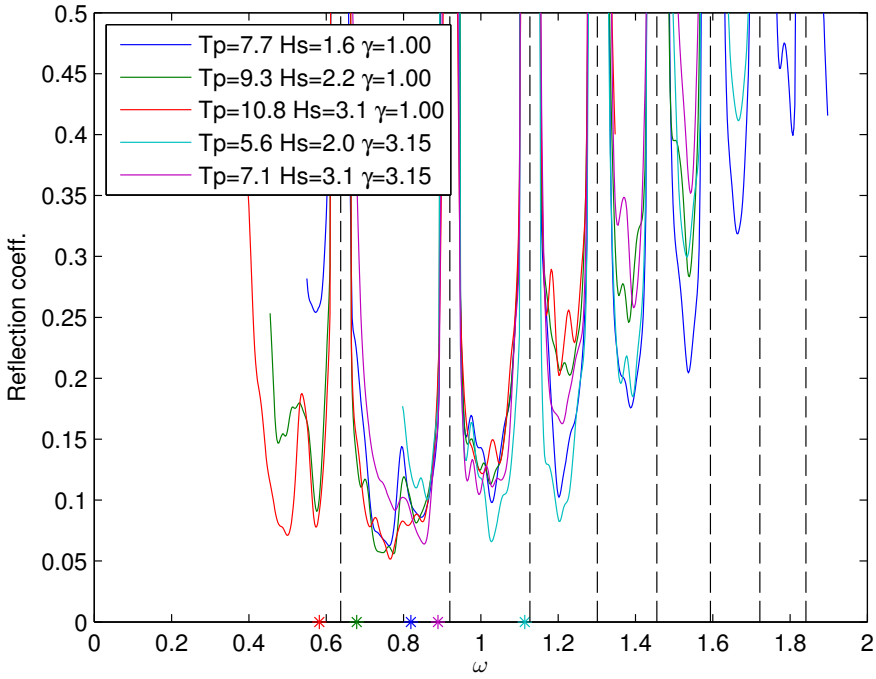

Figure 6.7: Beach reflection coefficients for all sea states. The coefficients are not trustworthy close to the singularity frequencies, indicated with vertical lines, and far off the peak frequency ω_p of each spectrum. ω_p is indicated with a colored star on the x-axis. The reflection as a function of frequency is smoothed by using eq. (4.73) with $2\delta = 0.05$ rad/s and $\sigma = \delta/3$ on the amplitudes before taking the ratio A_R/A_I.

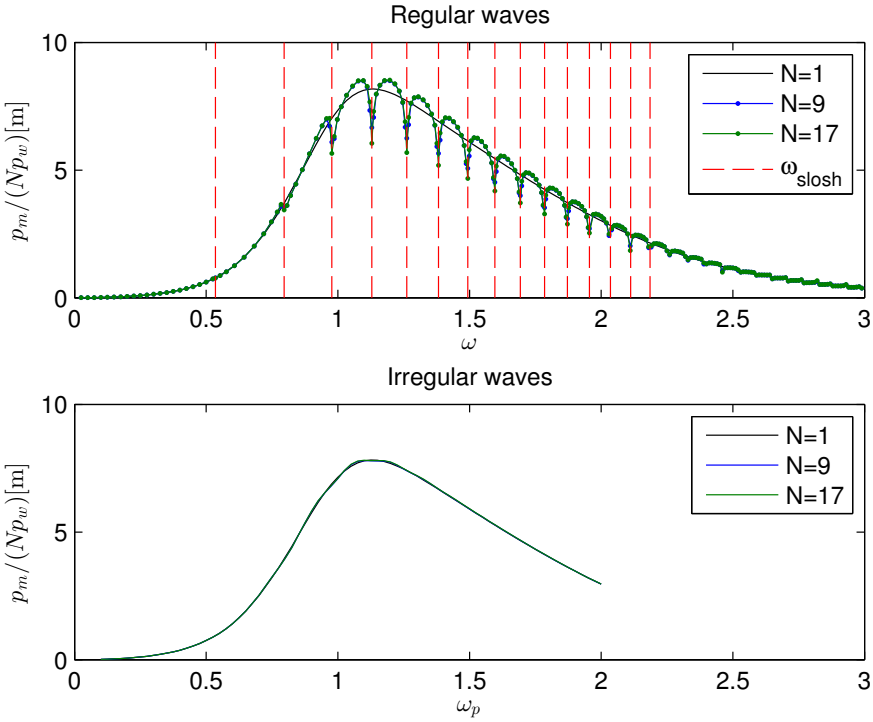

Figure 6.8: Effect of tank walls on the mean capture width of a single hemisphere with 45° sloped motion. Regular and irregular waves (JONSWAP, $\gamma = 3.15$) is considered. The tank wall effect is included using the method of images with 0, 8 and 16 mirror bodies.

the WEC. Although possible in principle, this approach is not explored for the hinged 5-body WEC due to the prohibitive CPU load associated with finding the hydrodynamic coefficients. Instead, we will employ the method here for a single hemisphere identical to one of the buoys of the WEC (diameter of 7.5 meters), in order to give an indication on the importance of wall effects. In order to show convergence, 1, 9 and 17 bodies will be considered, corresponding to 0, 4 and 8 mirror bodies on each side of the "physical" body. The method adopted here is described in some more detail in Section 3.8.2.

The hemispheres translate in a 45° degree slope such as to mimic the (small-angle) motion of the up-wave buoy of the 5-body WEC (with the center floater fixed). Since all hemispheres are rigidly connected and we only consider linear forces, this case study is identical to the SDOF case study presented in Section 2.2.1, except that we employ a fixed PTO damping coefficient $b_u = 92.6$ [kN/(m/s)] (corresponding to 15000 [kNm/(rad/s)] with $\sqrt{2} \cdot 9$ meters of lever arm). The water depth is 45 meters whereas the array spacing (full scale tank width) is 193.5 meters.

Figure 6.8 shows the mean capture width in regular and irregular waves. Since the response is linear and we don't consider amplitude constraints, the wave height has no influence on the capture width. In regular waves, it is seen that spikes occur at frequencies corresponding to the transverse sloshing frequencies in the tank. As discussed in Section 3.8.2, these spikes are mainly associated with the vertical component of the sloped motion. In irregular waves, the integration over frequencies smoothes out the spikes and results in capture widths which are almost identical for the 1, 9 and 17 body cases. This indicates that wall effects are insignificant for integrated quantities in irregular waves. This result agrees with the guidelines provided by Babarit (2013) for the layout of WEC arrays. There, it is stated that there is no indication that the number of WECs in a row perpendicular to the incoming waves should be limited in any manner, provided that their spacing is sufficiently large.

Assuming the same behavior to exist for the 5-body WEC, we should expect to see similar spikes in the response spectra. However, the strong spikes described above are *not* seen in the displacement spectra from measurements shown in Figure 6.14. The reason for this is not fully understood. One hypothesis is the slow buildup of the sloshing modes in combination with the "imperfect" and changing position of the bodies in the tank. The waves radiated by the heave motion of a body will change its location of origin when the body moves in the horizontal plane. This effect is not captured by linear theory. The slow build-up is demonstrated in Figure 3.8, showing the impulse response functions that describes the radiation forces in the time domain for the array of cylinders. The heave impulse response function of the channel problem is here seen to deviate from that of the open sea problem only for

large values of the time variable.

6.5 Mathematical models

6.5.1 Plane 3-body model

The WEC system tested in the towing tank consists in principle of 13 rigid bodies. One center floater, 4 buoys and 4 pneumatic cylinders each comprising two rigid bodies (the piston and cylinder housing). Since the cylinders have a relatively small mass, the mass of the piston can be lumped to the buoy whereas the mass of the cylinder housing can be lumped to the center floater mast (the vertical rod rigidly connected on top of the center floater). Then we are left with 5 rigid bodies having $6+4$ degrees of freedom. This is the 5-body system we developed equations of motion for in Chapter 4.

However, since two of the buoys remained fixed to the center floater due to static friction in the cylinders, the system can be described mathematically as a 3-body system. Moreover, symmetry in the body geometry and tank waves ensures that the 3 bodies only undergoes motion in the vertical longitudinal plane of the towing tank. Since we know a-priori that the sway, roll and yaw of the center floater will be zero, the number of collective modes are reduced to 3 and the total number of degrees of freedom becomes 5. The generalized coordinates can then be re-defined (compared with Section 4.2.4):

- q_1 is the collective surge, defined as the x-component of $\mathbf{r}_1$.
- q_2 is the collective heave, defined as the z-component of $\mathbf{r}_1$.
- q_3 is the collective pitch, defined as the angle between $\mathbf{k}_1$ and $\mathbf{k}$ obtained by a right-handed rotation of the center floater (frame 1) an angle q_3 about its y-axis.
- q_4 is the relative rotation in the up-wave hinge, defined as the angle between $\mathbf{k}_2$ and $\mathbf{k}_1$ obtained by a right-handed rotation of frame 2 an angle q_4 about its y-axis.
- q_5 is the relative rotation in the down-wave hinge, defined as the angle between $\mathbf{k}_3$ and $\mathbf{k}_1$ obtained by a right-handed rotation of frame 3 an angle q_5 about its y-axis.

The independent velocities also take a simpler form:

$$V_1 = v_{x,1}^{(1)} = \cos(q_3)\,\dot{q}_1 - \sin(q_3)\,\dot{q}_2 \tag{6.7a}$$
$$V_2 = v_{z,1}^{(1)} = \sin(q_3)\,\dot{q}_1 + \cos(q_3)\,\dot{q}_2 \tag{6.7b}$$
$$V_3 = \omega_{y,1} = \dot{q}_3 \tag{6.7c}$$
$$V_i = \dot{q}_i\,,\ i = 4, 5 \tag{6.7d}$$

Restraining motion in some degrees of freedom as we do here is facilitated simply be removing the corresponding rows and columns in the generalized mass and Coriolis-centrifugal matrices, and the corresponding elements of the generalized force vector.

6.5.2 Mooring, PTO and end-stop forces

The mooring system has already been discussed in Section 6.1. The mathematical representation of the mooring forces is:

$$\mathbf{F}_{moor} = -\mathbf{G}_{moor}\mathbf{q} \tag{6.8}$$

Here, the nonzero matrix entries are G_{11}, G_{22}, G_{33} and $G_{13} = G_{31}$ (recall that mode 1, 2 and 3 correspond to surge, heave and pitch for the plane 3-body model). These entries are calculated based on the (linear) stiffness and pre-tension of the mooring lines, as well as the position of the fairleads (on the center floater) and anchors (on the basin wall). Only G_{11} have a significant influence on the motions, and result in a surge natural period of 45 seconds (full scale).

The linear power take-off forces, including the end-stop spring, only affect the two hinge modes and can be written as,

$$F_{PTO,i} = -b_{u,i}V_i + F_{ES,i}\,,\ i = 4, 5 \tag{6.9a}$$
$$F_{ES,i} = \begin{cases} -k_{ES}\,(q_i - q_{min,i}) & q_i < q_{min,i} \\ 0 & q_{min,i} \le q_i \le q_{max,i} \\ -k_{ES}\,(q_i - q_{max,i}) & q_i > q_{max,i} \end{cases} \tag{6.9b}$$

where $b_{u,4}$ and $b_{u,5}$ is calculated with eq. (6.1) and illustrated in Figure 6.4. The end-stop spring is discussed in Section 6.3.

6.5.3 Viscous forces

The damping of a WEC should be dominated by wave radiation and PTO damping since both is a prerequisite for energy absorption. Viscous forces represent a loss that reduce the absorbed power and should therefore, by design,

have little importance for the power absorption. However, it can have a large effect on low-frequency motions, since the radiation damping is very small for low frequencies, as shown in Figure 3.1. The spherical buoys are believed to have small viscous forces, or at least small enough to have negligible effect on the hinge modes. The sharp edges on the center floater and slender beams is however believed to cause some vortex shedding and thus viscous forces. In the simulation model, we disregard drag excitation and include drag damping only on the collective modes, written as:

$$F_{visc,1} = -\frac{1}{2}\rho C_{D,1} DT \left|V_1\right| V_1 \,,\; C_{D,1} = 5 \tag{6.10a}$$

$$F_{visc,2} = -\frac{1}{2}\rho C_{D,2} \frac{\pi D^2}{4} \left|V_2\right| V_2 \,,\; C_{D,2} = 1.5 \tag{6.10b}$$

$$F_{visc,3} = -\frac{1}{2}\rho C_{D,2} \frac{\pi D^2}{4} \left(\frac{D}{2}\right)^3 \left|V_3\right| V_3 \tag{6.10c}$$

Here, D and T is the diameter and draft of the center floater. The horizontal drag coefficient of 5 is tuned to match the low frequency surge motions observed in the model tests. The value perhaps seems unrealistically large and indicates that we might lack sources of damping (e.g. wave drift damping) which is here (incorrectly) attributed to viscous effects. The large horizontal drag coefficient is also partly caused by using DT as the characteristic area, whereas the damping of the collective surge mode have contributions from all bodies, also the slender beams neglected in the potential flow analysis. The small drag forces acting on the buoys, assumed to be negligible for the hinge modes, can have a significant effect on collective surge, since this mode have almost zero low frequency damping. The quadratic nature of the drag forces can also lead to a magnification of the low frequency damping caused by the large amplitude wave frequency motion of the buoys (especially the up-wave buoy), and to some extent also the center floater.

The collective heave mode is almost unaffected by drag, and the vertical drag coefficient $C_{D,2} = 1.5$ is chosen as a rough estimate. The drag damping of the collective pitch mode is expressed in terms of the vertical drag coefficient and a characteristic lever arm, chosen as $D/2$, reflecting the fact that some drag forces can be attributed to the slender beams extending outside the center floater. A sensitivity study reveals that the absorbed power is insensitive to the uncertain parameter $C_{D,2}$. Using the value $C_{D,2} = 0$ instead imply an increase in mean absorbed power of at most 4.2% (in test 110). In the other end, using a value $C_{D,2} = 3$, imply a reduction of at most 3.3% (in test 119).

6.5.4 Non-linear hydrodynamics model (NonLin)

In this section we will synthesize the parts that make up the non-linear hydrodynamics model, which we will use in the simulations presented in Section 6.6. In that section, we will use the identification "NonLin" to annotate the results corresponding to this model. The complete model is similar to the one presented in Section 4.5, except that we will employ the plane 3-body model. Written on a non-linear state space form we have:

$$\dot{\mathbf{V}} = \left(\mathbf{M}\left(q_4, q_5\right) + \mathbf{A}_\infty\right)^{-1} \left(\mathbf{F}\left(\mathbf{V}, \mathbf{q}, t\right) - \mathbf{C}\left(\mathbf{V}, \left(q_4, q_5\right)\right)\mathbf{V} - \boldsymbol{\mathcal{C}}\boldsymbol{\mathcal{X}}\right) \tag{6.11a}$$

$$\dot{q}_1 = \cos\left(q_3\right) V_1 + \sin\left(q_3\right) V_2 \tag{6.11b}$$

$$\dot{q}_2 = -\sin\left(q_3\right) V_1 + \cos\left(q_3\right) V_2 \tag{6.11c}$$

$$\dot{q}_k = V_k\,,\ k = 3, 4, 5 \tag{6.11d}$$

$$\dot{\boldsymbol{\mathcal{X}}} = \boldsymbol{\mathcal{A}}\boldsymbol{\mathcal{X}} + \boldsymbol{\mathcal{B}}\mathbf{V} \tag{6.11e}$$

with,

$$\mathbf{F}\left(\mathbf{V}, \mathbf{q}, t\right) = \mathbf{F}_D\left(t\right) + \mathbf{F}_{HSFK}\left(\mathbf{q}, t\right) - \mathbf{G}_{moor}\mathbf{q} + \mathbf{F}_{PTO}\left(\mathbf{V}, \mathbf{q}\right) + \mathbf{F}_{visc}\left(\mathbf{V}\right) \tag{6.12}$$

Here, $\mathbf{F}_D\left(t\right) + \mathbf{F}_{HSFK}\left(\mathbf{q}, t\right)$ is the diffraction, hydrostatic and Froude-Krylov forces discussed in Chapter 5. $-\mathbf{G}_{moor}\mathbf{q}$ is the mooring forces and $\mathbf{F}_{PTO}\left(\mathbf{V}, \mathbf{q}\right)$ is the PTO forces, given in Section 6.5.2. The viscous forces $\mathbf{F}_{visc}\left(\mathbf{V}\right)$ is discussed in Section 6.5.3. Note that the PTO forces includes end-stop forces. We collect them here to comply with the measured PTO forces, which cannot be separated into its two contributions since we simply measure the compressive force in the pneumatic cylinder.

The mass, center of gravity, center of buoyancy and the radii of gyration of the different bodies of the scale model are given in Table 2.1. It is emphasized that all bodies are neutrally buoyant, meaning that there is no forces acting in the hinges in the absence of waves.

The fluid memory associated with the radiation forces is contained in the radiation state vector $\boldsymbol{\mathcal{X}}$. The identification of the state space matrices $\boldsymbol{\mathcal{A}}$, $\boldsymbol{\mathcal{B}}$ and $\boldsymbol{\mathcal{C}}$ are discussed in Chapter 3, and the corresponding added mass and damping is shown in Figure 3.1 (in terms of a complex transfer matrix).

The time-series of undisturbed pressure determining the Froude-Krylov forces and the time-series of diffraction forces was generated from the Fourier coefficients of the surface elevation measured in tank (without the WEC present in the tank). These time series therefore represent the same sea state realization as the one generated in the tank, both with and without the WEC present. This is discussed in more detail in Section 5.3.1.

6.5.5 Linear hydrodynamics model (Lin)

The linear hydrodynamics model is identical to the non-linear hydrodynamics model except that we linearize the Froude-Krylov and restoring forces. We then have,

$$\mathbf{F}_{HSFK}(\mathbf{q}, t) = \mathbf{F}_{FK,lin}(t) - \mathbf{G}\mathbf{q} \tag{6.13}$$

where $\mathbf{G} \in \mathbb{R}^{5\times5}$ is the generalized hydrostatic restoring matrix, defined as:

$$\mathbf{G} = \mathbf{J}_0^{'T} \text{diag}\left(\bar{\mathbf{G}}_{11}, \ldots, \bar{\mathbf{G}}_{55}\right) \mathbf{J}_0^{'} \tag{6.14}$$

$\bar{\mathbf{G}}_{jj} \in \mathbb{R}^{6\times6}$ is here the hydrostatic restoring matrix of body j. Because all bodies are neutrally buoyant (i.e. there are no hinge constraint forces in the absence of waves), $\bar{\mathbf{G}}_{jj}$ can be found in the traditional way, see e.g. Newman (1977). The small angle transformation matrix $\mathbf{J}_0^{'}$ is identical to the one we defined in Section 4.4, except that we remove the columns associated with the fixed degrees of freedom (sway, roll, yaw and the two fixed hinges).

It must be emphasized that the linear hydrodynamics model is in fact a non-linear model. It is only the hydrodynamic and hydrostatic forces that are linearized. Note that the importance of the inertia force nonlinearities were assessed in Section 4.6.

6.6 Results and discussion

Figure 6.9 summarizes the power absorption of the WEC in all test runs. The results of both the linear (Section 6.5.4) and nonlinear (Section 6.5.5) hydrodynamics model are compared to the experimental data.

It is seen that the linear hydrodynamics model over-predicts the mean power absorption in all test runs. The over-prediction $(p_{calc} - p_{meas})/p_{meas}$ ranges from 15% in test 120, up to 60% in test 110. The average over-prediction over all test runs is 32%. The nonlinear hydrodynamics model gives a better prediction of the total absorbed power in all test runs, with an over-prediction ranging from −15% (under-prediction) in test 112 up to 18% in test 114. The average deviation (absolute value of over-prediction) is 9%.

If we study the power absorption of the down-wave buoy alone we see that the linear hydrodynamics overpredicts by between −10% and 24% whereas the nonlinear hydrodynamics model overpredicts by between −1% and 37%. The sheltering from the other bodies makes the diffraction component more important for this buoy (see Figure 5.1), and it is therefore plausible that a consistent use of linear theory perform better than the more inconsistent mixing of nonlinear Froude-Krylov forces with linear diffraction forces in some sea states.

If we study the up-wave buoy alone, the over-prediction by the linear hydrodynamics model ranges from 17% up to 89%, whereas the nonlinear hydrodynamics model ranges from −21% up to 15%. The large amplitude motion with greatly varying submergence can explain this difference. The relatively small contribution from the down-wave buoy makes the nonlinear hydrodynamics model better overall.

Figure 6.10 shows the probability density distribution of the absorbed power from both measurements and the nonlinear hydrodynamics model. Static friction is here seen as a large probability of having close to zero absorbed power. However, knowing that the mean power is the first moment of this probability distribution, it is plausible that static friction does not affect the mean absorbed power significantly. Moreover, the close agreement between measurements and model for higher power indicate that the linear PTO model is reasonable. Note also that the end-stop spring forces is regarded as part of the PTO forces, both in the model and in the measurements. This explains why negative power is observed.

The power absorption is directly proportional to the squared angular velocity in the hinges. To further understand the effect of nonlinearities, we also have to study the displacements. Figure 6.11 and 6.12 show the mean, low and wave frequency standard deviation, as well as the smallest and largest observed hinge angles, for the up-wave and down-wave buoy, respectively. Note that the extreme hinge angles are influenced by the end-stop springs. The low and wave frequency response is found by filtering above/below half the target wave spectrum's peak frequency, below which very little wave energy exists. By definition all generalized coordinates are zero in the absence of waves. Hence, any significant displacements below this frequency (including zero) must be due to nonlinear interaction with wave frequency responses. It is seen that both hinges have a mean and low frequency angular displacement of the same order of magnitude as the wave frequency component. Similar behavior is seen for the collective pitch motion, shown in Figure 6.13. One physical explanation for this feature is linked to nonlinear hinge restoring: When a buoy beam approaches a vertical position, the restoring moment is reduced (see Figure (6.5)) as the horizontal distance between the center of gravity of the buoy and the hinge is reduced. The reduced hinge restoring leaves the buoy in an elevated (low buoyancy) state for a relatively long period of time, inducing a moment on the center floater. The effect is that the center floater pitches towards the buoy with the largest motions. This average position of the WEC is drawn quantitatively in Figure 2.8. The mean and low frequency angular displacements are captured by the nonlinear hydrodynamics model with reasonable accuracy. Note that there is a small, yet systematic, mean response in the linear hydrodynamics model as well. This can partly be due to the time

varying mass matrix and Coriolis-centrifugal forces.

The mean and low frequency rotations are partly created by wave frequency responses, as explained above. There will also be an influence on the wave frequency responses from the low frequency rotations. This is largely due to the sensitivity of the hydrostatic stiffness (and thus natural periods) to the hinge angle.

The mean angles produced by the simulation model imply that the linearization position in the BEM analysis is wrong. This is because the calculation of radiation forces and diffraction forces assume small perturbations around the *equilibrium* position of the bodies. An obvious improvement would have been to use the mean position as the linearization point in the BEM calculation. This would however imply an iterative procedure to find the mean position for each sea state.

Figure 6.14 shows the power spectral density of all generalized displacement coordinates in addition to the wave elevation for test 112. The spectra show that all motion modes except heave have considerable mean and low frequency displacements. It is also seen that the nonlinearity create response at frequencies higher than the wave frequencies. The nonlinear hydrodynamics model is able to describe these phenomena.

The nonlinearities also influence the probability distribution of the displacement amplitudes. Figure 6.15 shows the cumulative distribution of minima and maxima of all generalized displacement coordinates and the wave process based on test 112. The minima and maxima are here defined as the smallest and largest value between subsequent upcrossings of the mean level. The normalization of the y-axis is such that the data points will make a straight line if they happen to be Rayleigh distributed, as is the case for Gaussian, narrow-banded processes (Naess and Moan, 2012). The cumulative distributions show considerable nonlinearity and asymmetry about the mean level in all motion modes except for heave. The cumulative distribution of the minima and maxima of the measured wave process itself also shows some asymmetry, with peaks considerably larger than the troughs. This indicates that the assumption of Gaussian, narrow-banded wave process is questionable for irregular waves with steepness as high as 1/15. It should be mentioned that the bounded waves that create the wave asymmetry are not correctly accounted for in the calculation of undisturbed pressure and diffraction force for the numerical models. Here, the harmonic components of the measured wave is all treated as linear "free" waves having a linear relation to the undisturbed pressure and diffraction force without any interaction between the frequencies.

Figure 6.16 shows that the surge motion has the most prominent mean and low frequency displacement. This is due to the soft mooring and low natural frequency in this mode. These responses can be important in the design of

the mooring system and power cable connection. The traditional method for analyzing horizontal drift forces on large-volume structures is to use second order drift coefficients derived from the first order velocity potential. The drift coefficients represent the mean force in regular waves. In irregular seas, Newman's approximation (Newman, 1974; Faltinsen, 1990) is often used to obtain the slowly varying forces without having to calculate the second order velocity potential. A full second order analysis is also possible. This approach gives drift forces correct to second order in wave height, including the effect of radiation and diffraction.

The drift force resulting from the numerical model presented here is neither based on Newman's approximation nor a full second order analysis. It is not based on perturbation of wave elevation and body motions, and is as such of "infinite" order. On the other hand, the drift force is incomplete since it does not include the effect of diffraction and radiation pressure in the pressure integration over the time varying surface area. The diffraction and radiation (linear) will thus only have an indirect effect through its influence on the motions. The drift force is the low frequency part of the nonlinear Froude-Krylov and hydrostatic forces described by eqs. (5.3) and (5.4) and is related to the strongly varying submergence and large rotations of the bodies.

It should be mentioned here that the slowly varying surge motions are sensitive to the horizontal drag coefficient, which is estimated based on the model tests (see Section 6.5.2). As such, the agreement between measured and calculated LF standard deviation in surge is not *alone* a strong validation of the numerical models ability to represent drift forces. On the other hand, the mean offset, which also shows a good agreement, is insensitive to the drag coefficient since we don't include drag excitation (we only include drag damping). Furthermore, the cumulative distribution of minima and maxima, shown in Figure 6.15, and the displacement spectrum, shown in Figure 6.14, both shows good agreement between measurements and calculations. Note also that a single horizontal drag coefficient is used in all tests. Together, these results therefore indicate that the drift forces and resulting offset and motions are mainly due to a physical effect (strongly varying submergence and large rotations) that are captured by the numerical model.

A motivation for developing fast, simplified simulation models as the one presented here, is the ability to carry out extensive parameter variations efficiently, as a mean to optimize the design. Figure 6.17 shows such a parameter variation, using the two PTO damping coefficients as free variables. Wave time series number 5 from Table 6.1 is used. It is seen that the linear hydrodynamics model predicts substantially more power absorption than the nonlinear hydrodynamics model, even when the PTO damping is increased and consequently the hinge response reduced. It is also seen that the damping applied in test

112 were too large for buoy 2 and too small for buoy 1. In fact, interchanging the two pneumatic cylinders would have brought us closer to the optimal. However, this was not possible due to different length of the cylinders, giving cylinder 2 less stroke length. By choosing the optimal damping coefficients, we would have gained approximately 15 kW. More importantly, by using the optimal damping coefficients we would reduce the amplitudes of the up-wave buoy and avoid many of the hard end-stop events.

The present design emerged from a crude optimization using linear frequency domain methods and omnidirectional seas. The resulting device had submerged hinges connected to the buoys with beams inclined an angle about 45°. The simplified nonlinear model presented here is seen to capture physical phenomena that need to be accounted for in future optimization of the design. It is believed that such an optimization will result in a change of size of the bodies and also different beam angles.

The discrepancies between the numerical model and experimental data not only results from lack of important physics accounted for in the numerical model, but also measurement errors and lack of control of parameters and conditions in the experiment. The current non-linear hydrodynamics model is able to predict the mean absorbed power to within 20% in all considered sea states. Considering the uncertainties in the experiment, especially relating to the power take-off system and the confined water effects, it is likely that a more refined numerical model, including for instance nonlinear radiation and diffraction, would also require a more refined experiment for verification.

The current problem involves bodies undergoing large motions, in the extreme events being almost completely submerged and completely "dry". Hence, nonlinear radiation and diffraction forces are inevitable. During extreme events, large slamming forces of relatively short duration will also occur. The slamming forces are correlated with rapid change in wetted area and can cause water spray and dissipate energy. This type of energy dissipation is observed in the model test reported by Babarit et al. (2009) for the SEAREV WEC. The close agreement between measured and predicted minima and maxima of hinge angles reported here (see Figure 6.15), indicate that slamming is not a dominant effect for the hinged 5-body WEC, at least not for the global motions in the operating conditions.

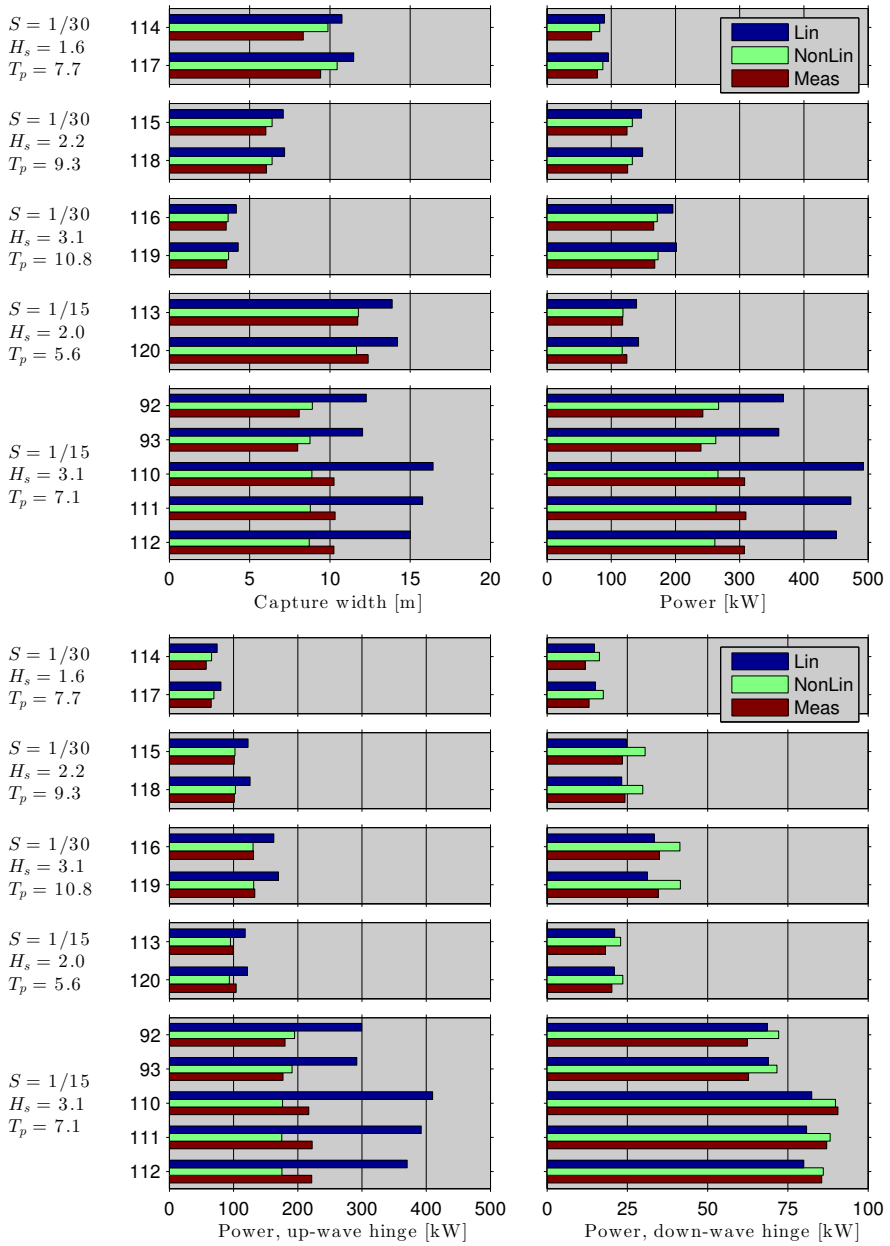

Figure 6.9: Mean absorbed power and capture width in the steady state portion of all test runs. The corresponding PTO parameters are given in Figure 6.4.

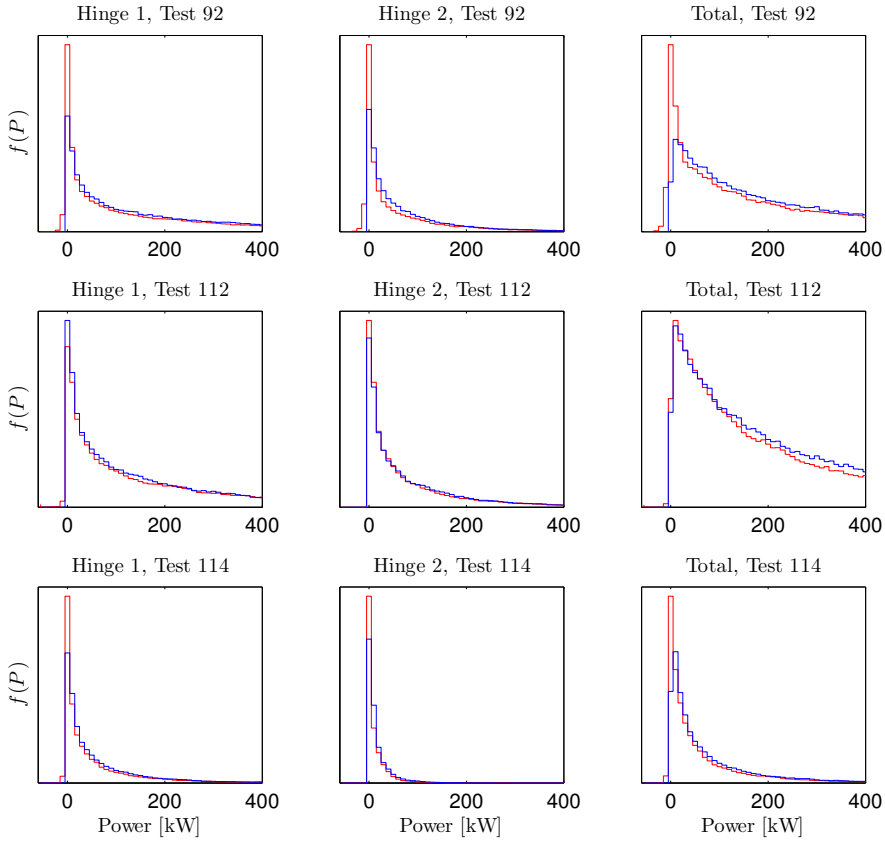

Figure 6.10: Probability density functions of absorbed power from measurements (red line) and nonlinear hydrodynamics model (blue line)

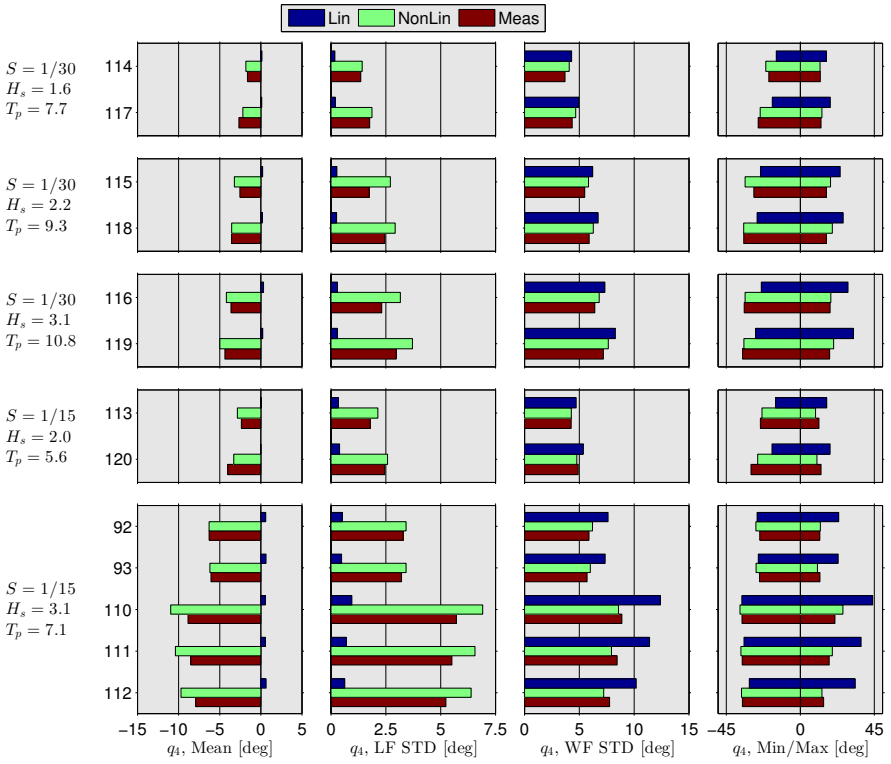

Figure 6.11: Displacement characteristics of up-wave hinge. The mean angle represent an offset from equilibrium. The low and wave frequency standard deviation (LF/WF STD) are found by filtering below/above half the peak frequency in the target wave spectrum. Min and max are the smallest and largest observed angle in the steady state portion of the time series.

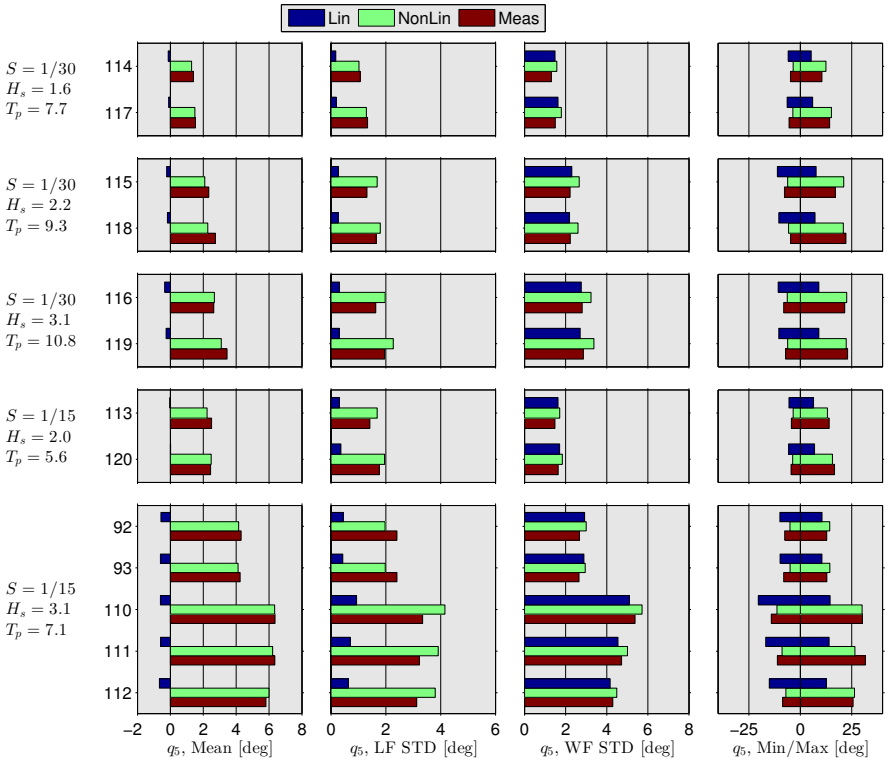

Figure 6.12: Displacement characteristics of the down-wave hinge. The mean angle represents an offset from equilibrium. The low and wave frequency standard deviation (LF/WF STD) are found by filtering below/above half the peak frequency in the target wave spectrum. Min and max are the smallest and largest observed angle in the steady state portion of the time series.

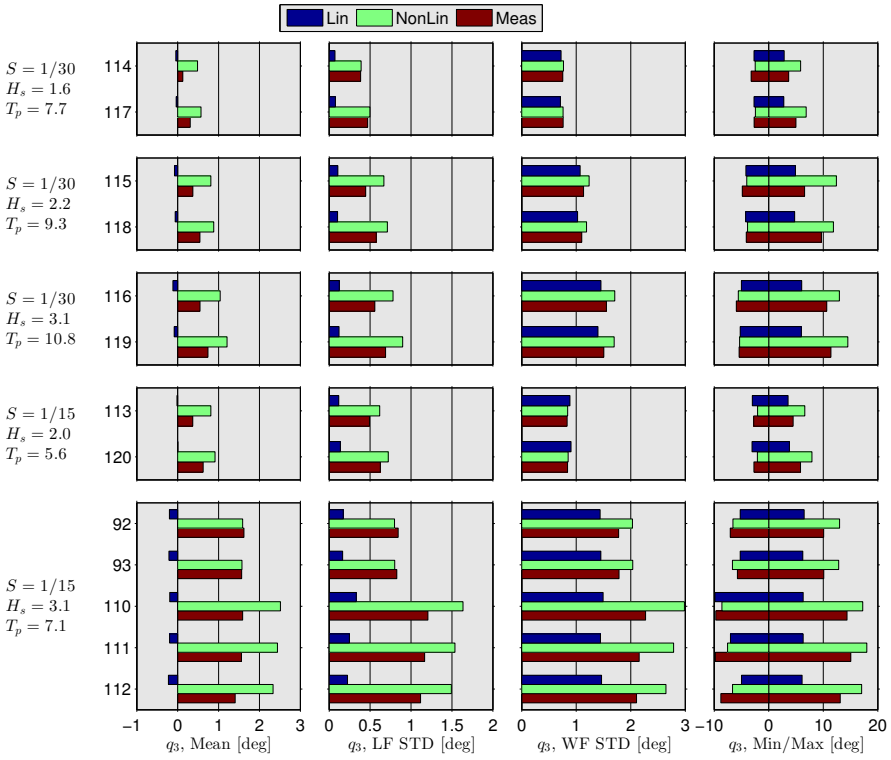

Figure 6.13: Displacement characteristics of pitch motion. The mean angle represents an offset from equilibrium. The low and wave frequency standard deviation (LF/WF STD) are found by filtering below/above half the peak frequency in the target wave spectrum. Min and max are the smallest and largest observed angle in the steady state portion of the time series.

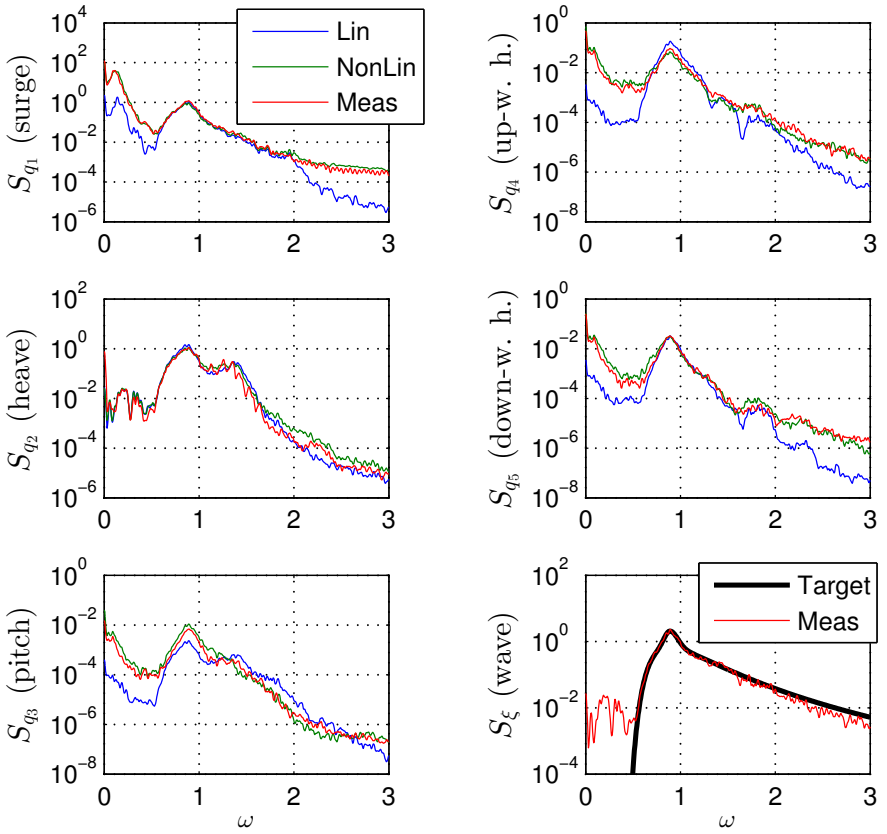

Figure 6.14: Power spectral density of all generalized coordinates and wave elevation in test 112. The target wave spectrum is a JONSWAP spectrum with $H_s = 3.1$ m, $T_p = 7.1$ s and $\gamma = 3.15$. The spectra have been smoothed using eq. (4.73) with $2\delta = 0.05$ rad/s and $\sigma = \delta/3$.

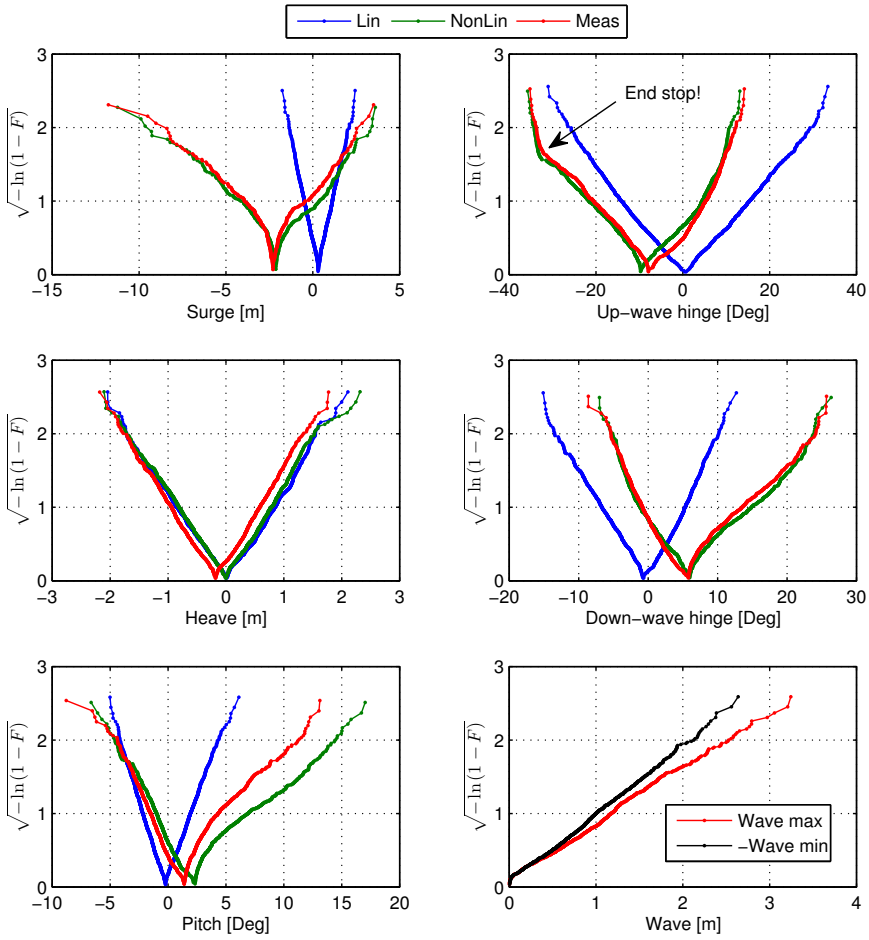

Figure 6.15: Cumulative probability distribution (F) of minima and maxima of all generalized coordinates and wave elevation in test 112. Minima and maxima are here defined as the smallest and largest value between subsequent up-crossings of the mean level.

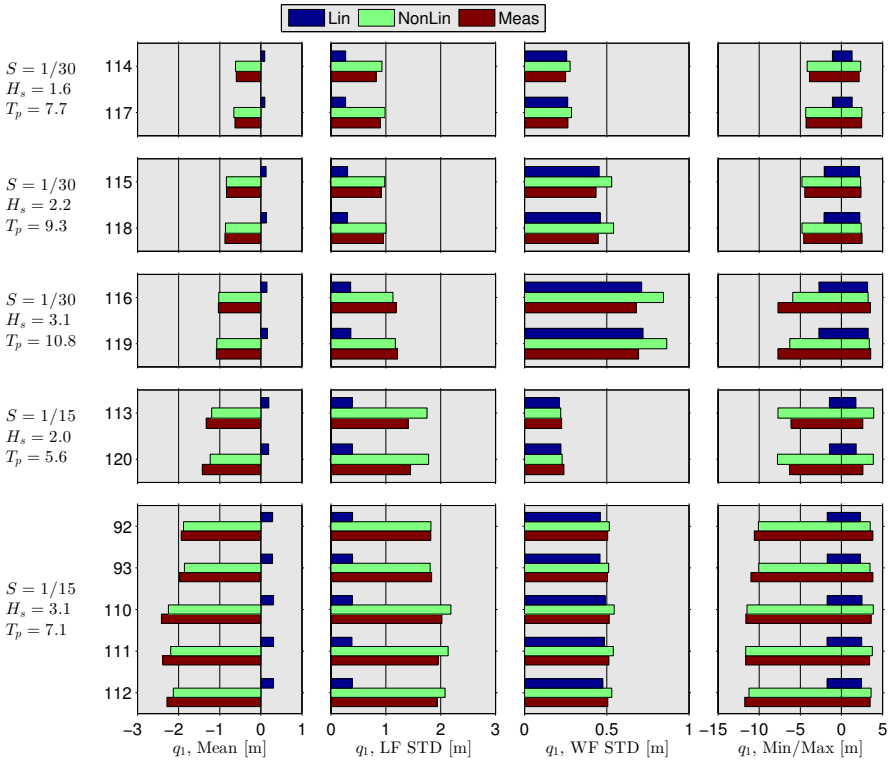

Figure 6.16: Displacement characteristics of surge. The mean angle represents an offset from equilibrium. The low and wave frequency standard deviation (LF/WF STD) are found by filtering below/above half the peak frequency in the target wave spectrum. Min and max are the smallest and largest observed angle in the steady state portion of the time series.

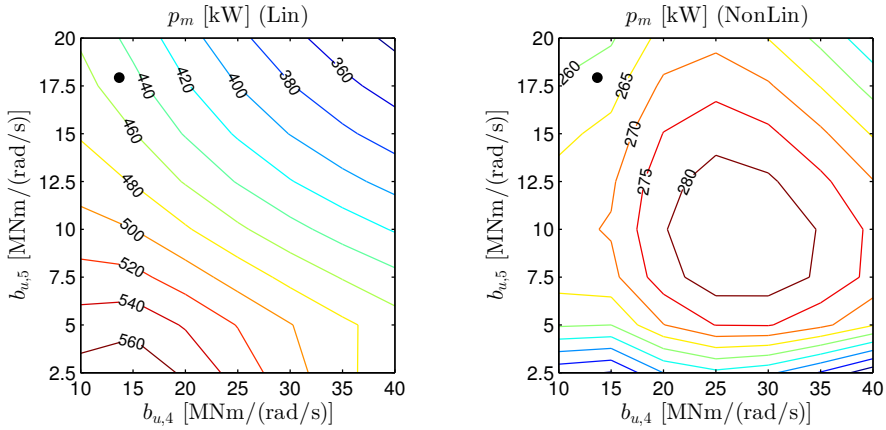

Figure 6.17: Sensitivity of mean absorbed power to the two PTO damping coefficients for a JONSWAP wave spectrum with $H_s = 3.1$ m, $T_p = 7.1$ s and $\gamma = 3.15$. The left diagram shows results from the linear hydrodynamics model (Section 6.5.5) and the right diagram shows results from the nonlinear hydrodynamics model (Section 6.5.4). The dot shows the damping coefficients used in test 112.

7 Conclusion

7.1 Summary

Chapter 2: Linear analysis of power absorption

This chapter reviews well established methods for linear frequency domain analysis of WECs oscillating in one (SDOF) or more (MDOF) degrees of freedom, including the important topic of amplitude constraints.

The SDOF case is exemplified by a semi-submerged spherical WEC oscillating in a sloped mode of motion. The influence of the slope angle and motion constraints on the power absorption is demonstrated. It is shown that the slope angle is an important parameter and that the sloped mode of motion yields efficient power absorption, especially for resistive PTO systems.

An optimization procedure for maximizing the power absorption of a MDOF WEC in regular waves is suggested. The method uses the velocities as the optimization variables and thus assumes that the PTO system is capable of delivering reactive power. Inclusion of released modes of motion (i.e. with zero PTO force) and motion constraints on the individual modes of motion are handled by the method. The optimization problem can be formulated either as a Quadratically Constrained Quadratic Program (QCQP) or a Quadratic Program (QP) (having linear constraints) and can thus be solved with widely available numerical tools. The convexity of the problem ensures that the global optimum is found. An additional constraint on the maximum allowed reactive power is also suggested. This additional constraint will however destroy the convexity of the optimization problem.

An optimization procedure for maximizing the power absorption of a MDOF WEC in irregular waves is suggested. The method assumes that the PTO impedance matrix is real, diagonal and frequency independent (i.e. zero reactive power in individual modes of motion). The damping coefficients on the diagonal of the PTO impedance matrix is used as variables in the optimization. Motion constraints and released modes of motion can be included. This optimization problem is non-convex and non-linear (neither linear nor quadratic constraints and objective function).

As an extension of the latter method, it is suggested to include the short term variability of the absorbed power in the optimization problem, giving

a multi-objective optimization problem that tries to maximize the absorbed power in a sea state, while at the same time minimizing the variability. The variability is here derived based on the co-variance matrix of velocities for the MDOF WEC.

Chapter 3: Wave radiation forces in the time domain

The main contribution in this chapter is the introduction of Vector Fitting (VF) (Gustavsen and Semlyen, 1999) as an efficient and robust method for obtaining state space representations of the strongly frequency dependent added mass and damping matrices often associated with multibody systems. For these systems, requiring high order state space models, the widely used fitting techniques based on rational transfer functions written as a ratio of two polynomials will often fail due to numerical problems. The VF method originates from the electrical power systems community, and to the author's knowledge, it has not been applied on the (water) wave radiation problem before.

The VF method is based on rational transfer functions written on a pole-residue form. Since hydrodynamic radiation forces possess special properties not necessarily shared by other systems (such as electrical power systems), a discussion of pole-residue models of radiation forces is given. Parameter constraints enforcing some of the hydrodynamic properties are also suggested. The effect of frequency truncation (lack of high frequency data) are discussed.

Passivity is an inherent property of wave radiation forces and many other physical systems. Passivity should be preserved in the rational model to avoid unstable computer simulations, and simply because it is physically correct. Methods for assessing the passivity of state space models have been developed by Semlyen and Gustavsen (2009) and an accompanying passivity enforcement method by Gustavsen (2008). The assessment method is not directly applicable to wave radiation forces because the damping is zero in the low frequency limit. The assessment method have therefore been modified in order to be valid also in this case. The enforcement method have also been modified in order to suit systems with geometrical symmetries. Floating bodies (or multibody systems) with geometrical symmetries will have sparse added mass and damping matrices with a special structure. With the original passivity enforcement method, the sparsity and structure of the matrices will be lost. The modified enforcement method will retain this sparsity and structure and utilize it to reduce the computational time of the enforcement.

Chapter 4: Equations of motion for hinged bodies

This chapter deals with establishing exact (large angle) kinematic descriptions and equations of motion for the hinged 5-body WEC in a structured fashion.

The procedure can be generalized to other systems of hinged bodies as well, and the generalization will be straightforward for systems having the same structure, i.e. for systems having one body as a common link to all other bodies.

Equations of motion are derived using two different approaches. The Newton-Euler approach is largely based on the work of Ó'Catháin et al. (2008). The alternative (more cumbersome) approach is based on Lagranges equation. The two approaches (and numerical implementations) are shown to be equivalent, which is an important quality assurance. The benefit of using collective and relative modes of motion, and to use a body fixed description of the collective velocities, is emphasized. A requirement to the time varying generalized mass and Coriolis-centrifugal matrices is formulated based on conservation of energy.

A numerical study of the hinged 5-body WEC is provided showing that a linearization of the equations of motion can be justified in many cases, especially if the power absorption is more interesting than extreme values. With linear equations of motion, a linear kinematic description will suffice. Still, the exact kinematic displacement relations are essential in obtaining the non-linear Froude-Krylov and restoring forces, which turn out to be much more important.

Chapter 5/6: Non-linear restoring and Froude-Krylov forces/Comparison between simulations and experimental results

In Chapter 5 the nonlinear Froude-Krylov (FK) and restoring forces are formulated. The two force components are formulated as a single force term obtained by integrating the undisturbed pressure (static+dynamic) over the instantaneous wetted area of the bodies and include the force and moment from the weight of the bodies. Determination of wetted area is based on linear undisturbed (irregular) waves.

Chapter 6 deals with experimental results for the hinged 5-body WEC and a comparison between experimental and numerical results. The importance of including non-linear FK and restoring forces are emphasized. Five sea-states representing typical operating conditions was chosen for the experiments and simulations. With linearized restoring and FK forces, the simulation model over-predicts (relative to experimental results) the power absorption with as much as 60% for the sea state with the largest motion amplitudes, and with 15% over-prediction as the closest result, occurring for a milder sea-state.

With non-linear restoring and FK forces, the over-prediction range from −15% (under-prediction) up to 18%. The non-linear model was also able to capture characteristic non-linear behavior. The most prominent non-linear feature is the presence of mean offset and slowly-varying motion in all modes of motion except heave. This non-linear behavior is captured by the non-linear simulation model with reasonable accuracy.

7.2 Original contributions

The author considers his main original contributions to be

1. To show that it is possible to obtain a passive, accurate state space representation of the wave radiation forces of multibody systems having strongly frequency dependent added mass and damping by using Vector Fitting and accompanying passivity assessment and enforcement methods. As part of this, the existing passivity assessment and enforcement methods have been modified to suit hydrodynamic problems. Parameter constraints relevant for wave radiation forces are suggested. One of these constraints are believed to be novel and is particularly relevant when added mass and damping are only available up to a certain frequency.

2. To establish a structured methodology for obtaining exact kinematic relations and equations of motion for the hinged 5-body WEC and similar WECs. As part of this, the importance of using collective and relative modes of motion as a mean to simplify the equations of motion are emphasized.

3. To establish a numerical model which includes non-linear Froude-Krylov and restoring forces, and to demonstrate that this model gives good agreement with model tests. The non-linear model improves the accuracy of power absorption predictions as compared with a linear model and captures important non-linear behavior typical for systems with large rotations.

4. To formulate a convex optimization problem for maximizing the absorbed power of a MDOF WEC in regular waves, including amplitude constraints on individual motion components and released modes of motion (modes of motion without PTO forces).

5. To formulate a multi-objective optimization problem for MDOF WECs in irregular waves that maximizes the mean absorbed power while at the same time minimizing the short term variability of absorbed power.

7.3 Recommendations for future work

Suggestions for future work should be categorized in two: 1) Improvements to existing analysis methods, and 2) improvements to the design of the hinged N-body WEC (with N=5 assumed in the thesis work). The bullet points below contains suggestions in both categories. The first points are device independent and focus on improved analysis methods. Towards the end of the list, increasing focus is on the design of the hinged N-body WEC.

- In Chapter 3 about state space representation of wave radiation forces, we suggested parameter constraints that are relevant when the added mass and damping is only available for frequencies up to a certain threshold ω_{max} which may be so low that the radiation damping matrix $\mathbf{B}(\omega_{max})$ have significant non-zero elements. In this case, the transient radiation forces will be inaccurate due to the frequency truncation, and the parameter constraints are expected to improve the accuracy. In this study, a general nonlinear optimization was required in order to enforce these parameter constraints without compromising on the quality of the fit. A simpler and much more efficient approach would have been to modify the Vector Fitting (VF) algorithm such as to respect these constraints (which is believed to be possible). It should however be noted that the body motions are typically insensitive to inaccuracies in the transient radiation forces (as discussed in Section 3.8.1). Improvements to the modeling of transient radiation forces is as such more of interest for the academic than the engineer.

- The results presented in this thesis shows that the inclusion of nonlinear Froude-Krylov and hydrostatic forces in the numerical model gives rise to mean and slowly varying horizontal motions that compares well with the model test results *without* the inclusion explicit second order drift forces. The calculation of second order drift forces is possible with WAMIT, but this has not been carried out for the hinged 5-body WEC. It would be interesting to compare the mean and slowly varying drift forces obtained by WAMIT with those arising from the nonlinear Froude-Krylov and hydrostatic forces. If the two contributions are to be combined, careful consideration should be made to avoid counting the same effect twice. With regard to the slowly varying part of the drift forces, it would also be interesting to compare the results of Newman's approximation with that of a full second order analysis.

- The simulations and experiments presented in this thesis are restricted to operating conditions. Still, large hinge rotations occurred, with the consequence that "hard" end-stop events was experienced. This was partly

because the up-wave hinge had too little PTO damping, both from a power absorption point of view (see Figure 6.17) and from a survivability point of view. This shows that the force provided by the PTO system should be controlled not only to maximize the power absorption, but also to avoid these end-stop events. It would be interesting to investigate the performance of a slowly tuned, resistive PTO model of the type $f(t) = b(t)\, v(t)$, where $b(t)$ is restricted to be positive, but allowed to vary slowly on a time scale corresponding to the wave groups (see discussion in Section 2.4.3). The results presented here shows that a linear model will overpredict the power absorption when the motion amplitudes are large. Hence, such slow tuning, where $b(t)$ are increased during the occurrence of large wave groups, may both increase the power absorption and lower the probability of experiencing end-stop events. Such investigations should also assess if such slow tuning would require prediction of incoming waves (a-causal control) in order to be successful.

- The aforementioned PTO model is generic. There is also a need to develop more realistic PTO models. In the case of a hydraulic PTO system, such a model may include sub-models of valves, pipelines and accumulators. There is an increasing body of literature that considers PTO models of varying complexity that will aid in such developments. How the slowly tuned PTO strategy outlined above could be incorporated (approximately) in a realistic PTO system should be considered.

- The large hinge rotations observed in the model tests are partly due to the large mean and slowly varying contribution to the rotations. It would be interesting to investigate if these slowly varying rotations can be controlled by controlling the PTO system. The sensitivity of the slowly varying rotations to the COG of the center floater and other design parameters, and the effect this has on the power absorption, should also be investigated further.

- The behavior in extreme sea states and the applicability of the nonlinear simulation model in these conditions should be investigated. This will require dedicated model tests. One important consideration is how the PTO system should be controlled (for survivability) in these severe storms and in the transition periods before and after the storms.

- WECs are "fatigue machines" since large PTO forces in sea states with large probability of occurrence is a prerequisite for a large annual power absorption. Calculation of fatigue life requires knowledge of structural design details, which is typically not determined in an early design stage. Hence, response quantities that gives an indication of fatigue problems,

independent of structural details, should be identified. The focus should be on minimizing the non-useful forces that contribute to fatigue, since minimization of the useful PTO forces necessarily gives less absorbed power unless large PTO velocities are allowed. For the hinged 5-body WEC, the non-useful constraint forces in the hinges are expected to contribute to fatigue and its minimization should be a focus in future improvements of the design.

- Future design optimizations should (ideally) be based on the minimization of a cost function that incorporate many aspects of the WEC. Average and variability of power absorption on different time scales should be included on the income side of the cost function. Volume displacement, surface area, mooring forces, fatigue inducing forces and extreme responses may be included on the cost side. Automatic optimization based i.e. on genetic algorithms may be a useful tool in combination with "engineering judgment". The hinged 5-body WEC is designed to be efficient in a wave environment with large variation of wave directionality without the need for weather vaning. In a wave climate with a dominant direction (which is often the case), this design principle may not be the best. A comparison between a unidirectional device (like the hinged 5-body WEC) vs. a weather vaning device sharing the most important design principles (hinged bodies, diagonal-like mode of motion etc.) should be made. The latter will give the possibility to optimize a "bow" that is different from the "stern".

References

Babarit, A., 2013. On the park effect in arrays of oscillating wave energy converters. Renewable Energy 58 (0), 68 – 78.

Babarit, A., Clement, A. H., Gilloteaux, J. C., June 2005. Optimization and time-domain simulation of the SEAREV wave energy converter. In: Proc. ASME 2005 24th Int'l Conf. Ocean, Offshore and Arctic Engineering (OMAE'05). Halkidiki, Greece.

Babarit, A., Hals, J., Muliawan, M., Kurniawan, A., Moan, T., Krokstad, J., 2012. Numerical benchmarking study of a selection of wave energy converters. Renewable Energy 41 (0), 44 – 63.

Babarit, A., Mouslim, H., Clement, A., Laporte-Weywada, P., 2009. On the numerical modelling of the non linear behaviour of a wave energy converter. ASME Conference Proceedings 2009 (43444), 1045–1053.

Bendat, J., 1998. Nonlinear system techniques and applications. Wiley-Interscience publication. Wiley.

Boyd, S., Vandenberghe, L., 2004. Convex Optimization. Cambridge University Press.

Bretl, J. G., 2009. A time domain model for wave induced motions coupled to energy extraction. Ph.D. thesis, The University of Michigan.

Budal, K., 1977. Theory of absorption of wave power by a system of interacting bodies. Journal of Ship Research 21, 248–253.

Budal, K., Falnes, J., 1975. A resonant point absorber of ocean waves. Nature 256, 478–479, with Corrigendum in Vol. 257, p.626.

Budal, K., Falnes, J., 1980. Interacting point absorbers with controlled motion. In: Count, B. (Ed.), Power From Sea Waves. pp. 381–399.

Chen, C.-T., 1998. Linear System Theory and Design, 3rd Edition. Oxford University Press, Inc., New York, NY, USA.

Cruz, J., 2008. Ocean wave energy: current status and future prespectives. No. XII. Springer Berlin Heidelberg.

Cummins, W., 1962. The impulse response function and ship motions. technical report 1961. Schiffstechnik 9, 101–109.

Damaren, C. J., 2000. Time-domain floating body dynamics by rational approximation of the radiation impedance and diffraction mapping. Ocean Engineering 27 (6), 687 – 705.

De Backer, G., Vantorre, M., Beels, C., De Rouck, J., Frigaard, P., 2010. Power absorption by closely spaced point absorbers in constrained conditions. Renewable Power Generation, IET 4 (6), 579–591.

Deschrijver, D., Mrozowski, M., Dhaene, T., De Zutter, D., June 2008. Macromodeling of multiport systems using a fast implementation of the vector fitting method. Microwave and Wireless Components Letters, IEEE 18 (6), 383 –385.

DNV, 2007. Recommended practice DNV-RP-C205, april 2007.

Duclos, G., Clement, A. H., Chatry, G., 2001. Absorption of outgoing waves in a numerical wave tank using a self-adaptive boundary condition. International Journal of Offshore and Polar Engineering 11 (3), 168–175.

Egeland, O., Gravdahl, J., 2002. Modeling and simulation for automatic control. Marine Cybernetics.

Evans, D. V., 1976. A theory for wave power absorption by oscillating bodies. Journal of Fluid Mechanics 77, 1–25.

Evans, D. V., 1979. Some theoretical aspects of three dimensional wave energy absorbers. In: Proc. of the 1st symposium on Wave Energy Utilization, Gothenburg, Sweeden.

Evans, D. V., 1981. Maximum wave-power absorption under motion constraints. Applied Ocean Research 3, 200–203.

Falcão, A. O., 2008. Phase control through load control of oscillating-body wave energy converters with hydraulic pto system. Ocean Engineering 35, 358 – 366.

Falnes, J., 1980. Radiation impedance matrix and optimum power absorption for interacting oscillators in surface waves. Applied Ocean Research 2, 75–80.

Falnes, J., 2002. Ocean Waves and Oscillating Systems: Linear Interactions Including Wave-Energy Extraction. Cambridge University Press.

Faltinsen, O., 1990. Sea Loads on Ships and Offshore Structures. Cambridge Ocean Technology Series. Cambridge University Press.

Folley, M., Babarit, A. l., Child, B., Forehand, D., O'Boyle, L., Silverthorne, K., Spinneken, J., Stratigaki, V., Troch, P., 2012. A review of numerical modeling of wave energy converter arrays. In: International conference on ocean, offshore and arctic engineering, Proceedings. ASME, pp. 1–11.

Gilloteaux, J., Bacelli, G., Ringwood, J., 2008. A Non-Linear Potential Model to Predict Large-Amplitudes-Motions: Application to a Multi-Body Wave Energy Converter. pp. 934–940.

Goda, Y., Suzuki, Y., 1976. Estimation of incident and reflected waves in random wave experiments. In: Proceedings of 15th ICCE, ASCE. pp. 828–845.

Greenhow, M., 1986. High- and low-frequency asymptotic consequences of the Kramers-Kronig relations. Journal of Engineering Mathematics 20, 293–306.

Gustavsen, B., july 2006. Improving the pole relocating properties of vector fitting. Power Delivery, IEEE Transactions on 21 (3), 1587 –1592.

Gustavsen, B., oct. 2008. Fast passivity enforcement for pole-residue models by perturbation of residue matrix eigenvalues. Power Delivery, IEEE Transactions on 23 (4), 2278 –2285.

Gustavsen, B., 2012. The vector fitting web site (accessed 16. nov. 2012).

Gustavsen, B., Semlyen, A., July 1999. Rational approximation of frequency domain responses by vector fitting. IEEE Trans. Power Delivery 14 (3), 1052 –1061.

Gustavsen, B., Semlyen, A., July 2004. A robust approach for system identification in the frequency domain. Power Delivery, IEEE Transactions on 19 (3), 1167 – 1173.

Hals, J., 2010. Modelling and phase control of wave-energy converters. Ph.D. thesis, Norwegian University of Science and Technology.

Hals, J., Falnes, J., Moan, T., 2011. A comparison of selected strategies for adaptive control of wave energy converters. Journal of Offshore Mechanics and Arctic Engineering 133(3).

Hals, J., Taghipour, R., Moan, T., 2007. Dynamics of a force-compensated two-body wave energy converter in heave with hydraulic power take-off subject to phase control. In: Proc. of the 7th European Wave and Tidal Energy Conference, Porto, Portugal.

Isaacson, M., 1991. Measurement of regular wave reflection. Journal of waterway, port, coastal, and ocean engineering 117 (6), 553–569.

Jefferys, E., 1987. Directional seas should be ergodic. Applied Ocean Research 9 (4), 186 – 191.

Kailath, T., 1980. Linear Systems. Prentice-Hall information and system sciences series. Prentice Hall.

Karnopp, D., Margolis, D., Rosenberg, R., 2006. System Dynamics: Modeling, Simulation, and Control of Mechatronic Systems. John Wiley & Sons.

Khalil, H., 2002. Nonlinear Systems. Prentice Hall.

Linton, C. M., Evans, D. V., 1992. The radiation and scattering of surface waves by a vertical circular cylinder in a channel. Philosophical Transactions: Physical Sciences and Engineering 338 (1650), pp. 325–357.

Lopes, M., Hals, J., Gomes, R., Moan, T., Gato, L., Falcão, A. O., 2009. Experimental and numerical investigation of non-predictive phase-control strategies for a point-absorbing wave energy converter. Ocean Engineering 36 (5), 386 – 402.

Meirovitch, L., 2004. Methods of Analytical Dynamics. Dover.

Merigaud, A., Gilloteaux, J., Ringwood, J., July 2012. A nonlinear extension for linear boundary element methods in wave energy device modelling. In: Proc. ASME 2012 31th Int'l Conf. Ocean, Offshore and Arctic Engineering (OMAE'12). Rio de Janeiro, Brazil.

Naess, A., Moan, T., 2012. Stochastic Dynamics of Marine Structures. Cambridge University Press.

Newman, J., 1974. Second-order, slowly-varying forces on vessels in irregular waves.

Newman, J., 1977. Marine Hydrodynamics. MIT Press.

Newman, J. N., 1976. The interaction of stationary vessels with regular waves. In: Proceedings of the 11th Symposium on Naval Hydrodynamics.

Newman, J. N., 2001. Wave effects on multiple bodies. Hydrodynamics in Ship and Ocean Engineering 2001 (April), 3–26.

Ó'Catháin, M., Leira, B., Ringwood, J., Gilloteaux, J., 2008. A modelling methodology for multi-body systems with application to wave-energy devices. Ocean Engineering 35 (13), 1381–1387.

Ogilvie, T., July 1964. Recent progress towards the understanding and prediction of ship motions. In: Sixth Symposium on Naval Hydrodynamics.

Perez, T., Fossen, T. I., 2007. Kinematic models for manoeuvring and seakeeping of marine vessels. Modeling, Identification and Control 28 (1), 19–30.

Perez, T., Fossen, T. I., 2008. A derivation of high-frequency asymptotic values of 3d added mass and damping based on properties of the cummins' equation. Journal of Maritime Research 5 (1), 65–78.

Perez, T., Fossen, T. I., 2009. A matlab toolbox for parametric identification of radiation-force models of ships and offshore structures. Modeling, Identification and Control 30 (1), 1–15.

Perez, T., Fossen, T. I., 2011. Practical aspects of frequency-domain identification of dynamic models of marine structures from hydrodynamic data. Ocean Engineering 38 (2-3), 426–435.

Pizer, D., 1994. Numerical modelling of wave energy absorbers. Tech. rep., University of Edinburgh.

Rogne, Ø. Y., 2007. Dynamic analysis of a wave energy converter - a frequency domain approach. Master's thesis, NTNU.

Rogne, Ø. Y., Ersdal, S., Moan, T., July 2012. Numerical and experimental investigation of a novel wave energy converter. In: Proc. ASME 2012 31th Int'l Conf. Ocean, Offshore and Arctic Engineering (OMAE'12). Rio de Janeiro, Brazil.

Rogne, Ø. Y., Moan, T., Ersdal, S., 2013. Identification of passive state-space models of strongly frequency dependent wave radiation forces. Submitted to Ocean Engineering.

Rogne, Ø. Y., Pedersen, E., 2012. Bond graph modeling of a multibody wave energy converter. In: In Proceedings of the International Conference on Bond Graph Modeling (ICBGM).

Sanathanan, C., Koerner, J., Jan 1963. Transfer function synthesis as a ratio of two complex polynomials. Automatic Control, IEEE Transactions on 8 (1), 56 – 58.

Sciavicco, L., Siciliano, B., 2000. Modelling and control of robot manipulators. Advanced textbooks in control and signal processing. Springer.

Semlyen, A., Gustavsen, B., Jan. 2009. A half-size singularity test matrix for fast and reliable passivity assessment of rational models. Power Delivery, IEEE Transactions on 24 (1), 345 –351.

Shorten, R., Curran, P., Wulff, K., Zeheb, E., June 2008. A note on spectral conditions for positive realness of transfer function matrices. Automatic Control, IEEE Transactions on 53 (5), 1258 –1261.

Stansberg, C. T., 1997. Linear and non-linear system identification in model testing. In: International conference on "non-linear aspects of physical model tests".

Taghipour, R., Moan, T., 2008. Efficient frequency-domain analysis of dynamic response for the multi-body wave energy converter in multi-directional waves. In: Proc. of the 18th International Offshore and Polar Engineering Conference.

Taghipour, R., Perez, T., Moan, T., 2008. Hybrid frequency-time domain models for dynamic response analysis of marine structures. Ocean Engineering 35 (7), 685 – 705.

Unneland, K., 2007. Identification and order reduction of radiation force models of marine structures. Ph.D. thesis, Norwegian University of Science and Technology.

Weller, S., Stallard, T., Stansby, P., 2010. Experimental measurements of irregular wave interaction factors in closely spaced arrays. Renewable Power Generation, IET 4 (6), 628–637.

Yu, Z., Falnes, J., 1995. State-space modelling of a vertical cylinder in heave. Applied Ocean Research 17, 265–275.

Yu, Z., Falnes, J., 1998. State-space modelling of dynamic systems in ocean engineering. Journal of Hydrodynamics 1, 1–17.

Previous PhD theses published at the Departement of Marine Technology
(earlier: Faculty of Marine Technology)
NORWEGIAN UNIVERSITY OF SCIENCE AND TECHNOLOGY

Report No.	Author	Title
	Kavlie, Dag	Optimization of Plane Elastic Grillages, 1967
	Hansen, Hans R.	Man-Machine Communication and Data-Storage Methods in Ship Structural Design, 1971
	Gisvold, Kaare M.	A Method for non-linear mixed -integer programming and its Application to Design Problems, 1971
	Lund, Sverre	Tanker Frame Optimalization by means of SUMT-Transformation and Behaviour Models, 1971
	Vinje, Tor	On Vibration of Spherical Shells Interacting with Fluid, 1972
	Lorentz, Jan D.	Tank Arrangement for Crude Oil Carriers in Accordance with the new Anti-Pollution Regulations, 1975
	Carlsen, Carl A.	Computer-Aided Design of Tanker Structures, 1975
	Larsen, Carl M.	Static and Dynamic Analysis of Offshore Pipelines during Installation, 1976
UR-79-01	Brigt Hatlestad, MK	The finite element method used in a fatigue evaluation of fixed offshore platforms. (Dr.Ing. Thesis)
UR-79-02	Erik Pettersen, MK	Analysis and design of cellular structures. (Dr.Ing. Thesis)
UR-79-03	Sverre Valsgård, MK	Finite difference and finite element methods applied to nonlinear analysis of plated structures. (Dr.Ing. Thesis)
UR-79-04	Nils T. Nordsve, MK	Finite element collapse analysis of structural members considering imperfections and stresses due to fabrication. (Dr.Ing. Thesis)
UR-79-05	Ivar J. Fylling, MK	Analysis of towline forces in ocean towing systems. (Dr.Ing. Thesis)
UR-80-06	Nils Sandsmark, MM	Analysis of Stationary and Transient Heat Conduction by the Use of the Finite Element Method. (Dr.Ing. Thesis)
UR-80-09	Sverre Haver, MK	Analysis of uncertainties related to the stochastic modeling of ocean waves. (Dr.Ing. Thesis)
UR-81-15	Odland, Jonas	On the Strength of welded Ring stiffened cylindrical Shells primarily subjected to axial Compression
UR-82-17	Engesvik, Knut	Analysis of Uncertainties in the fatigue Capacity of

		Welded Joints
UR-82-18	Rye, Henrik	Ocean wave groups
UR-83-30	Eide, Oddvar Inge	On Cumulative Fatigue Damage in Steel Welded Joints
UR-83-33	Mo, Olav	Stochastic Time Domain Analysis of Slender Offshore Structures
UR-83-34	Amdahl, Jørgen	Energy absorption in Ship-platform impacts
UR-84-37	Mørch, Morten	Motions and mooring forces of semi submersibles as determined by full-scale measurements and theoretical analysis
UR-84-38	Soares, C. Guedes	Probabilistic models for load effects in ship structures
UR-84-39	Aarsnes, Jan V.	Current forces on ships
UR-84-40	Czujko, Jerzy	Collapse Analysis of Plates subjected to Biaxial Compression and Lateral Load
UR-85-46	Alf G. Engseth, MK	Finite element collapse analysis of tubular steel offshore structures. (Dr.Ing. Thesis)
UR-86-47	Dengody Sheshappa, MP	A Computer Design Model for Optimizing Fishing Vessel Designs Based on Techno-Economic Analysis. (Dr.Ing. Thesis)
UR-86-48	Vidar Aanesland, MH	A Theoretical and Numerical Study of Ship Wave Resistance. (Dr.Ing. Thesis)
UR-86-49	Heinz-Joachim Wessel, MK	Fracture Mechanics Analysis of Crack Growth in Plate Girders. (Dr.Ing. Thesis)
UR-86-50	Jon Taby, MK	Ultimate and Post-ultimate Strength of Dented Tubular Members. (Dr.Ing. Thesis)
UR-86-51	Walter Lian, MH	A Numerical Study of Two-Dimensional Separated Flow Past Bluff Bodies at Moderate KC-Numbers. (Dr.Ing. Thesis)
UR-86-52	Bjørn Sortland, MH	Force Measurements in Oscillating Flow on Ship Sections and Circular Cylinders in a U-Tube Water Tank. (Dr.Ing. Thesis)
UR-86-53	Kurt Strand, MM	A System Dynamic Approach to One-dimensional Fluid Flow. (Dr.Ing. Thesis)
UR-86-54	Arne Edvin Løken, MH	Three Dimensional Second Order Hydrodynamic Effects on Ocean Structures in Waves. (Dr.Ing. Thesis)
UR-86-55	Sigurd Falch, MH	A Numerical Study of Slamming of Two-Dimensional Bodies. (Dr.Ing. Thesis)
UR-87-56	Arne Braathen, MH	Application of a Vortex Tracking Method to the Prediction of Roll Damping of a Two-Dimension Floating Body. (Dr.Ing. Thesis)

UR-87-57	Bernt Leira, MK	Gaussian Vector Processes for Reliability Analysis involving Wave-Induced Load Effects. (Dr.Ing. Thesis)
UR-87-58	Magnus Småvik, MM	Thermal Load and Process Characteristics in a Two-Stroke Diesel Engine with Thermal Barriers (in Norwegian). (Dr.Ing. Thesis)
MTA-88-59	Bernt Arild Bremdal, MP	An Investigation of Marine Installation Processes – A Knowledge - Based Planning Approach. (Dr.Ing. Thesis)
MTA-88-60	Xu Jun, MK	Non-linear Dynamic Analysis of Space-framed Offshore Structures. (Dr.Ing. Thesis)
MTA-89-61	Gang Miao, MH	Hydrodynamic Forces and Dynamic Responses of Circular Cylinders in Wave Zones. (Dr.Ing. Thesis)
MTA-89-62	Martin Greenhow, MH	Linear and Non-Linear Studies of Waves and Floating Bodies. Part I and Part II. (Dr.Techn. Thesis)
MTA-89-63	Chang Li, MH	Force Coefficients of Spheres and Cubes in Oscillatory Flow with and without Current. (Dr.Ing. Thesis
MTA-89-64	Hu Ying, MP	A Study of Marketing and Design in Development of Marine Transport Systems. (Dr.Ing. Thesis)
MTA-89-65	Arild Jæger, MH	Seakeeping, Dynamic Stability and Performance of a Wedge Shaped Planing Hull. (Dr.Ing. Thesis)
MTA-89-66	Chan Siu Hung, MM	The dynamic characteristics of tilting-pad bearings
MTA-89-67	Kim Wikstrøm, MP	Analysis av projekteringen for ett offshore projekt. (Licenciat-avhandling)
MTA-89-68	Jiao Guoyang, MK	Reliability Analysis of Crack Growth under Random Loading, considering Model Updating. (Dr.Ing. Thesis)
MTA-89-69	Arnt Olufsen, MK	Uncertainty and Reliability Analysis of Fixed Offshore Structures. (Dr.Ing. Thesis)
MTA-89-70	Wu Yu-Lin, MR	System Reliability Analyses of Offshore Structures using improved Truss and Beam Models. (Dr.Ing. Thesis)
MTA-90-71	Jan Roger Hoff, MH	Three-dimensional Green function of a vessel with forward speed in waves. (Dr.Ing. Thesis)
MTA-90-72	Rong Zhao, MH	Slow-Drift Motions of a Moored Two-Dimensional Body in Irregular Waves. (Dr.Ing. Thesis)
MTA-90-73	Atle Minsaas, MP	Economical Risk Analysis. (Dr.Ing. Thesis)
MTA-90-74	Knut-Aril Farnes, MK	Long-term Statistics of Response in Non-linear Marine Structures. (Dr.Ing. Thesis)
MTA-90-75	Torbjørn Sotberg, MK	Application of Reliability Methods for Safety Assessment of Submarine Pipelines. (Dr.Ing.

		Thesis)
MTA-90-76	Zeuthen, Steffen, MP	SEAMAID. A computational model of the design process in a constraint-based logic programming environment. An example from the offshore domain. (Dr.Ing. Thesis)
MTA-91-77	Haagensen, Sven, MM	Fuel Dependant Cyclic Variability in a Spark Ignition Engine - An Optical Approach. (Dr.Ing. Thesis)
MTA-91-78	Løland, Geir, MH	Current forces on and flow through fish farms. (Dr.Ing. Thesis)
MTA-91-79	Hoen, Christopher, MK	System Identification of Structures Excited by Stochastic Load Processes. (Dr.Ing. Thesis)
MTA-91-80	Haugen, Stein, MK	Probabilistic Evaluation of Frequency of Collision between Ships and Offshore Platforms. (Dr.Ing. Thesis)
MTA-91-81	Sødahl, Nils, MK	Methods for Design and Analysis of Flexible Risers. (Dr.Ing. Thesis)
MTA-91-82	Ormberg, Harald, MK	Non-linear Response Analysis of Floating Fish Farm Systems. (Dr.Ing. Thesis)
MTA-91-83	Marley, Mark J., MK	Time Variant Reliability under Fatigue Degradation. (Dr.Ing. Thesis)
MTA-91-84	Krokstad, Jørgen R., MH	Second-order Loads in Multidirectional Seas. (Dr.Ing. Thesis)
MTA-91-85	Molteberg, Gunnar A., MM	The Application of System Identification Techniques to Performance Monitoring of Four Stroke Turbocharged Diesel Engines. (Dr.Ing. Thesis)
MTA-92-86	Mørch, Hans Jørgen Bjelke, MH	Aspects of Hydrofoil Design: with Emphasis on Hydrofoil Interaction in Calm Water. (Dr.Ing. Thesis)
MTA-92-87	Chan Siu Hung, MM	Nonlinear Analysis of Rotordynamic Instabilities in Highspeed Turbomachinery. (Dr.Ing. Thesis)
MTA-92-88	Bessason, Bjarni, MK	Assessment of Earthquake Loading and Response of Seismically Isolated Bridges. (Dr.Ing. Thesis)
MTA-92-89	Langli, Geir, MP	Improving Operational Safety through exploitation of Design Knowledge - an investigation of offshore platform safety. (Dr.Ing. Thesis)
MTA-92-90	Sævik, Svein, MK	On Stresses and Fatigue in Flexible Pipes. (Dr.Ing. Thesis)
MTA-92-91	Ask, Tor Ø., MM	Ignition and Flame Growth in Lean Gas-Air Mixtures. An Experimental Study with a Schlieren System. (Dr.Ing. Thesis)
MTA-86-92	Hessen, Gunnar, MK	Fracture Mechanics Analysis of Stiffened Tubular Members. (Dr.Ing. Thesis)

MTA-93-93	Steinebach, Christian, MM	Knowledge Based Systems for Diagnosis of Rotating Machinery. (Dr.Ing. Thesis)
MTA-93-94	Dalane, Jan Inge, MK	System Reliability in Design and Maintenance of Fixed Offshore Structures. (Dr.Ing. Thesis)
MTA-93-95	Steen, Sverre, MH	Cobblestone Effect on SES. (Dr.Ing. Thesis)
MTA-93-96	Karunakaran, Daniel, MK	Nonlinear Dynamic Response and Reliability Analysis of Drag-dominated Offshore Platforms. (Dr.Ing. Thesis)
MTA-93-97	Hagen, Arnulf, MP	The Framework of a Design Process Language. (Dr.Ing. Thesis)
MTA-93-98	Nordrik, Rune, MM	Investigation of Spark Ignition and Autoignition in Methane and Air Using Computational Fluid Dynamics and Chemical Reaction Kinetics. A Numerical Study of Ignition Processes in Internal Combustion Engines. (Dr.Ing. Thesis)
MTA-94-99	Passano, Elizabeth, MK	Efficient Analysis of Nonlinear Slender Marine Structures. (Dr.Ing. Thesis)
MTA-94-100	Kvålsvold, Jan, MH	Hydroelastic Modelling of Wetdeck Slamming on Multihull Vessels. (Dr.Ing. Thesis)
MTA-94-102	Bech, Sidsel M., MK	Experimental and Numerical Determination of Stiffness and Strength of GRP/PVC Sandwich Structures. (Dr.Ing. Thesis)
MTA-95-103	Paulsen, Hallvard, MM	A Study of Transient Jet and Spray using a Schlieren Method and Digital Image Processing. (Dr.Ing. Thesis)
MTA-95-104	Hovde, Geir Olav, MK	Fatigue and Overload Reliability of Offshore Structural Systems, Considering the Effect of Inspection and Repair. (Dr.Ing. Thesis)
MTA-95-105	Wang, Xiaozhi, MK	Reliability Analysis of Production Ships with Emphasis on Load Combination and Ultimate Strength. (Dr.Ing. Thesis)
MTA-95-106	Ulstein, Tore, MH	Nonlinear Effects of a Flexible Stern Seal Bag on Cobblestone Oscillations of an SES. (Dr.Ing. Thesis)
MTA-95-107	Solaas, Frøydis, MH	Analytical and Numerical Studies of Sloshing in Tanks. (Dr.Ing. Thesis)
MTA-95-108	Hellan, Øyvind, MK	Nonlinear Pushover and Cyclic Analyses in Ultimate Limit State Design and Reassessment of Tubular Steel Offshore Structures. (Dr.Ing. Thesis)
MTA-95-109	Hermundstad, Ole A., MK	Theoretical and Experimental Hydroelastic Analysis of High Speed Vessels. (Dr.Ing. Thesis)
MTA-96-110	Bratland, Anne K., MH	Wave-Current Interaction Effects on Large-Volume Bodies in Water of Finite Depth. (Dr.Ing. Thesis)
MTA-96-111	Herfjord, Kjell, MH	A Study of Two-dimensional Separated Flow by a Combination of the Finite Element Method and

		Navier-Stokes Equations. (Dr.Ing. Thesis)
MTA-96-112	Æsøy, Vilmar, MM	Hot Surface Assisted Compression Ignition in a Direct Injection Natural Gas Engine. (Dr.Ing. Thesis)
MTA-96-113	Eknes, Monika L., MK	Escalation Scenarios Initiated by Gas Explosions on Offshore Installations. (Dr.Ing. Thesis)
MTA-96-114	Erikstad, Stein O., MP	A Decision Support Model for Preliminary Ship Design. (Dr.Ing. Thesis)
MTA-96-115	Pedersen, Egil, MH	A Nautical Study of Towed Marine Seismic Streamer Cable Configurations. (Dr.Ing. Thesis)
MTA-97-116	Moksnes, Paul O., MM	Modelling Two-Phase Thermo-Fluid Systems Using Bond Graphs. (Dr.Ing. Thesis)
MTA-97-117	Halse, Karl H., MK	On Vortex Shedding and Prediction of Vortex-Induced Vibrations of Circular Cylinders. (Dr.Ing. Thesis)
MTA-97-118	Igland, Ragnar T., MK	Reliability Analysis of Pipelines during Laying, considering Ultimate Strength under Combined Loads. (Dr.Ing. Thesis)
MTA-97-119	Pedersen, Hans-P., MP	Levendefiskteknologi for fiskefartøy. (Dr.Ing. Thesis)
MTA-98-120	Vikestad, Kyrre, MK	Multi-Frequency Response of a Cylinder Subjected to Vortex Shedding and Support Motions. (Dr.Ing. Thesis)
MTA-98-121	Azadi, Mohammad R. E., MK	Analysis of Static and Dynamic Pile-Soil-Jacket Behaviour. (Dr.Ing. Thesis)
MTA-98-122	Ulltang, Terje, MP	A Communication Model for Product Information. (Dr.Ing. Thesis)
MTA-98-123	Torbergsen, Erik, MM	Impeller/Diffuser Interaction Forces in Centrifugal Pumps. (Dr.Ing. Thesis)
MTA-98-124	Hansen, Edmond, MH	A Discrete Element Model to Study Marginal Ice Zone Dynamics and the Behaviour of Vessels Moored in Broken Ice. (Dr.Ing. Thesis)
MTA-98-125	Videiro, Paulo M., MK	Reliability Based Design of Marine Structures. (Dr.Ing. Thesis)
MTA-99-126	Mainçon, Philippe, MK	Fatigue Reliability of Long Welds Application to Titanium Risers. (Dr.Ing. Thesis)
MTA-99-127	Haugen, Elin M., MH	Hydroelastic Analysis of Slamming on Stiffened Plates with Application to Catamaran Wetdecks. (Dr.Ing. Thesis)
MTA-99-128	Langhelle, Nina K., MK	Experimental Validation and Calibration of Nonlinear Finite Element Models for Use in Design of Aluminium Structures Exposed to Fire. (Dr.Ing. Thesis)
MTA-99-	Berstad, Are J., MK	Calculation of Fatigue Damage in Ship Structures.

129		(Dr.Ing. Thesis)
MTA-99-130	Andersen, Trond M., MM	Short Term Maintenance Planning. (Dr.Ing. Thesis)
MTA-99-131	Tveiten, Bård Wathne, MK	Fatigue Assessment of Welded Aluminium Ship Details. (Dr.Ing. Thesis)
MTA-99-132	Søreide, Fredrik, MP	Applications of underwater technology in deep water archaeology. Principles and practice. (Dr.Ing. Thesis)
MTA-99-133	Tønnessen, Rune, MH	A Finite Element Method Applied to Unsteady Viscous Flow Around 2D Blunt Bodies With Sharp Corners. (Dr.Ing. Thesis)
MTA-99-134	Elvekrok, Dag R., MP	Engineering Integration in Field Development Projects in the Norwegian Oil and Gas Industry. The Supplier Management of Norne. (Dr.Ing. Thesis)
MTA-99-135	Fagerholt, Kjetil, MP	Optimeringsbaserte Metoder for Ruteplanlegging innen skipsfart. (Dr.Ing. Thesis)
MTA-99-136	Bysveen, Marie, MM	Visualization in Two Directions on a Dynamic Combustion Rig for Studies of Fuel Quality. (Dr.Ing. Thesis)
MTA-2000-137	Storteig, Eskild, MM	Dynamic characteristics and leakage performance of liquid annular seals in centrifugal pumps. (Dr.Ing. Thesis)
MTA-2000-138	Sagli, Gro, MK	Model uncertainty and simplified estimates of long term extremes of hull girder loads in ships. (Dr.Ing. Thesis)
MTA-2000-139	Tronstad, Harald, MK	Nonlinear analysis and design of cable net structures like fishing gear based on the finite element method. (Dr.Ing. Thesis)
MTA-2000-140	Kroneberg, André, MP	Innovation in shipping by using scenarios. (Dr.Ing. Thesis)
MTA-2000-141	Haslum, Herbjørn Alf, MH	Simplified methods applied to nonlinear motion of spar platforms. (Dr.Ing. Thesis)
MTA-2001-142	Samdal, Ole Johan, MM	Modelling of Degradation Mechanisms and Stressor Interaction on Static Mechanical Equipment Residual Lifetime. (Dr.Ing. Thesis)
MTA-2001-143	Baarholm, Rolf Jarle, MH	Theoretical and experimental studies of wave impact underneath decks of offshore platforms. (Dr.Ing. Thesis)
MTA-2001-144	Wang, Lihua, MK	Probabilistic Analysis of Nonlinear Wave-induced Loads on Ships. (Dr.Ing. Thesis)
MTA-2001-145	Kristensen, Odd H. Holt, MK	Ultimate Capacity of Aluminium Plates under Multiple Loads, Considering HAZ Properties. (Dr.Ing. Thesis)
MTA-2001-146	Greco, Marilena, MH	A Two-Dimensional Study of Green-Water Loading. (Dr.Ing. Thesis)

MTA-2001-147	Heggelund, Svein E., MK	Calculation of Global Design Loads and Load Effects in Large High Speed Catamarans. (Dr.Ing. Thesis)
MTA-2001-148	Babalola, Olusegun T., MK	Fatigue Strength of Titanium Risers – Defect Sensitivity. (Dr.Ing. Thesis)
MTA-2001-149	Mohammed, Abuu K., MK	Nonlinear Shell Finite Elements for Ultimate Strength and Collapse Analysis of Ship Structures. (Dr.Ing. Thesis)
MTA-2002-150	Holmedal, Lars E., MH	Wave-current interactions in the vicinity of the sea bed. (Dr.Ing. Thesis)
MTA-2002-151	Rognebakke, Olav F., MH	Sloshing in rectangular tanks and interaction with ship motions. (Dr.Ing. Thesis)
MTA-2002-152	Lader, Pål Furset, MH	Geometry and Kinematics of Breaking Waves. (Dr.Ing. Thesis)
MTA-2002-153	Yang, Qinzheng, MH	Wash and wave resistance of ships in finite water depth. (Dr.Ing. Thesis)
MTA-2002-154	Melhus, Øyvin, MM	Utilization of VOC in Diesel Engines. Ignition and combustion of VOC released by crude oil tankers. (Dr.Ing. Thesis)
MTA-2002-155	Ronæss, Marit, MH	Wave Induced Motions of Two Ships Advancing on Parallel Course. (Dr.Ing. Thesis)
MTA-2002-156	Økland, Ole D., MK	Numerical and experimental investigation of whipping in twin hull vessels exposed to severe wet deck slamming. (Dr.Ing. Thesis)
MTA-2002-157	Ge, Chunhua, MK	Global Hydroelastic Response of Catamarans due to Wet Deck Slamming. (Dr.Ing. Thesis)
MTA-2002-158	Byklum, Eirik, MK	Nonlinear Shell Finite Elements for Ultimate Strength and Collapse Analysis of Ship Structures. (Dr.Ing. Thesis)
IMT-2003-1	Chen, Haibo, MK	Probabilistic Evaluation of FPSO-Tanker Collision in Tandem Offloading Operation. (Dr.Ing. Thesis)
IMT-2003-2	Skaugset, Kjetil Bjørn, MK	On the Suppression of Vortex Induced Vibrations of Circular Cylinders by Radial Water Jets. (Dr.Ing. Thesis)
IMT-2003-3	Chezhian, Muthu	Three-Dimensional Analysis of Slamming. (Dr.Ing. Thesis)
IMT-2003-4	Buhaug, Øyvind	Deposit Formation on Cylinder Liner Surfaces in Medium Speed Engines. (Dr.Ing. Thesis)
IMT-2003-5	Tregde, Vidar	Aspects of Ship Design: Optimization of Aft Hull with Inverse Geometry Design. (Dr.Ing. Thesis)
IMT-2003-6	Wist, Hanne Therese	Statistical Properties of Successive Ocean Wave Parameters. (Dr.Ing. Thesis)

IMT-2004-7	Ransau, Samuel	Numerical Methods for Flows with Evolving Interfaces. (Dr.Ing. Thesis)
IMT-2004-8	Soma, Torkel	Blue-Chip or Sub-Standard. A data interrogation approach of identity safety characteristics of shipping organization. (Dr.Ing. Thesis)
IMT-2004-9	Ersdal, Svein	An experimental study of hydrodynamic forces on cylinders and cables in near axial flow. (Dr.Ing. Thesis)
IMT-2005-10	Brodtkorb, Per Andreas	The Probability of Occurrence of Dangerous Wave Situations at Sea. (Dr.Ing. Thesis)
IMT-2005-11	Yttervik, Rune	Ocean current variability in relation to offshore engineering. (Dr.Ing. Thesis)
IMT-2005-12	Fredheim, Arne	Current Forces on Net-Structures. (Dr.Ing. Thesis)
IMT-2005-13	Heggernes, Kjetil	Flow around marine structures. (Dr.Ing. Thesis
IMT-2005-14	Fouques, Sebastien	Lagrangian Modelling of Ocean Surface Waves and Synthetic Aperture Radar Wave Measurements. (Dr.Ing. Thesis)
IMT-2006-15	Holm, Håvard	Numerical calculation of viscous free surface flow around marine structures. (Dr.Ing. Thesis)
IMT-2006-16	Bjørheim, Lars G.	Failure Assessment of Long Through Thickness Fatigue Cracks in Ship Hulls. (Dr.Ing. Thesis)
IMT-2006-17	Hansson, Lisbeth	Safety Management for Prevention of Occupational Accidents. (Dr.Ing. Thesis)
IMT-2006-18	Zhu, Xinying	Application of the CIP Method to Strongly Nonlinear Wave-Body Interaction Problems. (Dr.Ing. Thesis)
IMT-2006-19	Reite, Karl Johan	Modelling and Control of Trawl Systems. (Dr.Ing. Thesis)
IMT-2006-20	Smogeli, Øyvind Notland	Control of Marine Propellers. From Normal to Extreme Conditions. (Dr.Ing. Thesis)
IMT-2007-21	Storhaug, Gaute	Experimental Investigation of Wave Induced Vibrations and Their Effect on the Fatigue Loading of Ships. (Dr.Ing. Thesis)
IMT-2007-22	Sun, Hui	A Boundary Element Method Applied to Strongly Nonlinear Wave-Body Interaction Problems. (PhD Thesis, CeSOS)
IMT-2007-23	Rustad, Anne Marthine	Modelling and Control of Top Tensioned Risers. (PhD Thesis, CeSOS)
IMT-2007-24	Johansen, Vegar	Modelling flexible slender system for real-time simulations and control applications
IMT-2007-25	Wroldsen, Anders Sunde	Modelling and control of tensegrity structures. (PhD Thesis, CeSOS)
IMT-	Aronsen, Kristoffer Høye	An experimental investigation of in-line and

2007-26		combined inline and cross flow vortex induced vibrations. (Dr. avhandling, IMT)
IMT-2007-27	Gao, Zhen	Stochastic Response Analysis of Mooring Systems with Emphasis on Frequency-domain Analysis of Fatigue due to Wide-band Response Processes (PhD Thesis, CeSOS)
IMT-2007-28	Thorstensen, Tom Anders	Lifetime Profit Modelling of Ageing Systems Utilizing Information about Technical Condition. (Dr.ing. thesis, IMT)
IMT-2008-29	Berntsen, Per Ivar B.	Structural Reliability Based Position Mooring. (PhD-Thesis, IMT)
IMT-2008-30	Ye, Naiquan	Fatigue Assessment of Aluminium Welded Box-stiffener Joints in Ships (Dr.ing. thesis, IMT)
IMT-2008-31	Radan, Damir	Integrated Control of Marine Electrical Power Systems. (PhD-Thesis, IMT)
IMT-2008-32	Thomassen, Paul	Methods for Dynamic Response Analysis and Fatigue Life Estimation of Floating Fish Cages. (Dr.ing. thesis, IMT)
IMT-2008-33	Pákozdi, Csaba	A Smoothed Particle Hydrodynamics Study of Two-dimensional Nonlinear Sloshing in Rectangular Tanks. (Dr.ing.thesis, IMT/ CeSOS)
IMT-2007-34	Grytøyr, Guttorm	A Higher-Order Boundary Element Method and Applications to Marine Hydrodynamics. (Dr.ing.thesis, IMT)
IMT-2008-35	Drummen, Ingo	Experimental and Numerical Investigation of Nonlinear Wave-Induced Load Effects in Containerships considering Hydroelasticity. (PhD thesis, CeSOS)
IMT-2008-36	Skejic, Renato	Maneuvering and Seakeeping of a Singel Ship and of Two Ships in Interaction. (PhD-Thesis, CeSOS)
IMT-2008-37	Harlem, Alf	An Age-Based Replacement Model for Repairable Systems with Attention to High-Speed Marine Diesel Engines. (PhD-Thesis, IMT)
IMT-2008-38	Alsos, Hagbart S.	Ship Grounding. Analysis of Ductile Fracture, Bottom Damage and Hull Girder Response. (PhD-thesis, IMT)
IMT-2008-39	Graczyk, Mateusz	Experimental Investigation of Sloshing Loading and Load Effects in Membrane LNG Tanks Subjected to Random Excitation. (PhD-thesis, CeSOS)
IMT-2008-40	Taghipour, Reza	Efficient Prediction of Dynamic Response for Flexible amd Multi-body Marine Structures. (PhD-thesis, CeSOS)
IMT-2008-41	Ruth, Eivind	Propulsion control and thrust allocation on marine vessels. (PhD thesis, CeSOS)
IMT-2008-42	Nystad, Bent Helge	Technical Condition Indexes and Remaining Useful Life of Aggregated Systems. PhD thesis, IMT

IMT-2008-43	Soni, Prashant Kumar	Hydrodynamic Coefficients for Vortex Induced Vibrations of Flexible Beams, PhD thesis, CeSOS
IMT-2009-43	Amlashi, Hadi K.K.	Ultimate Strength and Reliability-based Design of Ship Hulls with Emphasis on Combined Global and Local Loads. PhD Thesis, IMT
IMT-2009-44	Pedersen, Tom Arne	Bond Graph Modelling of Marine Power Systems. PhD Thesis, IMT
IMT-2009-45	Kristiansen, Trygve	Two-Dimensional Numerical and Experimental Studies of Piston-Mode Resonance. PhD-Thesis, CeSOS
IMT-2009-46	Ong, Muk Chen	Applications of a Standard High Reynolds Number Model and a Stochastic Scour Prediction Model for Marine Structures. PhD-thesis, IMT
IMT-2009-47	Hong, Lin	Simplified Analysis and Design of Ships subjected to Collision and Grounding. PhD-thesis, IMT
IMT-2009-48	Koushan, Kamran	Vortex Induced Vibrations of Free Span Pipelines, PhD thesis, IMT
IMT-2009-49	Korsvik, Jarl Eirik	Heuristic Methods for Ship Routing and Scheduling. PhD-thesis, IMT
IMT-2009-50	Lee, Jihoon	Experimental Investigation and Numerical in Analyzing the Ocean Current Displacement of Longlines. Ph.d.-Thesis, IMT.
IMT-2009-51	Vestbøstad, Tone Gran	A Numerical Study of Wave-in-Deck Impact usin a Two-Dimensional Constrained Interpolation Profile Method, Ph.d.thesis, CeSOS.
IMT-2009-52	Bruun, Kristine	Bond Graph Modelling of Fuel Cells for Marine Power Plants. Ph.d.-thesis, IMT
IMT 2009-53	Holstad, Anders	Numerical Investigation of Turbulence in a Sekwed Three-Dimensional Channel Flow, Ph.d.-thesis, IMT.
IMT 2009-54	Ayala-Uraga, Efren	Reliability-Based Assessment of Deteriorating Ship-shaped Offshore Structures, Ph.d.-thesis, IMT
IMT 2009-55	Kong, Xiangjun	A Numerical Study of a Damaged Ship in Beam Sea Waves. Ph.d.-thesis, IMT/CeSOS.
IMT 2010-56	Kristiansen, David	Wave Induced Effects on Floaters of Aquaculture Plants, Ph.d.-thesis, CeSOS.
IMT 2010-57	Ludvigsen, Martin	An ROV-Toolbox for Optical and Acoustic Scientific Seabed Investigation. Ph.d.-thesis IMT.
IMT 2010-58	Hals, Jørgen	Modelling and Phase Control of Wave-Energy Converters. Ph.d.thesis, CeSOS.
IMT 2010- 59	Shu, Zhi	Uncertainty Assessment of Wave Loads and Ultimate Strength of Tankers and Bulk Carriers in a

		Reliability Framework. Ph.d. Thesis, IMT/ CeSOS
IMT 2010-60	Shao, Yanlin	Numerical Potential-Flow Studies on Weakly-Nonlinear Wave-Body Interactions with/without Small Forward Speed, Ph.d.thesis,CeSOS.
IMT 2010-61	Califano, Andrea	Dynamic Loads on Marine Propellers due to Intermittent Ventilation. Ph.d.thesis, IMT.
IMT 2010-62	El Khoury, George	Numerical Simulations of Massively Separated Turbulent Flows, Ph.d.-thesis, IMT
IMT 2010-63	Seim, Knut Sponheim	Mixing Process in Dense Overflows with Emphasis on the Faroe Bank Channel Overflow. Ph.d.thesis, IMT
IMT 2010-64	Jia, Huirong	Structural Analysis of Intect and Damaged Ships in a Collission Risk Analysis Perspective. Ph.d.thesis CeSoS.
IMT 2010-65	Jiao, Linlin	Wave-Induced Effects on a Pontoon-type Very Large Floating Structures (VLFS). Ph.D.-thesis, CeSOS.
IMT 2010-66	Abrahamsen, Bjørn Christian	Sloshing Induced Tank Roof with Entrapped Air Pocket. Ph.d.thesis, CeSOS.
IMT 2011-67	Karimirad, Madjid	Stochastic Dynamic Response Analysis of Spar-Type Wind Turbines with Catenary or Taut Mooring Systems. Ph.d.-thesis, CeSOS.
IMT - 2011-68	Erlend Meland	Condition Monitoring of Safety Critical Valves. Ph.d.-thesis, IMT.
IMT – 2011-69	Yang, Limin	Stochastic Dynamic System Analysis of Wave Energy Converter with Hydraulic Power Take-Off, with Particular Reference to Wear Damage Analysis, Ph.d. Thesis, CeSOS.
IMT – 2011-70	Visscher, Jan	Application of Particla Image Velocimetry on Turbulent Marine Flows, Ph.d.Thesis, IMT.
IMT – 2011-71	Su, Biao	Numerical Predictions of Global and Local Ice Loads on Ships. Ph.d.Thesis, CeSOS.
IMT – 2011-72	Liu, Zhenhui	Analytical and Numerical Analysis of Iceberg Collision with Ship Structures. Ph.d.Thesis, IMT.
IMT – 2011-73	Aarsæther, Karl Gunnar	Modeling and Analysis of Ship Traffic by Observation and Numerical Simulation. Ph.d.Thesis, IMT.
Imt – 2011-74	Wu, Jie	Hydrodynamic Force Identification from Stochastic Vortex Induced Vibration Experiments with Slender Beams. Ph.d.Thesis, IMT.
Imt – 2011-75	Amini, Hamid	Azimuth Propulsors in Off-design Conditions. Ph.d.Thesis, IMT.
IMT – 2011-76	Nguyen, Tan-Hoi	Toward a System of Real-Time Prediction and Monitoring of Bottom Damage Conditions During

		Ship Grounding. Ph.d.thesis, IMT.
IMT-2011-77	Tavakoli, Mohammad T.	Assessment of Oil Spill in Ship Collision and Grounding, Ph.d.thesis, IMT.
IMT-2011-78	Guo, Bingjie	Numerical and Experimental Investigation of Added Resistance in Waves. Ph.d.Thesis, IMT.
IMT-2011-79	Chen, Qiaofeng	Ultimate Strength of Aluminium Panels, considering HAZ Effects, IMT
IMT-2012-80	Kota, Ravikiran S.	Wave Loads on Decks of Offshore Structures in Random Seas, CeSOS.
IMT-2012-81	Sten, Ronny	Dynamic Simulation of Deep Water Drilling Risers with Heave Compensating System, IMT.
IMT-2012-82	Berle, Øyvind	Risk and resilience in global maritime supply chains, IMT.
IMT-2012-83	Fang, Shaoji	Fault Tolerant Position Mooring Control Based on Structural Reliability, CeSOS.
IMT-2012-84	You, Jikun	Numerical studies on wave forces and moored ship motions in intermediate and shallow water, CeSOS.
IMT-2012-85	Xiang ,Xu	Maneuvering of two interacting ships in waves, CeSOS
IMT-2012-86	Dong, Wenbin	Time-domain fatigue response and reliability analysis of offshore wind turbines with emphasis on welded tubular joints and gear components, CeSOS
IMT-2012-87	Zhu, Suji	Investigation of Wave-Induced Nonlinear Load Effects in Open Ships considering Hull Girder Vibrations in Bending and Torsion, CeSOS
IMT-2012-88	Zhou, Li	Numerical and Experimental Investigation of Station-keeping in Level Ice, CeSOS
IMT-2012-90	Ushakov, Sergey	Particulate matter emission characteristics from diesel enignes operating on conventional and alternative marine fuels, IMT
IMT-2013-1	Yin, Decao	Experimental and Numerical Analysis of Combined In-line and Cross-flow Vortex Induced Vibrations, CeSOS
IMT-2013-2	Kurniawan, Adi	Modelling and geometry optimisation of wave energy converters, CeSOS
IMT-2013-3	Al Ryati, Nabil	Technical condition indexes doe auxiliary marine diesel engines, IMT
IMT-2013-4	Firoozkoohi, Reza	Experimental, numerical and analytical investigation of the effect of screens on sloshing, CeSOS
IMT-2013-5	Ommani, Babak	Potential-Flow Predictions of a Semi-Displacement Vessel Including Applications to Calm Water Broaching, CeSOS

IMT-2013-6	Xing, Yihan	Modelling and analysis of the gearbox in a floating spar-type wind turbine, CeSOS
IMT-7-2013	Balland, Océane	Optimization models for reducing air emissions from ships, IMT
IMT-8-2013	Yang, Dan	Transitional wake flow behind an inclined flat plate-----Computation and analysis, IMT
IMT-9-2013	Abdillah, Suyuthi	Prediction of Extreme Loads and Fatigue Damage for a Ship Hull due to Ice Action, IMT
IMT-10-2013	Ramìrez, Pedro Agustìn Pèrez	Ageing management and life extension of technical systems- Concepts and methods applied to oil and gas facilities, IMT
IMT-11-2013	Chuang, Zhenju	Experimental and Numerical Investigation of Speed Loss due to Seakeeping and Maneuvering. IMT
IMT-12-2013	Etemaddar, Mahmoud	Load and Response Analysis of Wind Turbines under Atmospheric Icing and Controller System Faults with Emphasis on Spar Type Floating Wind Turbines, IMT
IMT-13-2013	Lindstad, Haakon	Strategies and measures for reducing maritime CO2 emissons, IMT
IMT-14-2013	Haris, Sabril	Damage interaction analysis of ship collisions, IMT
IMT-15-2013	Shainee, Mohamed	Conceptual Design, Numerical and Experimental Investigation of a SPM Cage Concept for Offshore Mariculture, IMT
IMT-16-2013	Gansel, Lars	Flow past porous cylinders and effects of biofouling and fish behavior on the flow in and around Atlantic salmon net cages, IMT
IMT-17-2013	Gaspar, Henrique	Handling Aspects of Complexity in Conceptual Ship Design, IMT
IMT-18-2013	Thys, Maxime	Theoretical and Experimental Investigation of a Free Running Fishing Vessel at Small Frequency of Encounter, CeSOS
IMT-19-2013	Aglen, Ida	VIV in Free Spanning Pipelines, CeSOS
IMT-1-2014	Song, An	Theoretical and experimental studies of wave diffraction and radiation loads on a horizontally submerged perforated plate, CeSOS
IMT-2-2014	Rogne, Øyvind Ygre	Numerical and Experimental Investigation of a Hinged 5-body Wave Energy Converter, CeSOS